UNIVERSITÀ
DEGLI STUDI
DI PADOVA

Head Office: Università degli Studi di Padova

Department of Industrial Engineering

Ph.D. COURSE IN INDUSTRIAL ENGINEERING

CURRICULUM: CHEMICAL AND ENVIRONMENTAL ENGINEERING

36th SERIES

MODEL-BASED APPROACHES TO SUPPORT THE OPTIMISATION OF MICROALGAE GROWTH IN PHOTOBIOREACTORS

Coordinator: Ch.mo Prof. Giulio Rosati

Supervisor: Ch.mo Prof. Fabrizio Bezzo

Ph.D. student: Alberto Saccardo

A dissertation submitted in partial fulfillment

of the requirements for the degree of

Doctor of Philosophy

(Industrial Engineering)

Curriculum: Chemical and Environmental Engineering

at the

University of Padova (Italy)

2023

ma già volgeva il mio disio e 'l velle

Dante Alighieri, *Par.* XXXIII 143

Foreword

The research project presented in this Dissertation has involved the financial and intellectual support of many people and institutions, to whom the author is enormously grateful. Most of the research activity reported and discussed in the Dissertation has been conducted at CAPE-Lab, Computer-Aided Process Engineering Laboratory (Department of Industrial Engineering, University of Padova, Italy) under the supervision of Prof. Fabrizio Bezzo and co-supervision of Prof. Eleonora Sforza. Part of the work has been carried out at the Institute for Molecular Bioscience at The University of Queensland (St Lucia QLD, AUSTRALIA) during a 7-month stay under the supervision of Prof. Ben Hankamer.

The research discussed in this Dissertation has been supported financially by Fondazione CARIPARO. Additional financial support has been provided by Fondazione Aldo Gini.

All the material presented in this Thesis is original, except for explicit references provided by the author.

The full list of publications originated from this Dissertation is reported below.

CONTRIBUTIONS IN PEER-REVIEWED JOURNALS

- Saccardo, A., Felices-Rando, B., Sforza, E. and Bezzo, F. (2023). Droop model identification via model-based design of experiments to describe microalgae nitrogen uptake in continuous photobioreactors. *Chem. Eng. J.* 468, 143577.
- Saccardo, A., Bezzo, F. and Sforza, E. (2022). Microalgae growth in ultra-thin steady-state continuous photobioreactors: assessing self-shading effects. *Front. Bioeng. Biotechnol.* 10: 1–9.

CONTRIBUTIONS IN PEER-REVIEWED JOURNALS (submitted)

- Saccardo, A., Wolf, J., Bezzo, F. and Hankamer, B. Modelling microalgae growth based on dynamic high throughput pulsed light screens. *Submitted*

CONTRIBUTIONS IN PEER-REVIEWED JOURNALS (in preparation)

- Saccardo, A., Porcelli, A., Borella, L., Sforza, E. and Bezzo, F. A model to capture microalgae growth under ultra-high frequency pulsed light conditions. *In preparation*

CONTRIBUTIONS IN PEER-REVIEWED CONFERENCE PROCEEDINGS

- Saccardo, A., Felices-Rando, B., Sforza, E. and Bezzo, F. (2023). Model-Based Design of Experiments for the identification of microalgae growth models with limiting nutrients. In: *Computer Aided Chemical Engineering* 52, *Proc. of the 33th European Symposium on Computer Aided Process Engineering* (A.C. Kokossis, M.C. Georgiadis, E. Pistikopoulos, Eds.), Elsevier, Amsterdam (The Netherlands), 2135-214.

CONFERENCE ORAL PRESENTATIONS

- Saccardo, A., Felices-Rando, B., Sforza, E. and Bezzo, F. (2023). Model-Based Design of Experiments for the identification of microalgae growth models with limiting nutrients. Oral presentation (Keynote lecture) at: 33th European Symposium on Computer Aided Process Engineering, 18-21 June 2023, Athens (Greece).
- Saccardo, A., Felices-Rando, B., Bezzo F. and Sforza, E. (2022). Modelling the dynamics of microalgae growth in continuous photobioreactors under different nitrogen concentrations. Presented at: Convegno AISAM 2022, 16-18 October 2022, Naples (Italy).
- Saccardo, A., Sforza, E. and Bezzo, F. (2021). Using a milli-scale continuous photobioreactor for steady state analysis of light and residence time on cell growth. Presented at: Workshop Giovani AISAM, 24th September 2021, Rome (Italy).

POSTER PRESENTATIONS

- Saccardo, A., Felices-Rando, B., Sforza, E. and Bezzo, F. (2023). Droop model identification via model-based design of experiments in continuous photobioreactors. Poster presentation at: Young Algaeneers Symposium (YAS) 2023, 9-11 May 2023, Faro (Portugal).

Abstract

Microalgae are a wide class of photosynthetic organisms that, through photosynthesis, use solar energy to fix CO_2, release O_2 as a by-product and produce a biomass rich in carbohydrates, proteins, lipids and bioactive compounds. Their high photosynthetic yield and ability of growing fast and in harsh environments make them a promising candidate for sustainable bio-based technologies in critical sectors such as pharmaceutics, cosmetics, human and animal nutrition, aquaculture, chemicals and fuels, and pollution prevention. Currently, a great obstacle to the actual industrialisation of microalgae technology is represented by a limited comprehension of microalgae growth processes and reliable tools for representing their response in an industrial environment. For this reason, the development of reliable mathematical models that are capable of quantitative predictions of biomass growth as a response to different cultivation conditions is of paramount importance.

The aim of this Thesis is to enhance the comprehension and representation of the phenomena that affect microalgae growth in photobioreactors by employing a combination of experimental photobioreactor development and formulation and application of mathematical models. First of all, the influence of light on microalgae on the microalgae photosynthetic response has been investigated, considering different aspects. Firstly, the effect of continuous light on ultra-thin photobioreactors has been examined. Parameters of a Haldane-like models were estimated from experimental data at different optical paths. It was found that, due to the inability to account explicitly for mixing-induced light-dark cycles, Haldane-like models have limited capability in capturing experimental results at ultra-thin light paths and thus can be unsuitable to scale up experimental results from ultra-thin scales to higher scales. Then, microalgae growth under pulsed light regimes has been addressed, with both low and high light frequencies. To describe the dynamic effect of low frequencies on microalgae growth, a dynamic reformulation of the Camacho Rubio model was proposed, based on the theoretical knowledge of photosynthetic characteristic times, and its parameters were precisely estimated from High Throughput Screening data. For high frequency pulsed light cultivation, a different mathematical model accounting for photons absorption, usage and dissipation was examined. The model was modified, and its parameters were retrieved from experimental data. The modified model was able to provide meaningful physical explanations of the observed data and was further employed to guide respirometry experiments. The understanding of nutrient dynamics is also crucial to ensure the sustainability of microalgal production. Although different modelling approaches are available,

their calibration is often a complex and time-consuming task. The second main contribution of the Thesis is thus concerned with the use of model-based design of experiments techniques for the precise estimation of the Droop model in continuous photobioreactors to capture the dynamic effect of nitrogen uptake on microalgae growth. Results demonstrate that the proposed methodology can help reducing the experimental effort needed to estimate the model parameters. It is also shown that the newly calibrated model can represent nitrogen uptake dynamics effectively.

Riassunto

Le microalghe sono una vasta classe di microorganismi fotosintetici che, attraverso la fotosintesi, utilizzano la luce per fissare anidride carbonica, rilasciare ossigeno come sottoprodotto e produrre una biomassa ricca di carboidrati, proteine, lipidi, fitonutrienti e composti bioattivi. Le microalghe sono caratterizzate da un elevato rendimento fotosintetico, capacità di crescere rapidamente anche in ambienti non adatti all'uso agricolo e quindi la loro coltivazione non è in competizione con l'agricoltura per uso alimentare. Le microalghe possono quindi costituire un importante elemento di innovazione in settori biotecnologici come l'industria farmaceutica, cosmetica, la nutrizione umana e animale, l'acquacoltura, la produzione di biocarburanti e la lotta all'inquinamento. Tuttavia, un grande ostacolo all'industrializzazione di questa tecnologia è attualmente rappresentato dalla scarsa comprensione dei processi di crescita delle microalghe. Infatti, la crescita delle microalghe è influenzata da una combinazione e interazione di fattori come luce, nutrienti, temperatura e condizioni di processo. L'ottimizzazione di questi fattori è necessaria per un'efficiente e competitiva industrializzazione delle tecnologie basate su microalghe. Per questo motivo, è di fondamentale importanza lo sviluppo di modelli matematici affidabili in grado di dare descrizioni quantitative della crescita della biomassa in risposta a diverse condizioni di coltivazione.

L'obiettivo di questa tesi concerne il miglioramento della comprensione e rappresentazione dei fenomeni che influenzano la crescita delle microalghe nei fotobioreattori, utilizzando una combinazione di attività sperimentale e modellistica tramite sviluppo di fotobioreattori e applicazione di modelli matematici. Il primo contributo della Tesi riguarda l'influenza della luce sulle microalghe. Questo è stato affrontato in diversi aspetti. In primo luogo, è stato esaminato l'effetto della luce continua sulla crescita delle microalghe in fotobioreattori ultra-sottili. Successivamente, è stata studiata la crescita delle microalghe in regimi di luce pulsata, sia a bassa che ad alta frequenza. In ogni attività, sono stati utilizzati modelli matematici per interpretare e catturare i fenomeni osservati sperimentalmente. In particolare, sono stati esaminati diversi modelli matematici a crescente complessità: modelli simili a quello di Haldane, modelli ad unità fotosintetiche e un modello recentemente sviluppato che rappresenta l'assorbimento, l'uso e la dissipazione dei fotoni.

Oltre alla luce, la comprensione dell'effetto dei nutrienti sulle dinamiche di crescita è cruciale per garantire la sostenibilità della produzione di microalghe. Il secondo contributo principale della tesi è quindi relativo all'uso del model-based design of experiments (MBDoE) per la stima precisa del

modello di Droop in fotobioreattori continui, al fine di catturare l'effetto dinamico dell'assorbimento di azoto sulla crescita delle microalghe. In particolare, è stato dimostrato che un approccio MBDoE all'indagine sperimentale può notevolmente ridurre lo sforzo e il tempo richiesti.

Table of contents

Chapter 1

Literature review and thesis objectives

Over the years, microalgae attracted considerable attention due to their characteristics. This interest spans from the academic to the industrial field, from physiology to engineering, thus motivating the development of a rich mathematical modelling substrate. In this Chapter, an initial excursus on the historical development of the microalgae field and the actual perspectives of this sector is presented, followed by a systematic view of the main fields of microalgae mathematical modelling.

1.1 Industrial exploitation of microalgae and open challenges

Microalgae are a wide variety of photosynthetic microorganisms, both prokaryotic and eukaryotic, that reproduce themselves using photosynthesis to convert light and CO_2 into chemical energy and oxygen. Microalgae can be found in a wide range of environments, including freshwater, marine habitats, and damp terrestrial settings. They play a crucial role in the ecosystems, being the basic components of food chains. Moreover, they are the main producers of oxygen, contributing to 40% of global photosynthesis (Hamed, 2016; Sharma & Rai, 2011)

Through photosynthesis, microalgae derive energy from light and acquire carbon from inorganic sources. In comparison to terrestrial plants, microalgae exhibit higher annual photon-to-biomass conversion efficiencies, around 3% compared to <1% for higher plants (Blankenship et al., 2011). Combining these attributes with the considerable diversification of microalgae strains, microalgae represent a promising tool for the production of valuable molecules as proteins, lipids, carbohydrates, and pigments with high yields (Levasseur et al., 2020). Moreover, microalgae can be cultivated in wastewater or on non-agricultural land without the use of pesticides, thus avoiding any competition in arable land and conflict with food or other crop-based product production (Levasseur et al., 2020). Additionally, they have the capacity to recycle atmospheric carbon dioxide, thereby mitigating associated environmental impacts.

These characteristics explain the attention gained by microalgae over the past 70 years for different industrial applications (Barbosa et al., 2023).

During World War II, Germany explored microalgae as a potential major food source. Later in the 1970s, microalgae were employed for wastewater purification and shellfish production through algal ponds and raceways. In the 1990s, markets for dry microalgal biomass and carotenoids for health food and aquaculture feeds started to develop and expand (Barbosa et al., 2023). Moreover, microalgae cultivation received notable for the production of biofuels. In fact, internal microalgae cell reserves of lipids can be converted into biodiesel, while carbohydrates can be employed for bioethanol production (Rizwan et al., 2018). This why the rise in crude oil prices in the 1990s and 2005–2010 spurred interest in microalgae for biofuels. However, this interest later diminished as oil prices decreased (Barbosa et al., 2023).

All these steps, though temporary, led to significant advancements in microalgae production technologies. In the last decade, the microalgal community has grown substantially, driving technological developments and scale-up of production facilities.

In particular, the recent rising need for sustainable protein sources and food ingredients prompted a shift in microalgal production companies towards this sector (Barbosa et al., 2023). Indeed, microalgae can contribute to food security by producing proteins and lipids to address population growth and environmental challenges. They have potential for the production of Single-Cell Protein (SCP) and lipids (TAG, PUFAs as EPA e DHA) that can serve as nutritional sources for both animal feed and human consumption (Barbosa et al., 2023). In particular, polyunsaturated fatty acids (PUFAs) like EPA and DHA, which can be produced by specific microalgae strains, are also beneficial for cardiovascular health (Khan et al., 2018). On the other hand, triglycerides (TAGs) are used in other applications as cosmetics and personal care (Barbosa et al., 2023).

Microalgae constitute a promising way to produce pigments. Microalgae photosynthetic pigments are classified in three groups: chlorophylls (responsible for green colour), carotenoids (responsible for yellow /orange colour), phycobiliproteins (responsible for red/blue colours) (Levasseur et al., 2020). These pigments exhibit interesting health-promoting attributes. They have antioxidant properties, precursors for essential vitamins, immune activators, and anti-inflammatory properties (Borowitzka, 1995; Hamed, 2016). Consequently, their application spans the domains of nutraceuticals, pharmaceuticals, and cosmetics (Levasseur et al., 2020). Specifically, they find utilization as natural pigments, nutritional adjuncts, and reservoirs of biologically active molecules, thus manifesting their multifaceted significance (García et al., 2017). In addition to pigments, different microalgae strains are rich sources of vitamins such as vitamin E and C (Khan et al., 2018).

Recently, increasing interest has been devoted to microalgae as versatile platforms for producing biopharmaceuticals, such as vaccines and therapeutic recombinant proteins (Barbosa et al., 2023).

Oral vaccines can be produced with microalgae due to their protective cell walls and ability to efficiently express and secrete antigenic proteins (Barbosa et al., 2023). It is foreseen that the development of genetic toolboxes and engineering methods for microalgae will be crucial for optimizing protein expression and secretion for biopharmaceutical applications (Barbosa et al., 2023).
In addition to the production of biocompounds, microalgae have environmental applications, and they have garnered significant attention as a viable response to environmental challenges (Quinn & Davis, 2015; Ward et al., 2014). For instance, they can use carbon from combustion gases as their main carbon source (Milledge, 2011; Razzak et al., 2013; Sierra et al., 2017) and exhibit the capability to live in wastewater environments, employing pollutants as nutrients (Gonçalves et al., 2017; Sierra et al., 2017). Microalgae chemical composition, characterized by elevated levels of carbohydrates and proteins, holds potential also for bioplastic production (Hempel et al., 2011; Rahman, 2020; Zeller et al., 2013) and can be harnessed as biofertilizers due to their rich micronutrient profile.
From an economic perspective, the global market value of products derived from microalgae was estimated to be around 32.60 billion USD in 2017, and this value is anticipated to rise to approximately 53.43 billion USD by 2026 (Rahman, 2020). At present, applications in food, animal feed, and nutraceuticals absorb over 75% of microalgae-derived product output (Rahman, 2020). This further highlights the economic potential of high-value microalgae products (Levasseur et al., 2020). Of particular interest among these products are colouring agents, with a revenue of 300 million USD in 2009, and nutraceuticals, with 30 million USD in the same year (Rahman, 2020). Currently, the United States, Asia, and Oceania are the leaders for the market of microalgae-based products. In the immediate future, it is likely that Europe will also become a prominent player in this market (Rahman, 2020).
Despite the great range of applications, the commercial bulk production of microalgae is still limited by a lack of scale, that is also required to reach competitive production costs (Barbosa et al., 2023).
One of the challenges that have not been solved yet is to close the disparity between the highest achievable theoretical biomass productivities, or even productivities observed at the lab scale, and the lower biomass productivities found on large scale industrial systems. This issue is still open, since the great complexity embedded in microalgal growth processes hinders its efficient application.
In fact, microalgae growth results from a complex interplay of different factors (Mata et al., 2010): thus, it is paramount to select favourable culture conditions to improve the productivity of desired product. This is also linked to the design and operation of efficient and economically feasible microalgae cultivation systems.

Among all the factors influencing microalgae growth, the optimisation of light supply is the most important. Indeed, microalgae growth can be strongly limited by the degree of light penetration in the cultivation system, often resulting in dilute cultures with low biomass concentrations (Levasseur et al., 2020). To overcome this problem, not only optimal theoretical light conditions must be determined, but also a suitable cultivation system to ensure that those illumination levels are met in the culture (Rizwan et al., 2018).

In addition to light, microalgae require nutrients (e.g. N, P, C) in specific proportions, only obtainable in controlled environments. Since the addition of nutrients represent a substantial energy and resource inputs cost, these cultivating conditions must be optimised too, to maximise the productivity and minimise the waste (Rizwan et al., 2018).

Moreover, microalgal cultures must be held in controlled conditions, since they are prone to contamination by bacteria, fungi, other competing microalgae and other microorganisms, which can disrupt the desired product yields and purity and even cause total collapses of the cultures (Rizwan et al., 2018).

In addition, while microalgae have the potential to produce valuable compounds, production levels of natural, wild microalgae strains might not be sufficient to meet industrial demands, thus necessitating optimization of metabolic pathways and genetic modifications (Barbosa et al., 2023).

Moreover, since the majority of the microalgae experimental activity is carried at laboratory scales, transitioning from laboratory to production at large scales requires appropriate scale up techniques.

The aforementioned challenges can be overcome only by a proper comprehension of the biological phenomena involved in microalgae growth. For this aim, mathematical modelling can be a useful resource (Bernard et al., 2016). Over the years, mathematical models have been developed to understand the effect of light, temperature and nutrients on microalgae growth (Darvehei et al., 2018), as well as the production of high value compounds as a result of those effects (Bekirogullari et al., 2020). The distribution of light in cultivation systems was modelled through mathematical equations (Béchet et al., 2013) and thus can be a valuable tool for the scale up to industrial scales. Microalgae metabolic pathways have been represented mathematically (Tibocha-Bonilla et al., 2018) and can guide the genetic engineering of photosynthetic metabolism (Perin et al., 2017). However, despite it is widely recognised that mathematical modelling is necessary to understand, optimise and control microalgal growth, currently its potentialities have not been fully exploited (Barbosa et al., 2023).

The following sections of this Chapter are devoted to the presentation of a systematic view of the state of the art of mathematical modelling of microalgae. Figure 1.1 shows a scheme of some of the most relevant fields in the modelling of microalgae cultivation systems. In this Chapter, blocks (I)-

(II)-(V) of Figure 1.1 will be analysed more accurately, since they are the focus of the following Chapters of this thesis. However, a general description of the blocks (III)-(IV)-(VI)-(VII) is also included, since they are essential to understand the "big picture" of the microalgae modelling world. The following Sections review the main classes of mathematical models of Figure 1.1. In the last Section, some fundamental gaps in the state of the art are highlighted: challenging of part of these gaps will be the focus of the following Chapters of this thesis.

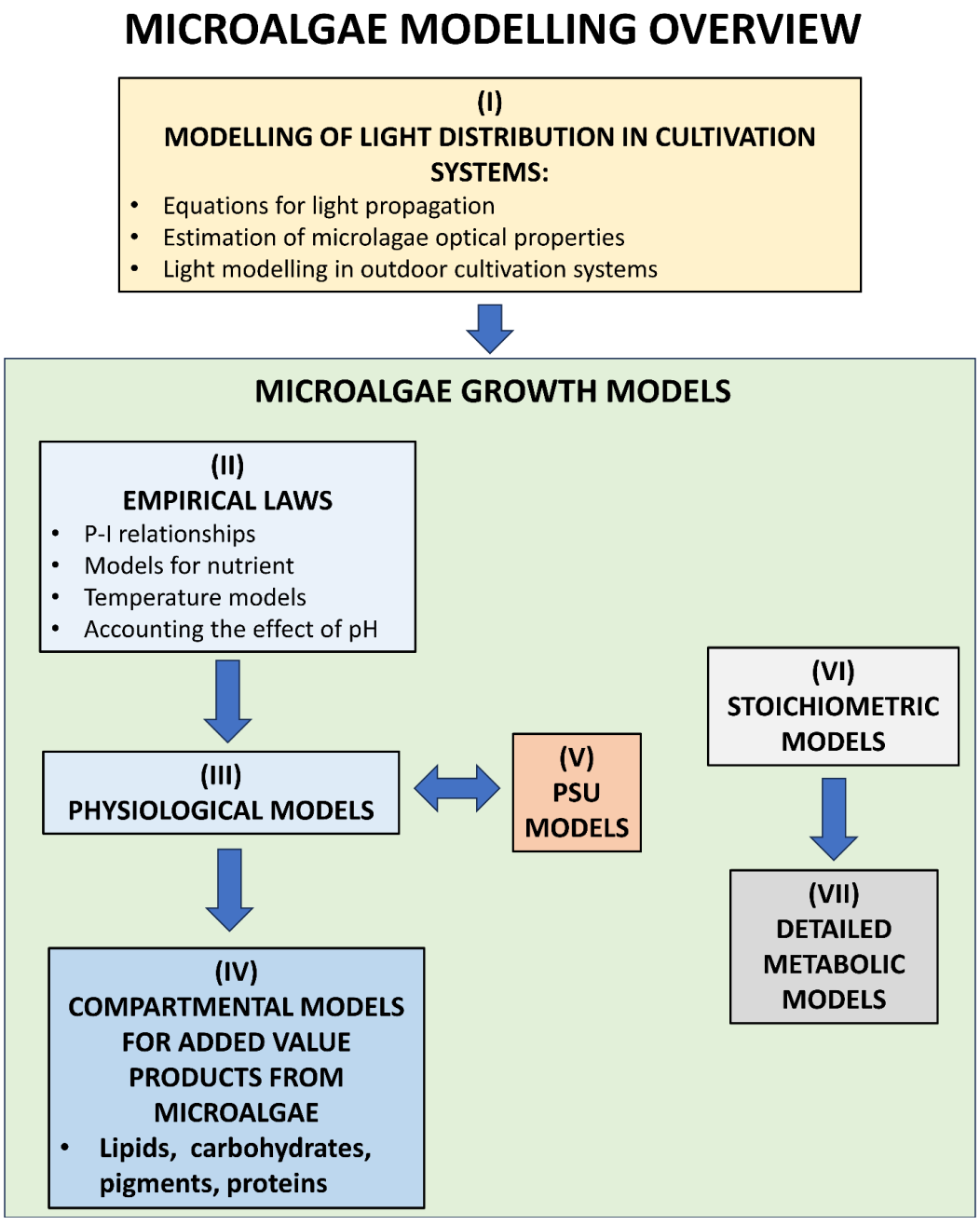

Figure 1.1: *Scheme of the main classes of mathematical models in the microalgal sector.*

1.2 Modelling of light distribution

In the area of modelling of microalgae systems, one of the most important issues is the representation of the light distribution in the culture. Microalgae are cultivated in open systems or closed photobioreactors (PBRs), which can have different arrangements (e.g. tubular or flat-plate). Nevertheless, a light gradient is always present in microalgae cultures and is affected by the geometry of the cultivation system (e.g. depth of the PBR) and by the properties of the culture (e.g. cell concentration and pigment content). Moreover, in all cultivation systems cells are exposed to two main phenomena that affect their exposure to light: self-shading and mixing induced dark cycles. Self-shading is the mutual shading of light from other cells, that results in the creation of a light gradient in the culture. Due to the mixing system, cells cyclically move from regions with high illumination to others with low illuminations, thus experiencing light-dark mixing induced cycles.

Different mathematical expressions were developed to model light distribution in PBRs. The most common is the Lambert-Beer law, that expresses light intensity $I(z)$ [µmol m^{-2} s^{-1}] at a specific spatial coordinate z [m] as:

$$I(z) = I_0 \exp(-k_a c_x z) \quad (1.1)$$

with I_0 [µmol m^{-2} s^{-1}] as the incident light intensity, k_a [m^2 g^{-1}] the light absorption coefficient, c_x [g m^{-3}] as the biomass concentration. The popularity of the Lambert-Beer law is principally due to its simplicity, with only one parameter to be estimated. However, its major limitations are that it is suited for isotropic media only and it neglects light scattering in the culture. Thus, its applicability is hindered in high density systems, usually associated with higher scattering (Béchet et al., 2013). To overcome this limitation, different empirical expressions have been proposed to account for scattering (Béchet et al., 2013; Bernard & Lu, 2022; Karam et al., 2021; Khichi et al., 2019).

A more rigorous method to calculate light distribution is represented by the radiative transfer equation (RTE) (Houf & Incropera, 1980). The formulation of RTE can be obtained by performing a radiation balance on a unit element of fluid accounting incident, absorbed, transmitted and scattered sources of radiation (Béchet et al., 2013). The main assumption for the RTE is that photons propagate in the culture medium with the same speed, and they do not interact with each other but only with the culture medium (Dauchet et al., 2016). The rigorous solution of the RTE in a three-dimensional geometry is not straightforward and required computationally intensive numerical (e.g., Monte Carlo) methods (Béchet et al., 2013). However, different simplification of the RTE were proposed in literature. Among those, the so-called P1 approximation and the two flux model are the most common. The P1 approximation is associated with high scattering but low absorbing media (Dauchet et al., 2016). The

two-flux approximation account for both in-scattering and anisotropic scattering assuming that it is only confined in the direction of propagation of light (Dauchet et al., 2016). Between the two approximations, the two-flux model is particularly popular, also thanks to the existence of an analytical solution (Cornet et al., 1992, 1994).

All the models mentioned required the determination of light parameters (e.g. k_a in the Lambert-Beer law of Equation 1.1). For simple models as the Lambert-Beer law, light parameters can be simply estimated from light absorption measurements, from different biomass concentrations. In other works, empirical relations have been employed to link light parameters to the pigment or chlorophyll contents (Karam et al., 2021). More rigorous methods employ the fundamental principles behind microalgae optical properties (Lehmuskero et al., 2018). Another approach was proposed in Dauchet et al. (2016), requiring information only of the pigment cell content and cells size distribution in the cultivation system.

Modelling of light distribution in outdoor cultivation systems adds a further level of complexity. In fact, the selection of a suitable light distribution law and estimation its parameters accurately are not sufficient. Illumination of outdoor cultivation systems is affected by the sunlight, and thus an atmospheric model for light propagation is needed (Duffie et al., 2020). Moreover, sunlight intensity and direction of propagation are influenced by the season, the geographical coordinates and the hour in the diurnal cycle (Slegers et al., 2011). The orientation of the reactor (e.g., north-south), the influence of neighbouring reactors, the reflection of light by surrounding surfaces have a further effect of the incident light on the surface of the cultivation system (Slegers et al., 2011). Depending on the geometry of the system (i.e., horizontal/verical; flat/open pond/tubular), there can be multiple incident light directions. All these elements must be accounted to obtain realistic model predictions (Slegers et al., 2011).

Up to this point, the effect of self-shading was accounted only, whilst no models were proposed to include mixing-induced light cycles. Indeed, modelling of mixing cycles is not straightforward, since the fluid dynamics of the system must be accounted in principle. To tackle this problem, different studies have employed Computational Fluid Dynamics (CFD) to model microalgae cultivation system, accounting rigorously for mixing cycles (Luzi & McHardy, 2022).

In addition to light intensity and direction, its spectrum also plays a fundamental role on microalgae growth (Darvehei et al., 2018). Microalgae grow better in a range of wavelength known as photosynthetically active radiation (PAR), that spans from 400 nm to 700 nm (Sukenik et al., 1987). However, most of the works focus on white light and neglect, while a smaller number of studies has been devoted on the effect of other light types on microalgal growth (Fuente et al., 2017).

1.3 Empirical models for microalgae growth

The earliest and most important class of models employed for the description of microalgae growth are called *empirical models*. This class of models is constituted by empirical relationships developed over the year to fit experimental data. For this reason, they mostly lack a deep physiological foundation. Nevertheless, their simple mathematical structures, with a small number of parameters, contributed to their popularity. Different empirical models were formulated to express the influence of light, nutrients, temperature, pH/CO_2 on microalgae growth. Typically, there is no unified consensus over the best model structures (Béchet et al., 2013). However, for engineering purposes, a general criterion should be to select the simplest model able to fit experimental data. For this reason, in this Section, particular attention has been devoted on the number of parameters for each model type.

1.3.1 Light and P-I relationships

Light is the most important factor affecting microalgae growth. The influence of light on the rate of photosynthesis is often expressed through Photosynthetic-Irradiance (P-I) curves. A typical P-I curve is showed in Figure 1.2.

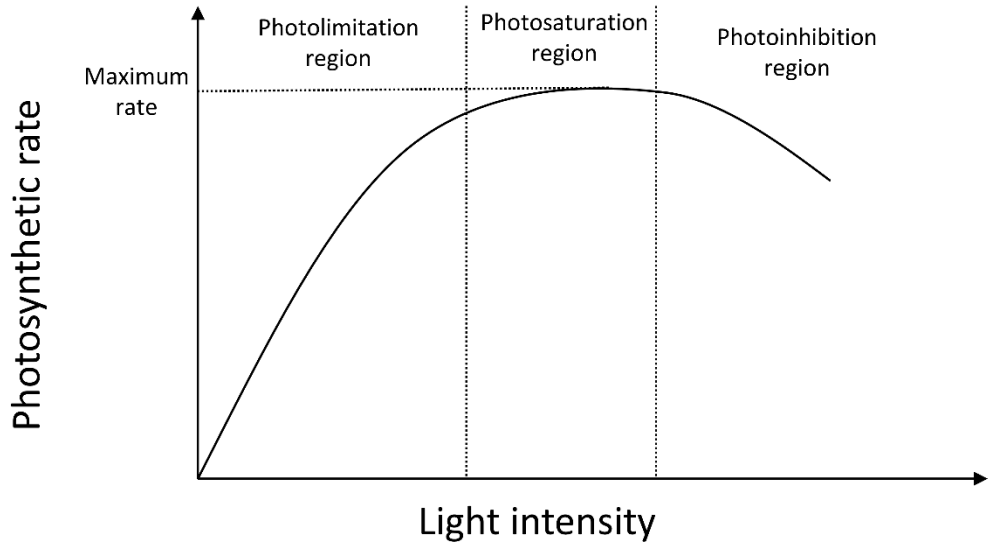

Figure 1.2: *Typical P-I curve* (adapted from Béchet et al., 2013).

Three different regimes can be identified (Béchet et al., 2013):

1. *Photolimitation* at low values of light intensity. Photosynthesis is limited by the amount of light captured by the cells and thus the growth rate is proportional to light intensity.

2. *Photosaturation*: after a certain value of light intensity, cells became light saturated. Photosynthesis is not limited by light capturing but by the subsequent reactions that process photons. In this condition, light intensity is optimal, and the photosynthetic rate is maximum.
3. *Photoinhibition*: at high light conditions cells are damaged by the excess of light. Due to the deactivation of proteins involved in photosynthesis (Camacho Rubio et al., 2003), growth rate diminishes with light.

Different empirical relationships (also called P-I relationships or models) were formulated to describe the P-I curves. The simplest P-I models have two parameters as the Monod model (Tamiya et al., 1953), hyperbolic tangent (Chalker, 1980) and Poisson model (Cullen, 1990). A typical form of the Monod model is:

$$\mu = \mu_{max} \frac{I}{K_I + I} \tag{1.2}$$

where μ [d^{-1}] is the specific biomass growth rate, μ_{max} [d^{-1}] is the maximum specific biomass growth rate and K_I [μmol m^{-2} s^{-1}] is the light half saturation constant, i.e., the value of light intensity at which the specific biomass growth rate is half the maximum one.

P-I relationships with 2 parameters are typically unable to represent photoinhibition (with the exception of models proposed by Steele (1962) and Lee et al. (1987)). For this reason, usually at least three parameters are required to capture photoinhibition. Three parameters P-I models were proposed by the Aiba (1982), Bernard & Rémond (2012), Talbot et al. (1991) and Muller-Feuga (1999). To obtain better fitting, additional parameters were added, as the five parameters model in García-Malea et al. (2006) and the six parameters model in Molina Grima et al. (1996).

When microalgae cultivations are exposed to dark conditions, a decrease in the biomass concentration happens due to cell respiration. To account for this effect, usually a negative respiration term is included in the formulation of the productivity rate (Béchet et al., 2013).

All the mentioned P-I relationships are function of light intensity. However, in microalgae cultivation systems a gradient of light will always be present, as discussed in Section (1.2). There are three main ways to account for this light gradient in empirical models (Béchet et al., 2013). The first way is to express the photosynthesis rate of the entire culture, as a function of the incident light intensity at the system external surface only. Due to the simplicity of measuring the incident light intensity, the implementation is straightforward. However, in this way the kinetic parameter values are specific to the unique operational conditions employed for model development and validation. This considerably constrains the range of model applicability.

A second strategy is to expresses the photosynthetic rate of well-mixed cultures as a function of the average light intensity within the culture. This is motivated by the fact that microalgae cells experience the same light intensity on average, resulting in a uniform photosynthesis rate across the culture (Béchet et al., 2013). However, a third and more effective approach involves the computation of local photosynthetic rates across the culture. For instance, by coupling a Monod-like model with the Lambert-Beer law, the local growth rate $\mu(z)$ at the coordinate z in a rectangular geometry can be calculated as:

$$\mu(z) = \mu_{max} \frac{I_0 \exp(-k_a c_x z)}{K_I + I_0 \exp(-k_a c_x z)} \quad (1.3)$$

To obtain and average photosynthetic rate of the culture, the local expression can be averaged along the light attenuation path through an integral average on the reactor thickness W [m] to obtain the average specific biomass growth rate $\bar{\mu}$ [d^{-1}]:

$$\bar{\mu} = \int_0^W \mu(z)\ dz \quad (1.4)$$

The last approach showed to be the most effective to accurately predict productivity in microalgae cultivation systems (Béchet et al., 2013). However, even with this integration method, P-I relationships do not explicitly account for mixing induced light-dark cycles, since they do not consider the "light story" of microalgal cells (i.e., the illumination conditions experienced by a single cell as it moves in the system due to turbulence).

1.3.2 Effect of nutrients

In light-saturating conditions, microalgae growth depends on nutrients such as nitrogen, phosphorus, and carbon sources available in the cultivation system. Kinetic models can be expressed as a function of the concentration of a single nutrient through empirical expressions.

The first category of models link growth to the concentration of a nutrient in the culture bulk. The Monod model (Monod, 1949) is one of the most important of this category. With only two parameters, it is easy to apply and was employed for different nutrients (N, P, CO_2) in many cases (Lee et al., 2015).

However, the Monod model is limited in the description of microalgae growth under high nutrients concentrations since is unable to capture substrate inhibition. Thus, similarly with the case of P-I relationships, it was modified to account for inhibition under high concentrations, as in the case of the three parameters model of Andrews (1968).

In nature, microalgae growth is often affected by the interplay among diverse nutrient resources and light instead than by a single factor. This concept has been applied to the development of kinetic

models, by establishing criteria to couple a single model (as Haldane or Andrew) for each nutrient together to represent co-limited growth. In particular, co-limitation-based expressions can be divided into two main types: threshold and multiplicative models. Threshold models assume that the overall growth is influenced only by the nutrient present in lowest concentration. The general expression for threshold models is thus:

$$\mu = \mu_{max} \min(f(S_1), f(S_2), \dots, f(S_n)) \quad (1.5)$$

With $f(S_i)$ [-] being the effect of the substrate S_i on growth. On the other hand, multiplicative models assume that all nutrients simultaneously affect biomass growth rate. Thus, the general expression for these models can be written as:

$$\mu = \mu_{max}\, f(S_1) \cdot f(S_2) \cdot \dots f(S_n) \quad (1.6)$$

Other formulation for co-limited models can be found in Darvehei et al. (2018).

The nutrient models mentioned so far are expressed as a function of the external nutrient concentration. Thus, in case of absence of nutrients, zero growth is predicted. However, when a nutrient is depleted from the cultivation media, microalgae can still grow because they rely on internal nutrients storage. To account for this phenomenon, Martínez Sancho et al. (1997) formulated a three parameters model able to account microalgae growth in nutrients-depleted media and Martínez et al. (1997) also included the description of inhibition for high concentrations of substrate. However, these models are rarely employed in literature (Lee et al., 2015).

To provide a more realistic representation of growth also in nutrients depleted conditions, the concept of the internal nutrient cell quota was introduced. The Droop model (Droop, 1968) is one of the most representative of this category, along with the Caperon and Meyer (Caperon & Meyer, 1972a, 1972b) and Flynn (Flynn, 2002) ones. In these models, the growth rate is dependent on the internal nutrient cell concentration. For instance, in the classical formulation of the Droop model, μ is linked to the internal quota of the considered nutrient q [-] as:

$$\mu = \mu_{max}\left(1 - \frac{q_{min}}{q}\right) \quad (1.7)$$

with q_{min} [-] the minimum nutrient quota in the cell. Expressions as Equation 1.7 are then coupled with material balances on the concentration of the nutrient in the bulk and on the internal quota, with kinetic expressions for the uptake and the consumption of the nutrient. Thus, these models can be applied both to conditions where the nutrient cell rate of uptake from the culture medium is equal to the nutrient consumption rate in the cell, and to cases where the two rates are different. As a result, these models are more suitable for describing nutrients-depleted conditions. However, the

applicability of quota models is hindered by the experimental difficulty in measuring the nutrient quota, as well as a lack of clear interpretation of the quota (Lee et al., 2015).

Despite their empiric nature, Droop-like quota models introduce the concept of *compartmental models*. Employing different compartments, compartmental models are able to account for intra-cellular phenomena in a simplified way. By adding additional compartments for cell quotas of different nutrients, compartmental models can easily be extended to capture microalgae co-limited growth. Moreover, compartmental models are fundamental for the establishment of advanced model structures beyond simple empirical fitting curves. This concept will be extensively employed in the mathematical models in Sections (1.4,1.5,1.6).

1.3.3 Modelling the effect of temperature

After light and nutrients, temperature plays a key role in microalgal growth. Different models have been proposed to account for the effect of temperature on microalgae growth. The first, and more employed, category for models for temperature are uncoupled models. Their mathematical expression is similar to multiplicative models for nutrients:

$$\mu = \mu_{max} f(T) \tag{1.8}$$

with $f(T)$ [-] being the effect of temperature T [K] on microalgal growth. With this mathematical framework, it is easy to integrate the influence of temperature with the one of light and nutrients. Models to formulate $f(T)$ include simple empirical relationships as the two parameters one in Ratkowsky et al. (1982), and the four parameters one in Ratkowsky et al. (1983) and in Zwietering et al., 1991). Mimicking classical kinetic expressions in chemistry, the Arrhenius law was also employed, as in the four parameters model by Rosso et al. (1993). Another widespread empirical model employs the concept of three cardinal temperatures $T_{min}, T_{opt}, T_{max}$. Microalgae can grow only when the temperature is between T_{min} and T_{max}, and the maximum growth rate occurs at T_{opt}. $T_{min}, T_{opt}, T_{max}$ are parameters specific for each microalgae strain. Three parameters cardinal temperature models were proposed by Rosso et al. (1991), Weikai & Hunt (1999) and Rosso et al. (1993). Other temperature models include six parameter models (Schoolfield et al., 1981; Sharpe et al., 1977; Sharpe & DeMichele, 1977), where growth inactivation due to high and low temperatures and active growth are modelled with equations similar to those in classical thermodynamics.

In addition to uncoupled models, a second class of temperature model was formulated in literature (Béchet et al., 2013). This class takes the name of coupled models. Coupled models develop a mathematical framework to account for the potential interdependence between light and temperature on the photosynthetic rate. This can be achieved by formulating light parameters of the P-I curves as

a function of temperature as in the nine parameters model in Dermoun et al. (1992). Despite the better theoretical representation of the impact of temperature of coupled models, uncoupled models are often preferred due to their simplicity (Béchet et al., 2013).

1.3.4 Modelling the effect of carbon and pH

Carbon is one of the most important nutrients for microalgae growth and its effect is often expressed through the empirical relations of Section (1.3.2). However, carbon concentration is closely related to the pH of the aqueous culture, since carbon is usually provided to the culture by injection of carbon dioxide (Darvehei et al., 2018). Also for pH, there is an optimum strain-specific range where microalgae growth is maximised. Thus, instead of carbon, the effect of pH on microalgae growth was accounted in different models in literature. Concentrations of H^+ ions are employed in the three parameters model in Bailey & Ollis (1976) and four parameters model in Zhang et al. (1999), while pH in the three parameters model in Jayaraman & Rhinehart (2015) and five parameters one in Costache et al. (2013). Dissolved inorganic carbon in an aqueous culture can exist in different forms as CO_2, HCO_3^-, CO_3^{2-}, that have different contributions on microalgae growth. Filali et al. (2011) thus formulated a comprehensive model, where all three types of inorganic carbon were considered. They employed mass transfer relation to calculate the amount of carbon dioxide in the culture, stoichiometric equations and thermodynamic balances to calculate the total inorganic carbon concentration in the culture and expressed its influence on microalgal growth rate. However, a common assumption is that carbon dioxide is in excess and thus its modelling is neglected (Darvehei et al., 2018).

1.3.5 Modelling the inhibiting effect of oxygen

Accumulation of oxygen in the culture poses a significant challenge to microalgal growth, since numerous studies confirmed its inhibition effect of microalgae growth (Darvehei et al., 2018). Oxygen is produced as a by-product of photosynthesis, resulting in concentrations that can exceed four times the air saturation level within the culture (Darvehei et al., 2018). Oxygen accumulation occurs both in open ponds and closed PBRs but is more prominent in the latter due to their closed structure. The inhibitory effect of oxygen on microalgae growth can be accounted in a multiplicative framework as the one of Equation 1.6. Different models were developed to describe oxygen inhibition, as the one parameter model of Miyachi et al. (1955), two parameters models of Concas et al. (2016) and Fernández et al. (2012) and three parameter model of Costache et al. (2013).

1.4 Physiological models of microalgae growth

Despite their usefulness, empirical relationships are unable to provide a detailed biologically sounding description of microalgae phenomena. Their lack of biological depth also makes empirical models inadequate for the representation of key phenomena as photoacclimation, i.e., the adaptation of microalgae pigment content to different light conditions (Bernard et al., 2016). A second class of models, called *physiological models,* was thus developed during the years, mostly in the ecology and oceanography fields. The principal objective of physiological models was to provide a detailed description of photosynthesis in microalgae cells. Differently from empirical models, physiological models attempt at capturing photosynthesis by "looking inside the cell", while aiming at maintaining a simple mathematical structure. Physiological models are characterised by two major features. They postulate a hypothetical, simplified photosynthetic (or, more in general, metabolic) scheme, focused on the phenomena of interest. With that scheme, they propose a compartmental mathematical model by formulating material balances on each compartment.

Depending on the specific model, physiological models can examine the effect of light, nutrients temperature on cell growth and biomass composition. Differently from simple empirical models, physiological models are suited to model dynamic variations in the biomass composition. This capability comes at the cost of higher complexity and more parameters than empirical relationships.

The first physiological models where specifically focused on the description of photosynthesis, including the effect of photoacclimation. Geider et al. (1996) formulated a physiological model by assuming a partition of the cellular carbon in three pools: light harvesting apparatus, biosynthetic apparatus and energy storage reserve.

Notably, authors employed P-I empirical relationships to express the effect of light on biomass growth. In fact, we found that P-I and other empirical relationships as those in Section (1.3) are often included in physiological models (e.g., see Flynn et al. (2001); Geider et al. (1996), (1997), (1998); Kroon & Thoms (2006); Marshall et al. (2000); Ross & Geider (2009) as examples). Thus, physiological models can be viewed as the natural extension of empirical models to capture additional phenomena. Through the formulation of dynamic balances between compartments, the model in Geider et al. (1996) is able to describe dynamical variations in the biomass concentration. Moreover, by adding additional compartments, the authors proposed a formulation to account for lag phenomena encountered experimentally in cultivation systems.

The compartmental structure of physiological model can vary between models. Instead of three carbon pool, Geider et al. (1997) formulated material balances on the chlorophyll and cell organic carbon. Moreover, authors considered the effect of nutrients and temperature through empirical

models in addition to the P-I curves. Model formulations in Geider et al. (1996) and Geider et al. (1997) evolved in the model proposed in Geider et al. (1998), arguably one of the most complete physiological models, considering material balances of carbon, nitrogen and chlorophyll compartments and expanding the description of photoacclimation description. Models presented above do not consider photoinhibition. The model in Marshall et al. (2000) includes the effect of photoinhibition by linking it to the damage and repair cycles of protein D1 and thus adding an additional compartment for this protein.

Other examples of physiological models can be found in Flynn et al. (2001), Kroon & Thoms (2006) and Ross & Geider (2009).

Despite the huge amount of work behind the development of physiological models, they application to industrial cultivation systems has been greatly hindered by the higher complexity and number of parameters of these models compared to empirical ones. However, physiological models were fundamental for the development of compartmental models for added value products.

Indeed, the initial focus of physiological models was to provide an accurate description of photosynthesis. To achieve this, they utilized a compartmental representation that described intracellular quotas of carbon, nitrogen, pigments, and energy reserve pools. By linking these intracellular compartments to a specific product of interest (e.g. lipids, carbohydrates, pigments), physiological models naturally offered a mathematical framework to model the microalgae synthesis of added-value compounds. Thus, these models evolved and, with the rising industrial interest on microalgae high-values compounds, their focus naturally shifted to the production of compounds as lipids, carbohydrates, pigments.

Due to the strong industrial interest in the past, the majority of microalgae added-value models were developed for the production of lipids and carbohydrates. For instance, Mairet et al. (2011) and Packer et al. (2011) were two of the earliest works to explicitly propose mathematical models for the production of lipids from microalgae, by modifying the physiological models by Ross & Geider (2009) and Geider et al. (1998) respectively. Other models for the production of lipids and carbohydrates can be found in Bekirogullari et al. (2020). Even if they are at an earlier development stage, models for the production of pigments and proteins have also been proposed (Borovkov et al., 2023; Enes & Saraiva, 1996; Fachet et al., 2017; Polimene et al., 2012; Rio-Chanona et al., 2017; Turetta et al., 2022; Zhang et al., 2022).

1.5 PSU models of microalgae growth

As mentioned in Section (1.4), physiological models are detailed and involve a large number of variables and parameters. This however is a major obstacle for the identifiability and applicability of such models. On the other hand, another class of compartmental model is represented by the PSU (or *state*) models. These models employ the concept of photosynthetic unit (PSU) to represent the photosynthetic phenomena, allowing a considerable reduction in the complexity of photosynthetic modelling, and for this reason, they are often the choice to simulate and optimise industrial cultivation systems (Bernardi et al., 2014). Moreover, they have been integrated in literature with measurements of fluorescence, allowing a high level of detail in the description of the photosynthetic processes, coupled with effective experimental tools for the parameter identification (Bernardi et al., 2014, 2015,2016; Nikolaou et al., 2015).

PSU models are usually the choice for application under pulsed-light cultivation regimes, as they can account for pulsed-light input profiles though proper model reformulations (Rudnicki et al., 2017). Different from continuous light regimes, pulsed light regimes are periodic, dynamic light inputs with a period characterised by a light phase and a dark phase. Pulsed light can be used in laboratory-scale experiments to mimic and study the effect of mixing light cycles normally encountered in higher scales microalgae cultivation. Apart from the use of pulsed light at laboratory scale to guide the scale up of industrial cultivation systems, it was also found that using high-frequency pulsed light for microalgae cultivation instead of continuous light can enhance biomass productivity 3-10 times (Zarmi et al., 2020), along with the composition of market-relevant pigments (Fu et al., 2013). This increase of biomass concentration under pulsed light is known as the *flashing light effect* (FLE) and has also been reported in previous studies (Hu & Sato, 2017; Martín-Girela et al., 2017; Park & Lee, 2000). However, obtaining the FLE requires a careful tuning of pulsed light parameters such as pulse intensity, ratio between the dark and light phases times, and duration of the light pulse. An improper selection of these factors can lead to the opposite effect of a decrease in biomass concentration with respect to the continuous light regime (Diotto et al., 2022).

More specifically, a PSU is the sum of antenna light harvesting complexes, reaction centres and the associated apparatus. Photosynthesis is thus modelled as the transition of PSUs between different states.

Different PSU models were developed over time. There are five main classes of PSU models: the Eilers-Peeters (EP) model (Eilers & Peeters, 1988) further modified in the Wu-Merchuk (WM) model (Wu & Merchuk, 2001); the Han model (Han, 2002), further developed in the Nikolaou model (Nikolaou et al., 2016); the Camacho-Rubio (CR) model (Camacho Rubio et al., 2003) further

modified in the Bernardi model (Bernardi et al., 2014); the Papadakis model (Papadakis et al., 2012); the Zarmi model (Zarmi et al., 2013). In their simplest form, these models do not consider any limitation on nutrients or temperature and are thus suited for light-limited growth.

Among these models, the EP/WM, CR and Han/Nikolau models are the most popular; their schemes of the EP/WM, Han/Nikolau and Camacho models are shown in Figure 1.3.

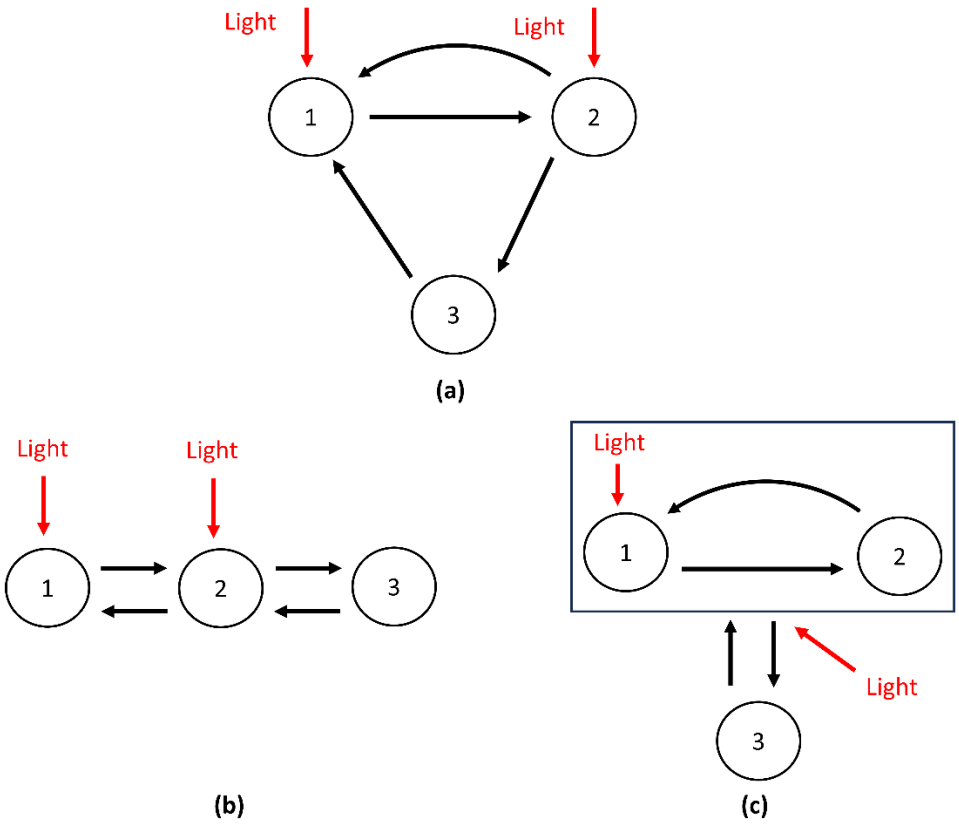

Figure 1.3: *Schemes of the (a) EP/WM, (b) Han/Nikolau and (c) CR models (adapted from Rudnicki et al. (2017)) representing transitions of PSU between the open (1), closed (2) and inhibited (3) states.*

EP/WM, CR and Han/Nikolau models all assume that a PSU can exist in three different states: (1) the resting (or open) state, before light absorption; (2) the activated (or closed) state, after photon absorption and excitation by light energy; (3) the inhibited state, that occurs when PSU are damaged by an excess of light (thus reflecting the phenomenon of photoinhibition).

The WM model assumes a constant number of PSUs in a cell and thus performs material balances on fractions of open, closed and damaged PSUs (x_1, x_2, x_3 [-], respectively). As shown in Figure 1.3a, open PSU can capture a photon and become closed. Closed PSUs can process absorbed light to start photosynthesis and return in the open state. However, if closed PSUs absorb an additional photon, they become inhibited. Inhibited PSUs can then recover from photodamage and return in the open state.

The biomass production rate is assumed to be proportional to the transition rate from closed to open PSUs. The WM model assumes that transitions $x_1 \rightarrow x_2$ and $x_2 \rightarrow x_3$ are first order with respect to the light intensity, whilst $x_3 \rightarrow x_1$ and $x_2 \rightarrow x_1$ are independent from it.

Differently from the WM, the Han/Nikolaou model assumes that PSU recovery from damage occurs from x_3 to x_2. Moreover, Han assumed that the transitions $x_1 \rightarrow x_2$ and $x_2 \rightarrow x_3$ are first order with respect to the irradiance and the effective absorption cross section σ_{PSII} [m^2 μmol^{-1}] of the photosystem II (PSII). Nikolaou further assumed that σ_{PSII} is an hyperbolic function of the carbon-specific chlorophyll quota θ_{chl} [-] (Rudnicki et al., 2017).

Differently from the EP/WU and Han/Nikolaou models, the CR model employs PSUs concentrations (a_1, a_2, a_3 [mol_{PSU} $cell^{-1}$]) instead of PSUs fractions. Moreover, as shown in the scheme of Figure 1.3c, photoinhibition is represented through the transition from the sum of active and closed PSUs (called functional PSUs) to the damaged ones.

Similarly with the WM and Nikolaou models, in the CR models the $x_1 \rightarrow x_2$ transition is assumed to be first order with respect to light intensity, whilst the $x_2 \rightarrow x_1$ transition is defined though a Michaelis—Menten kinetic. Also, the photoinhibition rate is assumed to be proportional to the square root of light intensity. Similarly to the WM model, the growth rate in the CR model is proportional to the transition from the activated to the closed to open state. Moreover, photoacclimation is accounted by considering the total number of PSUs to be dependent on the illumination levels.

The Papadakis and Zarmi models found less applications in literature. However, it is worth to show the underlying structures of these models as a sign of the flexibility in the PSU modelling framework. Differently from the PSU models presented above, the Papadakis model allows PSUs to exist in four different states: (1) open state, (2L) closed state serving the linear electron flow (LEF), (2C) closed state serving the cyclic electron flow (CEF), (3) inhibited. In the model, photoinhibition is due to the absorption of an additional photon by PSUs in (2L), and recovery from photodamage is represented by a transition from (3) to (1). The growth rate is proportional to the transition of PSUs from the closed state of both (2L) and (2C) to the open state, and LEF and CEF have different contributions to the overall productivity. The representation in the Papadakis model allows higher fidelity in the representation of photoprotective processes, i.e. the set of biological processes that limit damages from excessive light conditions. In fact, in low light conditions, the transition from (1) to (2L) is favoured, since in the LEF, both photosystems I and II are involved in the photoproduction processes. However, for higher light conditions, the transition from (1) to (2C) becomes preferred, since it allows the dissipation of the photon energy absorbed in the PSII, thus reducing damage from excessive light.

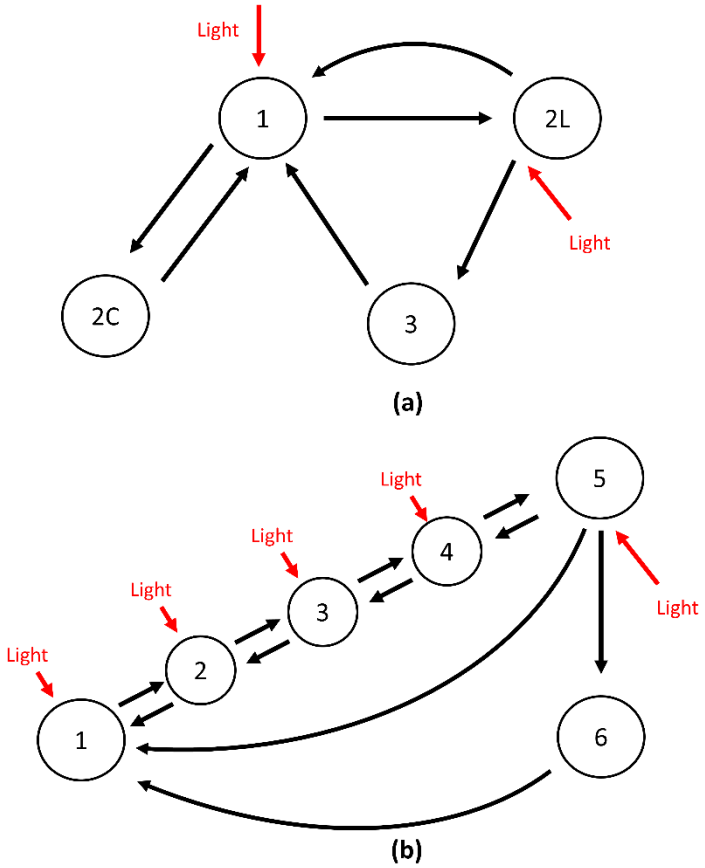

Figure 1.4: *Schemes of the (a) Papadakis model (adapted from Rudnicki et al. (2017)), (b) Zarmi PSU model (adapted from Zarmi et al. (2013)).*

Starting from the EP/WM model, the Zarmi model (Zarmi et al., 2013) was proposed for application in high density cultures and its scheme is shown in Figure 1.4b. The main difference with the WM model scheme is that it decomposes the PSU light absorption from the open state (1) in four different steps through four different states (2-3-4-5). PSUs in the closed state (5) are then able to process the absorbed photons and transition back to (1). The transition from (5) to (1) is assumed to be proportional to the growth rate. However, if PSUs in (5) absorb additional light, they will become inhibited (state (6) in Figure 1.4b). Finally, after recovering from photodamage, PSUs in (6) will be transferred back to (1). According to the authors (Zarmi et al., 2013), the four steps light absorption mechanism of the model provides a better description of light utilisation in high density cultures with respect to classical PSUs models, since it views the absorption of each photon as a separate rate process.

1.6 Stoichiometric and metabolic models

Both physiological and PSU models account for intra cellular biological processes by formulating a simplified scheme of the phenomena of interest and by building a corresponding compartmental model. Another class of model, originating from the formulation of the photosynthetic Z-scheme (Nicholls & Ferguson, 1992), was formulated to dig deeper into cell metabolism. This class of models, called *stoichiometric models* in this Chapter, was inspired by traditional chemical engineering approaches (Cornet et al., 1998), since, differently from physiological and PSU models, they employ the formulation of stoichiometric equations to describe cell metabolism.

From an assumed molecular composition of the biomass and its constituents, stoichiometric models account for the main metabolic pathways through the formulation of stoichiometric equations that satisfy elemental mass balances. After defining stoichiometric equations, the kinetic laws related to each equation are then determined. Due to the great complexity of cell metabolism, stoichiometric models aim at a simplified modelling framework, to reduce the modelling complexity (Cornet et al., 1998). The simplest stoichiometric model can be formulated with only one stoichiometric equation and a corresponding single kinetic law, e.g., to account for the effect of light on microalgal growth (Cornet et al., 1998). An example of this simplified model, valid only in light limiting conditions, can be made for *Spirulina platensis*, assuming a dry biomass composition as $CH_{1.59}O_{0.55}N_{0.14}S_{0.008}P_{0.005}$ (Pruvost & Cornet, 2012).

$$CO_2 + 0.71H_2O + 0.14HNO_3 + 0.008H_2SO_4 + 0.005H_3PO_4 \rightarrow CH_{1.59}O_{0.55}N_{0.14}S_{0.008}P_{0.005} + 1.32O_2$$

However, a single stoichiometric equation model is inadequate to capture the variations in biomass composition. Thus, it is possible to express stoichiometric models in a compartmental form, with a compartment for each cell component. Consequently, for each macromolecule in a compartment, its elemental composition can be proposed and a corresponding stoichiometric equation can be formulated to express its production (Cornet et al., 1998). In this way, in addition to light, it is also possible to account for the effect of other factors as nutrients on microalgal growth (Cornet et al., 1998) .

Stoichiometric models involve a number of unknowns (e.g., stoichiometric coefficients and coefficients of kinetic laws), which must be determined experimentally. However, it is possible to theoretically predict these unknown variables by increasing the complexity of the model and introducing structured stoichiometric equations that involve energy carriers as ATP, NADH, NADPH. In the model formulation, these energy carriers are not over produced or consumed and thus a pseudo-steady state assumption is usually made (Cornet et al., 1998).

Due to their compartmental form, stoichiometric models also allow modelling of the production of added values compounds and lipids, carbohydrates and pigments. Moreover, stoichiometric models are usually coupled to detailed models of light distribution in the cultivation system (Cornet et al., 1998). More information and examples of stoichiometric models can be found in Cornet et al. (1998), (2003); Cornet & Dussap (2009); Dauchet et al. (2016); Pruvost & Cornet (2012); Takache et al. (2010,2012).

As said previously, stoichiometric models aim at obtaining a simplified mathematical structure by considering only a limited number of stoichiometric reactions and compartments. However, by considerably increasing the number of compartments (i.e. macromolecules and metabolites) and stoichiometric equations, highly detailed metabolic models for microalgae growth can be formulated. Indeed, stoichiometric models can be regarded as simplified metabolic models. Differently from the other classes of models presented that seek simplicity in order to be identifiable, metabolic models aim for a detailed characterization of the metabolic pathways from CO_2 to protein, carbohydrate and lipid production (Bernard, 2011). In particular, flux metabolic models are able to describe the intracellular metabolism in response to genetic and environmental changes. The modelling framework relies on the construction of a detailed metabolic network that comprises each chemical reaction for the conversion of a specific substrate into the desired product (Legrand et al., 2021). More examples and details of metabolic models can be found in Baroukh et al. (2022); Cogne et al. (2003), (2011); Fleck-Schneider et al. (2007); Tibocha-Bonilla et al. (2018).

1.7 Motivation of this work

As shown in the previous Sections, an important modelling effort has been carried out by the scientific community over the last years. However, there are still several open issues in several areas concerning microalgae response to external outputs. The goal of this Thesis is to bridge some existing gaps, providing suitable modelling approaches to answer to questions as:

- What is the “true” effect of light in PBRs?
- Are there suitable models to describe both the effect of mixing induced light cycles in PBRs under continuous illumination and the dynamics of biomass growth under pulsed light cultivation regimes?
- How can we express the effect of high frequency pulsed light on biomass productivity through mathematical modelling?

- Is it possible to optimise the experimental campaigns to obtain data for high accuracy parameter estimation of mathematical models for microalgae growth?

The first examined aspect is thus related to light, the most relevant factor for microalgae growth. Many mathematical models have been proposed over the years and calibrated with experimental data. However, in every cultivation system, self-shading and mixing induced light-dark cycles hinder the true effect of light on microalgae cells. This can thus affect the experimental outcomes and bias the predictions of mathematical models identified with those data. This is especially true in the case of empirical models, that do not explicitly consider the effect of mixing induced light-dark cycles. To disclosure the neat effect of light on microalgae growth, these two phenomena must be minimised in experiments. This can be achieved by employing ultra-thin PBRs, with optical paths that must be smaller than those commonly employed in literature, operated at low biomass concentrations. Moreover, in literature most of the works on small scale PBRs are in batch mode. However, operations with continuous PBRs should be preferred since experimental outcomes at steady state highlight the effect of light on photoacclimated cultures. Thus, the objective of Chapter 2 is to develop ultra-thin continuous PBRs to analyse the effect of self-shading and mixing induced light-dark cycles for different thicknesses of the reactor and to present data obtained with those PBRs in operations at low biomass concentrations. Moreover, by fitting the parameters of an empirical P-I model, we will highlight the limitations of this class of models when self-shading and mixing cycles are experimentally minimised.

Differently from empirical models, PSUs models can be mathematically formulated to account for mixing-induced light-dark cycles. Moreover, it was found that microalgae cultivation under flashing light, instead of continuous light regimes, can enhance the biomass productivity (Zarmi et al., 2020). One of the main challenges in PSU models is to adequately link the internal dynamics of PSUs to biomass production. This is particularly true for application with pulsed right regimes, since most of the models in literature are unable to simultaneously capture the dynamics of PSU and of the biomass growth. The objective of Chapter 3, is thus to dynamically reformulated the CR model to capture both dynamics and to accurately estimate parameters of the model from pulsed light data from a High Throughput Screening experimental platform.

Pulsed light data from the HTS platform in Chapter 3 were obtained at low light frequencies, mimicking conditions of mixing-induced light-dark cycles normally found in PBRs operating under constant illumination. However, to obtain an enhancement in the biomass concentration, it was found that high light frequencies are more beneficial (Diotto et al., 2022). However, selecting the optimal input light conditions is not a trivial task since there is a general lack of biological understanding of

the effect of pulsed light on microalgae growth. PSU models, despite their flexibility, do not explicitly model photons absorption-usage-dissipation processes and could thus be limited to represent those phenomena. The objective of Chapter 4, is thus to present a new modelling approach, derived from the work by Zarmi et al. (2020), to aid the understanding of experimental data at ultra-high pulsed light frequencies.

Apart from light, understanding the dynamics of nutrient uptake and utilization is also crucial to ensure efficiency and environmentally sustainable microalgal production on an industrial scale. While the Droop model is adequate to describe nutrient effects on microalgal growth, the precise estimation of its parameters is challenging due to parameter correlation and substantial experimental demands and has thus been neglected in many works in literature. Moreover, though continuous cultures are favoured for microalgal production, their use in experimental campaigns can be time-intensive, due to the necessity of obtaining multiple steady states to provide experimental data for model identification. To challenge these obstacles, the objective of Chapter 5 is to couple modelling and experimental procedures to precisely estimate parameters of the Droop model and minimise the experimental time required. This will be achieved by employing model-based design of experiments (MBDoE), a mathematical approach for planning of informative experiments by employing the mathematical structure of the model to be identified.

To summarise, the Thesis is structured as follows.

Chapter 2 deals with the development of ultra-thin continuous PBRs to inspect the effects of self-shading and mixing cycles in different reactor thicknesses. An empirical P-I model will be applied to the experimental data obtained, highlighting limitations of empirical models in ultra-thin systems.

Chapter 3 proposes a dynamic reformulation of the CR model for pulsed light operation to simultaneously describe dynamics of PSU and biomass growth. Raw experimental pulsed light data from a High Throughput screening experimental platform will be cleaned from outliers with latent variables methods and employed for model identification and validation. The model will be validated also with continuous light data.

Chapter 4 proposes a mathematical formulation that focuses on photons-related processes to interpret qualitatively high frequency light pulsed data obtained in steady state and respirometry experiments. The model will also be employed for planning of respirometry experiments.

Chapter 5 deals with the precise estimation of Droop parameters through employment of MBDoE. Two optimal dynamic experiments will be designed and employed for parameter estimation, showing that the use of MBDoE can greatly reduce the time required for experimental campaigns.

1.8 Chapter Nomenclature

Abbreviations

CEF: cyclic electron flow

CFD: Computational Fluid Dynamics

CR: Camacho-Rubio

EP: Eilers-Peeters

FLE: Flashing Light Effect

LEF: linear electron flow

MBDoE: model-based design of experiments

P-I: photosynthetic-irradiance

PAR: photosynthetically active radiation

PBR: photobioreactor

PSI,PSII: photosystem I and II

PSU: photosynthetic unit

RTE: radiative transfer equation

SCP: Single-Cell Protein

WM: Wu-Merchuk

Symbols

$T_{min}, T_{opt}, T_{max}$: minimum, optimum and maximum temperature for microalgae growth

Variables

a_1, a_2, a_3 [mol_{PSU} $cell^{-1}$]: concentrations of open, closed and damaged PSU

c_x [g m^{-3}]: biomass concentration

$f(S_i)$ [-]: effect of the substrate S_i on growth

$f(T)$ [-]: effect of temperature on microalgae growth

I [µmol m^{-2} s^{-1}]: light intensity

I_0 [µmol m^{-2} s^{-1}]: incident light intensity

K_I [µmol m^{-2} s^{-1}]: light half saturation constant

k_a [m^2 g^{-1}]: light absorption coefficient

q [-]: nutrient quota

q_{min} [-]: minimum nutrient quota in the cell

T [K]: temperature

W [m]: reactor thickness

x_1, x_2, x_3 [-]: fractions of open, closed and damaged PSU

z [m]: spatial coordinate

σ_{PSII} [m^2 µmol^{-1}]: effective absorption cross section

θ_{chl} [-]: carbon-specific chlorophyll quota

μ [d^{-1}]: specific biomass growth rate

μ_{max} [d^{-1}]: maximum specific biomass growth rate

$\bar{\mu}$ [d^{-1}]: average specific biomass growth rate

Chapter 2

Microalgae growth in ultrathin steady-state continuous photobioreactors: assessing self-shading effects

To disclosure the net effect of light on microalgal growth in photobioreactors, self-shading and mixing induced light-dark cycles must be minimized and discerned by the transient phenomena of acclimation. In this Chapter we perform experiments of continuous microalgal cultivation in small scale photobioreactors with different thickness (from 2 mm to 35 mm). To interpret the experimental data, parameters of a Haldane-like model are estimated for different optical thicknesses, showing possible issues in the scalability of experimental results at different light paths when mixing induced light-dark cycles are not considered.

2.1 Introduction

Among all the factors that affect microalgae productivity and growth, light covers a major role since it provides all the energy required for metabolism. The effect of light on microalgal photosynthesis have been the subject of a number of studies in the past, that identify three different light-dependent regions for microalgal growth: photolimitation, photosaturation and photoinhibition.

The experimental observation of these three regions in photobioreactors is influenced by two adverse phenomena that hinder the true photosynthetic response to light: self-shading and mixing induced light-dark cycles (Barbosa et al., 2003; Graham et al., 2015). Self-shading is light attenuation by microalgae cell absorption, that reduces light availability in the inner parts of the photobioreactors (Flynn, 2020). Moreover, microalgae are exposed to light-dark cycles, because of the light-gradient induced by the self-shading and of the turbulent mixing in the reactor: due to these conditions, cells receive light intermittently (Barbosa et al., 2003; Zarmi et al., 2013). A strategy to minimize these adverse phenomena is to decrease the culture light path (Castaldello et al., 2019).

Part of the work presented in this Chapter has been published in *Saccardo, A., Bezzo, F., and Sforza, E. (2022). Microalgae growth in ultra-thin steady-state continuous photobioreactors: assessing self-shading effects. Front. Bioeng. Biotechnol. 10, 1–9. doi: 10.3389/fbioe.2022.977429.*

Decreasing the scale of a photobioreactors (to microphotobioreactors) can lead to multiple advantages, as faster experiments in large numbers of replicas with the possibility to precisely control growth conditions (Castaldello et al., 2019; Kim et al., 2018). Microphotobioreactors can reach scale volumes down to pico-liter (Kim et al., 2018) and have been used to cultivate microalgae in droplet-based flow systems (Saad, Dosoky, et al., 2019; Saad, Selahi, et al., 2019), single cells layer microfluidic chips (Luke et al., 2017; Westerwalbesloh et al., 2019), or fed batch microwell systems (Castaldello et al., 2019; Perin et al., 2016). Recently, microphotobioreactors have been especially employed to investigate light effects on microalgal growth: i.e. applications include microalgal growth under irradiance and nitrate stress conditions (Saad, Dosoky, et al., 2019; Saad, Selahi, et al., 2019), and the evaluation of light effects on microalgae culture under non limiting CO_2 conditions (Castaldello et al., 2019). A limitation of the aforementioned works is that, due to the micro-scale, continuous operations is not possible. This could be achieved by operating on a small scale (instead of a micro scale), that represents an intermediate between microphotobioreactors and traditional "high scale" systems. Several attempts were made in previous literature, as a flat plate photobioreactor of 2 cm thickness of (Busnel et al., 2021) or (Pfaffinger et al., 2019). Other papers worked at steady state in reactors of 1.2-1.5 cm deep (Sforza et al., 2014, 2015a, 2015b, 2018; Barbera et al., 2017; Pfaffinger et al., 2019), finding remarkably high concentration, confirming that self-shading is limited. However, it is not clear if a light path of 1.5-2 cm is actually able to avoid the self-shading effect.

The objective of this Chapter is to capture the net effect of light on microalgal growth in photobioreactors by minimizing phenomena of self-shading and mixing induced light dark cycles in acclimated cultures. To this aim, we designed small scale continuous closed photobioreactors with different reactor thicknesses of 2, 5, 8 mm, where *Tetradesmus obliquus* was cultivated at steady state. The employment of such small scale (2-8 mm thickness of the light path) in continuous mode represents a novelty of this work: to our knowledge, only few attempts of microalgae cultivations in closed photobioreactors with these light paths are reported in literature and none in continuous mode. Thin layer cascade (TLC) photobioreactors can exhibit light paths of few millimetres, with the possibility of semi continuous or continuous operation (Grivalský et al., 2019). However, TLCs are generally operated via flow recirculation usually comprising a retention chamber (Grivalský et al., 2019). This operation mode determines that microalgae are not continuously exposed to light, and make TLCs significantly different from continuous ultrathin flat plate photobioreactors.

We compared our experimental data at 2-8 mm with those at 15 mm and 35 mm for the same species and similar cultivation systems (Barbera et al., 2017; Borella, Sforza et al., 2021; Sforza et al., 2015b)

to highlight the effect of self-shading and mixing induced light cycles. A modelling approach was then used on all the experimental data, to better assess the impact of self-shading with reference to the available light path.

2.2 Materials and methods

2.2.1 Microalga and cultivation systems

Tetradesmus obliquus 276–7 was cultivated in sterile BG11 medium (Stanier et al., 1979) (modified to have a double concentration of all the nutrient in order to avoid limitation and to ensure that light was the only limiting factor), buffered with 10 mM HEPES pH 8 to keep pH of the culture between 7 and 8 and minimize the acidification given by the CO_2. The exact composition of the growth medium is reported in Table 2.1. We provided CO_2 in excess in a 5% volumetric air flowrate from the bottom of the reactors. Reactors were kept in a refrigerated incubator at a constant temperature of 24 °C. A LED lamp (Light Source SL3500, Photon System Instruments, Czech Republic) was used to supply light, with tunable intensities measured by a HD 2102.1 photoradiometer (Delta OHM, Italy).

Table 2.1: *Growth medium composition of BG11 2x.*

Component	Concentration [mg L^{-1}]
$Na_2Mg\ EDTA$	2
$Ferric\ Ammonium\ Citrate$	12
$Citric\ Acid \cdot H_2O$	12
$CaCl_2 \cdot 2H_2O$	72
$MgSO_4 \cdot 7H_2O$	150
K_2HPO_4	61
H_3BO_3	5.72
$MnCl_2 \cdot 4H_2O$	3.62
$ZnSO_4 \cdot 7H_2O$	0.44
$CuSO_4 \cdot 5H_2O$	0.16
$COCl \cdot 6H_2O$	0.1
$Na_2MoO_4 \cdot 2H_2O$	0.78
Na_2CO_3	40
$NaNO_3$	3000

All the photobioreactors operated in the same CSTR (continuous stirred tank reactor) mode and have the same inlet-outlet structure, with an inlet liquid stream for nutrients, and inlet gaseous stream of CO_2 in a 5% volumetric air flowrate and a liquid outlet stream to maintain the same liquid level over time. However, the shape of the reactors can be different for building purpose. Reactors of 2 mm thickness and 1.5 ml volume were made of PDMS and have a V shape, with bottom inlet for air, lateral inlet for nutrients and an overflow liquid exit. Mixing was ensured by bubbling. Reactors of 5 and 8 mm and 10 ml volume were made by polycarbonate with a bottom U shape, with optical properties similar to those of the PDMS employed for the 2 mm PBRS. Stainless steel needles were employed for the gaseous and liquid inlets and sampling outlet. The liquid overflow outlet was connected to a peristaltic pump for better level control. Mixing was obtained through bubbling and with the aid of a small magnetic stirrer. For all reactors, liquid inlet for the continuous supply of fresh medium was ensured by a two-way PHD ULTRA syringe pump (Harvard apparatus, USA). Pictures of the reactors are shown in the Figure 2.1. Cultivation systems in Barbera et al., 2017 (15 mm, 700 ml), Borella et al., 2021 (35 mm, 200 ml), Sforza et al., 2015b (15 mm, 250 ml) are similar to the aforementioned ones, with the exception that 1.5 cm and 3.5 cm light path reactors have a flat bottom rectangular shape.

2.2.2 Experiments and analytical procedures

With reactors from 2 to 8 mm, we performed experiments with different conditions of light and residence time as inputs and measuring cell concentration as the output. Cell concentration was monitored daily through manual cell counting with a Bürker counting Chamber (Optik Labor, Germany). Data were recorded for at least three days since the culture reached the steady state. Since the small scale of the reactors did not allow to perform reliable dry weight measurements, we converted measurements of cell concentration (cell/volume) in ponderal concentrations (mass of biomass/volume) by employing a linear correlation with experimental cellular weight.

2.2.3 Mathematical model

To interpret our experimental data, we employ a model by (Bernard & Rémond, 2012) presented in (Barbera et al., 2020). Assuming a rectangular geometry, the light extinction profile is predicted by the Lambert-Beer law as:

$$I(z) = I_0 \exp(-k_a c_x z) \tag{2.1}$$

where I_0 ($\mu mol\, m^{-2}\, s^{-1}$) is the incident light intensity, k_a ($m^2 g^{-1}$) is the Lambert-Beer light extinction coefficient, c_x ($g\, m^{-3}$) is the biomass concentration inside the reactor and z (m) is the axial

coordinate of the reactor depth. Since we model our PBR as a CSTR, c_x is assumed homogeneous inside the reactor and thus constant along the culture depth.

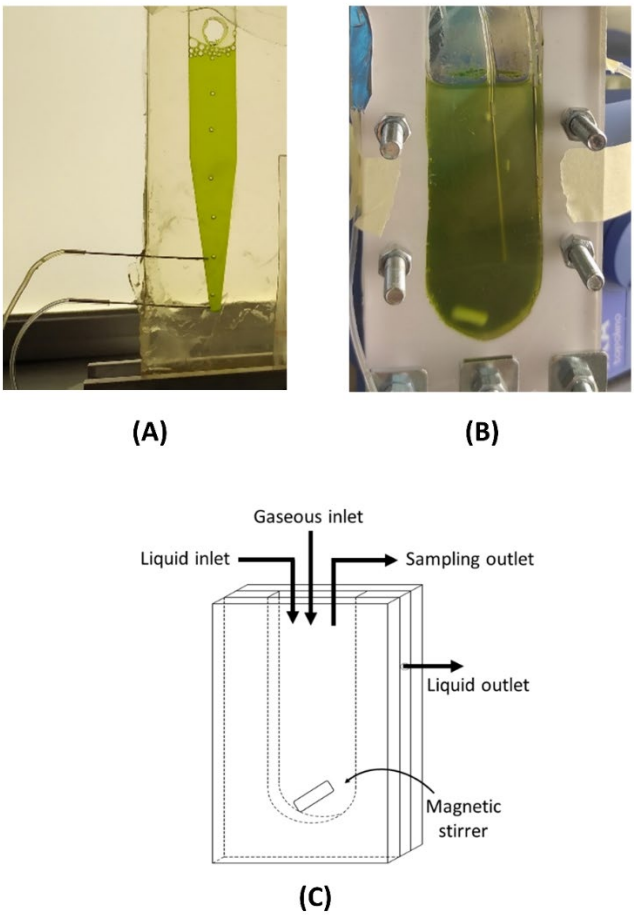

Figure 2.1: *Images of (A) 2 mm light path photobioreactor; (B) 5 mm light path photobioreactor (the shape of 5 and 8 mm thickness PBRs are similar); (C) A schematic representation of our cultivation system.*

For the reactor geometries used, the mixing conditions were measured by tracer experiments, confirming that they can be reasonably assumed as CSTRs.

Since nutrients and CO_2 are provided in excess, the biomass growth rate r_x (g m^{-3} d^{-1}) is a function of light only as an input:

$$r_x(z) = \mu_{max} \frac{I(z)}{I(z)+K_I\left(\frac{I(z)}{I_{opt}}-1\right)^2} c_x - M c_x \qquad (2.2)$$

In Equation 2.2, μ_{max} (d^{-1}) is the maximum specific growth rate, K_I and I_{opt} (µmol m^{-2} s^{-1}) are the half-saturation constant of the light response curve and the light intensity for maximal growth rate respectively and M (d^{-1}) is a specific decay rate that accounts for cell respiration and maintenance. The dependence of the biomass growth rate on light in Equation 2.2 is a reparameterization of the

Haldane cell growth model (Bernard & Rémond, 2012). Being dependent on the varying light intensity along the culture depth, biomass growth rate varies along the axial coordinate and can be integrated along the reactor depth to obtain an average biomass growth rate as:

$$\bar{r}_x = \frac{1}{W}\int_0^W r_x(z)dz \quad (2.3)$$

where W (m) is the reactor thickness. The material balance on biomass can be written as:

$$\frac{dc_x}{dt} = -\frac{1}{\tau}c_x + \bar{r}_x \quad (2.4)$$

where θ (d) is the biomass residence time in the PBR. θ is defined as:

$$\theta = \frac{V_R}{\dot{V}} \quad (2.5)$$

where V_R (m^3) is the volume of the reactor and $\dot{V}$ (m^3 d^{-1}) is the liquid flowrate.

Inputs of the model of Equations 2.1-2.5 are θ and I_0, the output is c_x and model parameters are μ_{max}, K_I, I_{opt}, M, k_a. Another known variable of the model is the reactor thickness W, that could also be treated as an input, since it changes for different experiments.

With the model in Equations 2.1-2.5, we fitted experimental data presented in the following section. For parametric regression, we employed a Maximum Likelihood algorithm on the software gPROMS (by Siemens Process Systems Engineering).

2.3 Results

2.3.1 Experimental results

Biomass concentration was measured at steady state in reactors with different light paths and as a function of light intensity and residence time, depending on the volume of the photobioreactor and the technological limits of the pumps used; experimental results are reported in Figure 2.2. Continuous small scale photobioreactors open new possibilities for investigation of light driven effects, but require particular attention when operated. Due to the small volume, microalgae cultivation is highly sensitive to perturbations of the system that can eventually lead to the failure of the experiment. According to our experience, failures can occur either because of washout or because of formation of irreversible biofouling. The arrangement of the reactor is critical: segregated zones should be avoided; materials must be biocompatible, with optimal optical properties and not sticky to minimize biofouling; and the mixing system (e.g. the magnetic stirrer or intensive bubbling) must not damage cells. Furthermore, monitoring operations must be performed carefully, and the sampling volumes should be carefully chosen in order to avoid introducing harmful perturbances (e.g. in the

residence time) and exposing the culture to contaminations. What above becomes more and more critical as the light path and volume of the reactor decreases.

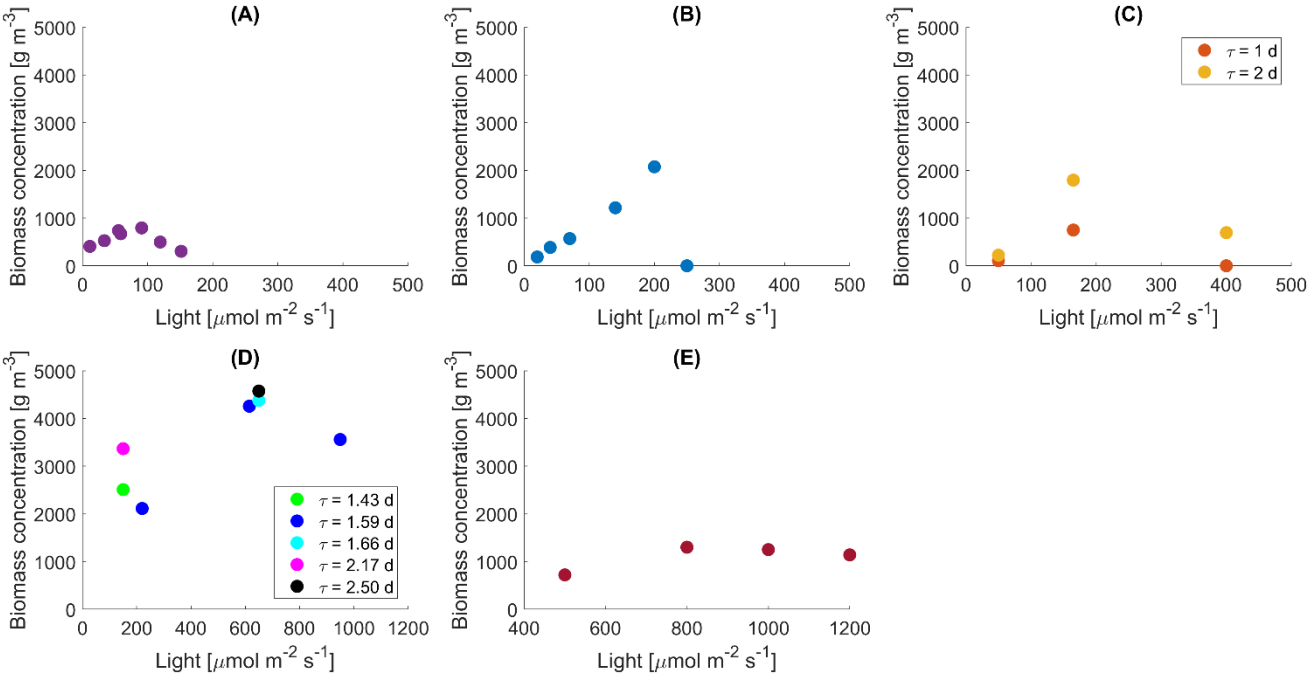

Figure 2.2: *Experimental results at different light intensities and residence times for reactor thicknesses of (A) 2 mm, 1.5 day; (B) 5, 1 days; (C) 8 mm, 1-2 days; (D) 15 mm, 1.43-2.5 days; (E) 35 mm, 1.05 days. Data at 15 mm are from Barbera et al. (2017) and Sforza et al. (2015b); data at 35 mm are from Borella et al. (2021).*

For instance, we were unable to reach steady state conditions for light paths below 2 mm and reactor volumes below 1.5 ml.

The stability of the small-scale reactor (2 mm) was tested by measuring the establishment of steady state in two separate reactors working at the same operating conditions and with different preinocula by maintaining a steady for at least three times the residence time. The steady state concentration obtained was equal for the two reactors, and it was found to be stable over time (Figure 2.3). With volume and thickness smaller than those used in this case, it was not possible to reach a steady state, due to the reasons explained before. To the author's knowledge, this is the first example of a continuously working photobioreactor for microalgal cultivation on such a small scale.

Accordingly, in these configurations, where a very small light path is present, it should be possible to discriminate the effect of light without self-shading effect and mixing induced light/dark cycle. From common knowledge, in reactors with high light paths photoinhibition is visible from a certain critical value of light intensity. However, Figure 2.2 shows that photoinhibition occurs at lower values of light intensities as we move to shorter light paths (e.g., from 600-800 µmol m^{-2} s^{-1} at 15-35 mm to 100-200 at 2-5 mm). Moreover, the trend of the concentration vs light curve changed with light path: data at low light paths (from 2 to 8 mm) showed a steeper decrease in biomass concentration for

inhibition than high reactor depths (15 and 35 mm), suggesting that inhibition is heavily augmented in PBRs with short light path.

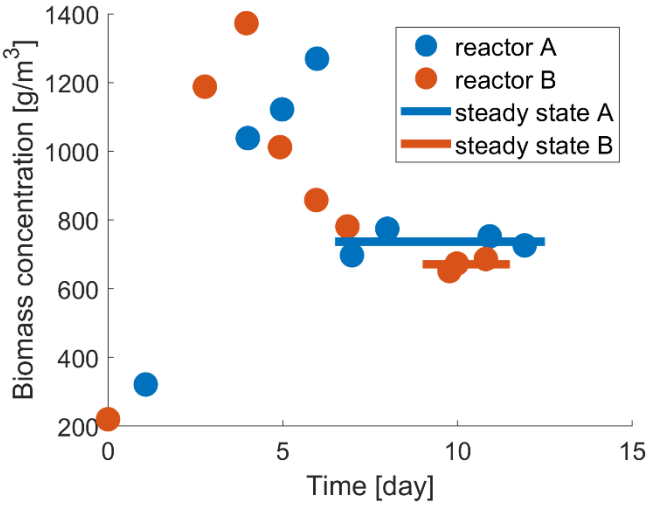

Figure 2.3: *Experimental cell growth data for two replicas (A and B) at 50 µmol m^{-2} s^{-1} and 1.5 d residence time with steady state values.*

For convenience, in Figure 2.2 2-8 mm data are plotted on a 0-500 µmol m^{-2} s^{-1} x-axis whilst 15-35 mm on 0-1200 µmol m^{-2} s^{-1}.

The decrease of reactor thickness from 35 to 15 mm turned into higher biomass concentrations at photosaturation. This behaviour is well confirmed by literature (e.g., (Richmond, 1996; Qiang et al., 1998; Zou and Richmond, 2000; Richmond et al., 2003)): at higher scales, a decrease in the light path corresponds to higher cell concentrations until a lower limit of 1-1.3 cm thickness. We found that this value represents a turning point, since a further decrease to ultra-thin light paths (2-8 mm) showed a decrease in biomass concentration, confirming again a higher influence of inhibition than expected at these scales. This is also reported by (Zou & Richmond, 2000), where higher inhibition was found in a thickness of 1 cm than in 3 cm. In literature, there are no reports on biomass growth in continuous systems with light paths lower than 1-1.3 cm. For a batch cultivation system, (Qiang et al., 1998) found an increase in biomass productivity from 200 to 7.5 mm: however, we experimentally verified that the behaviour of batch and continuous systems at ultra-thin light paths is considerably different. Experimental results and previous considerations show that an indefinite decrease of the reactor thickness cannot lead to an increase in cultivating performances in continuous systems, and suggest the existence of an optimal light path value (as conceptualized in other studies (Richmond et al., 2003; Zarmi et al., 2020)).

2.3.2 Parameter estimation results and modelling

To better describe the data obtained, a model was used, to ascertain if the common growth modelling approach can be used at different light paths. As the model used was not able to reproduce, with a unique set of parameters, all the data at different thicknesses, the model parameters were retrieved separately for sets of data obtained with the same light paths. The values of K_I and M were found to be comparable for each series, and similar to those reported by (Barbera et al., 2020). Thus, the values of such parameters were fixed and μ_{max}, I_{opt}, k_a where estimated separately for each reactor thickness. A comparison between experimental and predicted values for each reactor is shown in Figure 2.4. Estimated parameter values are reported in Table 2.2. Notice that, whereas μ_{max} estimates are quite stable (around 2 d^{-1}), I_{opt} and k_a exhibit the largest variations among different culture depths.

Table 2.2: *Fitted parameters for data at all reactor thicknesses.*

mm	μ_{max} [d^{-1}]	K_I [µmol m^{-2} s^{-1}]	I_{opt} [µmol m^{-2} s^{-1}]	M [d^{-1}]	k_a [m^2 g^{-1}]
35	2.0	110	405	0.45	0.098
15	2.0	‘’	405	‘’	0.14
8	2.1	‘’	74	‘’	0.40
5	2.1	‘’	59	‘’	0.57
2	1.8	‘’	50	‘’	0.9

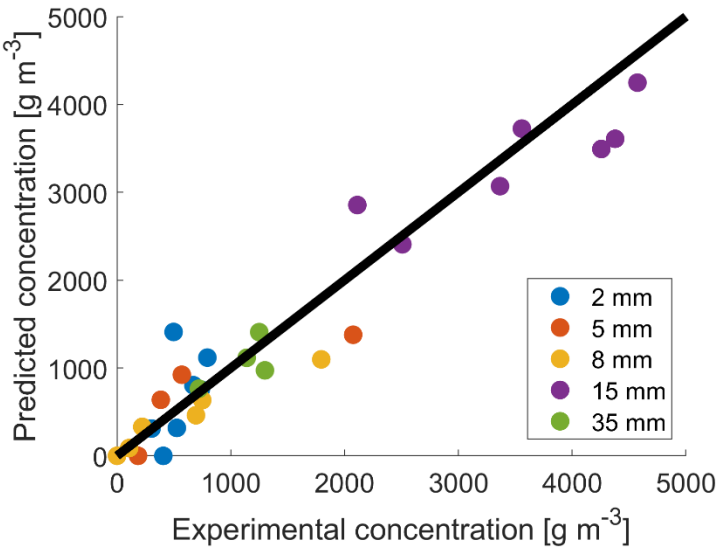

Figure 2.4: *Fitting results for data at different reactor thicknesses.*

Interestingly, the value of I_{opt} and k_a were found to be correlated to the reactor thickness, as shown in Figure 2.5. For convenience, in Figure 2.5 (A) I_{opt}' is shown, that is I_{opt} normalized on the

corresponding value of 413 µmol m^{-2} s^{-1} in Barbera et al., 2020. The increase of I_{opt} for higher reactor thicknesses reflects qualitative experimental results of Figure 2.2: self-shading increases with culture depth, and the amount of light for optimal growth increases accordingly. The sharp increase of k_a for lower reactor thickness needs additional considerations. Figure 2.5 B shows that k_a is constant for reactor thicknesses higher than 15 mm and reflect the experimental value of 0.09 m^2 g^{-1} reported in (Barbera et al., 2020), where cells experience mixing effects and move between different zones of the reactor at high and low irradiance values. For ultra-thin reactor light paths (2-8 mm) however, k_a increases to account for higher light absorption from cells, since they are not able to migrate to layers at lower light intensity, where the excited photosystems may recover and reopen. The higher light absorption at small scales determines a greater inhibition than in thicker systems.

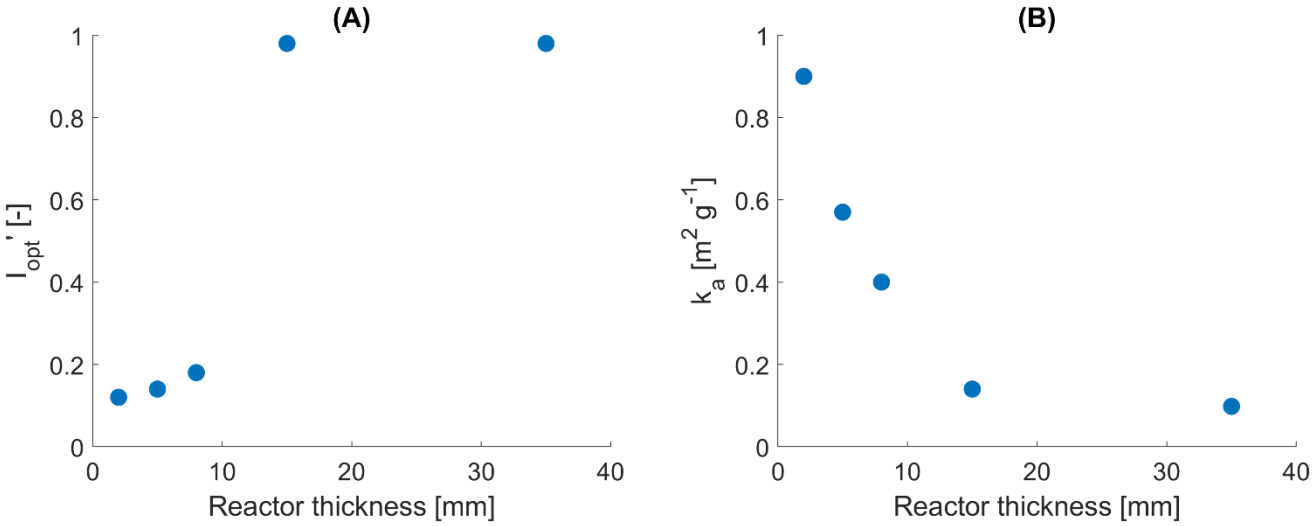

Figure 2.5: *Trends of the value of (A) I_{opt}' and (B) k_a for different reactor thicknesses. I_{opt}' is normalized on 413 µmol m^{-2} s^{-1} (from Barbera et al., 2020).*

This behavior in ultra-thin PBRs is close to what is encountered in the outer layers of a mass microalgal culture: cell in outer layers are exposed to the highest irradiating conditions and subtract a considerable amount of light to the other layers (V. Kumar et al., 2021). In order to reduce this phenomenon, an extensive research effort has been performed to develop microalgae mutants with reduced light harvesting apparatuses (V. Kumar et al., 2021). This also suggests that the standard Lambert-Beer law may not be able to represent the behaviour at different light paths within a Haldane-like light model when the behaviour of very thin photobioreactors need describing, and that it may be inappropriate to scale down experimental results below some light path threshold.

Table 2.3: *Cell travel times for all reactor thicknesses.*

	2 mm	5 mm	8 mm	15 mm	35 mm
Regular motion time [ms]	6.7	16.7	26.7	50	116.7

2.4 Discussion

To understand the aforementioned limitations, we recall the two main adverse phenomena that hinder the net effect of light on microalgal growth: self-shading and mixing induced light-dark cycles. In the model, self-shading is approached through light attenuation in Lambert-Beer law (Equation 2.1), whilst the effect of light-dark cycles is not considered. To gain a measure of this phenomenon, Richmond et al., (2003) introduce the concept of cell travel time, that is the average time required for cells to move back and forth in the reactor thickness, where they are exposed to different light conditions along the light attenuation profile. Richmond et al., (2003) defined some characteristic cell travel times, based either random, diffusion-like motions or on back and forth movement through the optical path. The latter, which is called regular motion time, is more relevant in the context of this work, and is defined as follows:

$$\tau_t = L/v_{cell} \tag{2.6}$$

where L (cm) is the optical path, and v_{cell} (cm s^{-1}) is cell lateral velocity, assumed equal to the bubble velocity (30-50 cm s^{-1}, according to Richmond et al., 2003). As a first approximation, bubble velocity can be assumed to be the same for the different PBRs considered here: more sophisticated analyses would required the use of computational fluid dynamics that, however, may not provide accurate results for bubbling systems with such small dimensions.

Cell travel time does not affect photosynthesis if it is one or two order of magnitude higher than a characteristic photosynthetic units (PSUs) turnover time (about 10 ms for Richmond et al., 2003). Usually, this is not an issue. However, for very thin reactors, cell travel time starts to approach PSUs turnover time, influencing light-cell interaction. Table 2.3 shows the cell travel times for the different reactor thicknesses used in our work. From 2 to 8 mm, travel times are very close to the PSU turnover time and are significantly smaller than travel times at 15 and 35 mm. This highlights that the behaviour at 2-8 mm is different than in 15-35 mm and in the smaller scales mixing-induced light dark cycles could have a significant impact.

In an ideal situation for efficient light exploitation, cells should be exposed to high light conditions in the photic zone for a duration required for light reactions to occur and then move in the dark zone, being replaced by other cells form the dark zone ready to receive incoming photons (Richmond et al.,

2003). However, if the time spent by cells in the dark zone is too low, dark reactions do not have enough time to occur and photosynthetic efficiency decreases (Zarmi et al., 2020). As introduced before, cells in ultra-thin reactors are exposed to strong illumination but, due to the flatter light profile and the absence of a proper dark zone, they do not fully recover from this strong light absorption, causing the photosynthetic efficiency to decrease. This is not the case of thick reactors, where cells are able to migrate to a dark zone and recovery: this explains why photoinhibition in these systems is observed only at very high light conditions (or never, in some cases). Previous considerations suggest that not only light conditions cells are exposed to, but also the duration of exposure of light along the attenuation light profile are necessary for the comprehension of cell-light interaction phenomena. To provide a systematic description, we can employ the theory of the mathematical modelling of pulsed light effects on microalgae: when cells move between zones with different irradiation they are exposed to an effective illumination regime close to a pulsed light one (Zarmi et al., 2020). As in Schulze et al. (2017), pulsed light models have different inputs: intensity of the pulse, time of the light phase (τ_{pulse}) and time of the dark phase (τ_{dark}). In an experimental pulsed light apparatus, these inputs are usually set by a lamp, whilst in our case we must calculate them with the aid of the travel time hypothesis in Richmond et al. (2003). The intensity of the pulse is here assumed equal to the light intensity of the light source. Here, we assume that the photic zone (expressed through the length coordinates z_{ph} (m)) is the zone in the reactor in which light intensity is inhibiting, thus higher than I_{opt}. Length z_{ph} can be computed as:

$$z_{ph} = -\frac{1}{k_a c_x} \log \frac{I_{opt}}{I_0} \tag{2.7}$$

Light phase time for cell regular motion is calculated as:

$$\tau_{pulse} = \frac{z_{ph}}{v_{cell}} \tag{2.8}$$

Corresponding dark phase time is calculated as:

$$\tau_{dark} = \frac{W - z_{ph}}{v_{cell}} \tag{2.9}$$

with W the reactor thickness.

With light and dark phase times the duty cycle ϕ (-) can be calculated as:

$$\phi = \frac{\tau_{pulse}}{\tau_{pulse} + \tau_{dark}} \tag{2.10}$$

In our case, ϕ represents in proportion the time a single cell is exposed to inhibitory conditions. We observed that parameter k_a decreases until stabilising at about W = 15 mm (Figure 2.5. (A)), where its value is about 0.1 $m^2\ g^{-1}$, which is consistent with other estimates in similar systems (e.g., Barbera et al., 2020). If that value is used to compute the duty cycle ϕ, it can be observed that $z_{ph} > W$ for

2-5-8 mm, and therefore ϕ can be assumed equal to 1 (Table 2.4). This means that in un ultra-thin photobioreactors, cells are exposed to light continuously and cannot adequately recover from the high photon absorption in the high irradiance region. The consequent inhibition is artificially captured by the model by increasing k_a, i.e. by assuming less average light in the photobioreactor than there is actually.

Table 2.4: *Duty cycle (non-dimensional) for all reactor thicknesses, computed for* $k_a = 0.1\ m^2\ g^{-1}$.

	2 mm	**5 mm**	**8 mm**	**15 mm**	**35 mm**
Duty cycle [-]	1	1	1	0.2	0.2

Previous considerations also show a touchpoint between thin-milli reactors and pulsed-light experiments toward the understanding and modelling of the effect of light on cell growth and confirm the importance of considering light-dark mixing cycles to ensure the scalability of laboratory results to higher scale systems. Indeed, Equations 2.7-2.10 may represent a starting point to integrate the effect of mixing cycles in traditional light modelling in microalgal growth.

2.5 Conclusions

In high scale microalgal cultivation systems, self-shading and mixing induced light-dark cycles heavily hinder the true effect of light interaction with cells. To minimize these phenomena, we designed, built and operated ultra-thin continuous photobioreactors. Experiments showed that at very low light paths (2-8 mm) high inhibition occurred at low irradiance values. We employed experimental data from different reactor thicknesses to retrieve parameters of a Haldane-like model and the trend of the fitted Lambert-Beer constant shows that there could be issues in the capability of the model to scale up experimental results at ultra-thin light paths. We infer that this is due to the averaged-nature of the model that does not consider the effect of mixing induced light-dark cycles. Indeed, the computation of parameters from the theory of mathematical modelling of pulsed light effects on microalgae suggested that only in ultra-thin light paths (2-8 mm) the “real” continuous light regimen occurs, whilst in thicker light paths (15-35 mm) cells are subjected to an effective pulsed light one due to mixing induced light-dark cycles.

2.6 Chapter nomenclature

Abbreviations

CSTR continuous stirred tank reactor

PBR photobioreactor

PSU Photosynthhetic unit

TLC Thin-layer cascade

Variables

c_x [g m^{-3}]: biomass concentration

I [µmol m^{-2} s^{-1}]: light intensity

I_0 [µmol m^{-2} s^{-1}]: incident light intensity

I_{opt} [µmol m^{-2} s^{-1}]: optimal light intensity

$I_{opt}{}'$ [-]: normalized optimal light intensity

K_I [µmol m^{-2} s^{-1}]: light half-saturation constant

k_a [m^2 g^{-1}]: biomass light absorption coefficient

L [cm]: optical path length

M [d^{-1}]: specific decay rate

r_x [g m^{-3} d^{-1}]: biomass production rate

$\bar{r}_x$ [g m^{-3} d^{-1}]: average biomass production rate

V_R [m^3]: volume of the reactor

$\dot{V}_i$ [m^3 d^{-1}]: volumetric liquid flowrate

v_{cell} [cm s^{-1}]: cell lateral velocity

W [m]: reactor thickness

z [m]: axial coordinate of the reactor depth

z_{ph} [m]: length of the photic zone

θ [d]: residence time

μ_{max} [d^{-1}]: maximum biomass specific growth rate

τ_{dark} [ms]: dark phase time

τ_{pulse} [ms]: light phase time

τ_t [ms]: cell travel time

ϕ [-]: duty cycle

Chapter 3

Modelling microalgae growth based on high throughput pulsed light screens

In this Chapter, a novel formulation of the Camacho-Rubio model is developed to dynamically model microalgae growth under pulsed light operation and simultaneously capture dynamics of both photosynthetic units and biomass concentration. A preliminarily data analysis with Principal Component Analysis (PCA) is performed to remove the biological noise from dynamic profiles of microalgae growth under pulsed light in a High-Throughput Screening experimental platform. After removing the outliers from the dataset, we obtain a precise estimation of model parameters.

3.1 Introduction

Photosynthetic single cell green algae, or microalgae, encompass a diverse array of species that have evolved to tap into the huge energy resource of the sun, to drive CO_2 fixation, the production of a wide variety of biomolecules that collectively form biomass, and oxygen. Microalgae therefore provide the chassis for light driven cell factories for emerging sustainable, biobased industrial systems (Khan et al., 2018) designed to help deliver circular bioeconomies, and key UN Sustainability goals while operating within our planetary boundaries (Ringsmuth et al., 2016). Understanding the operating conditions to maximize microalgae biomass productivity is thus key for energetically efficient and economically feasible industrial exploitation.

Of all the factors that affect microalgae growth, light is one of the most important. As discussed in Chapter 2, high efficiency cultivation of microalgae in photobioreactors (PBRs) is subject to two key light-related phenomena: cellular self-shading, and mixing-induced light-dark cycles (Barbosa et al., 2003; Graham et al., 2015). Mixing induced light-dark cycles can have a deep impact on microalgae cultivation efficiency, and to achieve maximum-efficiencies the PBR must be designed to deliver the physiological optimum light conditions of the target species. To identify optimum illumination conditions in terms of mixing induced light-dark cycles typical of industrial scale PBRs, a high-

The experimental data employed in this Chapter have been published in Sivakhaminathan et al. (2018).

throughput screen was developed (Sivakaminathan et al., 2018). In this screen cells were exposed to a periodic light-dark regime (with periods in the order of seconds) with light phases having a sinusoidal shape. Figure 3.1 shows this sinusoidal light profile and the three factors that control the light profile: the maximum light intensity of the cycle (I_{max} [µmol m^{-2} s^{-1}]); the total duration of the cycle (cycle time τ_{cycle} [s]); the fraction of the cycle that the algae cells are considered to be illuminated, also called light phase ϕ [-], defined as the ratio between the light time and the total cycle time τ_{cycle}. To simulate natural day-night conditions, I_{max} was further varied during experiments as discussed in Section 3.2.3. These studies provided a rich dataset that can guide the optimisation of PBRs design.

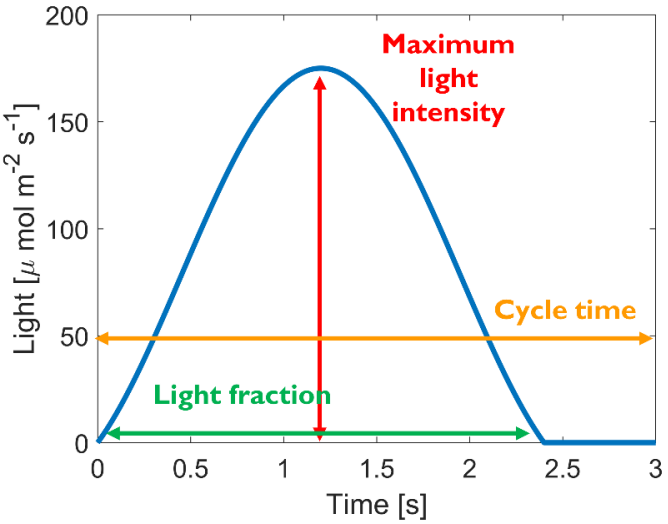

Figure 3.1: *Parameters and dynamic profile of intermittent light in experiments from* (Sivakaminathan et al., 2018).

Although mixing-induced light-dark cycles are a well know phenomenon, comprehensive modelling of microalgae growth under pulsed light regimes is at an early stage of development, and only a limited number of studies focus on the application of state models to pulsed light operation. Due to its capability to describe photo-acclimation, the Camacho-Rubio model (Camacho Rubio et al., 2003), falling into the category of PSU models introduced in Chapter 1, is often chosen to analyse pulsed light operations (Brindley et al., 2011, 2016; Camacho Rubio et al., 2003; Diotto et al., 2022; García-Camacho et al., 2012; Rudnicki et al., 2017). However, one of the main obstacles for the application of state models to pulsed light is the mathematical formulation of the effect of the intracellular PSUs mechanisms on biomass production in a given PBR. To date, models for pulsed light have mostly provided static descriptions of biomass productivity, with parameters that define the light regime set as time-invariants. In other words, PSU models applied to pulsed light only model the dynamics of

PSUs but not of the biomass concentration, making it impossible to capture the dynamic evolution of the biomass and its dependence on the application of different pulsed light regimes in time. This hinders the applicability of PSU models to dynamic simulation, process optimization and control of microalgae cultivation under pulsed light.

The main objective of this Chapter is the development of a novel formulation of the Camacho-Rubio model was developed to simultaneously consider the time-dependent dynamics of PSUs and biomass concentration. As it will be discussed in Section 3.2.5, this will be achieved by representing intra-cycle dynamics with an algebraic formulation, whilst inter-cycle dynamics through differential equations.

The structure of the work presented is summarised in Figure 3.2. Starting from theoretical considerations on photosynthetic characteristic time scales of the principal photosynthetic phenomena, the mathematical model of Rubio Camacho et al. (2003) was first reformulated. To provide data for the modelling activity, the HTS raw data from Sivakaminathan et al. (2018) were analysed and cleaned of biological noise by employing a latent-variables technique, namely principal component analysis (PCA). With the cleaned data, the new model formulation was calibrated: parameters were estimated precisely, and the model fitting performance was then assessed. Next, model prediction accuracy was validated against pulsed and continuous light experimental data, demonstrating its ability to represent a broad variety of growth conditions. The resulting calibrated model represents a useful tool to investigate the best operating conditions under pulsed light, to assess PBRs performances and it could thus be applied for process optimization and control.

3.2 Materials and methods

3.2.1 Strain and culture conditions

The HTS data employed in this work are from the experimental activity performed in Sivakaminathan et al. (2018). Experimental Liquid pre-cultures of *Chlorella* sp. 11_H5 (Wolf et al., 2016) [11] (Australian isolate) were inoculated from TAP (Gorman & Levine, 1965)agar (1.5%) plates and prepared in triplicate (40 mL culture in 100 ml flasks). To ensure that nutrients were non-limiting, previously optimised photoautotrophic medium was used for *Chlorella* sp (OpM_2 (Wolf et al., 2015), N source urea). Flasks were cultivated for 5 days on shakers (200 rpm) in an enclosed incubation system at 23 ^{0}C, 1% CO_2, 100 µmol m^{-2} s^{-1} (overhead white fluorescent light, 16/8 hour light/dark cycle). The synchronised pre-cultures were harvested via centrifugation (at 500 *g*, 20 min, 18 ^{o}C) and the pellet re-suspended in fresh medium to an optical density at 750 nm, or OD_{750}, (1 cm pathlength,

spectrometer, BioRad SmartSpec3000, Hercules CA, USA, blanked with culture media) of 0.5 to minimise cell shading effects.

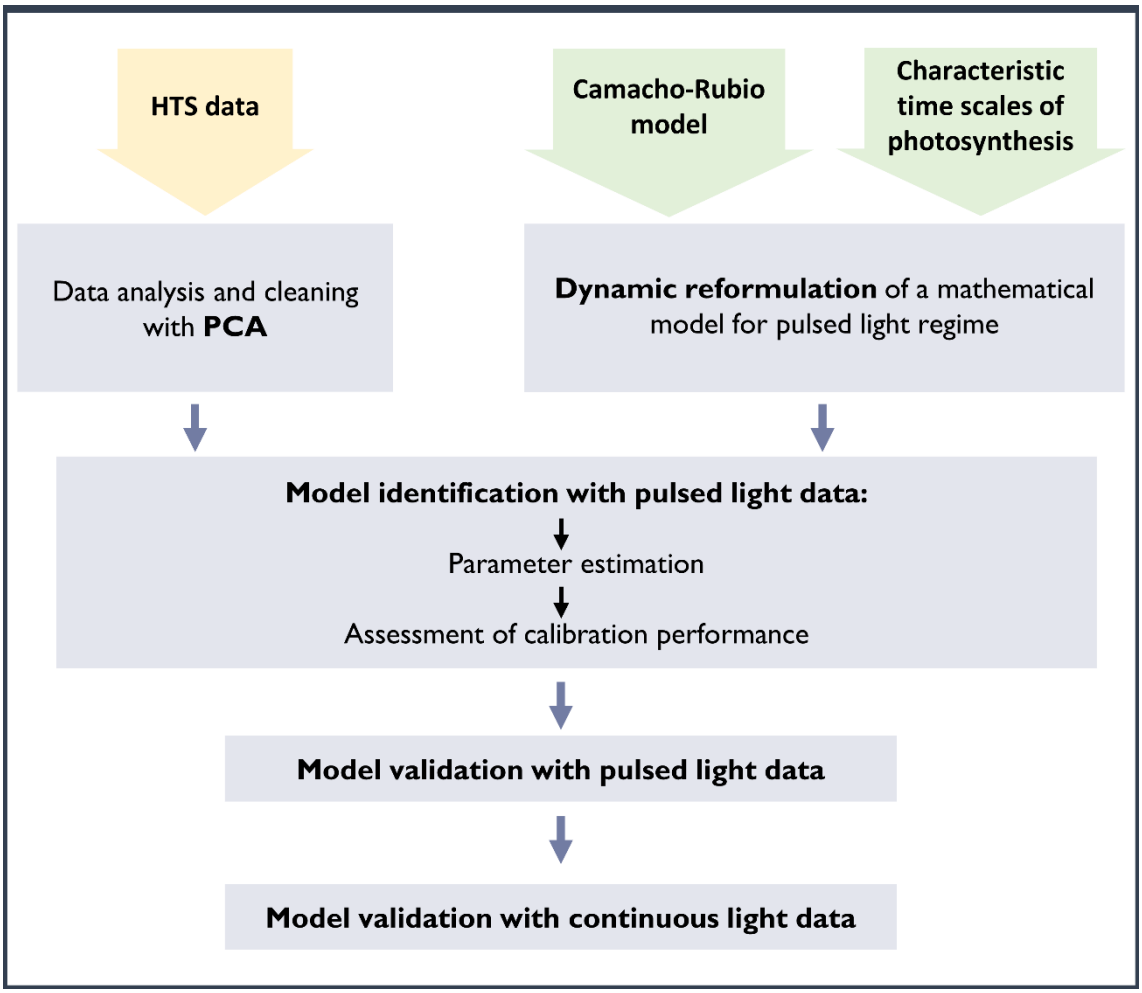

Figure 3.2: *Structure of this work.*

Ten wells (technical replicates) of a 96-well plate (one plate per light regime) were filled with 150 µl of the freshly diluted algae solution for the HTS cultivation (1% CO_2, 23 °C), and 12 wells containing 150 µl pure media were used as blank controls. Growth was monitored via automated OD_{750} and OD_{680} readings (single point reads).

3.2.2. HTS platform and measurements

The design, structure and operation of the HTS system is the one described in Sivakaminathan et al. (2018). The HTS platform consists of an enclosed chamber (Tecan Freedom Evo 150, Tecan Group Ltd., Männedorf, Switzerland) fitted with a robotic manipulator arm (RoMA) transfers plates between shaker and reader (Infinite M200 PRO, Tecan Group Ltd., Männedorf, Switzerland), three orbital shakers which hold six multi-well plates each, and an atmospheric CO_2 control system. Each of the

18 microwell plate positions was fitted with an array of 96 "warm white" LEDs, aligned as one LED per well. The dynamic light regime for each plate was controlled by user defined scripts on an Arduino® integrated circuit controller and software, permitting 18 different light conditions to be tested in parallel. LED intensity control was smoothened with a low pass LC filter from pulse width modulation to variable voltage, thereby eliminating 'flashing light' phenomena due to on/off signals. The RoMA was programmed to take the plates to a reader at determined time intervals where rapid measurements of optical density and fluorescence could be taken. High-throughput automated measurements of OD_{750} were used as a proxy for growth. Chlorophyll *a* has a maximum absorbance at 680 nm: therefore, OD_{680} measurements can be used to normalise against OD_{750} (OD_{680}/OD_{680}) as a proxy of changes in chlorophyll absorption in *Chlorella* between different light regimes.

3.2.3. High-throughput experimental setup for pulsed light regimes

Light experiments in Sivakaminathan et al. (2018) were performed on diluted 150 µl microwell cultures, each illuminated using individual LEDs. The intensity of photosynthetically active radiation (400-700 nm) emitted by the LEDs was programmed to mimic a sinusoidal trajectory of a cell cycling in a one-dimensionally illuminated culture (i.e. an open pond) from the illuminated surface to the dark zone (see light profile in Figure 3.1). In this way, the light regime encountered by the incubated cells in each well was a function of the LED's illumination profile, thereby allowing tight control of the levels of three factors across one light cycle time: (1) the maximum light intensity reached in the cycle I_{max} [µmol m^{-2} s^{-1}], that is the peak of the sinusoidal profile; (2) cycle time τ_{cycle} [s], the total duration of one cycle; and (3) light phase ϕ, the illuminated fraction of the cycle.

A total of 48 pulsed light experimental conditions were tested in Sivakaminathan et al. (2018) (Table 3.1), varying over 4 levels of intensity I_{max} (indicating solar radiation level), 4 levels of light phase ϕ (indicating culture density), and 3 levels of cycle time τ_{cycle} (influenced by mixing regime and/or reactor pathlength).

In addition, continuous light regime experiments were performed to compare the effect of light regime and light dose on cells exposed to fluctuating regimes, with cells exposed to continuous illumination, with the same average illumination regime (I_{avg}, µmol m^{-2} s^{-1}). I_{avg} is the time integration of light received, simulating the average irradiance or light dose received the by cell. The combination of each ϕ and I_{max} resulted in 16 unique integrated average irradiance levels.

HTS experiments in (Sivakaminathan et al., 2018) were designed to mimic the natural day-night cycles. All experiments started with the inoculation or dilution of the microwells and a measurement of OD_{750} and OD_{680}. After this step, an 8 hours dark period was imposed to the culture, during which

no light was provided to the culture (I_{max} = 0 µmol m^{-2} s^{-1}). After the dark time, the culture was exposed to light regimes of Table 3.1 for the subsequent 16 h. During each measurement, measurements of OD_{750} and OD_{680} were taken at the beginning of the experiment (0 h) and at time 13 h, 16h, and 19h.

Table 3.1: *Summary of pulsed light conditions cultivating Chlorella for the HTS experimental matrix comprising maximum light intensity, light phase and cycle time, and continuous light regimes representing the average illumination regime of the pulsed light conditions.*

Maximum light intensity	**Light phase**	**Cycle time**	**Cycle average light intensity**
I_{max} [µmol m^{-2} s^{-1}]	ϕ [-]	τ_{cycle} [s]	I_{avg} [µmol m^{-2} s^{-1}]
175	0.2	3	23
		10	
		20	
		continuous	
	0.4	3	48
		10	
		20	
		continuous	
	0.6	3	63
		10	
		20	
		continuous	
	0.8	3	80
		10	
		20	
		continuous	
375	0.2	3	50
		10	
		20	
		continuous	
	0.4	3	102
		10	
		20	
		continuous	
	0.6	3	136
		10	
		20	
		continuous	
	0.8	3	172
		10	

		20	
		continuous	
750	0.2	3	100
		10	
		20	
		continuous	
	0.4	3	204
		10	
		20	
		continuous	
	0.6	3	272
		10	
		20	
		continuous	
	0.8	3	345
		10	
		20	
		continuous	
1500	0.2	3	198
		10	
		20	
		continuous	
	0.4	3	409
		10	
		20	
		continuous	
	0.6	3	544
		10	
		20	
		continuous	
	0.8	3	689
		10	
		20	
		continuous	

3.2.4 Statistical methods for data analysis

Biological data usually exhibits a certain degree of inherent variability and experimental noise. Data used in this work is no exception, with a number of outliers blurring the distinction between different experimental settings. This can make the calibration of mathematical model a highly challenging task,

leading to imprecise parameter estimates with reduced physical significance. However, detecting outliers in a large database, considering a wide range of experimental conditions, is not an easy task. Visual inspection is not sufficient and more accurate statistical approaches should be used. Here, principal component analysis (PCA) (Wold et al., 1987) was employed for this task. PCA is multivariate statistical method that can reduce dimensionality of large datasets and reveal their underlying correlation structure while minimizing information loss. This is achieved by projecting data onto a hyperspace of new and uncorrelated variables called principal components (Wold et al., 1987). Moreover, when dynamic data are arranged properly in data matrices, PCA can condense the whole dynamic profile of an experiment to a single point on the latent variables hyperspace, enabling comparison of data evolution patterns in an intuitive way (Camacho et al., 2008; Nomikos & MacGregor, 1995). In practice, in the case where $\boldsymbol{X}$ is a [Y x J] matrix of historical data with Y observations and J variables, PCA models the dataset as:

$$\boldsymbol{X} = \boldsymbol{T}\boldsymbol{P}^T + \boldsymbol{E} \quad (3.1)$$

with $\boldsymbol{T}$ the [Y x L] scores matrix, $\boldsymbol{P}$ the [L x J] loadings matrix, $\boldsymbol{E}$ the [Y x J] residual matrix, and $L \leq \min(Y, J)$ the number of principal components. In dynamic experiments, different measurements are collected over time. Thus, a convenient rearrangement of dynamic data is in a three-dimensional matrix $\underline{\boldsymbol{X}}$ [Y x J x K], with Y experimental replicas of the same experiment, J measured variables and K time samples. To apply PCA, $\underline{\boldsymbol{X}}$ can be rearranged in an unfolded matrix $\boldsymbol{X_U}$ [Y x JK], where all time samples for all measured variables are arranged on the matrix rows (Camacho et al., 2008). Using this arrangement, and applying PCA, the dynamic profiles of all the measured variables of a single experimental replica are treated as a single object, and condensed to a single point with L coordinates on the mathematical hyperspace of the scores. Moreover, for each experimental replica it is possible to calculate the Hotelling T^2 and the squared prediction error (SPE) statistics. Given a level of significance and a probability distribution, appropriate threshold values for T^2 and SPE can be computed and employed to reject experimental replicas with values of T^2 and/or SPE above the threshold (Chiang et al., 2001).

Here, PCA was employed to clean the data of Sivakaminathan et al. (2018) of outliers. Dynamic OD_{750} data were used for PCA application and OD_{750} measurements were taken at four different sampling times for each experiment (see Section 3.2.3). OD_{750} was chosen over OD_{680} data as it is directly related to biomass concentration and because, cleaning both OD_{750} and OD_{680} datasets may lead to an excessive rejection of experimental data.

To calibrate the PCA model, data were autoscaled, to yield a zero mean and unit variance. Two latent variables were found to be sufficient. Outlier rejection was performed on 68% limits of SPE and T^2 statistics. MATLAB PLS_Toolbox v8.9.1 by Eigenvector Research, Inc was used for data analysis.
PCA was employed to clean the pulsed light dataset from Sivakaminathan et al. (2018) by calibrating a PCA on every single experiment and removing outliers through the T^2 and SPE statistics. However, PCA does not model the input-output relations of a system and thus is unsuitable to compare the outcomes of experiments made with different input variables combination. For this reason, partial-least-squares regression (PLS) (Geladi & Kowalsky, 1986; Wold et al., 2001) was employed to visualise data from Sivakaminathan et al. (2018) and inspect the goodness of the data cleaning outcomes.
PLS is a linear regression technique between an input matrix of predictors $\boldsymbol{X}$ [Y x H] with Y observations of H input variables, and an output matrix of response variables $\boldsymbol{Y}$ [Y x J] with the same number of observations of J measured variables. The fundamental mathematical relations of PLS are:

$$\boldsymbol{X} = \boldsymbol{T}\boldsymbol{P}^T + \boldsymbol{E} \quad (3.2)$$

$$\boldsymbol{Y} = \boldsymbol{U}\boldsymbol{Q}^T + \boldsymbol{F} \quad (3.3)$$

where $\boldsymbol{T}$ and $\boldsymbol{U}$ are the [Y x L] score matrixes of the predictors and response variables respectively. $\boldsymbol{P}$ and $\boldsymbol{Q}$ are the [L x H] and [L x J] loading matrixes of the predictors and response variables respectively. $\boldsymbol{E}$ and $\boldsymbol{F}$ are the [Y x H] and [Y x J] residual matrices of $\boldsymbol{X}$ and $\boldsymbol{Y}$ respectively. Similarly to PCA, dynamic measurements of the response variables can be organised in a tensor $\underline{\boldsymbol{Y}}$ [Y x J x K], with the same number of observations and variables but K time samples. If $\underline{\boldsymbol{Y}}$ is also unfolded in the response matrix $\boldsymbol{Y_U}$ [Y x JK], PLS can be applied to $\boldsymbol{X}$ and $\boldsymbol{Y_U}$ and the dynamic profiles of the response variables condensed in a single point on the score hyperspace of the response (Camacho et al., 2008). Moreover, in this work a single PCA model was applied on all replicates of a single experiment, and different PCA models were required for different experimental conditions. Differently from PCA, only a single PLS was calibrated to visualise the entire dataset, since in PLS the number of observations (Y) is the sum of all replicates of all experimental conditions in the matrix of the predictors. Thus, application of PLS is a useful tool to visualize data with score plots, where all the dynamic measurements of a single experimental replicate are condensed into a single point and where points are expected to be distributed in the same number distinct clusters as the number of different experimental conditions considered. Thus, if clusters from different experiments are dispersed or superimposed with others, this could indicate that the original dataset is noisy and requires the exclusion of outliers. Similarly to PCA, also in PLS T^2 and SPE can be computed for experimental replicates and compared with threshold values to reject outliers (Chiang at al., 2001).

For the application of PLS, $I_{max}, \phi, \tau_{cycle}$ were used as the input variables for the matrix of predictors. In addition to data autoscaling to zero mean and unit variance, a logarithmic linearisation of the data was applied to pre-treat data for PLS application.

To compare data from different experiments, visually inspecting whether the PCA-cleaning procedure was effective in removing the experimental noise, two PLS models were calibrated separately on raw and PCA-cleaned data.

Data were then visualized via a scores plot where each point corresponds to a replicate of a single experiment. Since it was shown that I_{max} and ϕ are the input variables that have the highest influence on microalgal growth (Sivakaminathan et al., 2018), points with the same I_{max} and ϕ and different τ_{cycle} were plotted with the same colour and symbol.

3.2.5. Modelling of pulsed light microalgae growth

The Camacho-Rubio model (Camacho Rubio et al., 2003) is suited for application to light-limiting microalgal growth experiments. It assumes that photosynthesis in microalgae occurs in the photosynthetic unit (PSU) and that all photosynthetic processes are the results of transitions of PSUs between different states, as shown in Figure 3.3. The PSUs are considered to exist in three different states: open (or resting-state), closed (or activated-state) and inhibited PSUs, that correspond to concentrations a_1, a_2, a_3 [mol_{PSU} $cell^{-1}$] respectively. During photosynthesis, open PSUs (a_1) are each activated by the absorption of a photon, up which they transition to being closed (a_2) in a rapid and non-enzymatic step. In subsequent steps, closed PSUs transition to the open state via slow, enzyme mediated reactions, during which energy is stored and ultimately drives cell metabolism. The transition from a_2 to a_1 is proportional to biomass productivity (Camacho Rubio et al., 2003). Open and close PSUs together are called active or functional PSUs, since they are available for photosynthetic processes and their concentration is a_f [mol_{PSU} $cell^{-1}$]. Under excess of light, functional PSUs become inhibited and are transferred from a_f to a_3. The passage from a_3 to a_f can also take place, with enzymatic cell recovering processes. Finally, the total number of PSUs a_t [mol_{PSU} $cell^{-1}$] in all the states is proportional to the chlorophyll content in microalgae and depends on the light conditions due to photoacclimation. During photoacclimation, microalgal chlorophyll content decreases for higher light conditions to prevent PSUs photodamage: thus, cells acclimated to high irradiance have less PSUs than those acclimated at low light levels.

The scheme in Figure 3.3 can be mathematically translated into a system of material (molar) balances for PSUs (Camacho Rubio et al., 2003). For closed PSUs (a_2) it is:

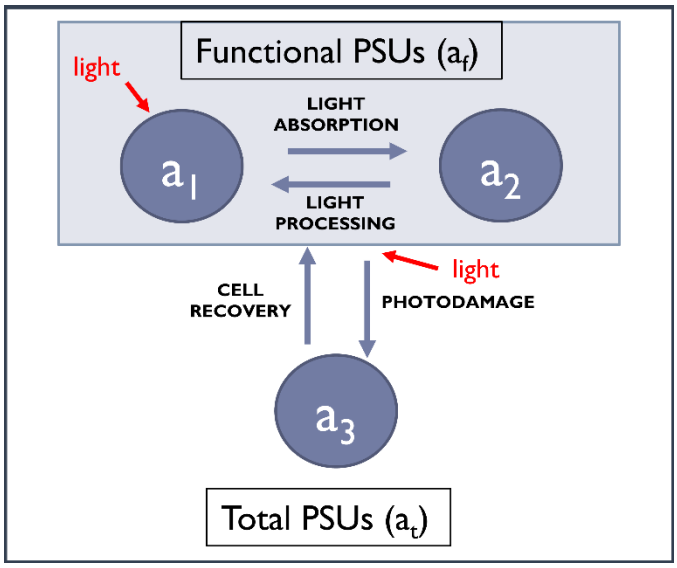

Figure 3.3: *Representation of photosynthetic processes in the Camacho-Rubio model (adapted from* Rubio Camacho et al., 2003*).*

$$\frac{da_2}{dt} = k_a I(a_f - a_2) - \frac{r_m}{k_s + a_2} a_2 \qquad (3.4)$$

where k_a [m^2 µmol^{-1}] is the light absorption coefficient, r_m [mol$_{PSU}$ cell^{-1} s^{-1}] the maximum rate of energy consumption, k_s [mol$_{PSU}$ cell^{-1}] the closed PSU (a_2) concentration at which photosynthesis is equal to half the maximum concentration and I [µmol m^{-2} s^{-1}] is the light intensity.

The concentration of functional PSUs (a_f) is calculated as the difference:

$$a_f = a_t - a_3 \quad , \qquad (3.5)$$

and PSUs in the three states are related to the total number of PSUs with:

$$a_1 + a_2 + a_3 = a_t \quad . \qquad (3.6)$$

The molar balance of inhibited PSUs in a cell can be expressed as:

$$\frac{da_3}{dt} = k_i \sqrt{I}(a_t - a_3) - k_r a_3 \quad , \qquad (3.7)$$

where k_i [m µmol$^{-0.5}$ s$^{-0.5}$] is the photoinhibition rate constant from a_2 to a_3 and k_r [s^{-1}] is the recovery rate constant from a_3 to a_2 . The total number of moles of PSUs per cell is assumed to be a hyperbolic decreasing function of light intensity:

$$a_t = \frac{r_m}{k_c + \frac{k_a k_r}{k_i}\sqrt{I}} \quad , \qquad (3.8)$$

where k_c [s^{-1}] is a rate constant involved in the photoacclimation process. Equation 3.8 reflects that cells acclimate to high light intensities by decrease the amount of pigments with respect to those acclimated at lower light intensities. Finally, the biomass specific growth rate μ [h^{-1}] is assumed to be proportional to the transition from activated to resting state (Camacho Rubio et al., 2003):

$$\mu = k_p \frac{r_m}{k_s + a_2} a_2 - M \quad , \qquad (3.9)$$

where k_p [s cell h^{-1} mol_{PSU}^{-1}] is a proportionality factor that also takes into account that the model in Rubio Camacho et al. (2003) was originally formulated for oxygen production. M [h^{-1}] is a constant cell maintenance factor, or cell death rate, that accounts for cell respiration (Bernardi et al., 2014).

The Camacho-Rubio model of Equations 3.4-3.9 was originally formulated for continuous light. To account for microalgae growth under pulsed light operations, Equations 3.4-3.9 are typically solved for pseudo steady state conditions (Rubio Camacho et al. (2003)), where a time invariant biomass production rate is always considered, thus neglecting the dynamics of biomass production. In fact, as highlighted in Diotto et al. (2022), the fast dynamics of the input profile of pulsed light (with variations of the order of seconds in this work) would force the integration steps of differential equations to be smaller than seconds, making simulation of growth experiments computationally expensive or even unfeasible for long term cultivation scenarios.

Here, Equations 3.4-3.9 were reformulated under pulsed light operations to account for both PSUs and biomass concentration dynamics. The underlying principles are based on knowledge of characteristic time scales for key photosynthetic processes. It is known that *photoproduction*, i.e. the set of processes from photons utilization to fixation of CO_2, occurs in a fraction of a second, while *photoregulation* (i.e. the set of processes that protect the photosynthetic apparatus, occurs in minutes) and *photoinhibition* operates on time scales of minutes to hours (Nikolaou et al., 2015). Finally, *photoacclimation* is the slowest process, acting on timescales from hours to days. With cycle times in the order of seconds, it is possible to identify which variables are fast enough to dynamically change during a single light cycle, and which are not. PSUs concentrations in the open and closed states, a_1 and a_2, are directly responsible for photoproduction and, thus, were here assumed to change during a single light cycle on the order of seconds. In contrast, the concentration of inhibited PSUs a_3 results from a balance of photoinhibition and photoregulation mechanisms and was therefore assumed to be constant during a single light cycle, and to vary between different light cycles. Similarly, the total number of PSUs (a_t) is directly linked to photoacclimation and thus was also assumed to be constant during a single light cycle. Note that a_f is thus constant during a single light cycle according to its definition in Equation 3.5.

Our reformulation of the Camacho-Rubio model under pulsed light is presented in the following part of this Section. As proposed in Rubio Camacho et al. (2003) a non-dimensional time variable τ [-] was defined as the ratio of the actual time t [s] over the cycle time τ_{cycle} [s]:

$$\tau = \frac{t}{\tau_{cycle}} \tag{3.10}$$

that is equal to 0 at the beginning of the light cycle, ϕ at the end of the light phase and equal to 1 at the end of the light cycle, reflecting the light profile of Figure 3.1. Based on Camacho Rubio et al. (2003), Equation 3.4 was reformulated over τ; operations during the light and dark phases were considered separately and periodic boundary conditions were enforced. Moreover, as stated in Bernardi et al. (2014), the Michaelis-Menten kinetic in Equation 3.4 was approximated by a first order kinetic. Thus, for the light phase ($0 < \tau < \phi$) Equation 3.4 was modified as follows:

$$\frac{1}{\tau_{cycle}}\frac{da_2}{d\tau} = k_a I\left(a_f - a_2\right) - k_d a_2 \quad , \tag{3.11}$$

$$\tau = 0 \;\rightarrow\; a_2 = a_{2,min} \quad , \tag{3.12}$$

$$\tau = \phi \;\rightarrow\; a_2 = a_{2,max} \quad , \tag{3.13}$$

and for the dark phase ($\phi < \tau < 1$) as:

$$\frac{1}{\tau_{cycle}}\frac{da_2}{d\tau} = -k_d a_2 \quad , \tag{3.14}$$

$$\tau = \phi \;\rightarrow\; a_2 = a_{2,max} \quad , \tag{3.15}$$

$$\tau = 1 \;\rightarrow\; a_2 = a_{2,min} \quad . \tag{3.16}$$

The linearized term k_d [s^{-1}] in Equations 3.11,3.14 represents a kinetic constant of PSUs re-opening rate (Bernardi et al., 2014) and the differential equations 3.11,3.14 now use τ as the time variable. Equations 3.12-3.13,3.15-3.16 are boundary conditions: at the end of the light phase a_2 reaches the maximum number of moles of closed PSUs per cell $a_{2,max}$ [mol_{PSU} $cell^{-1}$], while the minimum one $a_{2,min}$ [mol_{PSU} $cell^{-1}$] is reached at the end of the dark phase in the light cycle (Camacho Rubio et al., 2003).

In contrast to the study of Camacho Rubio et al. (2003), in the experimental system of Sivakaminathan et al. (2018) the light intensity during the light phase (I) is not constant but varies sinusoidally: thus, it was not possible to integrate Equation 3.11 by separating the variables. Thus, the time-varying I in Equation 3.11 was replaced with the average value $\bar{I}$ [µmol m^{-2} s^{-1}] of light intensity during the light phase, expressed as in Equation 3.17.

$$\bar{I} = \frac{1}{\phi}\int_0^{\phi} I(\tau)d\tau \quad . \tag{3.17}$$

The approximation of I with $\bar{I}$ allowed to convert the light profile in Figure 3.1 to a square wave that delivers the same number of photons to the culture during the light phase, thereby neglecting the shape of the light profile during the light phase. This assumption does not limit the applicability of the model since the pulsed light profile in literature usually has a square wave shape (e.g. see (Camacho Rubio et al., 2003; Diotto et al., 2022) for reference). Since a_f is also constant during the light cycle, it was possible to separate the variables in Equation 3.11 and obtain:

$$\int_{a_{2,min}}^{a_2} \frac{1}{k_a\bar{I}(a_f-a_2)-k_d a_2} da_2 = \tau_{cycle}\tau \quad , \tag{3.18}$$

where we recall that k_a [m^2 μmol^{-1}] is the light absorption coefficient, k_d [s^{-1}] is a kinetic constant of PSUs deactivation rate, τ_{cycle} [s] is the cycle time, τ [-] is the non-dimensional time and $a_{2,min}$ [mol$_{PSU}$ cell^{-1}] is the minimum number of closed PSUs per cell reached in the light cycle. By integrating Equation 3.18 from the beginning of the light phase to any time within it, it was possible to obtain:

$$\frac{1}{k_a I+k_d} \ln\left(\frac{|-(k_a\bar{I}+k_d)a_2+k_a\bar{I}a_f|}{|-(k_a\bar{I}+k_d)a_{2,min}+k_a\bar{I}a_f|}\right) = -t_c\tau \quad . \tag{3.19}$$

In parallel with the integration of Equation 3.11, it was possible to separate variables and integrate Equation 3.14 for any time within the dark phase, obtaining:

$$\ln\left|\frac{a_2}{a_{2,max}}\right| = -k_d t_c(\tau-\phi) \quad , \tag{3.20}$$

where we recall that $a_{2,max}$ [mol$_{PSU}$ cell^{-1}] is the maximum number of closed PSUs per cell reached in the light cycle. Similarly to the procedure in Camacho Rubio et al. (2003), values of $a_{2,max}$ and $a_{2,min}$ were calculated by solving the system of Equations 3.19-20 for the entire duration of the light phase ($\tau = \phi$, $a_2 = a_{2,max}$) and of the dark phase ($\tau = 1$, $a_2 = a_{2,min}$) respectively, obtaining Equations 3.21-22:

$$\frac{1}{k_a I+k_d} \ln\left(\frac{-(k_a\bar{I}+k_d)a_{2,max}+k_a\bar{I}a_f}{-(k_a\bar{I}+k_d)a_{2,min}+k_a\bar{I}a_f}\right) = -\tau_{cycle}\phi \quad , \tag{3.21}$$

$$\ln\left(\frac{a_{2,min}}{a_{2,max}}\right) = -k_d\tau_{cycle}(1-\phi) \quad . \tag{3.22}$$

Note that the absolute values in Equations 3.19-20 were dropped here. In fact, both terms in the numerator and denominator of the logarithmic argument in Equation 3.19are higher or equal than zero, since they correspond to the time derivative of a_2, that is an increasing function in the light phase. Moreover, $a_{2,min}$ and $a_{2,max}$ are always positive quantities. Solving the system of Equations 3.21-22, $a_{2,max}$ and $a_{2,min}$ were calculated as:

$$a_{2,max} = \frac{k_a\bar{I}a_f\left(1-\exp\left(-\tau_{cycle}\phi(k_a\bar{I}+k_d)\right)\right)}{(k_a\bar{I}+k_d)(1-\exp(-\tau_{cycle}\phi k_a\bar{I}-k_d t_c))} \quad , \tag{3.23}$$

$$a_{2,min} = \exp\left(-k_d\tau_{cycle}(1-\phi)\right) a_{2max} \tag{3.24}$$

Note that in Equations 3.23-24, $a_{2,max}$ and $a_{2,min}$ can change between different light cycles, since they depend on a_f, linked through Equation 3.5 to a_3, i.e. the variable that is characterized by inter-cycles dynamics. With values of $a_{2,max}$ and $a_{2,min}$ from Equations 3.23-24, Equations 3.21-22 were used to calculate the dynamic profile of a_2 during light cycles. This allows to switch from the

differential equations in Equations 3.11,14 to a periodic algebraic solution: in other words, by applying Equations 3.21-22, it was assumed that the open and closed PSUs instantaneously reach a periodic, oscillating pseudo steady state, mathematically reflecting the high velocity of photoproduction processes (Nikolaou et al., 2015).

Dynamic profiles of open PSUs allowed calculation of the average biomass production rate $\bar{\mu}$ (h^{-1}) over a cycle by recalling Equation 3.9 and introducing the first order kinetics of Equation 3.11:

$$\bar{\mu} = \int_0^1 \left(k_p k_d a_2 - M\right) d\tau = k_p k_d \left(\int_0^\phi a_2 \, d\tau + \int_\phi^1 a_2 \, d\tau \right) - M \quad . \tag{3.25}$$

Similarly to the procedure used in Camacho Rubio et al. (2003), the two integrals of Equation 3.25 were calculated respectively from Equation 3.11 for the light phase:

$$\int_0^\phi k_d a_2 \, d\tau = \int_0^\phi k_a \bar{I} \left(a_f - a_2\right) d\tau - \frac{1}{t_c}\left(a_{2,max} - a_{2,min}\right) \tag{3.26}$$

and Equation 3.14 for the dark phase:

$$\int_\phi^1 k_d a_2 \, d\tau = \frac{1}{t_c}\left(a_{2,max} - a_{2,min}\right) \quad . \tag{3.27}$$

By combining Equations 3.25-27, $\bar{\mu}$ was thus expressed as:

$$\bar{\mu} = k_p k_a \bar{I} \int_0^\phi \left(a_f - a_2\right) d\tau - M \quad ; \tag{3.28}$$

note that in Equation 3.28 the average biomass production rate over a cycle depends on the closed PSUs during the light phase only, reflecting a similar finding in Camacho Rubio et al. (2003). By substituting the integration variable $d\tau$ with da_2 through Equation 3.11, $\bar{\mu}$ was finally calculated as:

$$\bar{\mu} = B\left[\left(a_{2,max} - a_{2,min}\right) + \left(A - a_f\right) \ln\left|\frac{a_{2,max} - A}{a_{2,min} - A}\right|\right] - M \quad , \tag{3.29}$$

with

$$A = \frac{k_a \bar{I} a_f}{k_a \bar{I} + k_d} \quad , \tag{3.30}$$

$$B = \frac{k_p k_a \bar{I}}{\tau_{cycle}\left(k_a \bar{I} + k_d\right)} \tag{3.31}$$

With the biomass production rate $\bar{\mu}$, the biomass material balance for a batch system during exponential growth rate was expressed as:

$$\frac{dOD_{750}}{dt} = \bar{\mu} OD_{750} \quad . \tag{3.32}$$

The biomass concentration in Equation 3.32 was expressed in OD_{750} [-] instead of mass per volume: however, this does not restrict the validity of the model, since OD_{750} is proportional to biomass concentration measurements (i.e., see Chioccioli et al. (2014) for reference).

Finally, the balance for a_3 was modified as:

$$\frac{da_3}{dt} = \left(k_i \sqrt{I_{avg}} \left(a_t - a_3\right) - k_r a_3\right) CNV \quad , \tag{3.33}$$

The term CNV [s h^{-1}] in Equation 3.33 is a conversion factor from seconds to hours, equal to 3600 s h^{-1}.

To account for its inter-cycle dynamics, a_3 was assumed to be dependent on the cycle average light intensity I_{avg} [µmol m^{-2} s^{-1}], defined as:

$$I_{avg} = \int_0^1 I(\tau) d\tau \quad . \tag{3.34}$$

Similarly, a_t was assumed to depend on I_{avg}, since it has been shown that for rapidly varying light levels microalgae acclimate to the average irradiance (Combe et al., 2015) in the cycle time:

$$a_t = \frac{1}{k_c + \frac{k_a k_r}{k_i}\sqrt{I_{avg}}} \quad , \tag{3.35}$$

Notice that with the new formulation of Equation 3.35, k_c is measured in [cell mol_{PSU}^{-1}]. An additional relation was proposed:

$$a_t = k_{OD} \frac{OD_{680}}{OD_{750}} \quad ; \tag{3.36}$$

with k_{OD} [cell mol_{PSU}^{-1}] being a proportionality factor. Equation 3.36 is motivated by the fact that the total number of PSUs is known to be related to the chlorophyll content in microalgae, whose variation, in turn, is proportional to the ratio of OD_{680} [-] and OD_{750} (Sivakaminathan et al., 2018).

Note that, in the final formulation, a DAE system was obtained where only the dynamics of biomass concentration and of the number of inhibited PSUs were expressed through differential equations, while the dynamic profiles of open and closed PSUs were modelled with algebraic equations. This enabled the ordinary differential equation (ODE) solvers to select larger integration steps, making calculations faster.

Moreover, due to the short light path (approximately 5mm) and low culture experimental concentrations (i.e., OD_{750} typically comprised between 0.1-1.0) of the HTS platform in Sivakaminathan et al. (2018), as a first approximation light attenuation was neglected in this work. This is further justified by the fact that the highest light variations in time experienced by cells are due to the highly oscillating pulsed light input, instead of the coupling of cell shading and mixing cycles in the short light path. However, for application to higher scale PBRs and high concentration cultures, the formulation proposed in this work must be appropriately integrated (i.e., with a Lambert-Beer expression), to account for the existence of a light attenuation profile.

The model formulation above was developed for pulsed light operations: with minor modifications of the equations and retaining the same parameters of Equations 3.17,23,24,29-36, it can be adapted for continuous light regimes. To capture the behaviour of the system under continuous light, additional modifications of the Camacho-Rubio model were performed for consistency with the

photosynthetic timescale-based assumptions. Under continuous light regimen, closed PSUs instantaneously reach a steady state condition, and thus a_2 was calculated through Equation 3.11 at steady state:

$$0 = k_a I\left(a_f - a_2\right) - k_d a_2 \quad . \tag{3.37}$$

Under continuous light conditions, the distinction between instantaneous and cycle-averaged light intensities is not meaningful. Finally, under continuous light, the specific biomass production rate was expressed as:

$$\overline{\mu} = k_p k_d a_2 - M \quad . \tag{3.38}$$

Despite the different formulation of Equations 3.37-38, parameters are the same of the model for the pulsed light case.

Parameters $k_a, k_c, k_d, k_i, k_p, k_r$ are directly related to the intracellular photosynthetic processes; thus, the goal of this work was to estimate them using the pulsed light data from Sivakaminathan et al. (2018) and to employ the additional continuous light data for model validation. In contrast, k_{OD} is a proportionality factor and M is related to cell maintenance, that did not exhibit a major role in the examined experimental conditions (Sivakaminathan et al., 2018). Thus, in this work k_{OD} and M were kept constant, with k_{OD} fixed after preliminary model application and M assigned to a value of the same order of magnitude as the one in Barbera et al. (2020) for the same microalgal species. Fixed values of k_{OD} and M are reported in Table 3.2. The parameter estimation task was performed with the software gPROMS v7.0.7 (Siemens Process Systems Engineering).

Table 3.2: *Fixed model parameters.*

Name	Value
k_{OD}	12.50 cell mol_{PSU}^{-1}
M	0.01 h^{-1}

3.3 Results

3.3.1 Statistical analysis of HTS data

HTS data were cleaned using the PCA methodology to remove outliers. To visualise the effect of the cleaning step, partial-least-squares regression (PLS) (Geladi & Kowalsky, 1986; Wold et al., 2001) was employed. The resulting PLS score plots are shown in Figure 3.4, for comparison between raw and PCA-cleaned data. The score plot of the PLS model applied on raw data under pulsed light is shown in Figure 3.4a. Data points with the same colour and symbol represent different replicates

exposed to the same maximum light intensity (I_{max}) and light phase (ϕ); these samples were exposed to the same average light intensity over a light cycle. The raw data are characterised by high scatter, with superimposition of replicas from different experiments that are impossible to separate. This justifies the following steps of outlier rejection to cluster the outcome of the different experiments.

Figure 3.4b shows the corresponding score plot of PLS applied on the PCA-cleaned data. After the removal of outliers, it is possible to identify the outcomes of experiments with different combinations of I_{max} and ϕ, and obtain distinct data cluster for different classes denoted by colour and symbol type. Notice that in Figure 3.4b, replicas with the same I_{avg} are not distributed around centroids, but aligned along parallel lines. This shows that, even without outliers, the data points still exhibit a certain degree of variability. This could be caused by a residual variance that is not captured in the projection of operating variables of the principal components, or by the presence of a minor effect of the cycle time τ_{cycle} on the response.

The PCA-cleaned data set was used in the following section for parameter estimation of the pulsed-light growth model developed in Section 3.2.5.

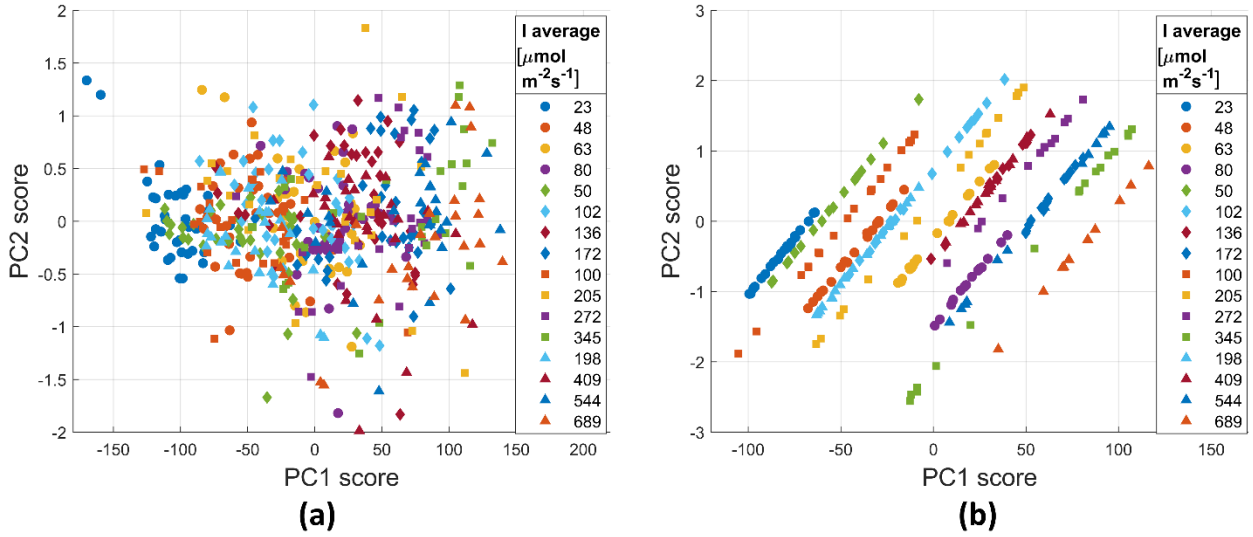

Figure 3.4: *Score plot of (a) raw data, (b) PCA-cleaned data for pulsed light.*

3.3.2 Parameter estimation with pulsed light data

Parameter estimation of the new model formulation presented in Section 3.2.5 was performed with the PCA-cleaned experimental dataset obtained under the pulsed light regime, with except for experiments conducted at I_{max}= 375 µmol m^{-2} s^{-1} and ϕ = 0.6, as these were used for model validation. Both OD_{750} and OD_{680} experimental measurements were available from Sivakaminathan et al. (2018). OD_{750} is the most important variable for the system, as it is proportional for biomass

concentration, and its measurements were thus used in Sivakaminathan et al. (2018) to calculate biomass productivity and photosynthetic efficiency. Moreover, by considering OD_{680}, a_t is linked to the cellular pigment content through Equation 3.36, obtaining a more realistic mathematical representation of photoacclimation, and parameters of the model with a deeper physical meaning, since a_t can not be directly measured. For these reasons, experimental measurements of both OD_{750} and OD_{680} were employed to estimate parameters of the model.

To obtain an effective measurement of the model fitting performance, the percentage mean root squared error $\%MRSE$ [%] between experimental data and model prediction was computed for each replica:

$$\%MRSE = \frac{1}{n}\sum_{i=1}^{n}\sqrt{\frac{\left(y_i - y_i^{predict}\right)^2}{y_i^2}} * 100 \qquad (3.39)$$

with y_i being the i^{th} experimental data point, $y_i^{predict}$ its corresponding model prediction, and n the total number of time points sampled in the replica.

Box plots of $\%MRSE$ values for model fitting are shown in Figure 3.5 for both OD_{750} and OD_{680} among all the experimental replicas. The median of $\%MRSE$ for OD_{750} is 8.2%, while the median $\%MRSE$ for OD_{680} is 12.1%, probably due to the higher noise of OD_{680} measurements.

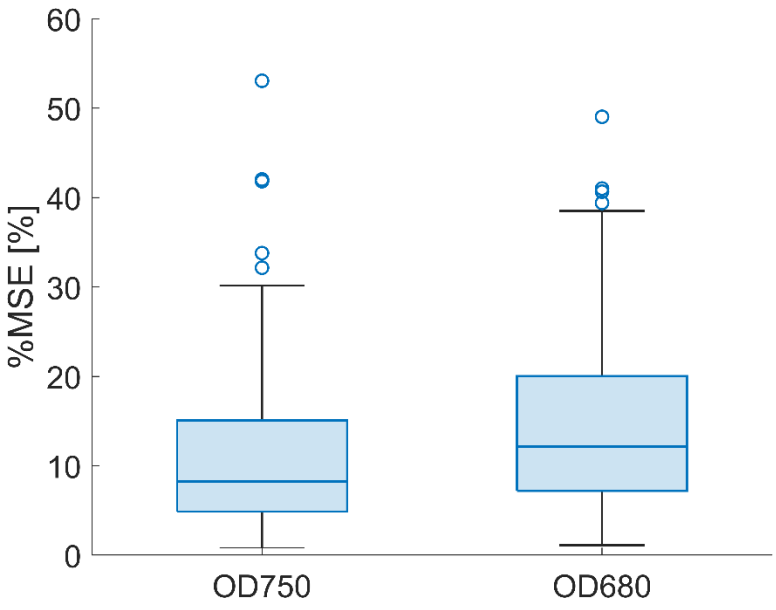

Figure 3.5: *Pulse-light fitting results: box plot of %MRSE for OD_{750} and OD_{680}.*

In addition to the analysis of $\%MRSE$ (Figure 3.5), parity plots are shown in Figure 3.6 for average values of OD_{750} (Figure 3.6a) and OD_{680} (Figure 3.6b) over time and experimental replicates. For both Figure 3.6a and b, points are aligned on the first bisectrix (black line), confirming the goodness

of the model fitting and the absence of systematic model error patterns. OD_{680} data points (Figure 3.6b) also align well but, with compared to OD_{750}, have a slightly higher scatter and deviation from the bisectrix (black line), with the modl slightly underestimating OD_{680}, reflecting the higher predictive performance of OD_{750} found previously.

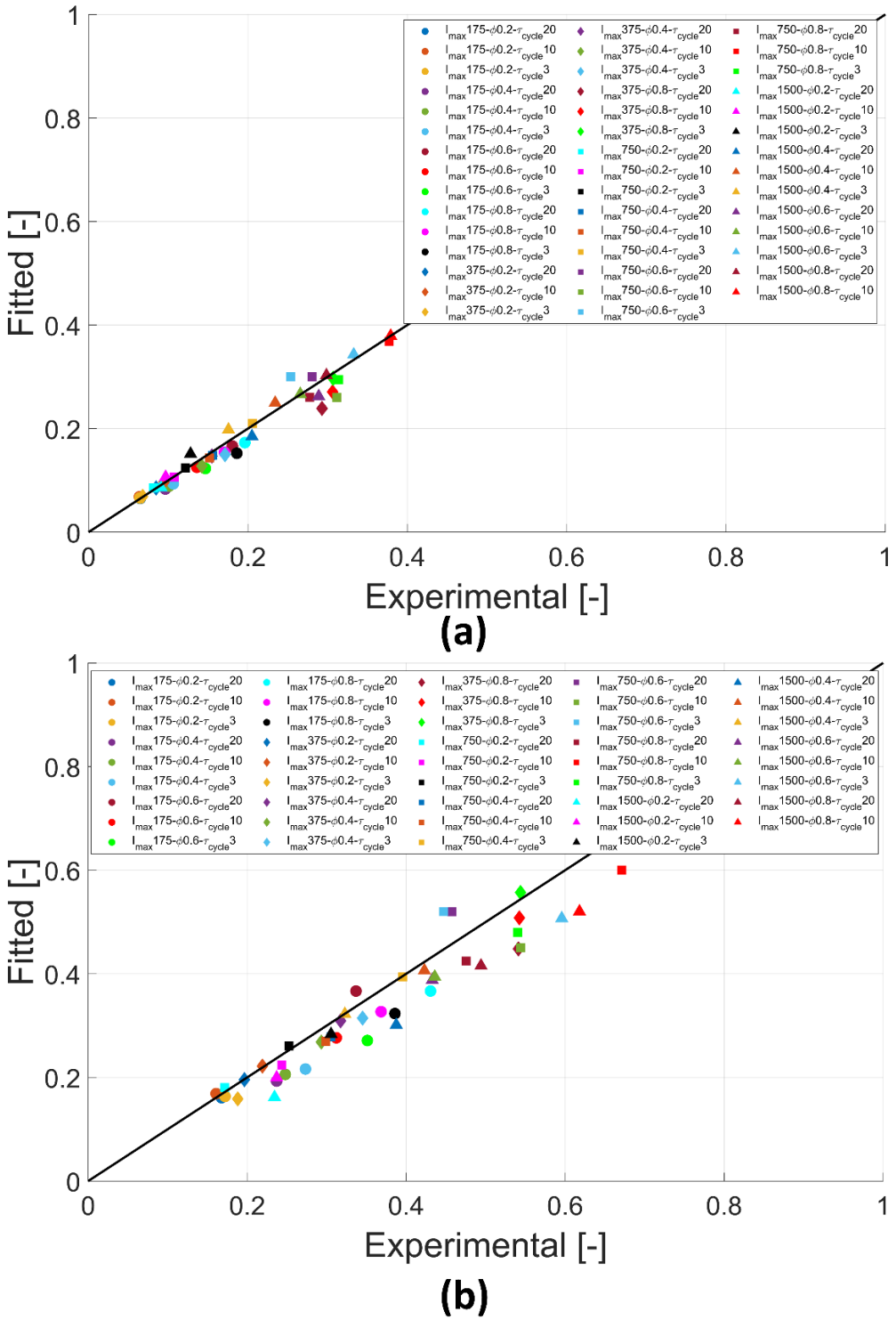

Figure 3.6: *Parity plots of average values of all replicates of the same experiment for (a) OD_{750} and (b) OD_{680} for pulsed light fitted data. Each point is the mean of all replicates of the same experiment.*

Table 3.3 shows values of the estimated parameters, along with their 95% confidence intervals and 95% *t*-values. *t*-values of all the parameters are higher than the reference *t*-value of 1.65, showing that the parameter estimation is precise.

Table 3.3: *Fitted parameters. Reference t-value is equal 1.65.*

Name	Value	95% confidence interval	95% *t*-value
k_a	$1.7*10^{-3}$ m^2 μmol^{-1}	$\pm 2.81*10^{-4}$ m^2 μmol^{-1}	6.21
k_c	$2.7*10^{-2}$ cell mol_{PSU}^{-1}	$\pm 3.10*10^{-3}$ cell mol_{PSU}^{-1}	8.65
k_d	$8.37*10^{-1}$ s^{-1}	$\pm 2.21*10^{-1}$ s^{-1}	3.79
k_i	$7.40*10^{-7}$ m $\mu mol^{-0.5}$ $s^{-0.5}$	$\pm 3.00*10^{-7}$ m $\mu mol^{-0.5}$ $s^{-0.5}$	2.46
k_p	$1.97*10^{-2}$ s cell h^{-1} mol_{PSU}^{-1}	$\pm 2.90*10^{-3}$ s cell h^{-1} mol_{PSU}^{-1}	6.82
k_r	$4.80*10^{-7}$ s^{-1}	$\pm 2.5*10^{-7}$ s^{-1}	1.92

3.3.3 Model validation and discussion

After parameter estimation, the calibrated model was validated against additional data. Figure 3.7 shows parity plots of OD_{750} and OD_{680} for the prediction of pulsed light data from Sivakaminathan et al. (2018) at I_{max}= 375 µmol m^{-2} s^{-1} and ϕ = 0.6 at different cycle times. Parity plots (Figure 3.7) reflect those in Figure 3.6, showing a similar performance of the calibrated model under validation.

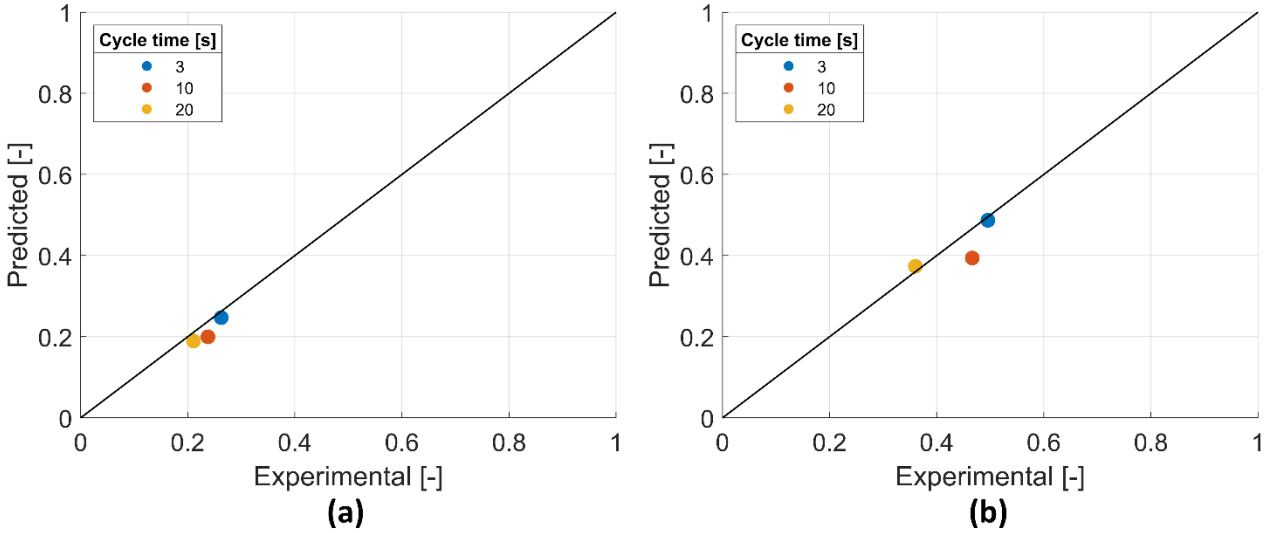

Figure 3.7: *Parity plots for validation (I_{max} = 375 µmol m^{-2} s^{-1} and ϕ = 0.6, for different time cycles): dots are average values of all replicas of the same experiment for (a) OD_{750} and (b) OD_{680} for pulsed-light data.*

Additional model validation was performed by comparing experimental data and model predictions of continuous light experiments from Sivakaminathan et al. (2018).

Figure 3.8 reports box plots of $\%MRSE$ for continuous light data validation. The median value of $\%MRSE$ for OD_{750} and OD_{680} in Figure 3.8 are 15% and 18%: as expected for validation, they are higher than the ones in Figure 3.5 for model calibration, but still close to experimental error ranges. Moreover, a parity plot of mean values of predicted OD_{750} and OD_{680} over time and experimental replicas is presented in Figure 3.9 for model validation with continuous light data. Similarly to model calibration, points in Figure 3.9 are distributed and aligned along the bisectrix and do not show any abnormal patters. Figures 3.8-9 thus show that, with parameters identified under pulsed light, the model can capture the system also under continuous light conditions, confirming the robustness and reliability of the estimated set of parameters.

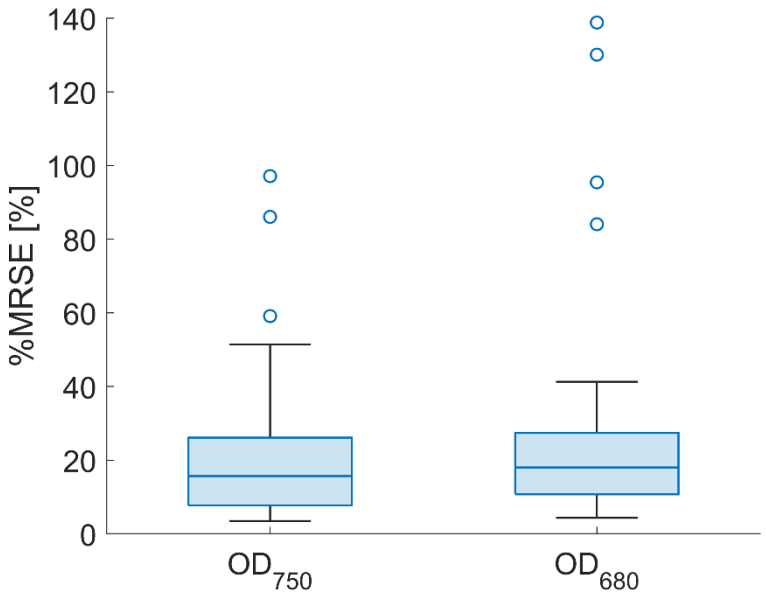

Figure 3.8: *Box plot of %MSE for OD_{750} and OD_{680} of continuous light data for model validation.*

Analysis of both calibration and validation results shows that the prediction of OD_{750} is better than OD_{680}. This is acceptable, since accurate modelling of OD_{750} and thus of biomass growth is the primary goal of this activity. Comparison of the median of the %MRSE between calibration and validation suggests that the difference is principally due to higher biological noise. However, the ability to predict OD_{680} shown in both calibration and validation suggests the suitability of the model to analyse larger scale PBRs.

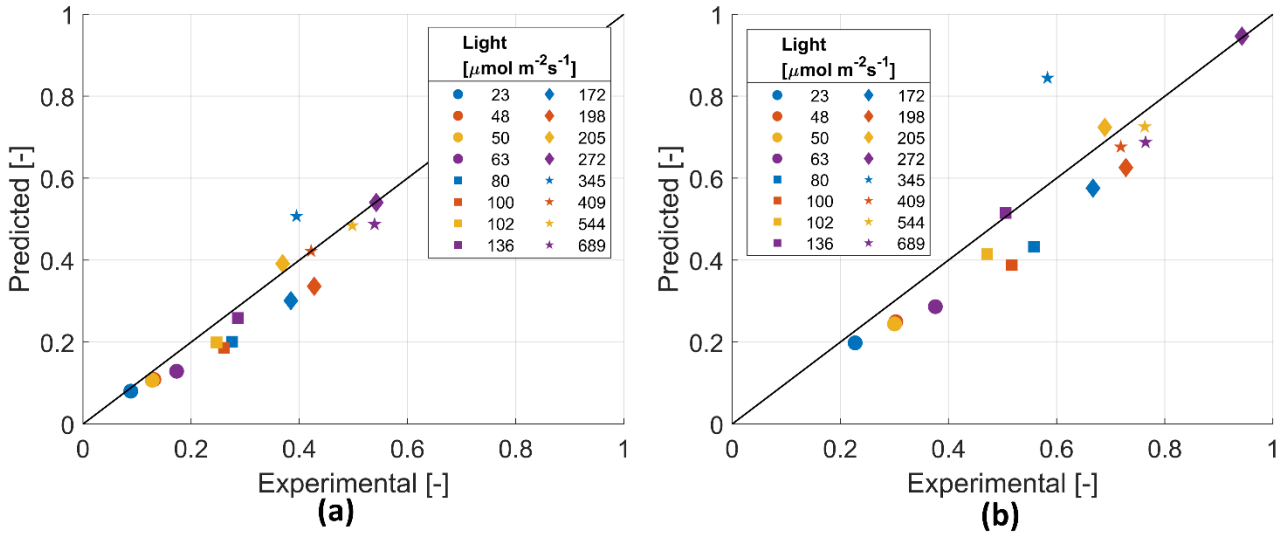

Figure 3.9: *Parity plots of (a) OD_{750} and (b) OD_{680} for continuous light data for model validation. Each point is the mean of all replicas of the same experiment.*

In fact, as reported in Sivakaminathan et al. (2018), OD_{680}/OD_{750} is a proxy for the cellular pigment content at different light conditions, which can be used to derive light attenuation parameters (Pottier et al., 2005) and thus calculate light profiles in PBRs. The ability to model light distribution in industrial scale PBRs and high concentration cultures is a key aspect in the design and efficient operation of high scale cultivation systems.

In addition to the validation activity, the model was employed to predict final biomass productivity $\bar{\mu}$ under pulsed light in the experimental space considered in Sivakaminathan et al. (2018) to better understand the behaviour of the model prediction upon the experimental space and to find the input conditions that lead to the highest biomass productivity. Figure 3.10 presents a 4D plot for the different conditions of I_{max} (x-axis), ϕ (z-axis), τ_{cycle} (y-axis) from Sivakaminathan et al. (2018). The colour of the points in Figure 3.10 accounts for the final biomass productivity according to the colorbar reported in the graph. Note that the model formulation proposed in this work can capture both photolimitation and photoinhibition under pulsed light. Photolimitation can be observed for τ_{cycle}=20 s at values of $\phi = 0.2$ (blue-cyan dots): the light phase is too short and thus the biomass productivity is low also for high values of I_{max}. However, for the same τ_{cycle} value, biomass productivity can be increased either by increasing the light fraction ϕ (and thus decreasing the dark fraction) at a fixed I_{max} (moving vertically in Figure 3.10), or by increasing I_{max} at a fixed ϕ (moving horizontally in Figure 3.10), until a photo-saturated region (red dots) of high productivities is reached at about I_{max} =700-800 μmol m^{-2} s^{-1} and ϕ= 0.75-0.8. By moving out of this region by increasing I_{max} only, a decrease in biomass productivity is found due to photoinhibition.

The results in Figure 3.10 at τ_{cycle} =20 s and τ_{cycle} = 10 s, showed that, for low values of cycle time (τ_{cycle}), I_{max} and ϕ are the variables that affect biomass productivity the most, confirming the findings in Sivakaminathan et al. (2018). However, Figure 3.10 indicates that the cycle time seems to have a higher impact on the biomass production at low values (i.e., at higher light frequencies), where an increase in biomass productivity is predicted and the predicted photosaturation region is larger. This prediction also reflects the findings from Borella et al. (2022) and Diotto et al. (2022), where it is reported that an increase in biomass productivity with pulsed light operations can be achieved under conditions of low cycle times (and thus high light cycle frequencies). In the range analysed, the highest predicted biomass productivity was equal to 0.074 h^{-1} at approximately I_{max} =800 µmol m^{-2} s^{-1} and ϕ= 0.8. Notice that, since the model was calibrated for values of τ_{cycle} between 3 s and 20 s, model extrapolation at extremely low values of cycle time may lead to inaccurate results. Moreover, model flexibility in capturing the effect of τ_{cycle} varying over wide intervals could be limited, since the Camacho-Rubio model does not explicitly account for the effect of cycle time on the processes of absorption, conversion, and dissipation of photons in the reaction centres (Zarmi et al., 2020).

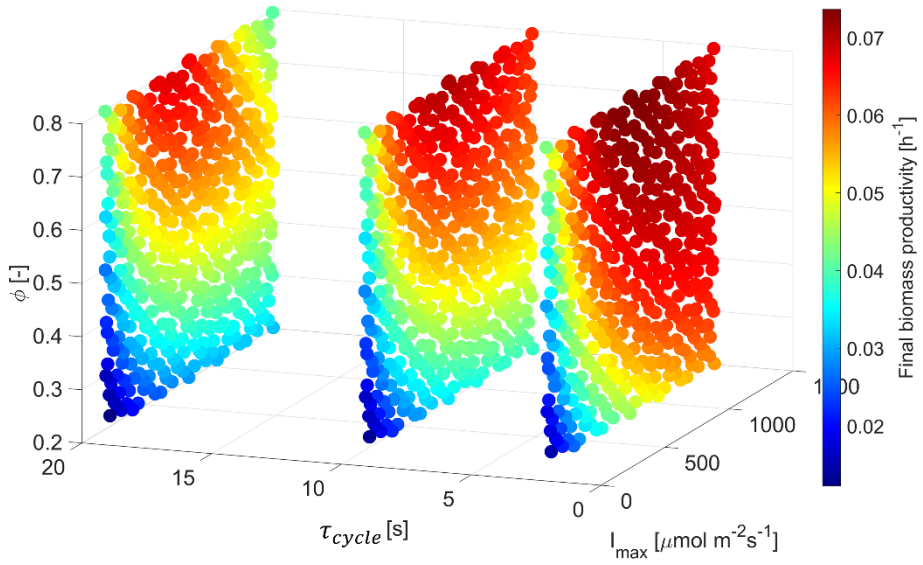

Figure 3.10: *4D plot of the predicted final biomass productivity under pulsed light conditions for all experimental conditions in* Sivakaminathan et al. (2018). *The input variables are reported on the x-y-z axes, while the colour of the dots accounts for the final biomass productivity according to the colorbar.*

3.4 Conclusions

In this study, a novel formulation of the Camacho-Rubio model (Camacho Rubio et al., 2003) was developed to simultaneously capture both PSUs and biomass dynamics. The theoretical knowledge of photosynthetic characteristic time scales guided the mathematical expressions of intra- and inter-

cycles variable dynamics with algebraic and differential equations respectively. The dataset made of dynamic experimental profiles of biomass growth under pulsed light operation from Sivakaminathan et al. (2018) was used for model calibration or, as it is commonly called, model identification. Due to the big-data nature of the dataset, PCA and PLS techniques were employed to reduce biological noise and reject outliers in pulsed-light data in a statistically sound way. The model was then identified with clean data under intermittent illumination, and a precise parameter estimation was obtained. Moreover, the model was validated against additional data with both pulsed and continuous light regimes. The average experimental error was of 8% under pulsed light and 15% under continuous light for the prediction of OD_{750}, while for OD_{680} it was of 12% under pulsed light and 18% under continuous light. The mismatch between pulsed and continuous data errors (shown respectively in Figures 3.5 and 8) is likely to be mainly related to the higher scattering of data under continuous light, while the higher error for OD_{680} with respect to OD_{750} could also have been caused by considering OD_{750} only for the data analysis. The resulting calibrated model is a robust and reliable tool that can be employed for dynamic modelling of microalgae cultivation systems under both pulsed and continuous light operation.

However, since experiments in Sivakaminathan et al. (2018) are batches with limited duration, the efficacy in representing photo-acclimation dynamics could be limited for simulations of long-term cultivation in continuous systems, and a recalibration of parameters with data obtained on longer experiments could be required. Moreover, for application of the model to simulate large scale system, equations proposed in this work must be integrated with suitable expressions to account for light attenuation in the culture.

The mathematical procedure presented in this work could in principle be applied to other state models to advance the field of mathematical modelling of microalgal growth under pulsed light conditions.

3.4 Chapter Nomenclature

Abbreviations:

HTS: High-Throughput Screening

OD_{680}: Optical Density at 680 nm

OD_{750}: Optical Density at 750 nm

ODE: Ordinary Differential Equation

PBR: Photobioreactor

PCA: Principal Component Analysis

PLS: Partial Least-Squares regression

PSU: Photosynthetic Unit

P-I: Photosynthetic-Irradiance

RoMA: robotic manipulator arm

SPE: Squared Prediction Error

Symbols:

$\boldsymbol{E}$: Residual Matrix/ Residual Matrix of Predictors of PLS

$\boldsymbol{F}$: Residual Matrix of Response Variables of PLS

H: Number of Input Variables of PLS

J: Number of Variables

K: Time Samples

L: Number of Principal Components

$\boldsymbol{P}$: Loadings Matrix/ Loading Matrix of Predictors of PLS

$\boldsymbol{Q}$: Loadings of Response Variables of PLS

$\boldsymbol{T}$: Scores Matrix/ Scores Matrix of Predictors of PLS

$\boldsymbol{U}$: Scores Matrix of Response Variables of PLS

$\boldsymbol{X}$: Matrix of Historical Data/ Matrix of Predictors of PLS

$\boldsymbol{X_U}$: Unfolded Matrix of Data

$\underline{\boldsymbol{X}}$: Tensor of Dynamic Data

$\boldsymbol{Y}$: Matrix of Response Variables of PLS

$\boldsymbol{Y_U}$: Unfolded Matrix of Measured Variables of PLS

$\underline{\boldsymbol{Y}}$: Tensor of Dynamic Measured Variables of PLS

Y: Number of Observations/Experimental Replicas of the same experiment

y_i: i^{th} Experimental Data Point

$y_i^{predict}$: Model Prediction of the i^{th} Experimental Data Point

Variables:

A [mol_{PSU} $cell^{-1}$]: Utility variable for the calculation of the cycle-average specific biomass production rate

a_1, a_2, a_3 [mol_{PSU} $cell^{-1}$]: Cellular concentration of PSU in the open, closed and inhibited state

$a_{2,min}$, $a_{2,max}$ [mol_{PSU} $cell^{-1}$]: Minimum and maximum number of moles of closed PSUs per cell

a_f [mol_{PSU} $cell^{-1}$]: Cellular concentration of functional PSUs

a_t [mol_{PSU} $cell^{-1}$]: Cellular total PSUs concentration

B [cell mol_{PSU}^{-1} h^{-1}]: Utility variable for the calculation of the cycle-average specific biomass production rate

CNV [s h^{-1}]: Conversion factor from seconds to hours

I [µmol m^{-2} s^{-1}]: Light intensity

I_{avg} [µmol m^{-2} s^{-1}]: Cycle average light intensity

I_{max} [µmol m^{-2} s^{-1}]: Maximum light intensity reached in the cycle

$\bar{I}$ [µmol m^{-2} s^{-1}]: Average value of light intensity during the light phase

k_a [m^2 μmol^{-1}]: Light absorption coefficient

k_c [cell mol_{PSU}^{-1}]: Rate constant involved in the photoacclimation process

k_d [s^{-1}]: Kinetic constant of PSUs deactivation rate

k_i [m $\mu mol^{-0.5}$ $s^{-0.5}$]: Inhibition rate constant

k_{OD} [cell mol_{PSU}^{-1}]: Proportionality factor for quantifying photoacclimation

k_p [s cell h^{-1} mol_{PSU}^{-1}]: Proportionality factor for biomass production rate

k_r [s^{-1}]: Recovery rate constant

k_s [mol_{PSU} $cell^{-1}$]: Concentration of closed PSUs at which photosynthesis is equal to half the maximum one

M [h^{-1}]: Maintenance factor

OD_{680} [-]: OD_{680}

OD_{750} [-]: OD_{750}

r_m [mol_{PSU} $cell^{-1}$ s^{-1}]: Maximum rate of energy consumption

t [s]: Time

$\%MRSE$ [%]: Percentage Mean Root Squared Error

μ [h^{-1}]: Biomass specific growth rate

$\bar{\mu}$ [h^{-1}]: Cycle-average specific biomass production rate

τ [-]: Non-dimensional time variable

τ_{cycle} [s]: Cycle Time

ϕ [-]: Light phase

Chapter 4

A model to capture microalgae growth under ultra-high frequency pulsed light conditions

In Chapter 3 a dynamic PSU-model was developed for application to pulsed light microalgae cultivation. However, experimental data in Chapter 3 were obtained for low light frequencies. Operations with high light frequency can lead to higher biomass productivities with respect to continuous light, but the selection of the optimal operations is not trivial due to the lack of understanding of the pulsed light phenomena. Available PSUs models may fail to capture the behavior at ultra-high frequencies since they do not explicitly represent photon absorption-usage-dissipating processes. In this Chapter, starting from a work by Zarmi et al. (2020) that explicitly considers these aspects, we developed a new model to understand the phenomena observed experimentally at high light frequencies (Diotto et al., 2022) and thus guide future experimental campaigns and operations of PBRs.

4.1 Introduction

In Chapter 3, the advantages of employing pulsed light for microalgal cultivation were discussed. Cultivation under high-frequency pulsed light can enhance biomass productivity with respect to continuous light thanks to the Flashing Light Effect (FLE) (Diotto et al., 2022), along with the composition of pigments relevant for the market (Fu et al., 2013). However, to achieve this performance enhancement, an accurate tuning of the operating pulsed light parameters is required. An improper selection of these factors can lead to the opposite effect and to a decrease of biomass production with respect to the continuous light regime. As mentioned in Chapter 3, this is a clear incentive for developing mathematical models for understanding, managing, and optimising the cultivation under pulsed light.

A major limitation of the PSU-based models presented in Chapter 3 is that, although they perform well for conditions at low pulsed light frequency, their predictive capability may be limited for high

---

The experimental activity carried out for this Chapter was performed by Dr. Lisa Borella and Mr. Adriano Porcelli.

frequencies of pulsed light and they require model modifications (Diotto et al., 2022). Indeed, typical PSU-models do not explicitly focus on the processes involving photons absorption, usage, or dissipation. Recently, Zarmi et al. (2020) developed a new mathematical model to explain the increase in productivity found under pulsed light conditions by accounting for photon absorption and usage.

The physical phenomena considered in the model from Zarmi et al. (2020) are shown in the scheme of Figure 4.1. Since the modelling focus is on the effect of light on biomass growth, the model is suited for application in excess of nutrients. Specifically, the model was formulated for pulsed light operation, where every light cycle is composed by an initial light pulse followed by a dark time. During the light pulse, in every reaction center (RC), photons are absorbed by the photosystem II (PSII), and the number of photons absorbed per unit of time depends on the absorbtion cross section A of the RC. Due to initial ultra-fast photochemical processes that involve the dissociation of water molecules, one electron is obtained from one absorbed photon. In the subsequent step, from one electron, one quinone acceptor Q_A is obtained. This step has a characteristic time τ_{02} of approximately 0.2 ms (Zarmi et al., 2020). Afterwards, from two Q_A, one reduced plastoquinone (PQ) molecule, PQH_2, is obtained. However, in a reaction center, PQs are in a limited number or *"pool"*, N_{pool}. This pool allows PSII to store the energy from the absorption of up to $2 \cdot N_{pool}$ photons by reducting two times each available PQ to PQH_2: if more than $2 \cdot N_{pool}$ photons are absorbed, the excess energy is then dissipated. Then, PQH_2 are re-oxidised and the resulting charges are delivered to subsequent slower processes in Photosystem I (PSI), while the re-oxidised PQs become available again in the PQs pool for reduction. Biomass production is thus assumed to be proportional to the re-oxidation rate of PQH_2 molecules. In this representation, the main bottleneck of the process is the PQH_2 reoxidation with the characteristic time τ_{del}, since the 0.2 ms bottleneck linked to electrons processing to Q_A is relevant only at conditions of high irradiance and/or low time pulse. Zarmi et al. (2020) report that τ_{del} is approximately equal to 10 ms. Thus, in this Chapter, the 10 ms bottleneck related to τ_{del} is denoted as BTN_{10}, and the 0.2 ms bottleneck related to τ_{02} as $BTN_{0.2}$.

From the framework highlighted in Figure 4.1, different qualitative considerations can be made. An increase in the pulse time will lead to a higher number of re-oxidised PQs per light cycle and thus to higher biomass production, until a limiting value where the whole plastoquinone pool is saturated. The clogging of the PQ pool is also the typical situation expected in continuous light operation. On the other hand, when pulsed light is employed, the reduced PQs can be re-oxidised during the dark phase of the light cycle, leading to higher productivities.

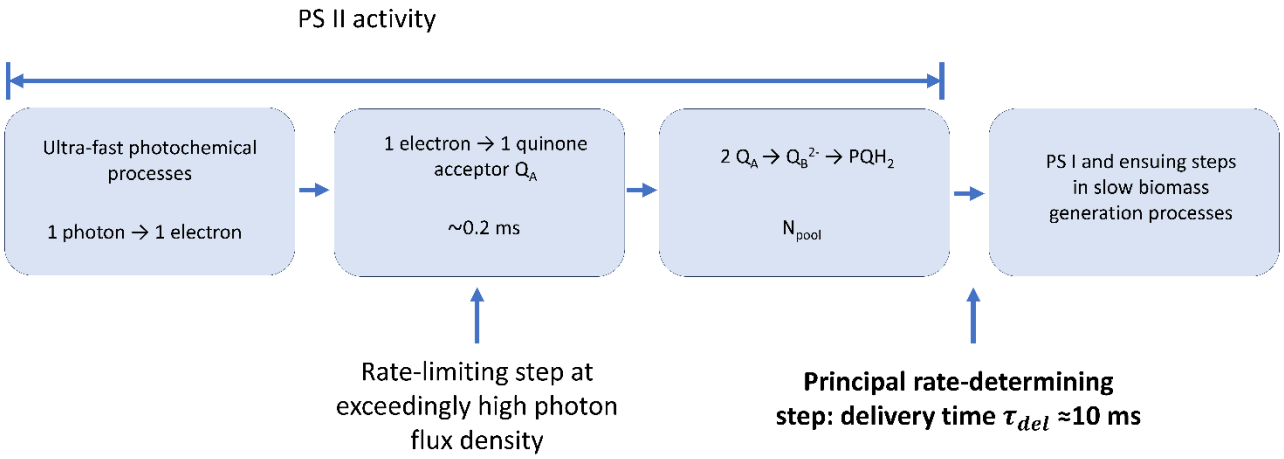

Figure 4.1: *Structure of the model from* Zarmi et al. (2020).

This suggests the existence of an optimal dark time: for very short dark times, there is not enough time to process all the oxidised PQs (until the case resembles continuous light operation), while for excessive dark times, the PQs pool would be completely oxidised, and the system may revert to respiration.

Zarmi et al. (2020), proposed a mathematical formalisation of the concepts expressed above. However, their mathematical model has some limitations:

1. it does not consider the quantitative effect of the dark time, assuming the dark time is "long enough" to process all the reduced PQs;
2. it neglects the 0.2 ms bottleneck;
3. it does not consider photoinhibition;
4. it does not include the N_{pool} distribution among the reaction centers;
5. it considers an ideal situation in which the cultivation system is subjected to the same illumination conditions everywhere, far from the real cultivation scenario in a photobioreactor, characterised by light attenuation and the effect of mixing.

The objective of this Chapter is to overcome the limitations above by developing a novel model formulation, that can be applied to understand the effect of ultra-high frequency pulsed light on cells in photobioreactors.

4.2 The mathematical model

4.2.1 Accounting for light attenuation and mixing cycle

In Zarmi et al., 2020, a square-wave shape of the light profile was adopted; since it is one of the most commonly found in literature (e.g. see Diotto et al. (2022); Camacho Rubio et al. (2003)), the same light profile is assumed in this work for the development of the model. However, this does not restrict the application of the model to other light profiles. The light profile in pulsed light operation is defined by three independent variables: the maximum light intensity reached in the cycle I_{max} [μmol m^{-2} s^{-1}], which also corresponds to the instantaneous light intensity during the light phase; the cycle time τ_{cycle} [s], i.e. the total duration of the cycle; the pulse time τ_{pulse} [s], i.e. the duration of the light phase/pulse of light. The ratio of τ_{pulse} on τ_{cycle} is called light phase (or duty cycle) ϕ [-]. Moreover, the dark time τ_{dark} [s], i.e. the duration of the dark phase, is calculated using the τ_{cycle} definition:

$$\tau_{cycle} = \tau_{pulse} + \tau_{dark} \quad . \tag{4.1}$$

The effective light conditions to which cells are exposed are affected by the cultivation system. When microalgae are cultivated in PBRs, they are subjected to two adverse phenomena: self-shading and mixing-induced light-dark cycles, which hinder the true effect of light (Barbosa et al., 2003; Graham et al., 2015). Self-shading is linked to absorption of light by cells that causes a light attenuation profile and reduces light availability in the inner parts of PBRs. Moreover, due to mixing, cells move to areas of the PBR with different illumination levels and thus, even in continuous light operation, they receive light intermittently (Zarmi et al., 2013). Mixing induced light-dark cycles can have a deep impact on microalgae cultivation (as explained in Chapter 2) and thus their effect must be accounted for to obtain a realistic representation of microalgae growth in PBRs. In fact, in PBRs, there is a periodic movement of cells due to the mixing system that affects light as perceived by cells. The rigorous mathematical representation of this phenomenon is not a trivial task, especially for complex geometries. However, for a flat PBR of depth W [m], Richmond et al., 2003 introduced the concept of cell travel time (or *mixing time* τ_{mix} [s]), which is the average (periodic) time of the mixing cycle required by one cell to move back and forth along the depth of the one-side illuminated PBR. It can be expressed as:

$$\tau_{mix} = \frac{2W}{v_{cell}} \tag{4.2}$$

with v_{cell} as the cell lateral velocity, assumed equal to bubble velocity in the range of 0.30-0.50 m s^{-1} (Richmond et al., 2003). With respect to Richmond et al. (2003), a multiplication factor of 2 was added in Equation 4.2, since, during τ_{mix}, a single cell covers two times the reactor thickness W in

its periodic movement. In this Chapter, a value of v_{cell} = 0.4 m s^{-1} is assumed based on the average on the ranges reported in Richmond et al. (2003).

Under pulsed light illumination, the comparison between τ_{cycle} and τ_{mix} can reveal interesting aspects of the PBR considered. If $\tau_{cycle} > \tau_{mix}$, the PBR is very thin and light attenuation can be neglected. On the other hand, the typical situation in PBRs occurs with $\tau_{cycle} < \tau_{mix}$ (e.g. under high frequency pulsed light with τ_{cycle}= 10 ms in a 5 cm thickness PBR, τ_{mix}=250 ms). Since we are focusing on high frequency light conditions, it is assumed that τ_{cycle} (and τ_{pulse}, τ_{dark} consequently) is "small" compared to τ_{mix}, thus $\tau_{cycle} < \tau_{mix}$. In particular, in this Chapter experimental values of τ_{pulse} and τ_{dark} will be in the range of μs and ms respectively. Thus, it is possible to calculate the number of light cycles n_{cycle} [-] a cell is subjected to during a mixing cycle:

$$n_{cycle} = \left\lfloor \frac{\tau_{mix}}{\tau_{cycle}} \right\rfloor \quad . \tag{4.3}$$

The definition of n_{cycle} allows to track the history of a single cell along one mixing cycle. The underlying idea behind the model formulation of this Chapter is that, at the *i*-th light cycle in the mixing cycle, the cell will be located at a specific coordinate in the PBR thickness that influences the attenuated amount of light received by the cell. This amount of light will have a specific effect on the cell during the light cycle time that also depends on the history of cell, thus on its state at light cycle *i*-1. This qualitative idea is the guide for the rigorous formulation presented in Section 4.2.2.

4.2.2 Effect of light on cells in a single light cycle

In Zarmi et al. (2020), the effect of light on cells is calculated for a single light cycle. Similarly, in this section all the calculated variables are for a single cell and are referred to the *i*-th light cycle (with $i \in [1 \ n_{cycle}]$). Every light cycle starts with the light phase at the beginning and finishes with the dark phase. If it is assumed that, at the beginning of the mixing cycle, the considered cell is at the illuminated surface of the vertical PBR, the position z [m] of the considered cell is $z = 0$ for time $t = 0$, $z = W$ for time $t = \tau_{mix}/2$ and $z = 0$ for time $t = \tau_{mix}$. Then, the position of the cell $z_{start,i}$ [m] at the beginning of the *i*-th light cycle is:

$$z_{start,i} = W - \left| W - \frac{2W}{n_{cycle}}(i-1) \right| \quad , \tag{4.4}$$

for i from 1 to n_{cycle}. Notice that the absolute values in Equation 4.4 accounts for the back-and-forth movement of the cell in the PBR thickness during one mixing cycle. Both Equations 4.2 and 4.4 are strongly related to the hydrodynamics of the PBR and represent a simplification necessary for the

development of the modelling structure. Due to light attenuation, the position of the cell in the PBR influences the light intensity the cell is exposed to. Since, as assumed in Section 4.2.1, τ_{pulse} is small with respect to τ_{mix}, the change in position of the cell during the light phase can be neglected and thus a constant irradiance value I_i [µmol m^{-2} s^{-1}] can be calculated through the Lambert-Beer law as:

$$I_i = I_{max} \exp(-k_a c_x z_{start,i}) \quad , \tag{4.5}$$

where I_{max} is the intensity of the light pulse, k_a [m^2 g^{-1}] is the Lambert-Beer light absorption coefficient, and c_x [g m^{-3}] is the biomass concentration in the PBR. I_i is the effective light intensity the cell is exposed to during the light phase in the *i*-th light cycle. Similarly to Zarmi et al. (2020), from Equation 4.5, it is possible to calculate:

$$n_{0,i} = (I_i \, 10^{-6} A_v)(A \, 10^{-18}) \quad , \tag{4.6}$$

where $n_{0,i}$ [photons s^{-1}] is the rate of photons hitting a single reaction center, A_v is the Avogadro's number ($6.022*10^{23}$) and A [nm^2] is the effective photon absorption cross section of each reaction-center antenna, responsible for photochemical conversion in the photosystem II (Zarmi et al., 2020). Notice that Equation 4.6 is formulated on a single RC, not on the whole cell: similarly, the following equations will be formulated on a single RC. According to Zarmi et al. (2020), the theoretic number of PQs $N_{g,theor,i}$ [-] reduced during the pulse of the *i*-th light cycle is:

$$N_{g,theor,i} = \frac{n_{0,i}\tau_{pulse}}{2} \quad . \tag{4.7}$$

$N_{g,theor,i}$ represents the theoretical number of reduced PQs, since it does not consider the effect of the $BTN_{0.2}$ shown in Figure 4.1. Differently from Zarmi et al. (2020), in this work this bottleneck is accounted by computing the maximum number of photons $phot_{max}$ [photons n_{RC}^{-1}] that can be processed during the light phase:

$$phot_{max} = \frac{\tau_{pulse}}{\tau_{02}} \quad . \tag{4.8}$$

Since two photons drive the reduction of a single PQ (see Figure 4.1), the maximum number of PQs that can be reduced is $phot_{max}/2$. Thus, the real number of PQs $N_{g,i}$ [-] reduced during the pulse of the *i*-th light cycle is:

$$N_{g,i} = \begin{cases} N_{g,theor,i} & if \; N_{g,theor,i} \leq \frac{phot_{max}}{2} \\ \frac{phot_{max}}{2} & if \; N_{g,theor,i} \geq \frac{phot_{max}}{2} \end{cases} \quad . \tag{4.9}$$

The second condition of Equation 4.9 is relevant for high light conditions (i.e., high values of I_{max} and/or τ_{pulse}), where the number of available photons can be higher than the number of photons that the system is able to process due to $BTN_{0.2}$. This condition also causes a corresponding dissipation of photons; thus, the number of photons dissipated in the $BTN_{0.2}$ can be calculated as:

$$phot_{diss02,i} = \begin{cases} 0 & if\ N_{g,theor,i} \leq \frac{phot_{max}}{2} \\ 2\left(N_{g,theor,i} - \frac{phot_{max}}{2}\right) & if\ N_{g,theor,i} > \frac{phot_{max}}{2} \end{cases} . \quad (4.10)$$

After the calculation of the reduced number of PQs in the light phase, the theoretical number of re-oxidised PQs $n_{0,theor,i}^{reox}$ [-] during the light phase can be computed as proposed by Zarmi et al. (2020):

$$n_{0,theor,i}^{reox} = \frac{\tau_{pulse}}{\tau_{del}} \quad , \quad (4.11)$$

which is the maximum number of PQs that can be re-oxidised during τ_{pulse} due to BTN_{10}. Notice that in Zarmi et al. (2020), Equation 4.11 is employed to calculate the real number of re-oxidised PQs during the light phase $n_{0,i}^{reox}$ [-], while in this work $n_{0,i}^{reox}$ is calculated as:

$$n_{0,i}^{reox} = \begin{cases} n_{0,theor,i}^{reox} & if\ \ n_{0,theor,i}^{reox} \leq N_{g,i} + n_{old,i} \\ N_{g,i} + n_{old,i} & if\ \ n_{0,theor,i}^{reox} > N_{g,i} + n_{old,i} \end{cases} \quad (4.12)$$

where we introduce the variable $n_{old,i}$ [-], which is the residual number of PQs already reduced from the light cycle *i*-1 in the mixing cycle. $n_{old,i}$ accounts for the history of the cell along the mixing cycle and shows the influence that light cycles have on each other. The first condition of Equation 4.12 is expected under high light conditions (i.e., high values of I_{max} and/or τ_{pulse}): many PQs are reduced and thus the number of PQs that can be re-oxidised is smaller due to BTN_{10}. The second condition is expected for low light conditions (i.e., small values of I_{max} and/or τ_{pulse}), where, due to the scarcity of available photons, the reduced PQs are in a limited number and thus BTN_{10} does not have any influence on the PQ re-oxidation.

In parallel with Zarmi et al. (2020), after the calculation of $n_{0,i}^{reox}$, it is possible to calculate $n_{add,theor,i}$ [-], i.e. the theoretical number of PQs reduced during the light pulse and not re-oxidized immediately or, in other words, the residual number of reduced PQs at the end of the light phase:

$$n_{add,theor,i} = N_{g,i} + n_{old,i} - n_{0,i}^{reox} \quad (4.13\text{-a})$$

$$= \left(\frac{N_{g,i}}{\tau_{pulse}} + \frac{n_{old,i}}{\tau_{pulse}} - \frac{n_{0,i}^{reox}}{\tau_{pulse}}\right)\tau_{pulse} \quad (4.13\text{-b})$$

The reduced PQs at the end of the light phase are stored in the PQ pool until it is full:

$$n_{add,theor,i} \leq N_{pool} \quad \rightarrow \quad \left(\frac{N_{g,i}}{\tau_{pulse}} + \frac{n_{old,i}}{\tau_{pulse}} - \frac{n_{0,i}^{reox}}{\tau_{pulse}}\right)\tau_{pulse} \leq N_{pool} \quad (4.14)$$

Equation 4.14 suggests that, in order to avoid clogging of the PQ pool, τ_{pulse} must be lower than a certain threshold. Thus, from Equation 4.14, it is possible, after employing Equation 4.13-b, to calculate the maximum time pulse $\tau_{pulse,i}^{max}$ [s] above which the PQ pool is completely full:

$$\tau_{pulse,i}^{max} = \frac{N_{pool}}{\frac{N_{g,i}}{\tau_{pulse}} + \frac{n_{old,i}}{\tau_{pulse}} - \frac{n_{0,i}^{reox}}{\tau_{pulse}}} \quad (4.15)$$

If $\tau_{pulse} > \tau_{pulse,i}^{max}$, the PQ pool is completely reduced at the end of the pulse and the PQs in excess are dissipated. Notice that in Equation 4.15 the term $\frac{N_{g,i}}{\tau_{pulse}} - \frac{n_{0,i}^{reox}}{\tau_{pulse}}$ does not depend on τ_{pulse} due to the formulation of $N_{g,i}$ and $n_{0,i}^{reox}$; the only dependence on τ_{pulse} is in $\frac{n_{old,i}}{\tau_{pulse}}$.

The real number of PQs reduced during the light pulse and not re-oxidized immediately $n_{add,i}$ [-] depends on the value of τ_{pulse} and can be calculated as:

$$n_{add,i} = \begin{cases} n_{add,theor,i} & if\ \ \tau_{pulse} \leq \tau_{pulse,i}^{max} \\ N_{pool} & if\ \ \tau_{pulse} > \tau_{pulse,i}^{max} \end{cases} \quad (4.16)$$

Moreover, if N_{pool} is saturated, this will lead to the dissipation of the excess PQs; the number of PQs dissipated $n_{disslight,i}$ [-] linked to BTN_{10} due to the saturation of the PQs pool can be calculated as:

$$n_{disslight,i} = \begin{cases} 0 & if\ \ \tau_{pulse} \leq \tau_{pulse,i}^{max} \\ n_{add,theor,i} - N_{pool} & if\ \ \tau_{pulse} > \tau_{pulse,i}^{max} \end{cases} \quad (4.17)$$

A clarification should be made for the case in which the denominator of Equation 4.15 is equal to 0, that occurs when $\frac{N_{g,i}}{\tau_{pulse}} + \frac{n_{old,i}}{\tau_{pulse}} - \frac{n_{0,i}^{reox}}{\tau_{pulse}} = 0$. In this case, all the PQs during the light cycle are re-oxidised and thus $n_{add,i} = 0$. Numerically, this would give a calculated $\tau_{pulse,i}^{max}$ equal to infinite, which has no physical meaning. However, in this case the condition $\tau_{pulse} \leq \tau_{pulse,i}^{max}$ would be satisfied and, from Equation 4.17, $n_{disslight,i} = 0$, which is a consistent result.

After the light phase, it is necessary to perform calculations for the subsequent dark phase, when, since no light is provided, the only phenomenon that occurs is the re-oxidation of the residual reduced PQs at the end of the light phase. In Zarmi et al. (2020) it is assumed that the dark time is sufficiently long to completely re-oxidise $n_{add,i}$. Considering that to re-oxidise a single PQ a τ_{del} amount of time is required, it is possible to compute:

$$\tau_{dark,i}^{max} = n_{add,i}\ \tau_{del} \quad (4.18)$$

the maximum dark time $\tau_{dark,i}^{max}$ [s] for the re-oxidation of PQs in the dark phase. If $\tau_{dark} < \tau_{dark,i}^{max}$, there will still be a number of reduced PQs at the end of the dark phase. However, if $\tau_{dark} > \tau_{dark,i}^{max}$, after the total re-oxidation of PQs in $\tau_{dark,i}^{max}$, there will be a $\tau_{dark,i}^{max} - \tau_{dark}$ excess time. This time in excess is wasted: thus, it is expected that working at $\tau_{dark} > \tau_{dark,i}^{max}$ is not convenient, since it does not enhance photoproduction processes.

Similarly to Equation 4.16, it is possible to calculate the number of PQs re-oxidised during the dark phase $n_{dark,i}^{reox}$ [-] that depends on τ_{dark}:

$$n_{dark,i}^{reox} = \begin{cases} \frac{\tau_{dark}}{\tau_{del}} & if\ \tau_{dark} \leq \tau_{dark,i}^{max} \\ n_{add,i} & if\ \tau_{dark} > \tau_{dark,i}^{max} \end{cases} \quad (4.19)$$

and the number of reduced PQs at the end of the dark phase $n_{dark,i}^{red}$ [-]:

$$n_{dark,i}^{red} = \begin{cases} n_{add,i} - n_{dark,i}^{reox} & if\ \tau_{dark} \leq \tau_{dark,i}^{max} \\ 0 & if\ \tau_{dark} > \tau_{dark,i}^{max} \end{cases} \quad (4.20)$$

The total number of the PQs re-oxidised during the entire light cycle $n_{tot,i}^{ox}$ [-] is:

$$n_{tot,i}^{ox} = n_{0,i}^{reox} + n_{dark,i}^{reox} \quad (4.21)$$

The total number of the dissipated PQs $n_{disstot,i}$ [-] due to both BTN_{10} and $BTN_{0.2}$ bottlenecks is:

$$n_{disstot,i} = n_{disslight,i} + \frac{phot_{0.2diss,i}}{2} \quad (4.22)$$

Finally, $n_{dark,i}^{red}$, the residual number of reduced PQs at the end of the *i*-th light cycle, corresponds to the initial number of reduced PQs of the *i+1*-th light cycle:

$$n_{old,i+1} = n_{dark,i}^{red} \quad (4.23)$$

4.2.3 Calculation of biomass productivity

Section 4.2.2 allows calculation of variables in the *i*-th light cycle. By iterating the calculations for *i* from 1 to n_{cycle}, the "history" of the effect of light on a cell in a mixing cycle can be obtained. All calculations were made on a single RC: the next step is to assess the impact of these quantities on the biomass productivity.

When cells are exposed to excessive illumination levels, they experience photoinhibition, followed by a decrease in the biomass productivity: this fact was neglected by Zarmi et al. (2020). In our model framework, photoinhibition can be represented by a decrease in the functional number of RCs per cell. Thus, it is possible to write:

$$n_{RC,tot} = n_{RC,a} + n_{RC,dam} \quad (4.24)$$

where $n_{RC,tot}$ [cell^{-1}] is the total number of RCs per cell, $n_{RC,dam}$ [cell^{-1}] is the number of damaged RCs per cell due to photoinhibition, and $n_{RC,a}$ [cell^{-1}] is the number of active RCs per cell, which are the only one that participate in the photosynthetic process. If all terms in Equation 4.24 are divided by $n_{RC,tot}$, a relation between the fractions of RCs can be written:

$$1 = x_{RC,a} + x_{RC,dam} \quad (4.25)$$

with $x_{RC,a}$ and $x_{RC,dam}$ [-] as the fraction of active and damaged RCs, respectively. In the modelling framework of Section 4.2.2, inhibiting light conditions will cause higher values of dissipated PQs. Thus, $x_{RC,dam}$ can be linked to average PQs dissipation in a mixing cycle, by writing:

$$x_{RC,dam} = d + \frac{a}{1+\exp\left[b\left(\frac{\left(\sum_{i=1}^{n_{cycle}} \frac{phot_{0.2diss,i}}{2} + w_{10}\sum_{i=1}^{n_{cycle}} n_{diss10,i}\right)}{n_{cycle}\,\tau_{cycle}} + c\right)\right]} \quad (4.26)$$

The effect average dissipation on the fraction of damaged RCs is expressed through a sigmoidal relation to account that, after a certain degree of dissipation, the inhibition level reaches a maximum, and all RCs are damaged. In Equation 4.26, the sigmoidal relation is defined by parameters a [-], b [s] (that must have negative value), c [s^{-1}], d [-] and by the relative weight w_{10} [-]. These five parameters will be tuned from experimental data as discussed in the following Sections.

In Equation 4.26, $x_{RC,dam}$ is proportional to the sum of the average PQs dissipation due to BTN_{10} and $BTN_{0.2}$ nromalised over the cycle time τ_{cycle}. In the expression, the relative weight w_{10} was included, since, in principle, the contribution of the two bottlenecks to photoinhibition can be different. Equation 4.26 shows that the higher the average dissipated PQs, the higher the inhibition effect.

From $x_{RC,dam}$, the active number of RCs can be calculated with Equations 4.24-4.25. According to Zarmi et al. (2020), the biomass production is proportional to the re-oxidation rate of PQs; thus, the specific biomass production rate μ [d^{-1}] can be written as:

$$\mu = k_{cx}\left(\frac{x_{RC,a}\,n_{RC,tot}}{n_{cycle}\tau_{cycle}}\sum_{i=1}^{n_{cycle}} n_{tot,i}^{ox}\right) \quad (4.27)$$

and is proportional to the number of active RCs $x_{RC,a}n_{RCtot}$ and to the number of PQs re-oxidised in a light cycle averaged over all the light cycles in a mixing cycle, with k_{cx} [cell s n_{PQ}^{-1} d^{-1}] as a proportionality constant. The variable $n_{RC,tot}$ can be embedded in the proportionality constant, obtaining:

$$\mu = K_{cx}\left(\frac{x_{RC,a}}{n_{cycle}\tau_{cycle}}\sum_{i=1}^{n_{cycle}} n_{tot,i}^{ox}\right) \quad (4.28)$$

with K_{cx} in [n_{RC} s n_{PQ}^{-1} d^{-1}].

Notice that all the calculations that led to μ in Equation 4.28 were made for a single value of N_{pool}. However, in a cell, a distribution of the PQ pool exists among different RCs (Zarmi et al., 2020), which are assumed to follow a normal distribution $P(N_{pool})$ with average N_{pool}^{mean} of 7 n_{PQ} and standard deviation N_{pool}^{std} of 2 n_{PQ} (Zarmi et al., 2020). These values derive from Zarmi et al. (2020), where the authors fit standard distribution using results from previous studies on the estimation of the size of PQ pool in photosystem II. To account for the distribution of the PQ pool, we define the specific biomass production rate $\bar{\mu}$ [d^{-1}] averaged over the N_{pool} distribution:

$$\bar{\mu} = \int_{-\infty}^{+\infty} \mu(N_{pool})\,P(N_{pool})\,dN_{pool} \quad (4.29)$$

where $\mu(N_{pool})$ expresses the dependence on N_{pool} of μ calculated in Equation 4.28.

From $\bar{\mu}$, it is possible to calculate the average biomass production rate $\bar{r}_x$ [g m^{-3} d^{-1}] in the PBR:

$$\bar{r}_x = \bar{\mu} c_x \quad (4.30)$$

Equation 4.30 allows to calculate the biomass production rate; to account for the oxigen production rate, it can be modified by introducing an oxygen to biomass yield $Y_{O_2/X}$ [mg_{O2} g^{-1}]:

$$\bar{r}_{O_2} = Y_{O_2/X}\, \bar{r}_x \quad (4.31)$$

with $\bar{r}_{O_2}$ [mg_{O2} m^{-3} d^{-1}] the average oxygen production rate.

To conclude, the model of Equations 4.1-4.31 accounts for the effect of pulsed light on biomass production by performing photon-balance calculations on a single RC, and expressing the effect of photoinhibition on the number of activated RCs and, as a consequence, on the biomass production rate. The developed model includes parameters with a strong physical meaning known *a priori*, such as τ_{del}, τ_{02}, A, and the mean and standard deviation of the N_{pool}, and parameters a, b, c, d, w_{10}, K_{cx} that needs to be tuned from experimental data.

4.2.4 Smoothness of the model equations

The model presented in Equations 4.1-4.31 presents different *if* conditions; to ease the practical implementation and usage of the model, these expressions were replaced with continuous, differentiable *switch functions* in the form proposed by Vanthoor et al. (2011). More details are reported in the Appendix A.

4.3 Experimental materials and methods

Experimental data employed in this work are from two different types of experiments: steady state growth experiments and respirometry experiments.

4.3.1 Steady state growth experiments

Experimental steady state data presented in the works by Borella et al. (2022) and Diotto et al. (2022) were used in this work, along with some additional experiments performed in this work. The experimental set-up is the one described in Borella et al. (2022) and Diotto et al. (2022): *A. maxima* SAG 49.88 (from SAG-Goettingen) was cultivated at 30°C in a polymethyl methacrylate (PMMA) 500 mL photobioreactor (PBR), of 15 cm depth and 35 cm^2 irradiated surface. Proper mixing was ensured through a magnetic stirrer and gas bubbling, and thus the system can be approximated to a Continuous Stirred Tank Reactor (CSTR). As culture medium, modified Zarrouk medium was supplied continuously at the desired flow rate (and residence time), with a PO_4^{3-} concentration of 25

mg L^{-1} to avoid phosphate starvation. Excess CO_2 was bubbled in a mixture with air (5% v/ v), allowing to keep the pH constant at 9.3−9.4. All nutrients supply was in excess to create light limiting conditions. A peristaltic pump (Watson-Marlow 120S) operating at a constant flow rate ensured the supply of the culture medium. And the reactor volume was kept constant through an overflow tube. To provide light, LED lamps were employed (Borella et al., 2022), with emission spectra with peaks at 660−680 nm (red) and 430 nm (blue), and with a red/blue ratio of 80/20. The irradiance was measured at the level of the transparent optical surface of the PBR, neglecting the absorption and reflection on the surface of the PBR, with an Ocean Insight STSVIS spectrometer, equipped with a cosine corrector. The spectrometer was calibrated in absolute spectral irradiance by means of a radiometrically calibrated light source (Ocean Insight DH-3PCAL) (Borella et al., 2022). Biomass concentration in the PBR was monitored daily, until constant steady state was reached. To measure biomass concentration, samples of 10 mL were filtered under vacuum with a 0.45 µm cellulose acetate membrane, that was then then dried for 2 h at 105 °C and weighed. For each SS, at minimum of four experimental points were collected on different days.

The experimental biomass productivity at steady state was obtained through the material balance for a CSTR at steady state:

$$r_x = \frac{c_x}{\theta} \tag{4.32}$$

Where c_x is the measured value of biomass concentration at steady state and θ [d] is the residence time in the PBR, defined as the ratio between the volume of the PBR and the volumetric flow rate.

4.3.2 Respirometry experiments

The experimental protocol for respirometry is the same as in Porcelli (2023). Respirometry experiments measure oxygen evolution profiles as a response to different input conditions. In the experiment, a microalgal sample with concentration between 0.2-0.4 g L^{-1} is inserted in a square flask with 4 cm thickness which temperature is set constant at 30°C by a thermostatic bath (Porcelli, 2023). In the flask, a magnetic stirrer ensures perfect mixing. The apparatus is placed in a dark box and exposed to controlled light-dark cycles, each of 10 minutes minimum, to evaluate oxygen production during the light phase thanks to photosynthetic processes and oxygen consumption during dark time due to respiration. An oximeter (Delta OHM HD 2109.1) controlled by the software DeltaLog9 measures dissolved oxygen concentration every 15 s. When oxygen concentration approaches saturation levels, oxygen is stripped though insufflation of gaseous nitrogen. For each condition, oxygen evolution is observed in at least 4 replicas. The time variation in oxygen concentrations

represents the production or consumption of oxygen and allows to obtain the experimental oxygen production rate, by also including the variations in concentration due to mass transfer (Pastore et al., 2020). During respirometry experiments, cells are exposed to pulsed light illumination during the light time. The microalgal samples are taken from continuous cultures that are acclimated to the experimental I_{max} to allow reproducibility of the results. During the experiment, different conditions can be inspected, each with a combination of light and dark times.

4.4 Results

The model developed in Section 4.2 comprises several parameters. Parameters $A, \tau_{02}, \tau_{del}, N_p{}^{me}{}_{ool}{}^{an}, N_p{}^{st}{}_{ool}{}^{d}$ represent key experimental phenomena and were introduced and quantified in Zarmi et al (2020): in this Chapter, their values are fixed as in Zarmi et al. (2020). Similarly, v_{cell} also has a strong physical meaning and it is fixed to the value proposed in Richmond et al (2003). Table 4.1 shows the values of parameters above that were not determined in this Chapter.

Table 4.1: *Values of the fixed parameters of the model.*

Parameter	Value	
v_{cell} [m s^{-1}]	0.4	(Richmond et al., 2003)
A [nm^2]	1.5	(Zarmi et al., 2020)
τ_{02} [s]	0.2*10^{-3}	‘’
τ_{del} [s]	10*10^{-3}	‘’
N_{pool}^{mean} [-]	7	‘’
N_{pool}^{std} [-]	2	‘’

Parameters $k_a, K_{cx}, w_{10}, a, b, c, d$ are unknown. k_a, the Lambert-Beer constant, was determined experimentally from preliminary measurements as in Borella et al. (2021). On the other hand, the unknown parameters K_{cx} (proportionality constant for biomass production) and w_{10}, a, b, c, d (parameters of the empirical expression for photoinhibition) were introduced in the model formulation of Section 4.2. By imposing the physical constraint that the maximum fraction of damaged RCs $x_{RC,dam}$ is equal to 1 in Equation 4.26, the parameter d can be calculated from the one of a as $d = 1 - a$, thus decreasing the number of parameters to be estimated from 6 to 5. Thus, K_{cx}, w_{10}, a, b, c were fitted from experimental data obtained with methods of Section 4.3. Parameters were estimated employing a least-squares method to minimise the difference between the prediction of the model and the observed experimental data. A Particle Swarm optimisation algorithm was

employed to solve the minimisation problem. The objective of the fitting was to inspect whether the model was able to (at least) qualitatively predict experimental profiles and to provide a physical explanation for the observed phenomena. In this way, the model could be used to shed light over the great complexity of pulsed light operation and to identify conditions of optimal productivity that can be further explored experimentally. Data that were employed for fitting are of three types: steady state data at continuous light, steady state data at pulsed light, and respirometry pulsed light experiments. The focus of the model developed in Section 4.2 is to represent cultivation under pulsed light. Thus, parameters K_{cx}, a, b, c, d where firstly fitted with pulsed light experiments. Due to the high light intensities and very low τ_{light}/τ_{dark} conditions employed experimentally (see Sections 4.4.2-4.4.3), after preliminary calculations, requiring parameters of Table 4.2 only, it was found that only $BTN_{0.2}$ was triggered in pulsed light experiments considered in Sections 4.4.2-4.4.3. On the other hand, it was also preliminarily found that in continuous light experiments only the BTN_{10} occurred. Thus, after determining K_{cx}, a, b, c, d from pulsed light experiments, the model was applied to continuous light experiments to fit the last unknown parameter w_{10}. Table 4.2 shows the values of parameters estimated with the experimental data. Comparison between experimental data and simulations are shown in Sections 4.4.1-4.4.2-4.4.3 for steady state continuous light experiments, steady state pulsed light experiments, and respirometry pulsed light experiments respectively.

Table 4.2: *Values of fitted parameters of the model.*

Parameter	Value	
k_a [$m^2\ g^{-1}$]	0.09	Measured experimentally
K_{cx} [$s\ d^{-1}$]	0.035	Fitted in this work
w_{10} [-]	0.44	‘’
a [-]	1.16	‘’
b [s]	-0.05	‘’
c [s^{-1}]	-32.00	‘’
d [-]	-0.16	Calculated as $d = 1 - a$

Finally, notice that for all the plots of Sections 4.4, values reported are averaged over the entire mixing cycle and on the PQ pool.

4.4.1 Continuous light experiments

To apply the model developed in Sections 4.2 to continuous light experiments, a $\tau_{dark} = 0$ s was set, along with an artificial pulse time of 1 ms. Notice that the actual value of this artificial pulse time does not affect the calculation results.

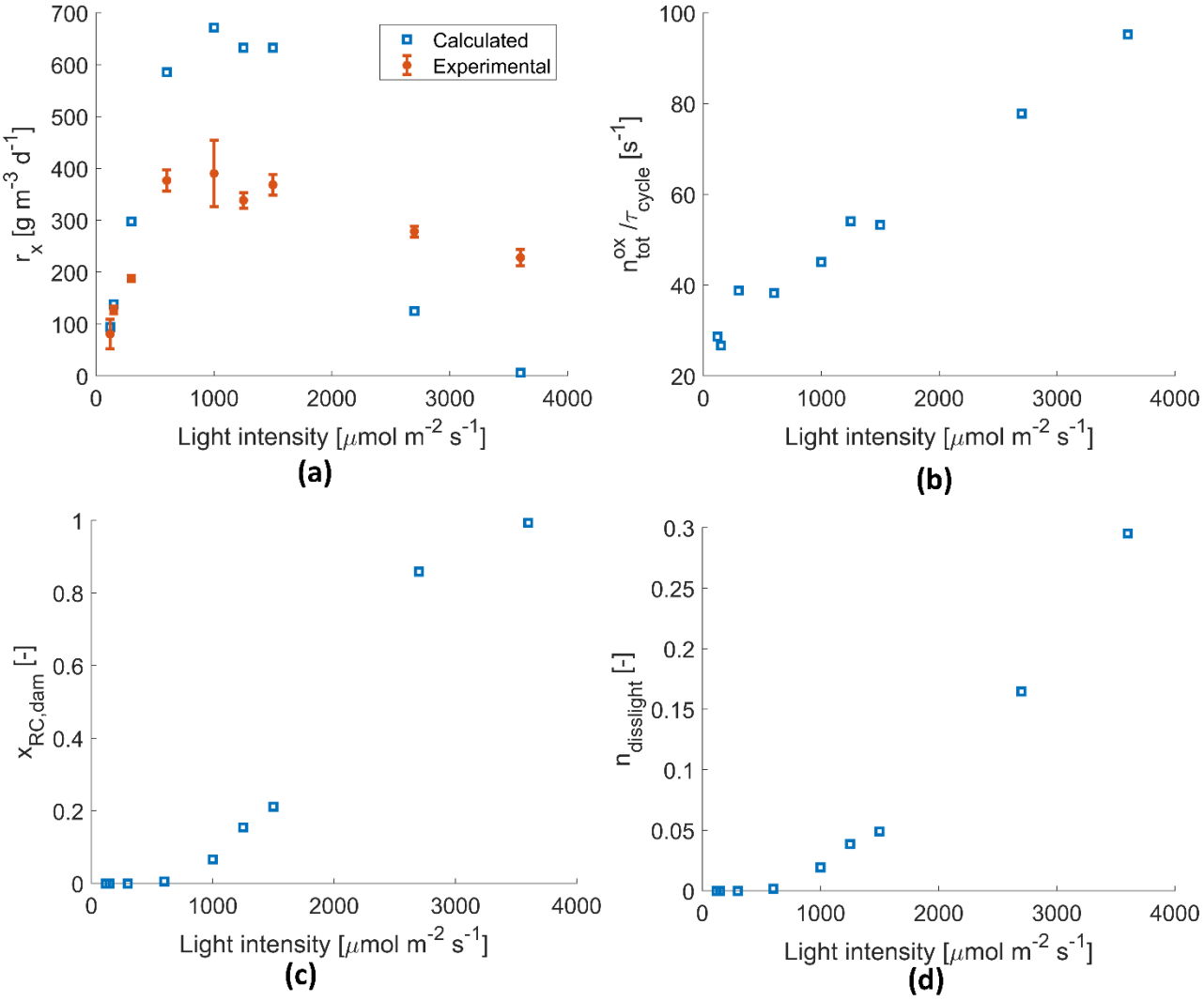

Figure 4.2: *Steady state results with continuous light at residence time of 1.33 d for (a) biomass productivity (both experimental and calculated), and simulated (b) number of re-oxidised PQs over a light cycle, (c) damaged fraction of RCs, (d) dissipated number of PQs due to the 10 ms bottleneck. Red dots are experimental measurements, while blue squares are calculated values.*

Figure 4.2 shows results for steady state experiments with continuous light at 1.33 d of residence time. Figure 4.2a shows a comparison between the experimental and calculated biomass production rates. Experimental data show the usual photosynthetic-irradiance (P-I) trend, with a photolimitation-photosaturation-photoinhibition behaviour that the model is able to represent only qualitatively. This is acceptable, since the focus of the modelling activity is on pulsed light and continuous light data were only employed to estimate w_{10}. Even if the model is not expected to be predictive for continuous

light, the qualitative trend of Figure 4.2a can be explained by the profiles of the intra-model variables of Figure 4.2b-d. As expected, in Figure 4.2b the number of re-oxidised PQs increases with light intensity. However, for higher light intensities the fraction of damaged PSUs also increases: it is constant until 700 µmol m^{-2} s^{-1} (at the boundary between the photolimitation and photosaturation regions) and then increases linearly. Interestingly, for the continuous light experiments considered, it was found that only dissipation of PQs due to BTN_{10} occurs and that only the dissipated number of PQs due to BTN_{10} of Figure 4.2c influences the damaged fraction of PSUs. As reported in Zarmi et al. (2020), in continuous light experiments the PQ pool is expected to be fully saturated most of the time, thus contributing to BTN_{10} dissipation.

4.4.2 Pulsed light steady state experiments

Pulsed light experiments of Sections 4.4.2-4.4.3 were used to estimate parameters K_{cx}, a, b, c, d. Thus, the model formulation of Section 4.2, along with fixed parameters of Table 4.1 and the estimated parameters K_{cx}, a, b, c, d was used to generate model predictions in Sections 4.4.2-4.4.3. By comparing the model predictions with experimental data, it became possible to interpret the underlying physical phenomena that led to the observed experimental outcomes.

In this section, the comparison of the model prediction and the experimental results is shown for steady state experiments at different residence times.

Similarly to Figure 4.2, Figure 4.3 shows results for steady state experiments with pulsed light at 0.9 d of residence time. Two experimental datapoints, at 11605 µmol m^{-2} s^{-1} ($\tau_{pulse} = 100$ µs; $\tau_{dark} =$ 3.6 ms) and 16216 µmol m^{-2} s^{-1} ($\tau_{pulse} =$ 500 µs; $\tau_{dark} =$ 26.5 ms) are shown and their corresponding variables are plotted against $I_{max} * I_{pulse}$, which is proportional to the amount of photons that cells receive during the pulse, and the dark cycle. Both points, however, are characterised by the same integral light intensity $I_{max} * \phi$ of approximately 300 µmol m^{-2} s^{-1}. As shown in Figure 4.3a, the point at 11605 µmol m^{-2} s^{-1} has the highest biomass productivity, as both experimental and model results show. Figures 4.3b-d allow to understand what is responsible of this behaviour (i.e., if the cause is photolimitation, photoinhibition, or excessively long dark time for 16216 µmol m^{-2} s^{-1}). Figure 4.3b highlights that the re-oxidation rate of PQ for 16216 µmol m^{-2} s^{-1} is just slightly higher to 11605 µmol m^{-2} s^{-1}, since the higher $I_{max} * t_{pulse}$ is counterbalanced by the longer τ_{dark}. However, the fraction of damaged PQs in 16216 µmol m^{-2} s^{-1} is sensibly higher and the longer τ_{dark} is not sufficient for photoregulation processes to repair the light damages. In summary, despite having the same integral light intensity, the lower biomass productivity in 16216 µmol m^{-2} s^{-1} is due to photoinhibition. This shows again that, when dealing with pulsed light, considering the integral light

intensity only is not sufficient to understand the behaviour of the system. Moreover, differently from the case in Figure 4.2, here PQ dissipation is caused only by $BTN_{0.2}$, confirming its relevance for higher values of I_{max} (Zarmi et al., 2020). The profile of dissipated PQs shown in Figure 4.3d reflects the one for $x_{RC,dam}$ in 4.3c.

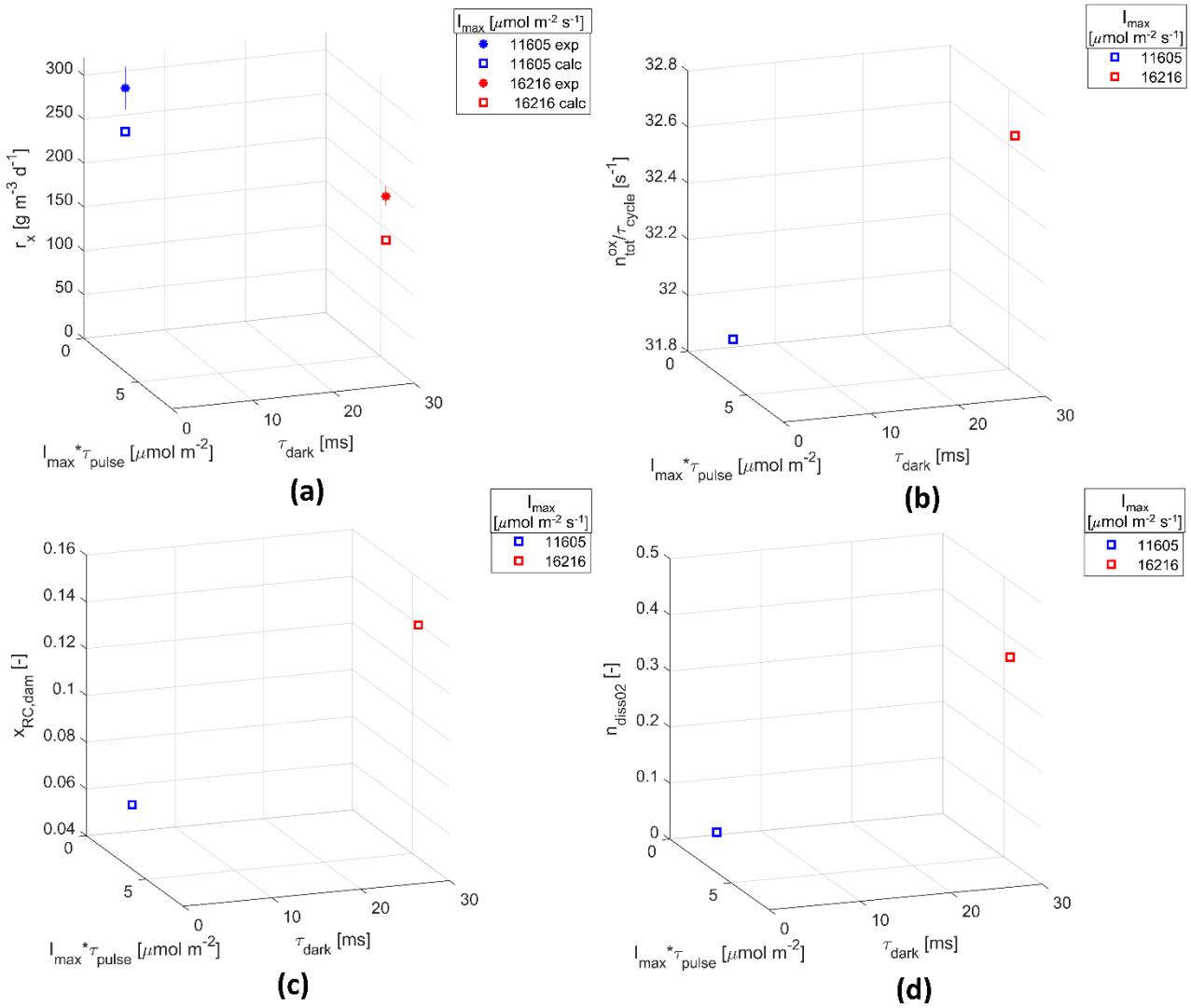

Figure 4.3: *Steady state results with pulsed light at residence time of 0.9 d for (a) biomass productivity (dot markers for experimental measurements, "exp"; square markers for calculated values, "calc"), and simulated (b) number of re-oxidised PQs over a light cycle, (c) damaged fraction of RCs, (d) dissipated number of PQs due to the 0.2 ms bottleneck for I_{max} = 11605 (blue markers) and 16216 μmol m^{-2} s^{-1} (red markers).*

Similarly to Figure 4.3, Figure 4.4 shows results for steady state experiments with pulsed light at 1.9 d of residence time, plotted against different dark times. All data are at the same I_{max}=8700 μmol m^{-2} s^{-1}, same integral light intensity of 120 μmol m^{-2} s^{-1}, and thus same ratio τ_{dark}/τ_{pulse}= 72. Even though the integral light intensity is constant, experimental r_x data in Figure 4.4a show an initial increase with τ_{dark} (and thus, τ_{pulse}) until an optimum condition is reached, followed by a decrease

for higher values of τ_{dark}. The mathematical prediction in Figure 4.4a only captures the qualitative trend of the data: this could be a sign that some additional phenomena (e.g., photoacclimation) are not represented by the model. In Figure 4.4b, the highest rate of PQ re-oxidation is where the experimental τ_{dark} (and thus τ_{pulse}) is maximum; however, this condition is also characterised by the highest photoinhibition as shown in Figures 4.4c-d. To explain the behaviour of the data at τ_{dark} from 0 to 40 ms in Figure 4.4b, it is necessary to recall the effect of light attenuation. Experimental biomass concentrations at τ_{dark} of 7 and 15 ms are close to each other (app. 240 g m^{-3}) and higher than those at 0.7 and 36 ms (app. 170 g m^{-3}): thus, due to light attenuation, at τ_{dark} of 7 and 15 ms, cells singularly receive less light than in the other conditions and thus the PQ re-oxidation rate is lower. Although the effect of photoinhibition does not change much for τ_{dark} < 40 ms (see 4.4c-d), it contributes to the final profile in Figure 4.4a. Finally, also for data at 1.9 d in Figure 4.4, dissipation occurs only due to the $BTN_{0.2}$.

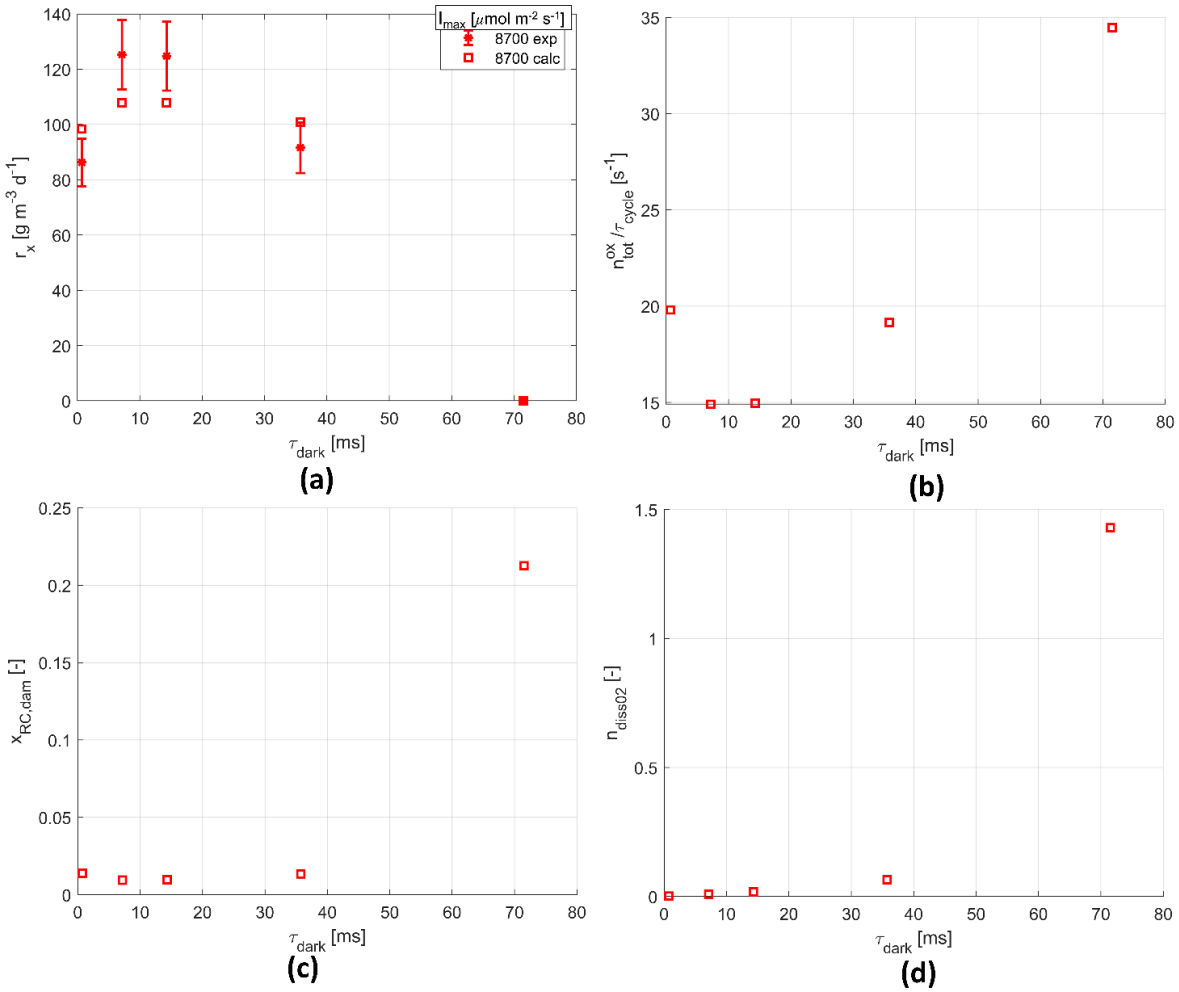

Figure 4.4: *Steady state results with pulsed light at residence time of 1.9 d for (a) biomass productivity (dots markers for experimental values, "exp"; square markers for calculated values, "calc"), and simulated (b) number of re-oxidised PQs over a light cycle, (c) damaged fraction of RCs, (d) dissipated number of PQs due to the 0.2 ms bottleneck.*

Results of experiments at residence time 2.7 d are plotted against both the integral light $I_{max} * \phi$ in Figure 4.5 and against τ_{dark} in Figure 4.6 to highlight the different experimental trends related to both variables. All experimental conditions are at τ_{pulse} = 100 ms, with exception to one point with τ_{pulse} = 10 ms at I_{max} = 35700 µmol m^{-2} s^{-1} and integral light of 61 µmol m^{-2} s^{-1}.

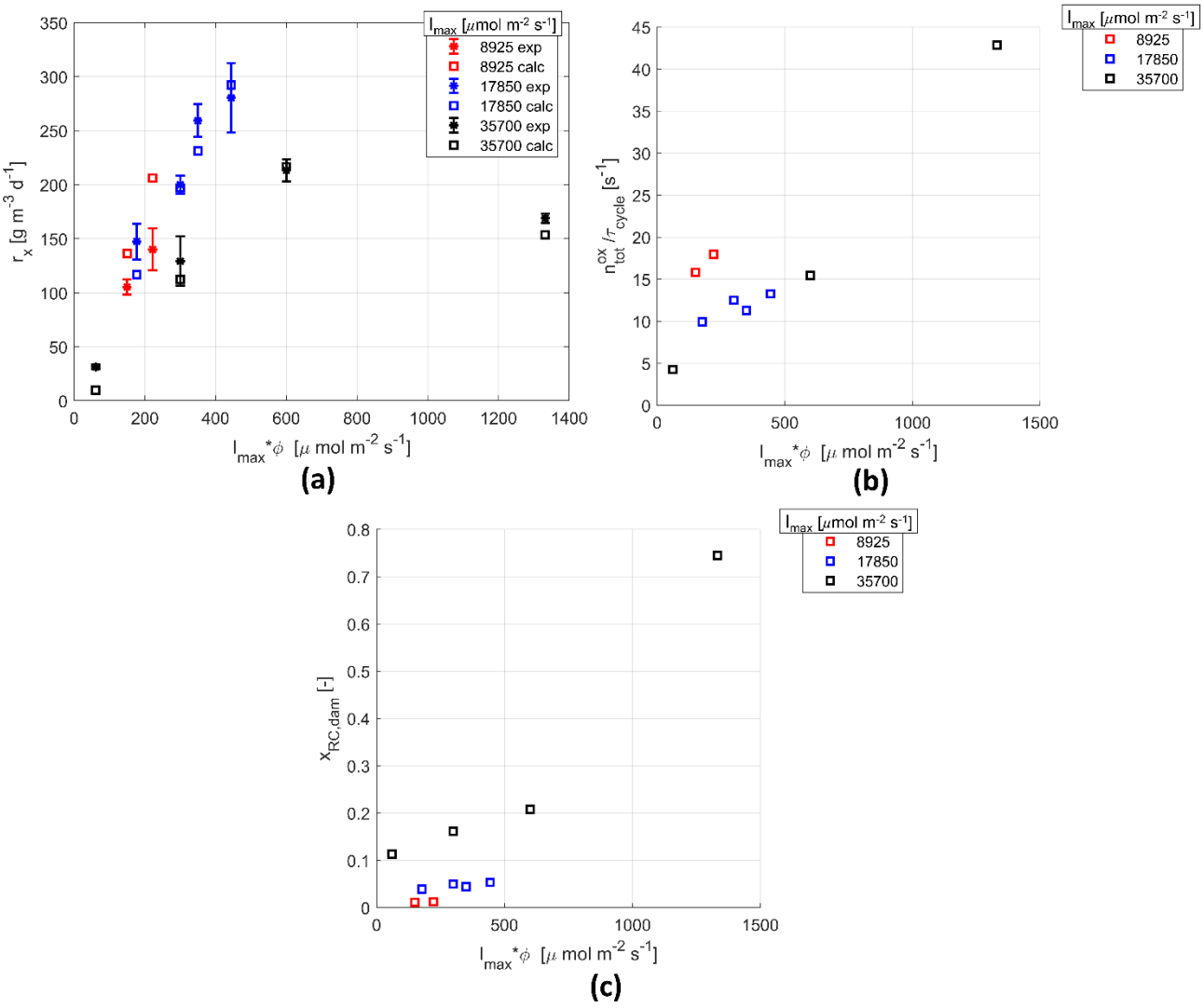

Figure 4.5: *Steady state, pulsed light results plotted vs $I_{max} * \phi$ at residence time of 2.7 d. Points at I_{max} = 8925 (red markers), 17850 (blue markers), 35700 µmol m^{-2} s^{-1} (black markers) are shown for (a) biomass productivity (dots markers for experimental values, "exp"; square markers for calculated values, "calc"), and simulated (b) number of re-oxidised PQs over a light cycle, (c) damaged fraction of RCs, (d) dissipated number of PQs due to the 0.2 ms bottleneck.*

Figure 4.5a shows experimental and calculated values of the biomass productivity at 2.7 d for experiments with pulse intensity of 8925, 17850, 35700 µmol m^{-2} s^{-1}. The trend of all the experimental data together approximates a P-I curve: in the photolimitation region at low integral lights, the influence of I_{pulse} is less strong, while it becomes clearer around the photosaturation region. For

35700 µmol m^{-2} s^{-1}, it is also possible to observe the start of photoinhibition after an integral light of 1200 µmol m^{-2} s^{-1}. Experimental profiles are also aligned with model predictions, especially at 17850 and 35700 µmol m^{-2} s^{-1}. Trends of Figure 4.4a are further motivated by those of the internal variables in Figures 4.5b-d. As expected, the PQ re-oxidation rate increases for all experiments with the integral light (Figure 4.5b), along with the fraction of damaged PSUs in Figure 4.5c. Here, values at 8925 and 17850 µmol m^{-2} s^{-1} are close to each other, reflecting the photolimitation/photosaturation conditions. Points at 35700 µmol m^{-2} s^{-1} have the highest values of $x_{RC,dam}$, thus explaining the lowest values of productivity in Figure 4.5a. At 35700 µmol m^{-2} s^{-1}, it is also clear the increase in $x_{RC,dam}$ from photolimitation/saturation to photoinhibition conditions.

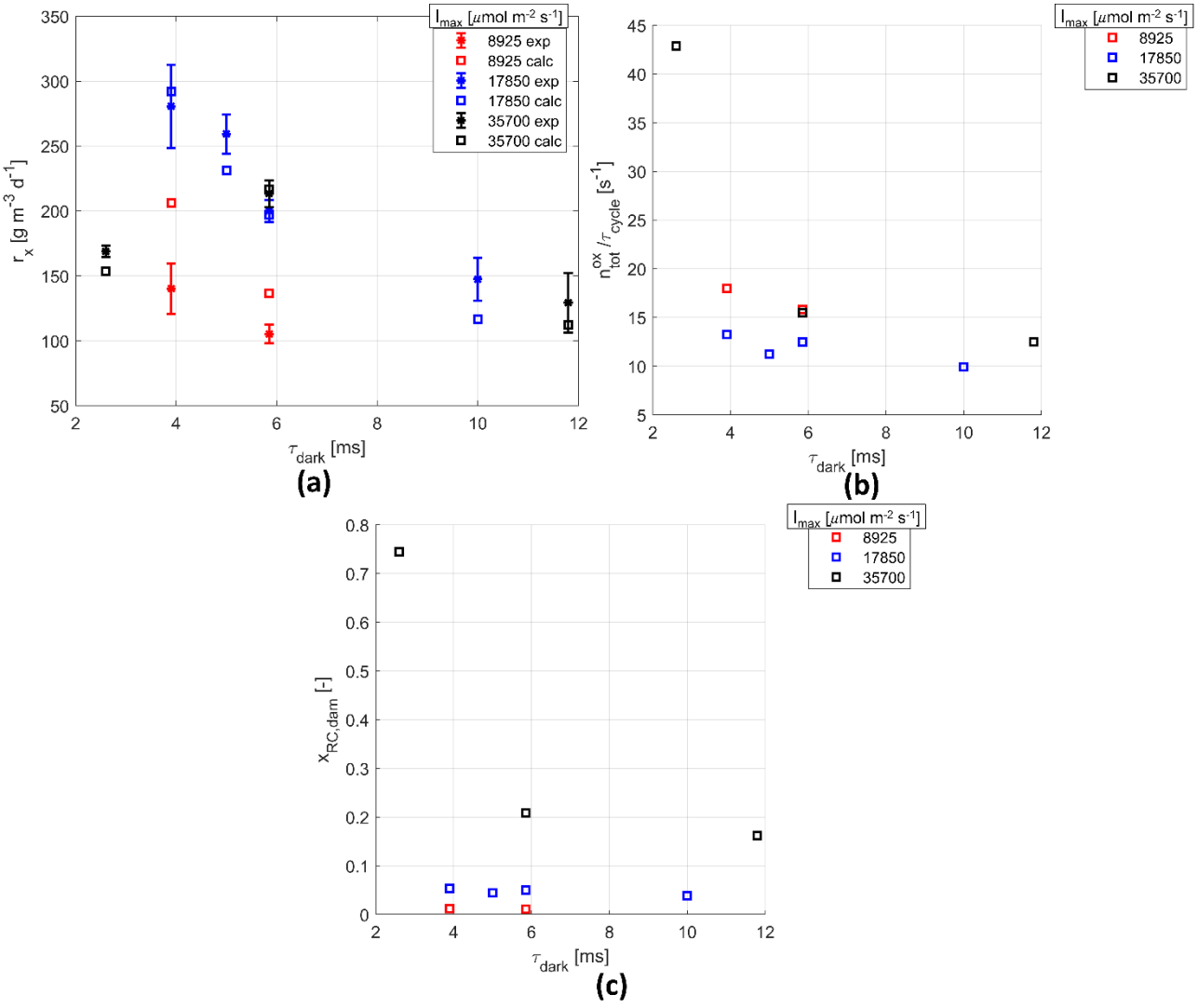

Figure 4.6: *Steady state, pulsed light results plotted vs τ_{dark} at residence time of 2.7 d. Points at I_{max} = 8925 (red markers), 17850 (blue markers), 35700 µmol m^{-2} s^{-1} (black markers) are shown for (a) biomass productivity (dots markers for experimental values, "exp"; square markers for calculated values, "calc"), and simulated (b) number of re-oxidised PQs over a light cycle, (c) damaged fraction of RCs, (d) dissipated number of PQs due to the 0.2 ms bottleneck.*

Figure 4.6a highlights the influence of τ_{dark} on biomass productivities at 2.7 d residence time. Similarly to Figure 4.5a, simulated profiles in Figure 4.6 are qualitatively in accordance with the experimental ones. For 17850 and 35700 µmol m^{-2} s^{-1} the model provides a quantitative description of the data, whilst for 8925 µmol m^{-2} s^{-1} the model prediction overestimates the experimental biomass productivities. For 8925 and 17850 µmol m^{-2} s^{-1}, r_x increases monotonically with lower τ_{dark}, while for 35700 µmol m^{-2} s^{-1} there is a value of τ_{dark} for which the biomass production rate is maximum. In order to comprehend this behavior, it is essential to take into account the impact of excessively high or low values of τ_{dark}. If τ_{dark} has very high values, all the reduced PQs at the end of the pulse will be re-oxidised at the beginning of the dark phase and a lot of time will be "wasted", possibly causing cells to turn into respiration. Due to the low light/dark ratios and high I_{max} experimentally employed in this work, the majority of PQs are re-oxidised during the dark time (e.g., on average, 88-96% of the PQs for experiments at 2.7 residence time). Thus, if τ_{dark} is excessively small, there will not be enough time during the light cycle to re-oxidise all the PQs, thus causing a decrease in the PQ re-oxidising rate and a consequent increase in the number of dissipated PQs due to the saturation of the PQ pool (i.e., due to BTN_{10}), that is also the situation commonly found in continuous light operations. On the other hand, an additional and separate consequence can be associated with extremely low values of τ_{dark}. Besides photoproduction, an excessively small τ_{dark} can also have a negative effect on photoregulation. Due to the high irradiation conditions of the light phase, cells will inevitably be photodamaged, but, during the dark phase, they have time to repair and recover from the damage. However, when the dark time is too small, cells cannot fully recover from photodamage and this cumulative damage will lead to higher photoinhibition (Zarmi et al., 2020). An analogous situation can also be encountered in cultivation in ultra-thin PBRs under continuous light as discussed in Chapter 2, where, due to the absence of a proper dark region in the PBR, cells experience higher levels of photoinhibition. Thus, the increase in biomass productivity at 8925 and 17850 µmol m^{-2} s^{-1} for lower τ_{dark} in Figure 4.6a can be explained by a "lower waste of time", further reflected by the trend of the PQ re-oxidation rate in Figure 4.6b. Moreover, for these data, values of $x_{RC,dam}$ of Figure 4.6c are low and do not show major variations. On the other hand, data at 35700 µmol m^{-2} s^{-1} show a decrease in biomass productivity at the very low value of τ_{dark}~2.6 ms: for this condition, the PQ re-oxidation rate in Figure 4.6b is maximum, and thus the decrease in r_x cannot be caused by a limitation in the number of re-oxidised PQs. This is also confirmed by the fact that, also for data at 2.7 d, all the dissipated PQs are due to $BTN_{0.2}$. However, for 35700 µmol m^{-2} s^{-1}, $x_{RC,dam}$ is considerably higher below 4 ms (Figure 4.6c), showing that photoinhibition is responsible for the decrease in biomass productivity. To conclude, Figure 4.6 experimentally shows the existence of an

optimal τ_{dark} maximising biomass productivity, which is also mathematically represented by the model formulation, that is thus characterised by a strong physical meaning.

4.4.3 Pulsed light respirometry experiments

As mentioned in Section 4.4.2, pulsed light respirometry experiments presented in this Section were used to estimate parameters K_{cx}, a, b, c, d, since, similarly to Section 4.4.2, also the experimental conditions in this Section do not trigger BTN_{10}. In all respirometry tests, the duration of the light phase has been set constant (both during the experiment and in the previous photoacclimation step) to $\tau_{pulse} = 100$ µs. On the other hand, as mentioned in Section 4.3.2, each experiment was characterised by different conditions of I_{max} and τ_{dark} (and τ_{cycle}) to which the culture had been previously photoacclimated, and by a set value of biomass concentration during the experiment (that influenced the light received by cells due to light attenuation). Experimental and acclimation conditions for the five experiments are reported in Table 4.3: the only variable allowed to vary during each experiment was τ_{dark}, in order to inspect its influence on the oxygen production rate.

Table 4.3: *Experimental conditions of respirometry experiments.*

Experiment	**Intensity of the pulse I_{max} [µmol m^{-2} s^{-1}]**	**τ_{dark} for acclimation [ms]**	**τ_{cycle} for acclimation [ms]**	**Biomass experimental concentration [g m^{-3}]**
1 - (a)	8925	3.9	4	310
2 - (b)	17850	4	4.1	280
3 - (c)	17850	4	4.1	410
4 - (d)	35700	5.85	5.95	400
5 - (e)	35700	5.85	5.95	430

Some minor modifications to the model have been introduced to simulate respirometry experimental profiles.

The value of $Y_{O_2/X}$ in Equation 4.31, is not constant, but depends on the acclimation conditions. Thus, in order to compare the experimental results with model predictions, it was necessary, for each experiment, to compute the non-dimensional oxygen production rate r'_{O_2} [-] at different τ_{dark}. For experimental data, r'_{O_2} was computed by normalising experimental values of oxygen production rate on the value at the lowest experimental dark time, while, for the model simulations, by normalising the average biomass production rate on the value at the lowest τ_{dark}.

Moreover, in steady state experiments cells have time to adapt and acclimate to the input conditions. On the other hand, as explained in Section 4.3.2, cells used in respirometry experiments are previously acclimated to a determined τ_{cycle}, and due to the short duration of the respirometry experiments, cells are not expected to acclimate to the new conditions.

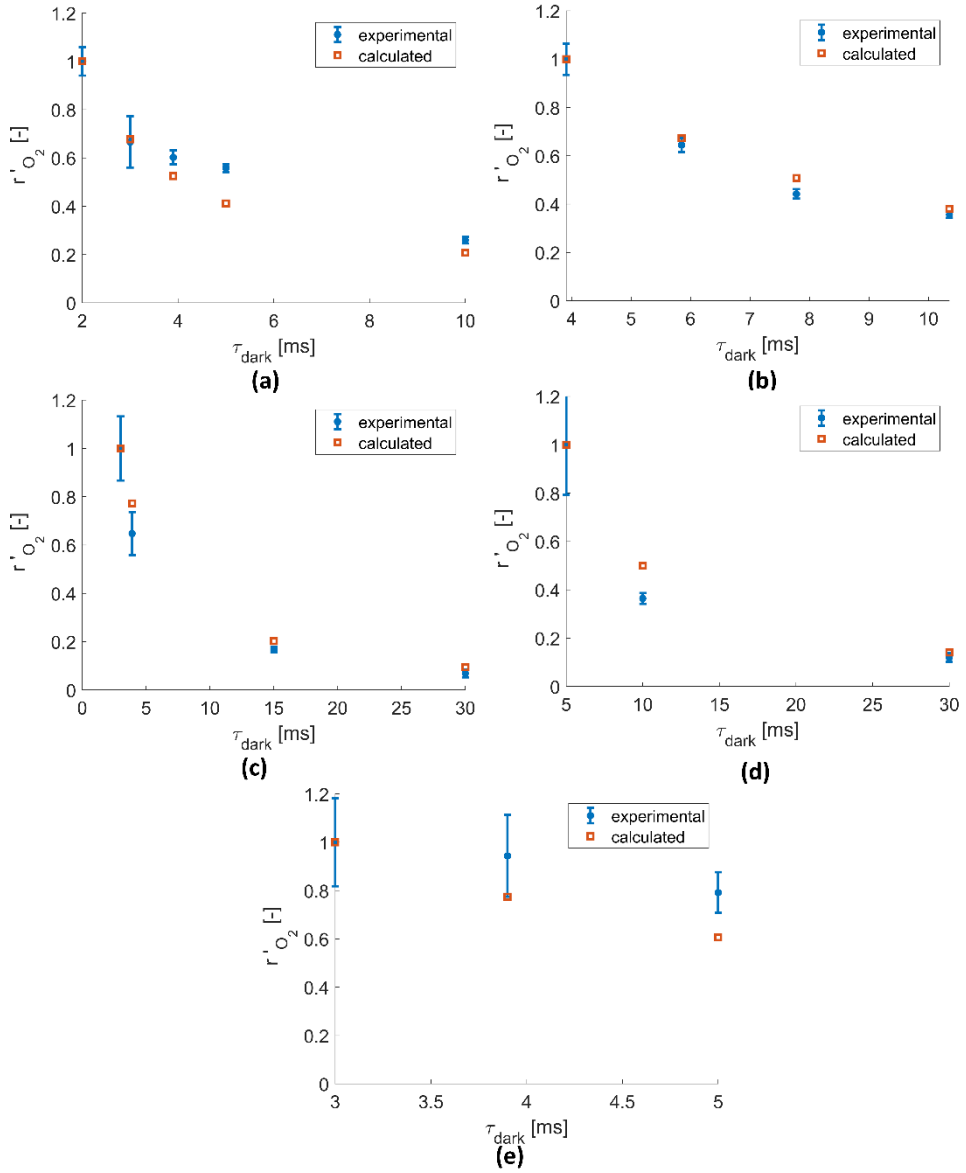

Figure 4.7: *Experimental (blue dots markers) and calculated profiles (red squares markers) of the non-dimensional oxygen production rate vs different levels of τ_{dark} for the five experimental conditions (a)-(e) of Table 4.3.*

Thus, the absolute oxygen production rate is dependent on the previous photoacclimation conditions. Since the focus of respirometry is describing the relative variations in oxygen production between different conditions in the same experiment, in modelling of respirometry experiments of this Chapter the term τ_{cycle} in Equation 4.26 was fixed to the previous acclimation value for each experiment.

This was also necessary since the model is not able to account for any possible dynamic effects of photoacclimation. Table 4.3 reports all experimental τ_{cycle} acclimation values.

Figure 4.7 shows experimental and calculated profiles of r'_{O_2} for all the five experimental conditions of Table 4.3.

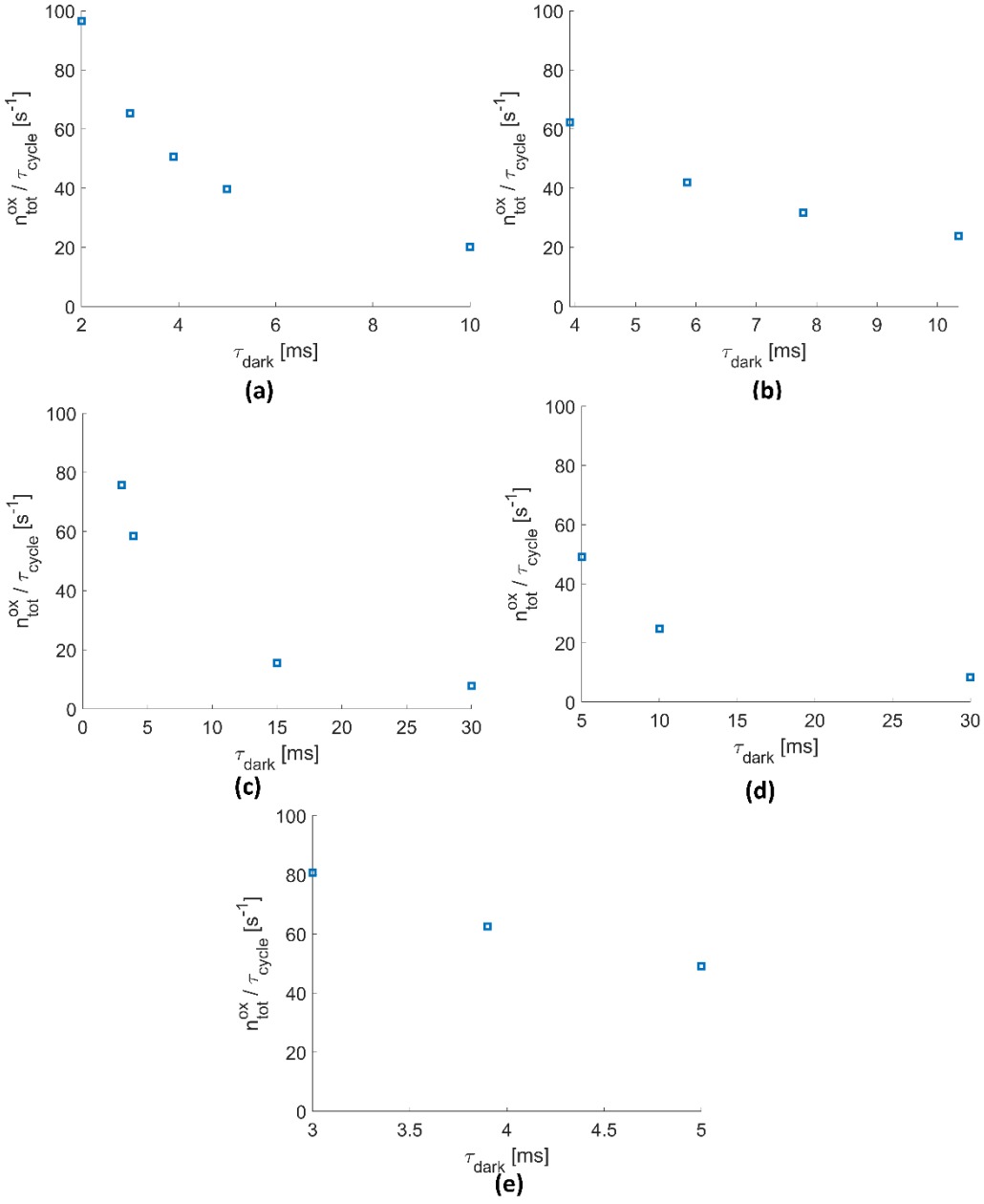

Figure 4.8: *Calculated profiles of the PQ re-oxidation rate vs different levels of τ_{dark} for the five experimental conditions (a)-(e) of Table 4.3.*

For all experimental conditions in Figure 4.7, it can be noticed that the non-dimensional oxygen production rate decreases with higher values of τ_{dark}. This scenario is similar to the one in Figure 4.6a for pulses of 8925 and 17850 µmol m^{-2} s^{-1}. The duration of the dark phase is approximately one

order of magnitude higher than the one of the light phase: thus, there is a "waste of time" during the dark phase, and its decrease leads to higher oxygen productivities. This is also confirmed by the calculated values of the PQ re-oxidation rate in Figure 4.8, which increase for lower τ_{dark} for all the experimental condition.

On the other hand, it was found that, during the same experiment, the photoinhibition levels (i.e., the fraction of damaged RCs) did not exhibit major changes for varying τ_{dark} in the same experiments, while the larger difference was found between different experiments. Levels of photoinhibitions are reported in Table 4.4 for all experimental conditions of Table 4.3. As expected, $x_{RC,dam}$ mainly increases with the intensity of the pulse, showing again 35700 µmol m^{-2} s^{-1} as the most inhibiting condition. Moreover, the experimental biomass concentration influences light attenuation in the system and thus photoinhibition: for instance, at 17850 µmol m^{-2} s^{-1}, an increase of 46% in the biomass concentration leads to a 30% decrease in $x_{RC,dam}$.

To conclude it appears that the model can capture also the experimental respirometry results and give a physical explanation of the observed phenomena as in Figure 4.8 and Table 4.4.

Table 4.4: *Average fraction of damaged RCs for the five respirometry experimental conditions of Table 4.3.*

Experiment	I_{max} [µmol m^{-2} s^{-1}]	τ_{dark} for acclimation [ms]	Biomass experimental concentration [g m^{-3}]	Average $x_{RC,dam}$[-]
1 (a)	8925	3.9	310	0.0534
2 (b)	17850	4	280	0.7656
3 (c)	17850	4	410	0.5244
4 (d)	35700	5.85	400	0.9719
5 (e)	35700	5.85	430	0.9577

4.4.4 Model-based selection of respirometry experimental conditions

After verifying the capability of the developed model in capturing the qualitative behaviour of the already existing experimental data, along with providing a strong physical explanation of the observed phenomena, we inquired whether it was able to predict optimal operating conditions for pulsed light experiments. Thus, we employed the model to select respirometry experimental conditions maximising the oxygen production rate. Before applying the model to select the experimental conditions, different variables were fixed. For photoacclimation of the culture, we fixed variables I_{max}=17850 µmol m^{-2} s^{-1}, τ_{pulse}=100 µs and τ_{dark}=5.85, that are in the ranges of experiments presented in Section 4.4.3. To perform the actual experiments, we fixed I_{max}=17850

µmol m^{-2} s^{-1} and the biomass concentration to 300 g m^{-3}. A PBR with a thickness of 4.5 cm was then selected. After fixing the previous variables, the inputs of the respirometry experiments were different combinations of τ_{pulse} and τ_{dark}, with corresponding measurements of the oxygen production rate as the output. To select appropriate experimental values of τ_{pulse} and τ_{dark}, predictions of the fitted model were employed.

The model was exploited to simulate the oxygen production rate over a wide input space, revealing experimental regions with different productivities: the model simulation is shown in Figure 4.9 (coloured dots). By visual inspection of the simulation results (and especially of the area with highest productivity), four experimental combinations of τ_{pulse} and τ_{dark} were selected for the experiment and are reported in Table 4.5. Here, point II is close to the maximum of oxygen productivity, with another point III selected to verify the accuracy of the predicted decrease of the oxygen production rate when moving away from the optimal region. Points I and IV were then selected to explore the experimental space far away from the areas of maximum oxygen productivity. Figure 4.9a shows both the model simulation (coloured dots) over the design space and the experimental results (black diamonds), with experimental conditions highlighted by cyan circles; the exact experimental combinations are reported in Table 4.5. Oxygen productivities in Figure 4.9 are normalised over the point characterised by maximum productivity.

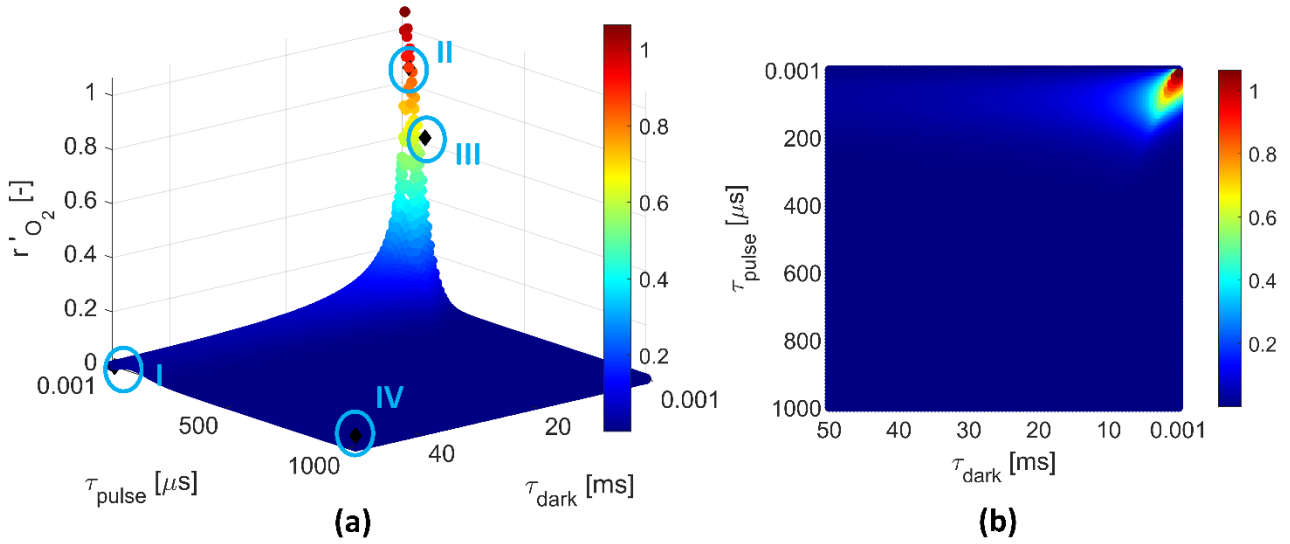

Figure 4.9: *Non-dimensional oxygen production rate for the optimal respirometry experiment: (a) comparison between model simulation (coloured dots markers) over the entire experimental space and experimental points (black diamonds markers, highlighted by cyan circles); (b) contour plot of the simulations over the entire experimental space.*

Simulated values of r'_{O_2} in Figure 4.9a show a peculiar trend, for which the maximum is obtained for a specific combination in the region where both τ_{pulse} and τ_{dark} have relatively small values (τ_{pulse} =20 µs and τ_{dark} = 0.5 ms). Based on the simulated scenario of Figure 4.9, a global

sensitivity analysis was also performed to assess the model practical identifiability as discussed in the Appendix A.2.

Table 4.5: *Experimental conditions investigated in the optimal respirometry experiment.*

Experimental condition	τ_{light} **[us]**	τ_{dark} **[ms]**
I	10	50
II	50	1
III	140	2
IV	1000	50

The simulation in Figure 4.9a guided the design of the respirometry experiment in Table 4.5. There, experimental points I and IV were chosen to explore the extreme parts of the experimental space.

Due to the extreme low values of τ_{pulse} and τ_{dark}, it is difficult to obtain experimentally the input conditions for the maximum r'_{O_2} in Figure 4.9b. Thus, the experimental point II (τ_{pulse} =50 μs and $\tau_{dark} = 1$ ms) was chosen close but not equal to the optimal condition. Finally, experimental point III was selected in the same region as point I to inspect whether the descent from the peak in Figure 4.9a was realistic.

Comparison between simulated and experimental values in Figure 4.9a show the accuracy of the model prediction. However, understanding the physical reason behind the trends in Figure 4.9a it requires to interpret the graphs of the internal variables shown in Figure 4.10, simulated over the entire experimental space. Figure 4.10a shows the PQ re-oxidation rate, which, as expected, for a fixed value of τ_{dark} tends to increase for higher values of τ_{pulse} since cells receive more photons. For a fixed value of τ_{pulse}, it decreases when τ_{dark} increases, since more time is "wasted" during the dark phase. Interestingly, there is a ratio $\tau_{pulse}/\tau_{dark} = 1/24$ approximately, above which the increase of τ_{pulse} (or decrease in τ_{dark}) does not lead to an increase in the PQ re-oxidation rate, that reaches a plateau at a value of 100 s^{-1}. With a delivery time of 10 ms, a maximum of 100 PQs can be re-oxidised in a second for single RC. Thus, 100 s^{-1} is the maximum theoretical PQ re-oxidation rate, obtained when there is no "waste of time" after all the PQs have been re-oxidised. From an operating point of view, this represents a limiting condition for the photoproduction processes: above $\tau_{pulse}/\tau_{dark} = 1/24$ it is not convenient to work, since the PQ re-oxidation rate is constant, but the additional photons received in the light cycles are just dissipated due to the BTN_{10} that is triggered above this ratio as shown in parallel by the increasing number of dissipated PQ in Figure 4.10c. On the other hand, as shown in Figure 4.10d, the number of dissipated PQs due to the $BTN_{0.2}$ increases

with τ_{pulse} as expected, but it is almost independent from τ_{dark}, which, similarly as in Section 4.4.3, was fixed in Equation 4.26 to the acclimation value. The total fraction of damaged RCs in Figure 4.10b mostly reflects the increase of dissipation by $BTN_{0.2}$ (Figure 4.10d), for higher τ_{pulse}.

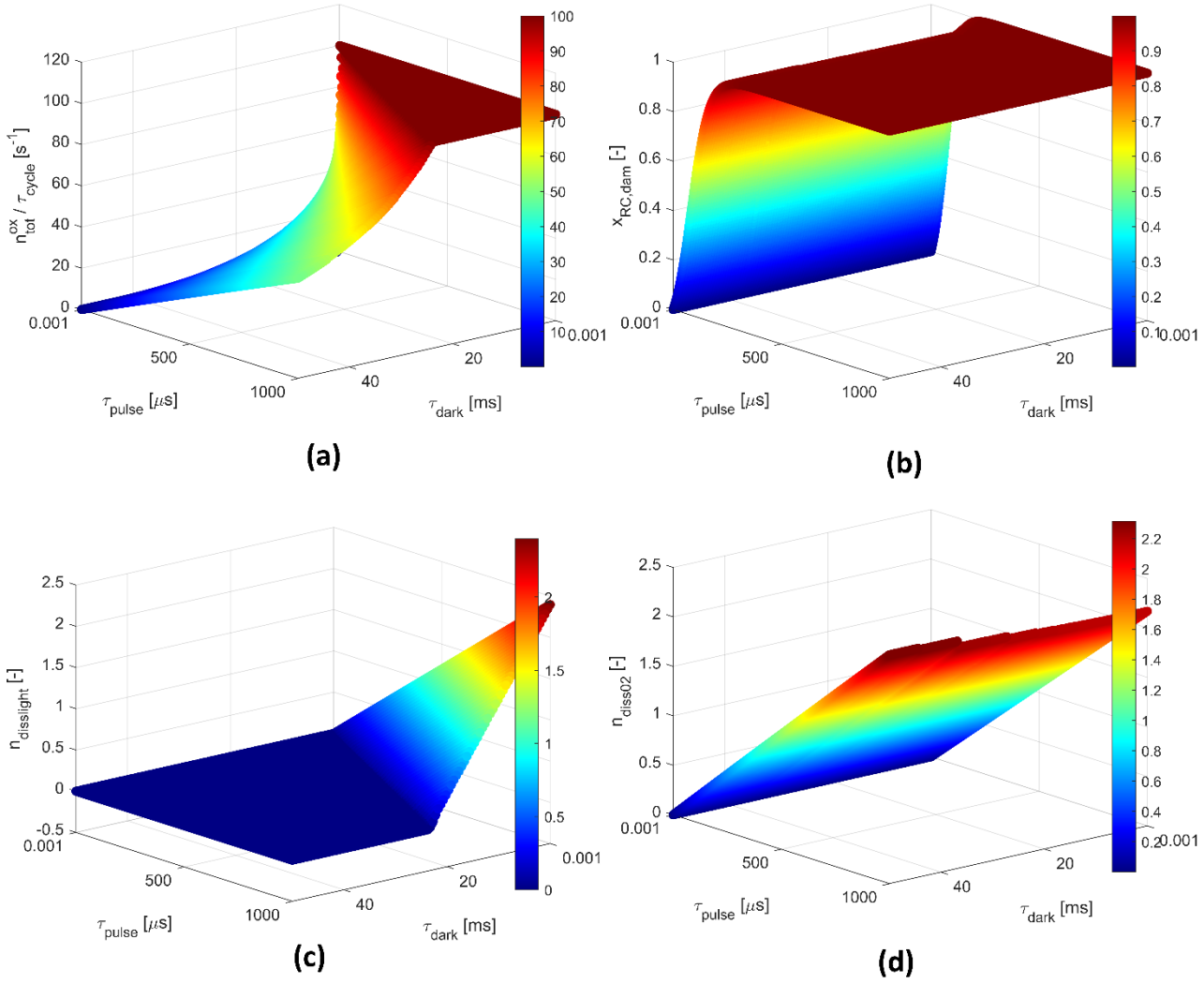

Figure 4.10: *Simulations over the entire experimental space for the optimal respirometry experiment of Figure 4.9 with (a) PQ re-oxidation rate, (b) damaged fraction of RCs and number of dissipated PQs per RC due to the (c) 10 ms bottleneck, (d) 0.2 ms bottleneck.*

To sum up, Figure 4.10 shows that the optimal operating point is situated in a location with the maximum PQ re-oxidation rate and minimum PQs dissipation from both bottlenecks (and thus, no damaged RCs): moving away from this condition leads to lower oxygen productivities both due to a decrease in photoproduction for $\tau_{pulse}/\tau_{dark} < 1/24$ and mostly for the higher impact of $BTN_{0.2}$ for higher values of τ_{pulse}. Notice that all the points in the experimental space in Figures 4.9-10 are subjected to the same acclimation conditions: a different photoacclimation would probably shift the

position of the maximum peak in Figure 4.9, since it would change the total number of RCs in Equation 4.27.

Results from Figures 4.9-10 have an important impact on establishing general criteria for optimal operation of PBRs under pulsed light. Firstly, finding of the optimal ratio $\tau_{pulse}/\tau_{dark} = 1/24$ for the photoproduction process suggests that operations must be constrained on this line: a deviation from this value can cause a diminishing of photoproduction ($\tau_{pulse}/\tau_{dark} < 1/24$) or the triggering of BTN_{10} dissipation with the same photoproduction rates ($\tau_{pulse}/\tau_{dark} > 1/24$). However, selecting the optimal τ_{pulse}/τ_{dark} is not sufficient to achieve the highest productivity, due to the different impact of the $BTN_{0.2}$ dissipation (and photoinhibition), that considerably increases with τ_{pulse}. Moving on the optimal τ_{pulse}/τ_{dark} line, the optimal condition is found at low values of τ_{pulse} that minimise the $BTN_{0.2}$ dissipation; for low values of τ_{dark} (and thus τ_{pulse}), it is expected that cell recovery phenomena during the dark phase do not have time to occur, negatively impacting the productivity. However, practical operations in such region of extremely low values of τ_{pulse} are hindered by limitations in the experimental apparatus. Moreover, notice that $\tau_{pulse}/\tau_{dark} = 1/24$ is expected to change for different conditions of I_{max}, c_x, reactor thickness and photoacclimation levels.

4.5 Conclusions

Microalgae cultivation under high-frequency pulsed light can increase the productivity with respect to continuous light: however, it requires a careful selection of the input conditions. This is not a trivial task, especially due to the lack of understanding of the physical phenomena also to the absence of proper modelling explanations of the system that could guide the experimental activity. The objective of this Chapter was to propose a modelling framework able to capture the trends observed experimentally, especially with pulsed light operations, and to provide meaningful physical explanations of the phenomena. Starting from the model in Zarmi et al. (2020), we developed a new model structure to represent pulsed light cultivation in a PBR. The model was capable to qualitatively capture the experimental trends and provided strong physical explanations for the observed phenomena. To inspect the capability of the model to guide experiments, it was employed to select respirometry experimental conditions to maximise the oxygen production rate with pulsed light and the experimental results showed good adherence with the model prediction. Moreover, the respirometry experiment suggested that, if operations are constrained in specific limits (e.g., to $\tau_{pulse}/\tau_{dark} = 1/24$ in the examined scenario), an increase in productivity in PBRs could be reached under pulsed light. A future activity can thus be the experimental validation of these operational

constraints. Moreover, the model still presents some limitations, that will be addressed in future activities:

- The model qualitatively captures experimental trends and provides strong physical explanations of the phenomena. However, in several situations the model fails to quantitatively describe experimental data. This could be a sign that additional phenomena (e.g. photoacclimation) need to be considered in the modelling structure. Theoretically, this could be done by allowing parameters $A, \tau_{02}, \tau_{del}, N_{pool}^{mean}, N_{pool}^{std}$ to vary as a function of the light conditions (Zarmi et al., 2020). This would require a more extensive dataset for model identification, with additional pulsed light respirometry and steady state experiments.
- In this work, the model was employed for prediction of biomass and oxygen productivities employing the biomass concentration. However, to enhance the practical applicability of the model, the capability of calculating the biomass concentration as the output is needed. In principles, this could be achieved by integrating the developed model in a material balance for biomass concentration.

4.6 Chapter nomenclature

Abbreviations:

$BTN_{0.2}$: 0.2 ms bottlenenck

BTN_{10}: 10 ms (τ_{del}) bottleneck

CSTR: continuous stirred-tank reactor

FLE: Flashing Light Effect

P-I: Photosynthetic Irradiance

PBR: photobioreactor

PMMA: polymethyl methacrylate

PQ: plastoquinone

PSI: photosystem I

PSII: photosystem II

PSU: Photosynthetic Unit

Q_A: quinone acceptor

RC: reaction centre

Symbols:

k: dependent variable in the differentiable switch function

k_{switch}: switch value for the differentiable switch function

$S(k, k_{switch}, s_k)$: value of the differentiable switch function

s_k: the slope of the differentiable switch at k_{switch}

Variables:

A [nm^2]: absorbtion cross section

A_v [-]: the Avogadro's number

a [-]: parameter of the sigmoid for inhibition

b [n_{RC} n_{PQ}^{-1}]: parameter of the sigmoid for inhibition

c [-]: parameter of the sigmoid for inhibition

c_x [g m^{-3}]: biomass concentration in the PBR

d [-]: parameter of the sigmoid for inhibition

I_i [µmol m^{-2} s^{-1}]: attenuated light irrandiance of the *i*-th light cycle

I_{max} [µmol m^{-2} s^{-1}]: maximum light intensity/intensity of the pulse

k_a [m^2 g^{-1}]: Lambert-Beer light absorption coefficient

K_{cx} [s d^{-1}]: apparent proportionality constant for biomass production rate

k_{cx} [s d^{-1}]: proportionality constant for biomass production rate

$N_{g,i}$ [-]: real number of PQs reduced during the pulse of the *i*-th light cycle

$N_{g,theor,i}$ [-]: theoretic number of PQs reduced during the pulse of the *i*-th light cycle

N_{pool} [-]: size of the PQ pool

N_{pool}^{mean} [-]: mean of the distribution of PQ pool

N_{pool}^{std} [-]: standard deviation of the distribution of PQ pool

$n_{0,i}$ [photons s^{-1}]: rate of photons hitting a single reaction center

$n_{0,i}^{reox}$ [-]: real number of re-oxidised PQs during the light phase

$n_{0,theor,i}^{reox}$ [-]: theoretical number of re-oxidised PQs during the light phase

$n_{add,i}$ [-]: number of reduced PQs at the end of the light phase

$n_{add,theor,i}$ [-]: theoretical number of reduced PQs at the end of the light phase

n_{cycle} [-]: number of light cycles

$n_{dark,i}^{red}$ [-]: number of reduced PQs at the end of the dark phase

$n_{dark,i}^{reox}$ [-]: number of PQs re-oxidised during the dark phase

$n_{disslight,i}$ [-]: number of PQs dissipated linked to the 10 ms bottleneck

$n_{disstot,i}$ [-]: total number of dissipated PQs

$n_{old,i}$ [-]: residual number of PQs already reduced from the light cycle *i-1*

$n_{RC,a}$ [cell^{-1}]: number of active RCs per cell

$n_{RC,dam}$ [cell^{-1}]: number of damaged RCs per cell due to photoinhibition

$n_{RC,tot}$ [cell^{-1}]: total number of RCs per cell

$n_{tot,i}^{ox}$ [-]: total number of the PQs re-oxidised during the entire light cycle

$phot_{max}$ [photons n_{RC}^{-1}]: maximum number of photons that can be processed during the light phase

$\bar{r}_{O_2}$ [mg_{O2} m^{-3} d^{-1}]: average oxygen production rate

r'_{O_2} [-]: non-dimensional oxygen production rate

$\bar{r}_X$ [g m^{-3} d^{-1}]: average biomass production rate

v_{cell} [m s^{-1}]: cell lateral velocity

W [m]: PBR depth

w_{10} [-]: weighting factor for the 10 ms bottleneck

$x_{dam,02}$ [-]: contribute of the 0.2 ms bottleneck on photoinhibition

$x_{dam,10}$ [-]: contribute of the 10 ms bottleneck on photoinhibition

X_{diss02} [-]: fraction of PQs dissipated through the 0.2 ms bottleneck

X_{diss10} [-]: fraction of PQs dissipated through the 10 ms bottleneck

$x_{RC,a}$ [-]: fraction of active RCs

$x_{RC,dam}$ [-]: fraction of damaged RCs

$Y_{O_2/X}$ [mg_{O2} g^{-1}]: oxygen to biomass yield

z [m]: position of the cell

$z_{start,i}$ [m]: position of the cell at the beginning of the *i*-th light cycle

ϕ [-]: light phase/duty cycle

θ [d]: residence time in the PBR

μ [d^{-1}]: specific biomass production rate

$\bar{\mu}$ [d^{-1}]: specific biomass production rate averaged on the N_{pool} distribution

τ_{02} [ms]: characteristic time of the 0.2 ms bottleneck

τ_{cycle} [s]: duration of the light cycle

τ_{dark} [s]: duration of the dark phase

$\tau_{dark,i}^{max}$ [s]: maximum dark time above which all the PQs will be reoxidised in the dark phase

τ_{del} [ms]: delivery time

τ_{mix} [s]: mixing time

τ_{pulse} [s]: duration of the light phase/pulse of light

$\tau_{pulse,i}^{max}$ [s]: maximum time pulse above which the PQ pool is completely full

Chapter 5

Droop model identification via model-based design of experiments to describe microalgae nitrogen uptake in continuous photobioreactors

The Droop model is suitable for the description of the effect of nutrients on microalgal growth but presents challenges in parameter identification due to the high correlation between parameters and the significant experimental effort required. In this Chapter, we employ Model-based design of experiments to plan information-rich experiments for precise parameters estimation of the Droop model, based on dynamic variations of dilution rate and nitrogen concentration in a continuous photobioreactor growing microalga *Tetradesmus obliquus*. The proposed methodology is shown to be a valuable tool for the study of nutrients dynamics in continuous microalgal cultivation systems.

5.1 Introduction

Autotrophic microalgae and cyanobacteria present a wide spectrum of applications, ranging from the production of biofuels, pigments, nutraceuticals and pharmaceuticals to their use as fertilisers, aquaculture feed or wastewater treatment. Thanks to their ability to fix CO_2 and to consume inorganic nitrogen and phosphorous from wastewater, their utilisation offers a sustainable approach for multiple industrial applications (M. Kumar et al., 2020). The production and accumulation of valuable compounds by microalgae is generally related to the environmental conditions and the growth phase, and it often occurs as a response to environmental stresses (Turetta et al., 2022).

Modelling the effect of nutrients is of particular interest due to their strong relevance in different microalgal industrial processes: subjecting microalgae to nutrient deprivation stresses is often used

---

Part of the work presented in this Chapter has been published in *Saccardo, A., Felices-Rando, B., Sforza, E., and Bezzo, F. (2023). Droop model identification via model-based design of experiments to describe microalgae nitrogen uptake in continuous photobioreactors. Chem. Eng. J. 468, 143577. doi: 10.1016/j.cej.2023.143577.* and in *Saccardo, A., Felices-Rando, B., Sforza, E. and Bezzo, F. (2023). Model-Based Design of Experiments for the identification of microalgae growth models with limiting nutrients. In: Computer Aided Chemical Engineering 52, Proc. of the 33th European Symposium on Computer Aided Process Engineering, Elsevier, Amsterdam, 2135-214.* Part of the experimental activity was carried out by Ms. Beatriz Felices-Rando as part of her PhD project.

to enhance lipid accumulation as well as other valuable compounds (Cirulis et al., 2013; Peng et al., 2020). For instance, cyanophycin (a molecule that is attracting a lot of interest as a raw material in various industrial sectors) is synthesised by several species of cyanobacteria when they are exposed to nutrient limitations, acting as a reservoir for energy (Trentin et al., 2021). Understanding nutrient assimilation by microalgae is also essential in wastewater treatment applications, where the main goal is to optimise both nutrient assimilation rates (i.e., nutrient removal from wastewater) and biomass production (Leong et al., 2021). This is particularly challenging since wastewater is a very heterogeneous nutrient source: nutrient availability in wastewater can be insufficient or pose negative effects on microalgal growth, compromising the commercial viability of the process (Pastore et al., 2020; Sforza et al., 2018). When it comes to biofuel production from microalgal biomass, special attention must be paid to microalgae biochemical composition (in particular, lipid content), which is also highly affected by nutrient supply (Leong et al., 2022; Mayers et al., 2014). Finally, microalgae cultivation represents a promising biomass source to complement agricultural crops; however, it requires considerable amounts of nutrients and thus it is desirable to improve nutrient assimilation efficiency in order to avoid competition for fertiliser supply (Markou et al., 2014).

For these reasons, the availability of mathematical models capable of accurately describing the effect of nutrients on microalgae growth is a key to optimise the design and control of the aforementioned industrial processes (Barbera et al., 2022)

The Monod equation and the Droop equation are two of the earliest and most applied models that describe the effect of nutrients on microalgae growth rate (μ). The first relates μ to the dissolved concentration of the limiting nutrient, while the latter relates μ to the intracellular concentration of the limiting nutrient ("cell quota", q), defined as the amount of internal nutrient per unit of biomass. The Monod equation is conventionally used to describe microalgal growth; however, it is known that microalgae can continue to grow after dissolved nutrients are exhausted, as they have the ability to decouple nutrient uptake from biomass growth (Bernard, 2011; Sommer, 1991). The Droop model is able to capture this phenomenon, giving a more accurate description of the effect of nutrients on microalgae growth rate (Benavides et al., 2015).

The identification of the Droop model is however challenging: also because of correlation between model parameters, a high number of measurements and experiments is needed to reliably calibrate the model, which results in long and time-consuming experimental campaigns. Furthermore, although steady-state continuous cultures are preferred in terms of microalgal production, working with continuous systems can become highly time consuming, as the transition between different steady states requires time, and several steady states are needed to obtain large set of experimental data for

the identification of the parameters related to each nutrient (Turetta et al., 2022). Model-based design of experiments (MBDoE) is a mathematical technique that exploits the knowledge of the system, embedded in the equations of a mathematical model, to plan highly informative experiments for accurate estimation of model parameters (Muñoz-Tamayo et al., 2014), (Franceschini & Macchietto, 2008).

MBDoE has been applied successfully in numerous fields: for instance, recently, Fleitmann et al. (Fleitmann et al., 2022) used MBDoE to minimise the thermodynamic and economic performance metrics of solvent-based processes; De-Luca et al. (De-Luca et al., 2020) identified a crystallisation model for pharmaceutical application based on MBDoE approach; and Waldron et al. (Waldron et al., 2020) exploited MBDoE to estimate kinetic parameters in transient flow experiments. In the microalgae field, Bernardi et al. (Bernardi et al., 2016) applied MBDoE to address the identification of a state model describing light-limited photosynthetic production in microalgae.

In this work, MBDoE is applied to optimise experiments with dynamic input variations of dilution rate and nitrogen concentration for precise parameter estimation of the Droop model. Microalga *Tetradesmus obliquus* is used in this study, and data for parameter estimation are obtained from measurements of biomass and nitrogen concentrations. We will demonstrate the MBDoE application allows reducing significantly the experimental effort needed to estimate the parameters of the Droop model in a continuous PBR, and that the calibrated model can be exploited for the reliable representation of the dynamics of nitrogen uptake.

This Chapter is organised as follows. Section 5.2 describes the experimental setup and the modelling framework, including the mathematical foundation of MBDoE. Section 5.3 presents the experimental results and discusses them critically. Some final remarks and future perspectives conclude the work.

5.2 Materials and methods

5.2.1 Microalgal species and cultivation system

Tetradesmus obliquus 276-7 (obtained from SAG-Goettingen) was cultivated in sterile BG11 medium modified to have a double (2x) concentration of all the nutrients (except for nitrogen concentration, which will be specifically described further in this section) and buffered with HEPES 1M pH 8 to avoid acidification caused by CO_2 bubbling and maintaining the pH between the values of 7 and 8. The exact composition of the original medium (1x) can be found in (Rippka et al., 1979).

For each experiment, two vertical panel photobioreactors (PBRs) were run in CSTR (Continuous Stirred Tank Reactor) mode, with a volume of 200 mL and a thickness of 35 mm, working at two

light intensities: 220 µmol m^{-2} s^{-1} and 420 µmol m^{-2} s^{-1}, which are limiting and saturating conditions of light, respectively. Performing the same experimental protocol also at a higher light intensity allowed to obtain additional data, increasing the robustness of the estimated parameters with respect to light variations.

The medium was pumped into the reactors by means of a multi-channel peristaltic pump (120S/DM3, Watson Marlow, USA), while an overflow exit was placed on the opposite side of the reactors, ensuring a constant liquid level. A thin baffle was added to avoid short-circuiting of the inlet medium flow rate and increase liquid turbulence. Mixing was ensured by a magnetic stirrer placed at the bottom of the reactor, so that the reactor can reasonably considered as a CSTR. The layout of the experimental apparatus is show in Figure 5.1a and an image of the PBRs during one experiments is shown in Figure 5.1b.

CO_2 was provided in excess by means of a CO_2-air flow (5% v/v, corresponding to a dissolved concentration of 1.7 mM approximately) supplied through a tube from the bottom of the reactors. The experiments were carried out in a refrigerated incubator, which kept the temperature constant at 24°C. A LED lamp (Light Source SL3500, Photon System Instruments, Czech Republic) was used for light supply, and light intensity was measured by means of an HD of 2102.1 photoradiometer (Delta OHM, Italy).

5.2.2 Analytical procedures

The dilution rate was set by the peristaltic pump and checked twice a day by measuring the volume of liquid in the outlet of the reactors. Biomass concentration was monitored by optical density measurements at 750 nm (OD_{750}), after diluting the samples accordingly so that the OD values fall within the measuring range of the apparatus (from 0 to 1). OD_{750} was measured with a UV-Visible double beam spectrophotometer (UV1900, by Shimadzu, Japan). At the end of each experiment, dry weight was determined by filtering 10 mL of the culture sample on a previously dried 0.45 µm nitrocellulose filter with a vacuum flask. The filters were then dried at 110°C in a laboratory oven for at least 2h. This allowed to obtain a correlation between the OD_{750} measurements and the mass concentration of biomass. Nitrogen concentrations were measured by means of an NO_3^- ion selective electrode (perfectION comb NO_3, Mettler-Toledo, Schwerzenbach, Switzerland). The inlet nitrogen concentration in the reactors was monitored by analysing a sample of the medium every time a new batch of medium was prepared. To measure nitrogen concentration in the bulk of the reactors, every sample taken from the reactor was filtered with a 0.2 µm filter. All the samples were diluted with deionised water until having a volume of 5 mL with NO_3^- concentrations falling within the measuring

range of the electrode (from 1 to 1000 mg NO_3^- L^{-1}). Before each measurement, 100 µL of ISA (Ionic Strength Adjuster) were added to each sample.

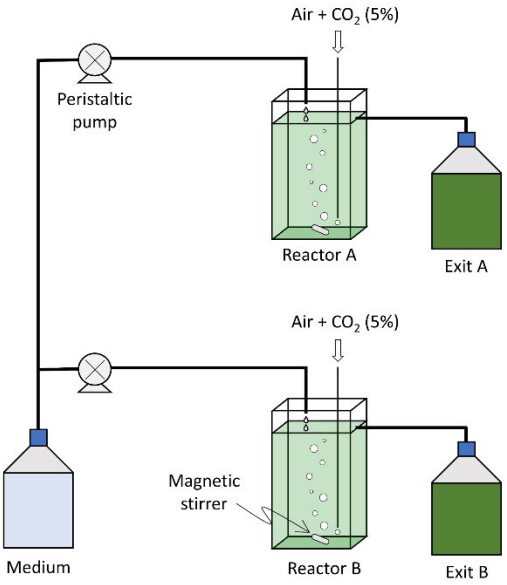

(a)

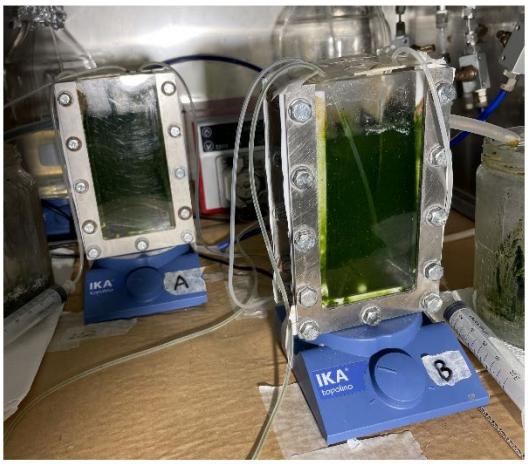

(b)

Figure 5.1: *(a) Scheme of the experimental setup, (b) photography of the reactors during one of the experiments .*

5.2.3 The Droop model

In the Droop model framework considered in this Chapter, the specific biomass growth rate μ (d^{-1}) is expressed as a function of both light intensity I (µmol m^{-2} s^{-1}) and the internal quota q (g_N g_x^{-1}) of the

limiting nutrient. In this work, nitrogen is the limiting nutrient. According to Bernard (Bernard, 2011), the specific biomass growth can be expressed as:

$$\mu = \mu_{max} \frac{I}{I+K_I\left(\frac{I}{I_{opt}}-1\right)^2}\left(1-\frac{q_{min}}{q}\right)-M \quad . \tag{5.1}$$

In Equation 5.1, μ_{max} (d^{-1}) is the maximum specific growth rate of the microorganism, K_I (µmol m^{-2} s^{-1}) is the half-saturation light constant, I_{opt} (µmol m^{-2} s^{-1}) is the optimal light intensity for microalgae growth, M (d^{-1}) is the specific decay rate and q_{min} (g_N g_x^{-1}) is the minimum internal nitrogen cell quota. Because of self-shading, light intensity can vary along the depth of the reactor and for a flat plate reactor it can be expressed through the Lambert-Beer law:

$$I = I_0 \exp(-k_a c_x z) \quad , \tag{5.2}$$

where c_x (g_x m^{-3}) is biomass concentration, I_0 (µmol m^{-2} s^{-1}) is the incident light intensity in the PBR, k_a (m^{-2} g_x^{-1}) is the biomass light absorption coefficient, and z (m) is the spatial coordinate along the thickness of the reactor. The local biomass growth rate r_x (g_x m^{-3} day^{-1}) at z can be expressed as

$$r_x = \mu c_x \tag{5.3}$$

and can be averaged along the culture depth W (m) to calculate the average biomass growth rate r_x^{avg} (g_x m^{-3} day^{-1}):

$$r_x^{avg} = \frac{1}{W}\int_0^W r_x \, dz \quad . \tag{5.4}$$

In the Droop model, the limiting nutrient uptake rate ρ (g_N g_x^{-1} d^{-1}) depends both on the external dissolved nitrogen concentration c_N (g_N m^{-3}) and on its internal quota according to (Lehman et al., 1975).

$$\rho = \rho_N \frac{c_N}{K_N+c_N}\left(1-\frac{q}{q_{max}}\right) \quad , \tag{5.5}$$

where ρ_N (g_N g_x^{-1} d^{-1}) is the maximum uptake of the limiting nutrient, K_N (g_N m^{-3}) is the limiting nutrient half-saturation constant, and q_{max} (g_N g_x^{-1}) represents the maximum limiting nutrient quota in the biomass. Material balances for biomass in a continuous PBR are written as:

$$\frac{dc_x}{dt} = \mu(q)c_x - Dc_x \quad , \tag{5.6}$$

$$\frac{dc_N}{dt} = -\rho(c_N)c_x - Dc_N + Dc_{N,in} \quad , \tag{5.7}$$

where D (d^{-1}) is the dilution rate and $c_{N,in}$ (g_N m^{-3}) is the nitrogen concentration of the inlet flowrate. The internal nutrient quota is maintained by uptake from external medium and consumed by cells metabolism. Thus, the material balance of internal quota can be expressed as:

$$\frac{dq}{dt} = \rho(c_N) - \mu(q)q \quad . \tag{5.8}$$

The goal is to estimate Droop parameters K_N, q_{max}, q_{min}, ρ_N, which are specifically related to the interaction between cells and nitrogen. Parameters $\mu_{max}, K_I, I_{opt}, M, k_a$ are mostly related to the effect of light on cell growth: we assume they are not affected by nitrogen dynamics, and are therefore fixed as in Table 5.1 based on experiments in Chapter 2 in a similar reactor of 3.5 cm thickness and the same species.

Table 5.1: *Fixed light parameters.*

Name	Value
μ_{max}	2.8 d^{-1}
K_I	262.8 µmol m^{-2} s^{-1}
I_{opt}	178.3 µmol m^{-2} s^{-1}
M	0.3 d^{-1}
k_a	0.09 m^{-2} g_x^{-1}

5.2.4 Model-based design of experiments

MBDoE is a mathematical technique that, exploiting an *a priori* knowledge embedded in a mechanistic mathematical model, aims at obtaining the maximum information from an experiment that will yield, in a statistical sense, the most informative data for modelling activity avoiding waste of time and resources (Franceschini & Macchietto, 2008). With this approach, model equations and current parameter values are employed to estimate and then maximise the information content of the experiment.

To apply MBDoE, Equations 5.1-5.8 can be rearranged in a compact form:

$$\begin{cases} \mathbf{f}(\dot{\boldsymbol{x}}(t), \boldsymbol{x}(t), \boldsymbol{u}(t), \boldsymbol{\theta}, \boldsymbol{k}, t) = 0 \\ \hat{\boldsymbol{y}}(t) = \mathbf{h}(\boldsymbol{x}(t)) \end{cases} \tag{5.9}$$

in which $\boldsymbol{x}$ is the N_x-dimensional vector of the model state variables and $\dot{\boldsymbol{x}}(t)$ is the vector of time derivatives, $\hat{\boldsymbol{y}} = [c_x, c_N]^T$ is the N_y-dimensional vector of measured response variables, $\boldsymbol{u} = \left[D, c_{N,in}\right]^T$ is the N_u-dimensional set of time-varying inputs to the system, $\boldsymbol{\theta} = [K_N, q_{max}, q_{min}, \rho_N]^T$ is the N_θ-dimensional vector of parameters to be estimated, $\boldsymbol{k} = [\mu_{max}, K_I, M, k_a, I, W]^T$ the N_k-dimensional vector of constants of the model and $0 < t < \tau$ is time, with τ as the total duration of the experiment. Symbol ^ is employed to define the estimate of a variable: e.g. $\hat{\boldsymbol{\theta}}$ represents the vector of model parameter estimates. Samplings times are collected in the N_{sp}-dimensional vector $\boldsymbol{t}_{sp}$. Each experiment is thus mathematically defined by the experiment design vector $\boldsymbol{\phi} = \left[\boldsymbol{u}(t), \boldsymbol{t}_{sp}, \tau\right]^T$.

Mathematically, the decrease of the size of the inference regions of the model parameters allows the improvement of parametric precision. This is equal to decreasing the value of the elements of the parameter variance-covariance matrix $\boldsymbol{V}$, which can be defined as in (Walter & Pronzato, 1990):

$$\boldsymbol{V}(\widehat{\boldsymbol{\theta}}, \boldsymbol{\phi}) = \left[\sum_i^{N_y} \sum_j^{N_y} s_{ij} \boldsymbol{Q}_i^T \boldsymbol{Q}_j\right]^{-1} \quad (5.10)$$

with

$$\boldsymbol{Q}_i = \left.\frac{\partial \hat{y}_i}{\partial \theta_m}\right|_{t_l} \quad l = 1, \dots, N_{sp} \quad m = 1, \dots, N_\theta \quad . \quad (5.11)$$

In Equation 5.10, $\boldsymbol{Q}_i$ is the (N_{sp} x N_θ) dynamic sensitivity matrix of the i^{th} response variable. The term s_{ij} in Equation 5.10 is the element (i, j) of the inverse of the experimental error variance-covariance matrix. Here, a constant relative variance error model was adopted:

$$\sigma_{y_i}^2 = (\alpha \hat{y}_i)^2 \quad , \quad (5.12)$$

where $\hat{y}_i$ is the response i and $\sigma_{y_i}^2$ is its variance. Values of α employed in this work were retrieved from preliminary measurements and are 0.1 for biomass concentration and 0.08 for nitrogen concentration.

The final designed experiment $\boldsymbol{\phi}^{opt}$ was then calculated as the solution of the minimisation/maximisation problem:

$$\boldsymbol{\phi}^{opt} = \text{ argmin } \{\det[\boldsymbol{V}(\widehat{\boldsymbol{\theta}}, \boldsymbol{\phi})]\} = \text{ argmax } \{\det[\boldsymbol{V^{-1}}(\widehat{\boldsymbol{\theta}}, \boldsymbol{\phi})]\} \quad (5.13)$$

defined according to the so-called D-criterion, which aims at minimising the volume of the joint parametric confidence region (Walter & Pronzato, 1990). The optimum experiment is thus the one that minimises the parametric uncertainty and maximises the experimental information content.

After parameter estimation, it is possible to obtain a statistical metric of parameter precision for the i^{th} parameter by computing a Student *t*-value (Asprey & Naka, 1999):

$$t_i = \frac{\widehat{\theta}_i}{\sqrt{V_{ii}}} \quad (5.14)$$

where V_{ii} is the i^{th} diagonal element of $\boldsymbol{V}$. The *t*-value can be tested against a reference *t*-distribution with (*n*-*p*) degrees of freedom, where *n* is the total number of experimental observations and *p* is the number of parameters (Franceschini & Macchietto, 2008). If the *t*-values are higher than the reference ones, then the estimation is considered reliable, while *t*-values lower than the reference value show estimates with low statistical significance. In models involving multiple parameters, a low *t*-value can be caused by high correlation between parameters (Franceschini & Macchietto, 2008).

For experimental practical feasibility, the length of the experiments was set to 8 days, and the vector of sampling times was fixed as well: measurements of both biomass nitrogen concentration were taken at 9:00 and 17:00 from day 1 to 5 and on day 8; the final measurement was on day 9 at 9:00.

Control intervals were also set: input variables were allowed to vary immediately after sampling times.

Constraints were imposed on both input and output variables based on the experimental apparatus. The dilution rate interval was set as 0.01-1.78 d^{-1}, with the upper bound value to avoid regions of experimental instability, while the inlet nitrogen concentration interval was set as 10-1000 mg L^{-1}. For output variables, nitrogen concentration was allowed to vary in the interval 0.3-10000 mg L^{-1}; the lower bound was set accordingly to the lower measurement limit of the nitrate probe of 1 mg L^{-1} of NO_3^- (corresponding to 0.23 mg L^{-1} of N).

Although measurements of internal nitrogen quota were not performed in this work, initial values were required to solve differential equations. Thus, the initial values for the internal nitrogen quota used for the calculations were estimated according to equation:

$$q = \frac{c_{N,in} - c_N}{c_x} \quad . \tag{5.15}$$

The outcomes of MBDoE are piece-wise constant profiles of the input variables for optimal experiments. To specifically account for experimental constraints, input variables were kept constant considering control intervals of 8 hours (from 9:00 to 17:00) and 16 hours (from 17:00 to 9:00 of the following day) for each day, except days 6 and 7, where a single constant value was used.

A sequential approach is adopted, where three consecutive steps are needed to determine the model parameters: (1) the design of a new set of experiments, based on current knowledge and on the maximisation of the information content of the experiment; (2) the execution of the designed experiment and collection of new data; and (3) the estimation of new model parameters and their statistical assessment. The accuracy of the estimated parameters is statistically assessed through a *t*-test.

If the estimation is not precise, the whole procedure is repeated until a satisfactory parameter precision is attained. Each estimation task is based on all available data up to that point.

MBDoE and parameter estimation tasks were performed using software gPROMS v7.0.7 by Siemens Process Systems Engineering.

5.3 Results

5.3.1 Sensitivity analysis

Model practical identifiability, i.e., the possibility to estimate the model parameters considering the actual experimental conditions, is a key preliminary requirement. Local sensitivity analysis is a simple

test for assessing the model practical identifiability (Bernardi et al., 2014) where dynamic trajectories of the measured output variables are obtained by perturbing the parameters to be estimated one-at-a-time. The dynamic sensitivity $s_{i,p}(t)$ for the i^{th} variable perturbed by the p^{th} parameter at time t is computed as:

$$s_{i,p}(t) = \frac{\hat{y}_i(t) - \hat{y}_{i,p}^{pert}(t)}{\Delta\% \ \ \hat{y}_{i,REF}} \quad , \tag{5.16}$$

where $\hat{y}_i(t)$ is the value calculated with the nominal parametric set, $\hat{y}_{i,p}^{pert}(t)$ is the perturbed value calculated with the variation in the p^{th} parameter, $\Delta\%$ is the percentage perturbation of the parameter (here set equal to 1% for all parameters) and $\hat{y}_{i,REF}$ is a reference value for normalisation. In other words, local sensitivity analysis measures how the measured model responses are affected by a variation in the parameter value during an experiment, and accordingly, if the dynamics of a measured variable are informative on the parameter value and can be exploited for its estimation.

Two simulated experiments with two step perturbations for the dilution rate and the inlet nitrogen concentration were used for the sensitivity analysis. The input profiles and results of the sensitivity analysis are shown in Figure 5.2. As shown in Figure 5.2 c, q_{min} appears to be the parameter with the highest impact on the biomass concentration and thus its estimation is expected to be linked to this measurement. K_N, q_{max}, ρ_N have a minor impact on biomass concentration, but Figure 5.2 d, shows that their main effect is on the nitrogen concentration; thus, this variable is expected to be mainly responsible for their estimation. In Figure 5.2 d the nearly symmetric profiles for K_N and q_{max} indicate that there is anticorrelation between those parameters, and hint that possible issues may arise in their estimation. It can be observed that there is some correlation, too, between q_{max} and ρ_N. However, the analysis suggests that measurements of biomass and nitrogen concentration are sufficient for precise estimation of all Droop parameters if experiments are planned adequately.

5.3.2 Optimal experiments and parameters estimation

As discussed in Section 2.4., MBDoE was applied in an iterative procedure involving experiments and parameters estimation. As a result, two optimally designed experiments were performed, and the experimental data were employed for two subsequent parameters estimations.

For the first optimal experiment, Figure 5.3 shows the theoretical (expected from MBDoE) and real profiles of input variables, and Figure 5.4 a comparison between experimental profiles and model predictions of the output variables after the second and final parameter estimation for both light conditions. Similarly, the second optimal experiment is shown in Figures 5.5-5.6, with profiles of input variables in Figure 5.5 and output variables in Figure 5.6.

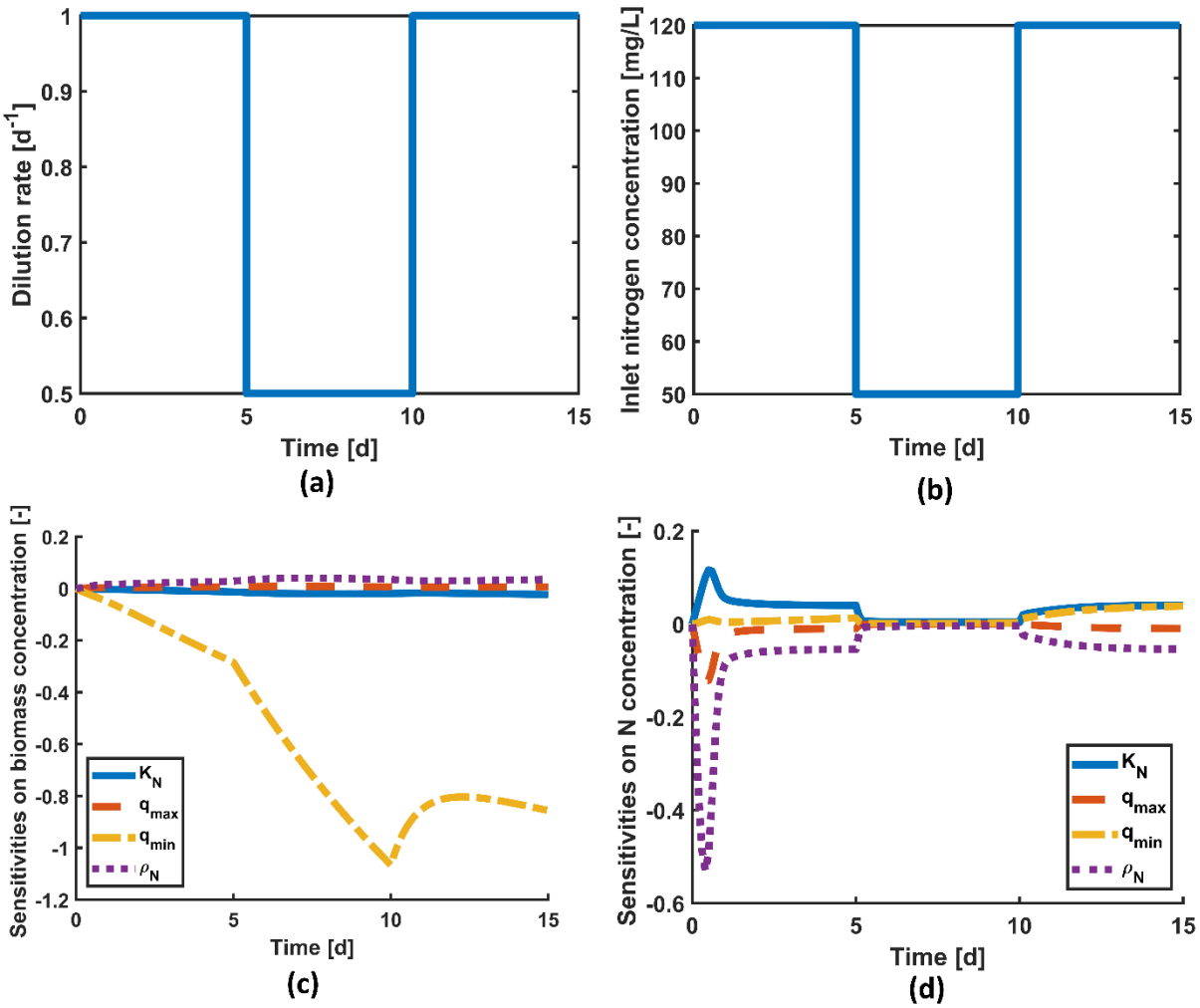

Figure 5.2: *Dynamic sensitivity analysis: dilution rate (a) and inlet nitrogen concentration (b) input profiles; sensitivities of model parameters on biomass (c) and nitrogen concentration (d).*

Table 5.2 summarises the two parameter estimations with the corresponding *t*-values: the first estimation was performed after completing the first experiment and used as the parametric guess for the second MBDoE; the second (and final) estimation was performed after the second experiment, employing data from both the first and second experiment. Notice that in Figure 5.3 b and Figure 5.5 b the experimental nitrogen concentration is the same for both light conditions since the nitrogen source is the same.

Some mismatch between theoretical and real profiles for dilution rate and inlet nitrogen concentration can be seen in Figure 5.3 a-b and Figure 5.5 a-b. This not surprising as real experimental conditions can deviate from the theoretical ones due to external disturbances and technological limitations of the experimental apparatus (e.g., clogging of tubes, malfunctioning of the pumping or electrical system).

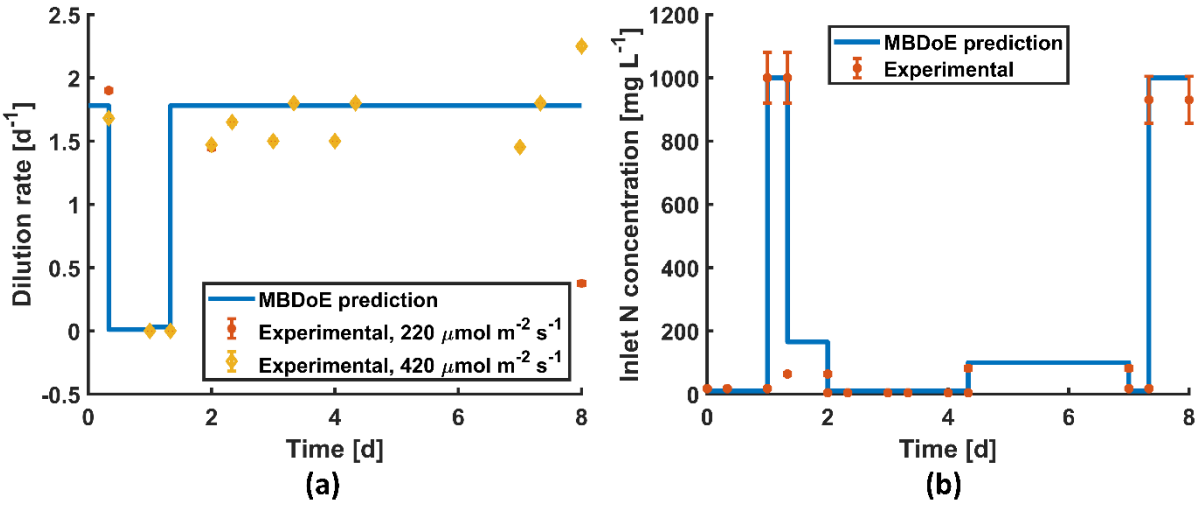

Figure 5.3: *Input profiles of the first optimal experiment; (a) comparison between theoretical and experimental dilution rates at 220 µmol m^{-2} s^{-1} and 420 µmol m^{-2} s^{-1}; (b) comparison between theoretical and experimental inlet nitrogen concentration.*

For this reason, not only the output (biomass concentration, c_x, and nitrogen concentration in the PBR, c_N) but also the input variables (D and $c_{N,in}$) have been measured to obtain their true experimental values and ensure that the parameter estimation is performed with the most accurate information.

For the first experiment, the experimental profile of biomass concentration is higher in the PBR with higher illumination (Figure 5.4 b). The difference between initial conditions for both reactors is due to the operation in continuous mode. In continuous systems, only the input variables (i.e. dilution rate, inlet nutrients concentrations, light intensity) are manipulated, while values of variables inside the PBR (i.e. biomass and nitrogen concentration) change in response to those inputs. Dynamic profiles of measured variables are thus deeply affected by the operation mode, either batch or continuous, and it was shown that a continuous PBR arrangement strongly influences both biomass productivity and nutrient uptake (Sforza et al., 2018). Apart from the initial values, the different illumination intensities do not have a major effect on the experimental dynamic trajectories of nitrogen concentration in Figure 5.4 c-d, which are similar for both the reactors. As regards the dynamics of input variables, the dilution rate drops to values close to zero between day 1 and 2 (Figure 5.3 a): in this time interval, PBRs are practically in batch mode, as reflected by the sharp increase in biomass concentration between day 1 and 2 in Figure 5.4 a-b, typical of batch systems.

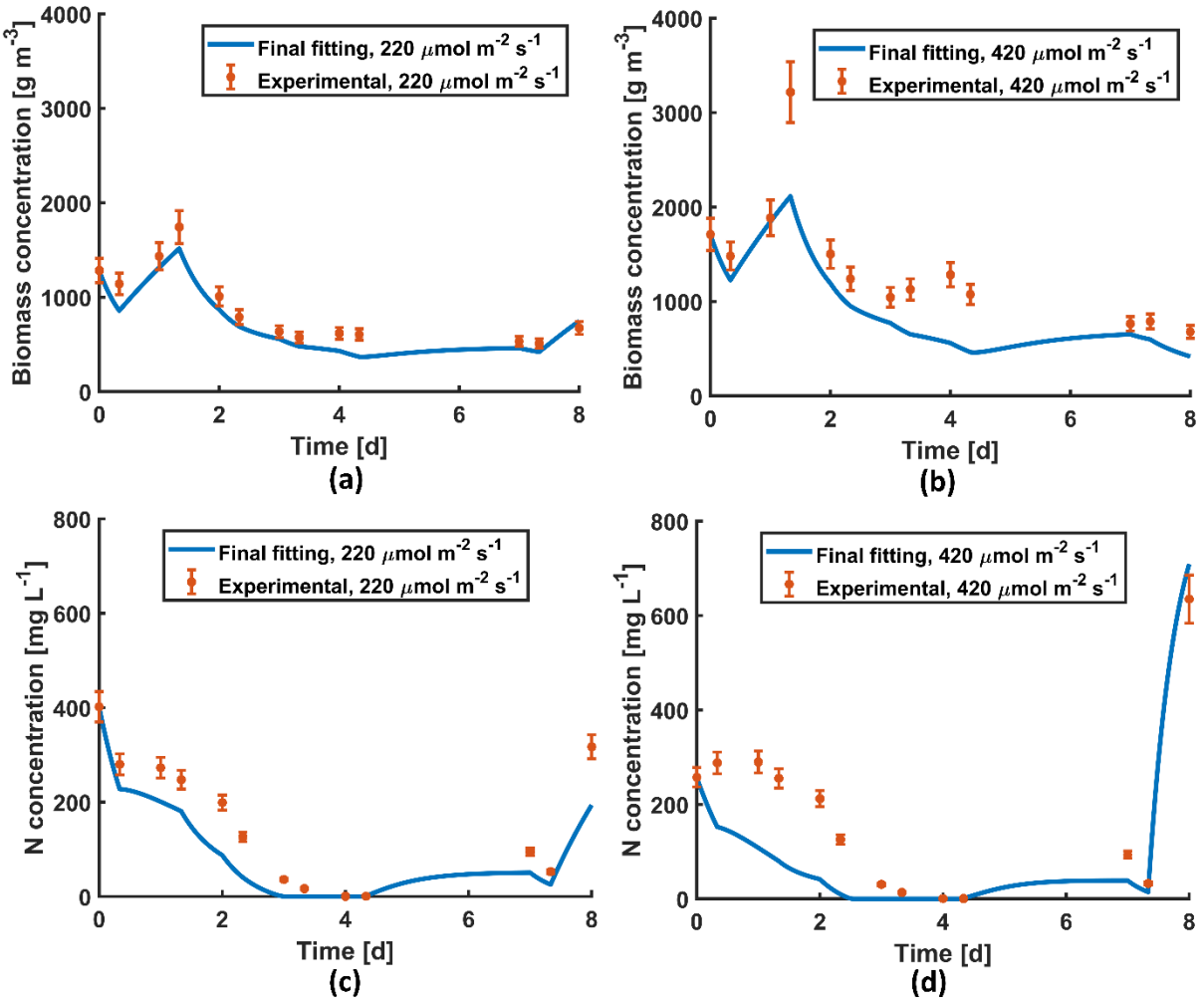

Figure 5.4: *Output profiles of the first optimal experiment; comparison between experimental and final fitting profiles of biomass concentration at (a) 220 µmol m^{-2} s^{-1} and (b) 420 µmol m^{-2} s^{-1}; comparison between experimental and final fitting profiles of nitrogen concentration at (c) 220 µmol m^{-2} s^{-1} and (d) 420 µmol m^{-2} s^{-1}.*

Despite this fact, the experimental nitrogen concentration in the PBRs remains almost constant between day 1 and 2 (Figure 5.4 c-d), showing a certain degree of inertia for the system. This behaviour can be explained with the consumption of internal nitrogen reservoirs between day 1 and 2, when the supply of nitrogen to PBRs is almost zero. In fact, it is well known that microalgae can internally store nutrients when they are in non-limiting concentration and use these internal reservoirs for growth in nutrients-depleted conditions (Sommer, 1991). This decoupling between biomass growth and nitrogen uptake can result in an inertial behaviour of the system (Sommer, 1991), also observed for other nutrients (Sforza et al., 2018).

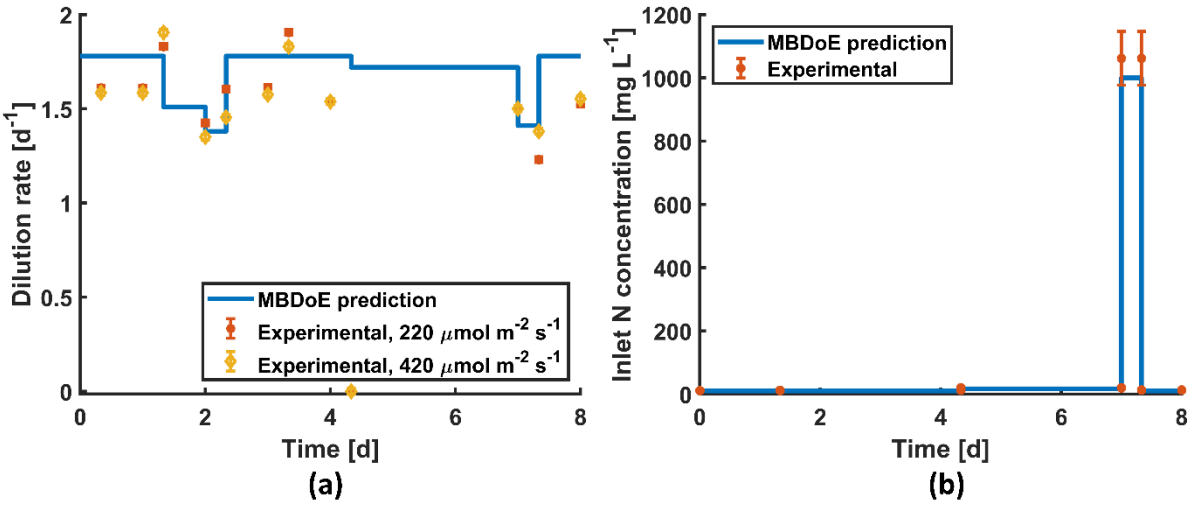

Figure 5.5: *Input profiles of the second optimal experiment; (a) comparison between theoretical and experimental dilution rates at 220 µmol m^{-2} s^{-1} and 420 µmol m^{-2} s^{-1}; (b) comparison between theoretical and experimental inlet nitrogen concentration.*

The second and third columns of Table 5.2 show the parameter estimates after the first optimal experiment. It can be noticed that only one parameter, q_{min}, is estimated with precision, while the *t*-values of the others are below the refence value. This reflects the outcome of the sensitivity analysis in Figure 5.2 c, where q_{min} had the highest impact on measured biomass concentration, and was therefore expected to be relatively easy to estimate.

Table 5.2: *Estimated model parameters. Reference t-value is equal to 1.68 for first and 1.66 for second fitting; t-values marked with * indicate estimates with a t-values below the threshold.*

Parameter	First fit	First fit 95% *t*-value	Second fit	Second fit 95% *t*-value
K_N [g_N m^{-3}]	2.88	1.65*	0.70	1.75
q_{max} [g_N g_x^{-1}]	0.1390	1.39*	0.1080	3.39
q_{min} [g_N g_x^{-1}]	0.0051	1.95	0.0051	5.83
ρ_N [g_N g_x^{-1} d^{-1}]	0.076	1.53*	0.237	2.00

Figures 5.5-5.6 show the theoretical and experimental profiles in the second optimal experiment. As shown in Figure 5.5 a, the second experiment is conducted at very high values of dilution rate (app. 1.7-2 d^{-1}), close to washout conditions. Moreover, apart from a sharp peak around day 7, inlet nitrogen concentration of Figure 5.5 b is almost at zero for the entire duration of the experiment. These experiments can thus represent conditions of nitrogen starvation, as shown in Figure 5.6 c-d, where the nitrogen concentration inside PBRs drops to values close to zero after day 2 and remains at that level for most of the experimental time.

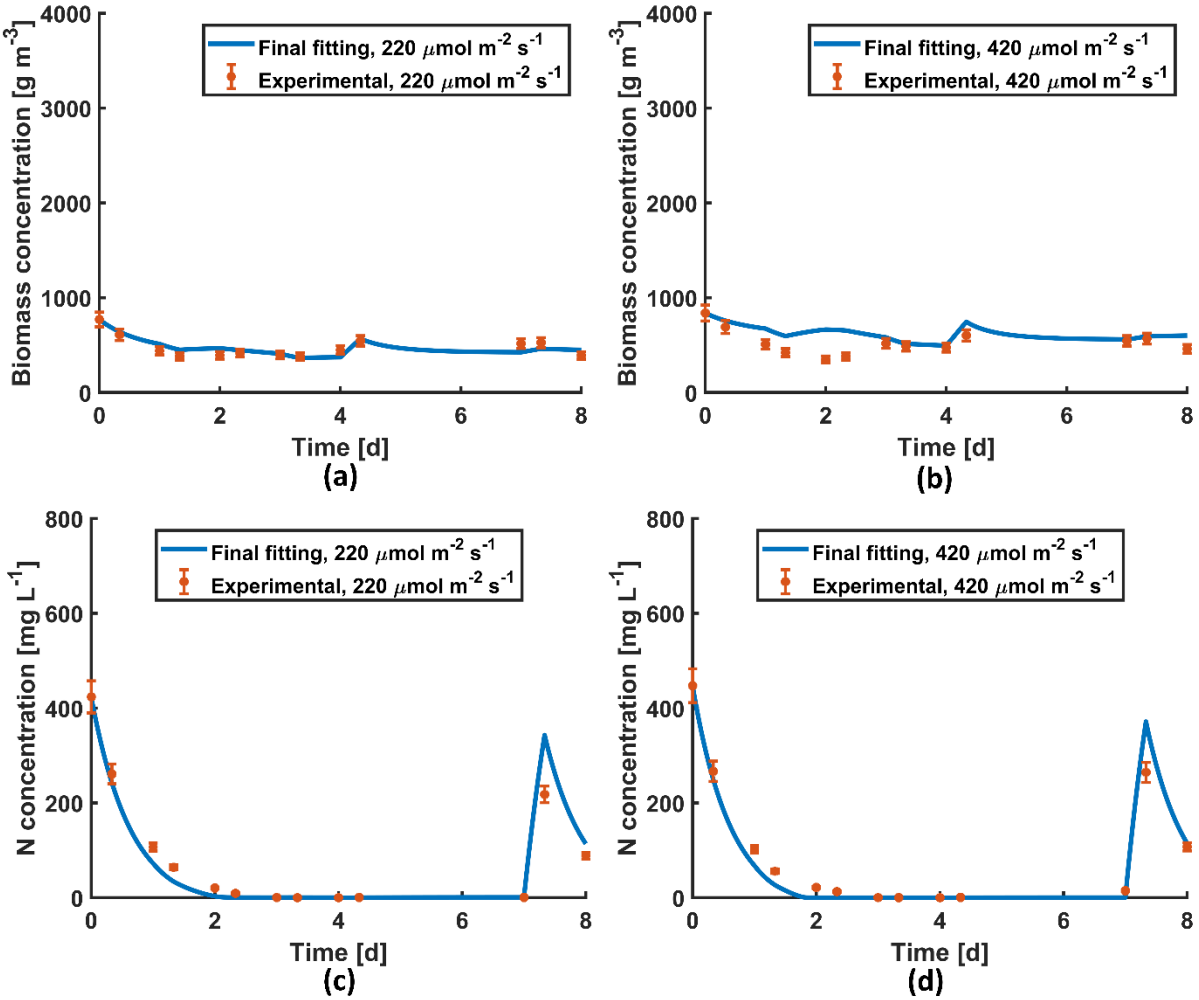

Figure 5.6: *Output profiles of the second optimal experiment; comparison between experimental and final fitting profiles of biomass concentration at (a) 220 µmol m^{-2} s^{-1} and (b) 420 µmol m^{-2} s^{-1}; comparison between experimental and final fitting profiles of nitrogen concentration at (c) 220 µmol m^{-2} s^{-1} and (d) 420 µmol m^{-2} s^{-1}.*

The difference in experimental biomass concentration profiles found in Figure 5.4 a-b for the two lights is considerably reduced for the second experiment, as shown in Figure 5.6 a-b, highlighting that under extreme nutrient depletion the key factor limiting biomass productivity is nitrogen concentration (Markou et al., 2014). Moreover, experimental biomass concentration remains almost constant: even if nitrogen concentration in the reactors is almost equal to zero after day 2 (Figure 5.6 c-d), biomass concentration has a slight increase for both reactors between day 2 and 5, and it decreases only after day 7. This shows again how the consumption of the internal nitrogen content is critical for sustaining microalgae growth and highlights the dependence of biomass productivity on the internal quota (Pastore et al., 2020). This is a key phenomenon to consider to fully capture nutrients dynamics, and it confirms the need to employ the Droop model instead of a traditional Monod-like one (Pastore et al., 2020; Sforza et al., 2018; Sommer, 1991).

Data from both optimal experiments were employed for the second parameter estimation, shown in the last two columns of Table 5.2. Adding a second optimal experiment allows for a precise estimation of all the parameters. Between the first and second estimation, the highest variation is recorded for K_N and ρ_N, that also have the lowest *t*-values among the parameters. This could be caused by the correlation between K_N and ρ_N highlighted from the sensitivity analysis in Figure 5.2 d, which makes a precise estimation more difficult. To conclude, Table 5.2 shows two optimal experiments to be sufficient for precise parameters estimation. In particular, a significant result is that MBDoE allows for precise estimation of the maximum (q_{max}) and minimum (q_{min}) quotas, whose identification through direct experimental measurements is known to be a challenging task (Sommer, 1991).

Parameters from Table 5.2 were compared to other estimations for similar microalgae strains, such as *S. obliquus* RISE (Gojkovic et al., 2020), *S. obliquus* (Deschênes & Wouwer, 2016), and a consortium of *Chlorella sorokiniana* and *Scenedesmus* sp. (Wágner et al., 2016). It should be stated, however, that very few works deal with the estimation of Droop model parameters for the genus *Scenedesmus* (homotypic synonym of *Tetradesmus*); moreover, literature data are often obtained in conventional batch systems. It can be observed that our estimate of parameter q_{max} (0.1390 $g_N\ g_x^{-1}$) falls within the range from 0.099 $g_N\ g_x^{-1}$ (Deschênes & Wouwer, 2016) to 0.1806 $g_N\ g_x^{-1}$ (Wágner et al., 2016) as reported in the literature. Despite the high parameter correlation, the low uncertainty in literature for the range of q_{max} is due to the existence of experimental methods for its direct estimation. The fact that our estimate falls within the literature range further shows the accuracy and power of the proposed methodology that minimises the need of experimental measurements. On the other hand, q_{min} (0.0051 $g_N\ g_x^{-1}$) is outside the literature range of 0.011 $g_N\ g_x^{-1}$ (Deschênes & Wouwer, 2016) to 0.047 $g_N\ g_x^{-1}$ (Gojkovic et al., 2020). However, it should be remarked that q_{min} is the parameter most affecting the measured output (see the sensitivity analysis), and therefore the one that is more precisely and reliably estimated as confirmed by the high value in the *t*-test. We are therefore confident about the reliability of the estimated obtained in this work. The estimated values of parameters K_N and ρ_N are within the literature range (respectively, from 0.020 $g_N\ m^{-3}$ (Deschênes & Wouwer, 2016) to 12.61 $g_N\ m^{-3}$ (Wágner et al., 2016), and from 0.0597 $g_N\ g_x^{-1}\ d^{-1}$ to 2.95 $g_N\ g_x^{-1}\ d^{-1}$ (Wágner et al., 2016)), but intervals are so wide that a comparison is hardly meaningful. The large variability in the K_N and ρ_N estimates from the literature is not surprising since their correlation can make their estimation a difficult task. The fact that by using MBDoE it was possible to achieve a statisticaly sound estimation of both parameters is a valuable result, and further demonstrates the effectiveness of the methodology and the importance of designing experiments in such a way as to maximise their information content.

Fitting results of the second parameter estimation are shown in Figure 5.4 for the first and in Figure 5.6 for the second experiment. Both figures highlight an overall good agreement between experimental data and model prediction, although some mismatch exists. The mismatch can be partly caused from limitations of the experimental apparatus (e.g., there was a malfunctioning in the mixing system during the second experiment at 420 µmol m^{-2} s^{-1}, concerning biomass experimental points 4-6). However, it could also highlight limitations of the model in capturing the dynamic behaviour of the system. As an example, in the first experiment, nitrogen experimental points 2-6 for both reactors (Figure 5.4 c-d) show that the experimental system has a certain degree of "inertia" that the model only partly describes.

Overall, model fitting is better in conditions of nutrients scarcity as the ones in the second experiment (Figures 5.5-5.6). For the first experiment, fitting of data at 220 µmol m^{-2} s^{-1} is generally better than at 420 µmol m^{-2} s^{-1}: e.g., biomass concentration at 420 µmol m^{-2} s^{-1} in Figure 5.4 b tends to be underestimated. This may denote an interaction between the effects of light and nitrogen (Simionato et al., 2013) that the model cannot represent.

5.3.3 Model validation and discussion

Two additional experiments were performed to validate the model through the comparison of data with model simulations at the same experimental conditions. These experiments were performed at 220 µmol m^{-2} s^{-1} and 420 µmol m^{-2} s^{-1}, with an approximate duration of 1.5 and 2.5 days respectively, and with varying dilution rates.

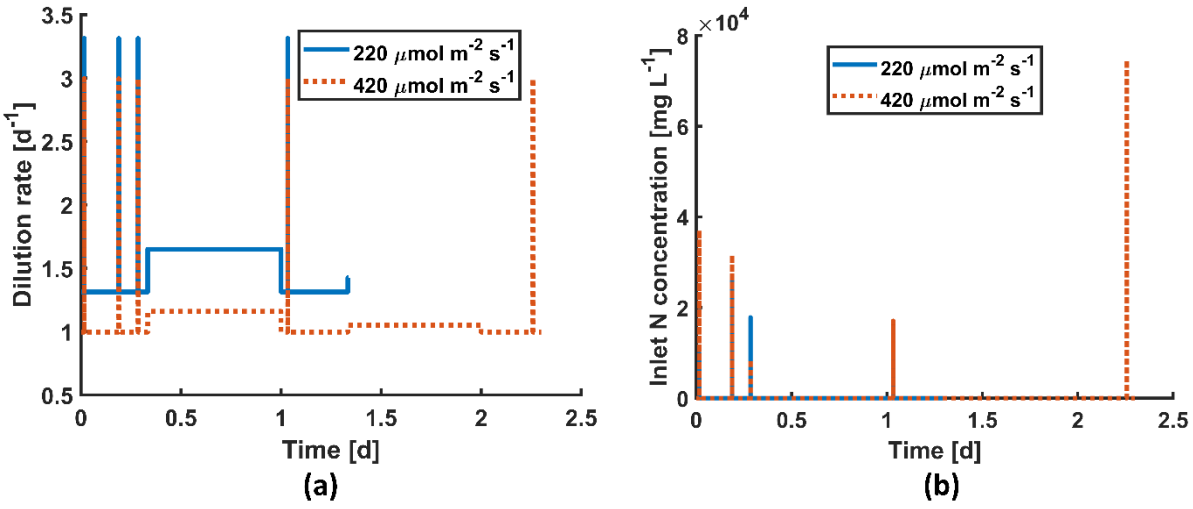

Figure 5.7: *Input variables of validation experiments at 220 µmol m^{-2} s^{-1} and 420 µmol m^{-2} s^{-1}; (a) dilution factor; (b) inlet nitrogen concentration.*

Figure 5.7 shows profiles of the input variables for both experiments and Figure 5.8 the comparison between experimental data and model prediction for biomass (Figure 5.8 a-b) and nitrogen concentration (Figure 5.8 c-d).

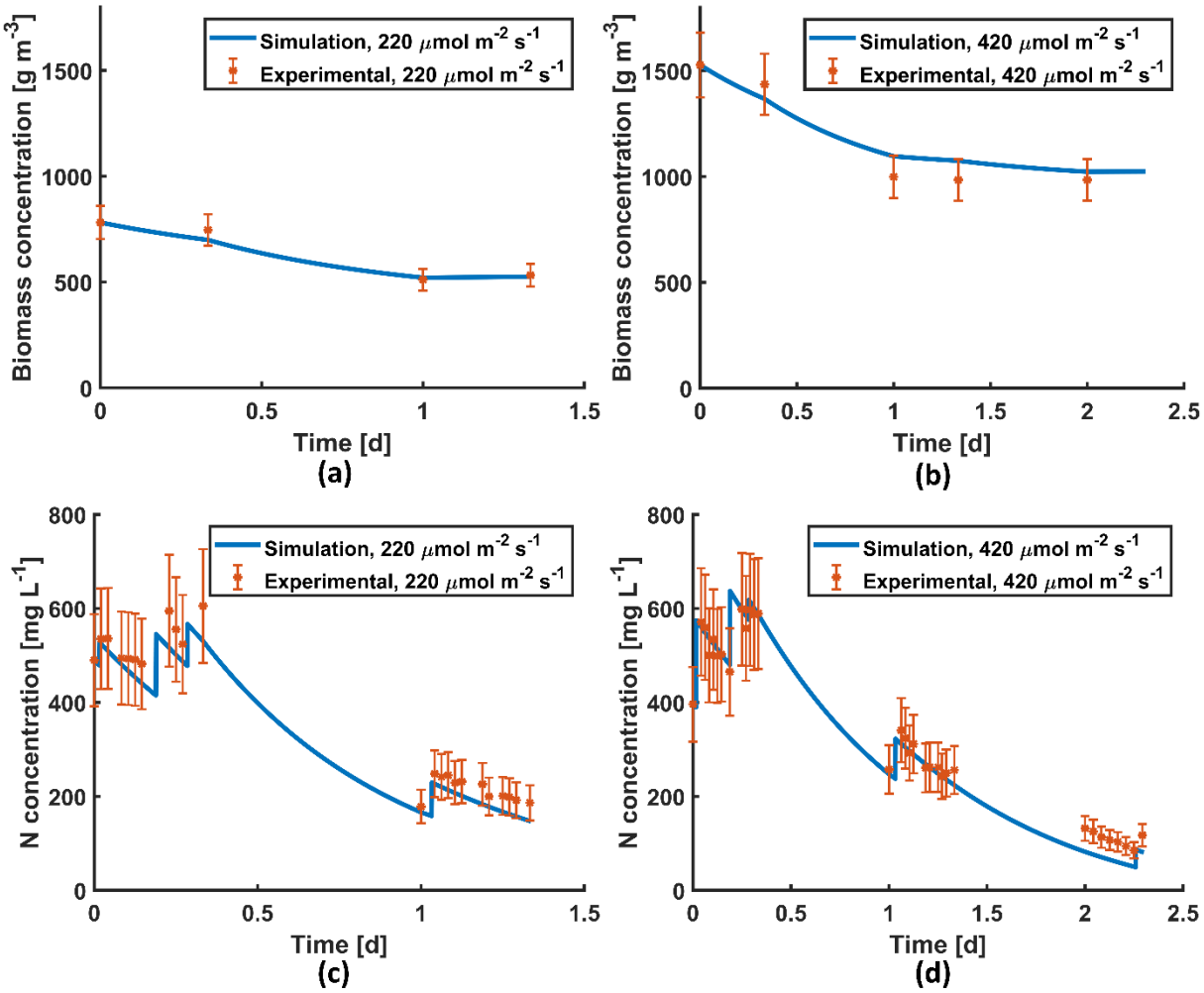

Figure 5.8: *Model validation results; comparison between experimental and predicted profiles of biomass concentration at (a) 220 µmol m^{-2} s^{-1} and (b) 420 µmol m^{-2} s^{-1}; comparison between experimental and predicted profiles of nitrogen concentration at (c) 220 µmol m^{-2} s^{-1} and (d) 420 µmol m^{-2} s^{-1}.*

The objective of the validating experiments was to challenge the model and to assess whether it was capable of capturing fast dynamic variations in the system, which were not considered during the calibration step. Thus, in addition to step change input variations of the dilution rate, nitrogen inlet pulses were also directly injected in the PBRs as shown in Figure 5.7 b. Nitrogen pulses with the desired concentration were delivered to PBRs by manual pipetting of small volumes (1-2 ml approximately) of solution at given time instants. Nitrogen pulses also have a minor effect on the dilution rate profile, as shown in Figure 5.7 a: despite their low volume (1 ml per pulse), nitrogen inlet pulses cause an increase in the dilution rate since they are delivered in a very short time. Inlet

nitrogen pulses mainly affect the nitrogen concentration in the PBRs (Figure 5.8 c-d), while biomass concentration has slower variations (Figure 5.8 a-b), affected principally by the dilution rate and the nitrogen concentration of the inlet flowrate. Biomass experimental profile at 420 µmol m^{-2} s^{-1} is considerably higher than at 220 µmol m^{-2} s^{-1} and model prediction accounts for this difference as shown in Figure 5.8 a-b. Moreover, as shown in Figure 5.8 c-d, the model simulation can capture both slow and fast nitrogen dynamics derived from inlet pulses.

To summarise, prediction performances of the calibrated model are generally good as shown in Figure 5.8. In particular, the close agreement between experimental data and model prediction in the validation experiment (mean root square error, %MRSE, of 4% for biomass and 11% for nitrogen) proves that the model is capable to follow both fast and slow variations in the system. With all the experiments being performed in low nitrogen or nitrogen deprivation conditions (Figures 5.3,5.5,5.7) the model proved to be suitable for application in nutrients-scarcity conditions and it can be used to represent dynamic conditions (e.g. for process optimisation purposes).

However, note that, especially for long time spans like those in Figures 5.4,5.6, the experimental system can show an inertial behaviour toward conditions of nitrogen deprivation. This behaviour is only partially captured in the model prediction: this could be a sign that the mathematical structure of the Droop model is too simple and a structural modification of the model itself is needed to account for this inertia, which may be related to acclimation dynamics, which are not accounted for in the standard model formulation.

Moreover, in this work, light conditions were kept constants in the experiments at values in the range of photosaturation, since this is generally the most favourable condition for microalgae cultivation. As shown in Figures 5.4,5.6,5.8, the model can predict well the experimental behaviour at both light intensities employed. However, a minor discrepancy between predictions of the biomass concentrations in the first optimal experiment (Figure 5.4 b) can highlight possible interaction between the effects of light and nitrogen variations on cells.

Results from this work also showed that the application of MBDoE for dynamic experiments can allow reducing the experimental effort required to estimate the Droop model parameters. For instance, if we consider the experimental set up used in this work and rely on steady-state conditions only as in Turetta et al. (2022), we estimated that the experimental campaign would require over two months instead of 16 days as in this case.

5.4 Conclusions

Model-based design of experiments was employed to estimate the Droop model parameters for microalga *Tetradesmus obliquus* cultivated in a continuous photobioreactor. It was demonstrated how the design of optimal experiments based on the model structure and capable of maximizing the information experiment allowed to:

1. estimate all model parameters in a statistically satisfactory way, even if some parameters were affected by high correlation;
2. limit the duration of the experimental campaign to only two 8-days optimal dynamic experiments, thus avoiding the need of a large number of time and resource consuming experiments.

The identified model proved to be able to represent the dynamics of both calibration and validation experiments with good accuracy, also highlighting some potential shortcomings of the Droop model itself, particularly for slow phenomena. The model is nonetheless able to capture the behaviour of the system, and to represent the dynamics of nitrogen uptake effectively.
Future work will aim at testing the model for optimisation purposes, and extending its description accuracy by incorporating additional phenomena, particularly with concern to slow dynamics.

5.5 Chapter nomenclature

Abbreviations:

CSTR: continuous stirred-tank reactor

MBDoE: Model-based design of experiments

OD: optical density

OD_{750}: optical density at a wavelength of 750 nm

PBR: photobioreactor

Symbols:

α: constant term of the variance error model

$\Delta\%$: percentage perturbation of the parameter

$\boldsymbol{\theta}$**:** vector of model parameters to be estimated

$\widehat{\boldsymbol{\theta}}$**:** vector of model parameter estimates

$\sigma_{y_i}^2$: variance of the measured response

τ: total duration of the experiment

$\boldsymbol{\phi}$**:** experiment design vector

$\boldsymbol{\phi}^{opt}$: final designed experiment

$\boldsymbol{k}$: vector of constants of the model

N_θ: number of model parameters

N_k: number of model constants

N_{sp}: number of sampling times

N_x: number of model state variables

N_y: number of measured response variables

N_u: number of model inputs

$\boldsymbol{Q}_i$: sensitivity matrix of the i^{th} response variable

$\boldsymbol{t}_{sp}$: vector of sampling times

$\boldsymbol{u}$: set of time-varying inputs

$\boldsymbol{V}$**:** parameter variance-covariance matrix

s_{ij} : element (i, j) of the inverse of the experimental error variance-covariance matrix

$s_{i,p}(t)$: dynamic sensitivity for the i^{th} variable perturbed by the p^{th} parameter at time t

t_i: t-value of the i^{th} parameter

$\boldsymbol{x}$: vector of the model state variables

$\dot{\boldsymbol{x}}(t)$: vector of time derivatives

$\hat{\boldsymbol{y}}$: vector of measured response variables

$\hat{y}_{i,p}^{pert}(t)$: perturbed response value after variation in the p^{th} parameter

$\hat{y}_{i,REF}$: reference response value for normalisation

Variables:

$c_{N,in}$ (g_N m^{-3}): concentration of nitrogen at the inlet

$c_{N,out}$ (g_N m^{-3}): concentration of nitrogen at the outlet

c_x (g_x m^{-3}): biomass concentration

D (d^{-1}): dilution rate

I (µmol m^{-2} s^{-1}): light intensity

I_0 (µmol m^{-2} s^{-1}): incident light intensity

I_{opt} (µmol m^{-2} s^{-1}): optimal light intensity

K_I (µmol m^{-2} s^{-1}): half-saturation light constant

K_N (g_N m^{-3}): limiting nitrogen half-saturation constant

k_a (m^{-2} g_x^{-1}): biomass light absorption coefficient

M (d^{-1}): specific decay rate

q ($g_N\ g_x^{-1}$): internal nitrogen quota in the cell

q_{min} ($g_N\ g_x^{-1}$): minimum nitrogen quota

q_{max} ($g_N\ g_x^{-1}$): maximum nitrogen quota

r_x ($g_x\ m^{-3}\ day^{-1}$): local biomass growth rate at coordinate z

r_x^{avg} ($g_x\ m^{-3}\ day^{-1}$): average biomass growth rate

W (m): culture depth

z (m): spatial coordinate along the thickness of the reactor

μ (d^{-1}): specific biomass growth rate

μ_{max} (d^{-1}): maximum specific biomass growth rate

ρ ($g_N\ g_x^{-1}\ d^{-1}$): nitrogen uptake rate

ρ_N ($g_N\ g_x^{-1}\ d^{-1}$): maximum nitrogen uptake rate

Chapter 6

Conclusions and future perspectives

Over the years, microalgae attracted substantial attention as a promising sustainable solution in many industrial fields. However, the commercial-scale production of microalgae continues to face limitations due to the great complexity embedded in microalgal growth processes. Many environmental factors, light in the first place, affect the biological response in an interactive way, and the comprehension of these phenomena is not sufficient yet, thus hindering the practical application of microalgae-based technologies. In this context, mathematical modelling represents a valuable tool for enhancing the comprehension of microalgae growth processes. Mathematical models can indeed play a crucial role in uncovering the mechanisms underlying photosynthesis and metabolic processes. Moreover, mathematical models are invaluable instruments for the design, operation and control of microalgae culture systems, and thus represent the preferential way for an effective development of the microalgae field.

6.1 Summary of thesis achievements

Despite the great effort made over the years in the development of mathematical models, there are still gaps in the comprehension of different key phenomena for microalgae growth. Through a proper combination of experimental and modelling activities, the main aim of this Thesis was to bridge some gaps between the theoretical knowledge of microalgae biology and the phenomena practically observed in real cultivations in PBRs. The main achievements of this Thesis are summarized in the following

(i) Self-shading and mixing induced light-dark cycles heavily hinder the true effect of light on cell growth. In Chapter 2, we designed, built and operated ultra-thin continuous photobioreactors with optical path from 2 to 8 mm. To our knowledge, these systems represent the smaller example of continuous PBRs operating in continuous. We compared data at 2-89 mm with others at 15 and 35 mm and found that with ultra-thin scales, high inhibition occurs also at low irradiance values. With experimental data from different

reactor optical paths (2-35 mm), we fitted the parameters of a Haldane-like model. We found that two parameters (the optimal light intensity and the lambert Beer constant) are heavily dependent on the optical thickness, and postulated that traditional Haldane-like and P-I models could have limited capability in capturing experimental results at ultra-thin light paths. Thus, particular care must be taken when employing P-I curves to scale up experimental results from ultra-thin light paths to higher scales. We inferred that this limitation arises from the averaged nature of empirical models, which do not account for the influence of mixing-induced light-dark cycles. Notably, computations based on the theory of mathematical modelling of pulsed light effects on microalgae indicated that true continuous light conditions are only found in ultra-thin light paths (2-8 mm), while in thicker light paths (15-35 mm), cells are exposed to an effective pulsed light regime due to the presence of mixing-induced light-dark cycles. This highlighted that a possible point of connection exists between the use of ultra-thin PBRs under continuous light and experiments with pulsed light regimes to highlight the fundamental cell responses to the effect of light in microalgae cultivation.

(ii) Pulsed light cultivation experiments can mimic mixing-induced light cycles found in high scale cultivation systems. To model pulsed light cultivation, PSU models are often chosen. However, one of the main challenges of PSU models is the representation of the impact of PSU dynamics on biomass growth. In particular, most of the models in literature are unable to simultaneously capture dynamics of PSUs and of biomass growth. Thus, a reformulation of the Camacho-Rubio model (Camacho Rubio et al., 2003) was developed in Chapter 3 to simultaneously capture both dynamics. To guide the model development, the theoretical knowledge of photosynthetic characteristic time scales was employed, leading to the formulation of intra- and inter- light cycles dynamics with algebraic and differential equations respectively. For parameter estimation, a rich dataset of High Throughput Screening dynamic growth experiments under pulsed light from Sivakaminathan et al. (2018) was employed. PCA and PLS techniques were employed to reduce the biological variability of the data by rejecting outliers in pulsed-light data in a statistically sound way. The parameters of the model were precisely estimated with the cleaned data under intermittent illumination. The model was then validated against additional data with both pulsed and continuous light regimes. For OD_{750}, the average experimental errors were of 8% under pulsed light and 15% under continuous light and

for OD_{680} of 12% under pulsed light and 18% under continuous light. The resulting calibrated model is a robust and reliable tool that can be employed for dynamic modelling of microalgae cultivation systems under both pulsed and continuous light operation.

(iii) Artificial pulsed light can be employed for optimising the performance microalgae cultivation. High-frequency pulsed light showed to increase the productivity with respect to continuous light when input conditions are specifically selected (Diotto et al., 2022). Selecting the optimal pulsed light operating conditions is not trivial due to a lack of fundamental understanding of its effect on microalgae growth. The objective of Chapter 4 was thus to develop a model formulation to interpret the observed effect of pulsed light on experimental data and guide the planning of future experiments. In Chapter 4, a novel model proposed by Zarmi et al. (2020) for application to describe microalgae growth under high frequency pulsed light was thus examined and modified. In particular, we reformulated the model to account for the specific effect of the dark phase on growth, we linked photon dissipation to photoinhibition, and adapted the model to represent realistic cultivation scenarios in a PBR. We calibrated the model on steady state and respirometry pulsed light experiments and found that the model is able to provide meaningful physical explanations of the observed data. We employed model simulations to guide respirometry experiments under pulsed light by exploring the experimental space and selecting conditions to maximise the oxygen production rate. The outcomes of the respirometry experiment suggested that an increase in productivity can be reached under pulsed light when constraining operations in specific limits (e.g., $\tau_{pulse}/\tau_{dark} = 1/24$ in the examined scenario).

(iv) In Chapter 5, we applied model-based experimental design to design an experimental campaign for the estimation of the parameters of the Droop model for the microalga *Tetradesmus obliquus*, cultivated in continuous photobioreactors. High parameter correlation is a typical challenge that often jeopardise the significance of the estimated values. Experiments were designed to maximize the information obtained from the data and enabled to estimate all model parameters in a statistically satisfactory way, and to limit the duration of the experimental campaign to only two 8-days optimal dynamic experiments, thus avoiding the need of time and resource consuming experiments. The identified model allowed to represent the dynamics of both calibration and validation

experiments with good accuracy, also highlighting some potential shortcomings of the Droop model for slow phenomena. The model was able to capture the dynamics of nitrogen uptake effectively.

6.2 Future perspectives

The research outcomes of the PhD projects opened the path for future investigations. Some possible directions are discussed in the following.

(i) **Multiscale modelling.** The use of ultra-thin PBRs can be an important resource to help developing a multi-scale modelling approach to represent the behaviour of industrial cultivation systems. The objective should be to calibrate a model at ultra-thin scales where self-shading and mixing cycles are minimized, to obtain a precise parameter estimation unaffected by these phenomena. To this end, the peculiar behaviors found at ultra-thin optical paths call for the application of models more sophisticated than Haldane-like models (e.g., PSU models). Then, the model should be expanded by considering the effects of self-shading and mixing-induced light-dark cycles on different scales.

(ii) **Modelling of long-term dynamics for the representation of industrial systems.** Often, dynamic experiments at laboratory scales have short time scales. For instance, in Chapter 3, the model was identified through batch experiments with limited duration. On the other hand, the ability of the models to capture long-term growth dynamics is extremely important for applications in industrial cultivation systems. Thus, in the future the model developed in Chapter 3 could be tested against long-term pulsed light experiments in continuous systems to verify whether additional modifications are needed to represent photo-acclimation dynamics over longer time frames. Eventually, a recalibration of model parameters could be needed, employing the additional experiments with longer duration. This will enhance the model applicability to industrial cultivation scenarios. Additionally, equations developed in Chapter 3 should be integrated with suitable representations of light attenuation in the culture, to represent microalgae cultivation in large scale system. The dynamic reformulation procedure applied to the Camacho-Rubio model could in principle be applied to other PSUs models, to inspect whether there are differences in the capability of different PSU models to capture the short and long-term dynamics of microalgae growth under pulsed light. PSU models can describe the effect of light over

long term cultivation; however, the impact of nutrients also plays a fundamental role, as discussed in Chapter 5. Thus, the limitations of the Droop model in capturing slow uptake dynamics could be the starting point in the future for a structural modification of the Droop model itself in order to enhance the description of long-term nutrients dynamics.

(iii) **High frequency pulsed-light modelling.** In this Thesis, a preliminary exploration of the cultivation under high frequency pulsed light was made by reformulation of a model accounting for photons absorption, usage and dissipation. Indeed, model simulations of respirometry experiments suggested general operation criteria to enhance cell growth and experimental respirometry results further confirmed the model prediction. In the future, it will be paramount to verify whether the conditions found in respirometry experiments can effectively enhance biomass productivity also in steady state growth experiments. Performing additional experiments is also necessary to increase the available data for model calibration and to allow for a rigorous estimation of model parameters. Furthermore, the modelling framework should be extended to represent the dynamics of biomass growth as a consequence of variation on frequency and/or intensity of pulsed light. This could pave the way to more sophisticated strategies for model-based process control and optimisation.

(iv) **MBDoE application.** MBDoE is a powerful aid for the modelling activity and in the future it should be exploited every time a precise parameter estimation is required. Future activities will thus necessarily involve MBDoE for planning optimal high frequency pulsed light experiments. In addition, MBDoE could be applied to the design of complex dynamic experiments with multiple inputs, as light, nutrients, temperature, for the identification of growth models with multiple nutrient quotas. This is particularly relevant since, as explained in Chapter 1, there is a connection between these compartmental models and models for the synthesis of added-value compounds. Thus, by also including output measurements of pigments, proteins, lipids or carbohydrates, MBDoE could effectively support the development and application of microalgae models for the production of high value compounds.

Appendix A

A.1 Smoothness of the model equations

The model presented in Chapter 4 presents different *if* conditions. To enhance the practical implementation and usage of the model, these expressions were replaced with continuous, differentiable *switch functions* in the form proposed by Vanthoor et al. (2011):

$$S = \frac{1}{1+\exp(s_k(k-k_{switch}))} \quad \text{(A.1)}$$

where S is the value of the differentiable switch, that is bounded between 0 and 1. S is dependent on the variable k, that would also appear in the *if* condition that is replaced by Equation A.1. k_{switch} and s_k are additional parameters that define the sigmoidal function to calculate S in Equation A.1. k_{switch} is the value of k where $S = 0.5$ (i.e., the value on which the sigmoid is centred), and s_k is the slope of the curve at k_{switch}. The sign of s determines if S increases (for $s_k < 0$) or decreases (for $s_k > 0$) with k. With a generic $s_k > 0$, the model was reformulated as follows:

- Equation 4.9 was modified in:

$$N_{g,i} = N_{g,theor,i}\, S\left(N_{g,theor,i}, \frac{phot_{max}}{2}, +s_k\right) + \frac{phot_{max}}{2}\, S\left(N_{g,theor,i}, \frac{phot_{max}}{2}, -s_k\right) \quad \text{(A.2)}$$

- Equation 4.10 was modified in:

$$phot_{diss02,i} = 2\left(N_{g,theor,i} - \frac{phot_{max}}{2}\right) S\left(N_{g,theor,i}, \frac{phot_{max}}{2}, -s_k\right) \quad \text{(A.3)}$$

- Equation 4.12 was modified in:

$$n_{0,i}^{reox} = n_{0,theor,i}^{reox}\, S\left(n_{0,theor,i}^{reox}, N_{g,i} + n_{old,i}, +s_k\right) + (N_{g,i} + n_{old,i})\, S\left(n_{0,theor,i}^{reox}, N_{g,i} + n_{old,i}, -s_k\right) \quad \text{(A.4)}$$

- Equation 4.16 was modified in:

$$n_{add,i} = n_{add,theor,i}\, S\left(\tau_{pulse}, \tau_{pulse,i}^{max}, +s_k\right) + N_{pool}\, S\left(\tau_{pulse}, \tau_{pulse,i}^{max}, -s_k\right) \quad \text{(A.5)}$$

- Equation 4.17 was modified in:

$$n_{disslight,i} = \left(n_{add,theor,i} - N_{pool}\right) S\left(\tau_{pulse}, \tau_{pulse,i}^{max}, -s_k\right) \quad \text{(A.6)}$$

- Equation 4.19 was modified in:

$$n_{dark,i}^{reox} = \frac{\tau_{dark}}{\tau_{del}} S\left(\tau_{dark}, \tau_{dark,i}^{max}, + s_k\right) + n_{add,i} S\left(\tau_{dark}, \tau_{dark,i}^{max}, - s_k\right) \quad \text{(A.7)}$$

- Equation 4.20 was modified in:

$$n_{dark,i}^{reox} = \left(n_{add,i} - n_{dark,i}^{reox}\right) S\left(\tau_{dark}, \tau_{dark,i}^{max}, + s_k\right) \quad \text{(A.8)}$$

A.2 Global sensitivity analysis

Global sensitivity analysis is a numerical technique that allows full exploration of the parameters space and the study of interactions between parameters. Thus, it can provide valuable information on which has the highest impact on the model response, whether there is an interaction between parameters and if the model is practically identifiable. Here, we focus on variance-based methods that allow the calculation of sensitivity indices as main and total effects (Saltelli et al., 2008).

According to Sobol (Saltelli et al., 2008), the variance $V(y_i)$ of the *i*-th model model response y_i can be decomposed using Equation A.9:

$$V(y_i) = \sum_{j=1}^{k} V_j + \sum_{j=1}^{k} \sum_{l=j+1}^{k} V_{j,l} + \cdots + V_{1,2,\ldots,k} \quad \text{(A.9)}$$

where V_j is the first-order contribution of parameter *j* on the output variance of y_i, while second and *k*-th order interactions contribute to the total variance with $V_{j,l}$ and $V_{1,2,\ldots,k}$.

The impact of the *j*-th parameter on the model output is quantified by two metrics: the first-order effect index (S_j), denoting the direct influence of the parameter on the output, and the total effect index (S_{Tj}), comprising both the first-order effect of the parameter and higher-order interactions with all other model parameters. The sensitivity index for the first-order effect is calculated as:

$$S_j = \frac{V\left(E\left(y|\theta_j\right)\right)}{V(y)} \quad \text{(A.10)}$$

With $V(y)$ being the unconditional variance and $V\left(E\left(y|\theta_j\right)\right)$ the variance computed on the expected value of the model output when varying all parameters but θ_j.

Instead, the total effect index is calculated as:

$$S_{Tj} = \frac{E\left(V\left(y|\theta_{\sim j}\right)\right)}{V(y)} \quad \text{(A.11)}$$

with the term $E\left(V\left(y|\theta_{\sim j}\right)\right)$ that can be interpreted as the expectation of the conditional variance of the model output computed by varying the *j*-th parameter while keeping all the others fixed. More details on variance-based indexes can be found in Saltelli et al. (2008).

From a practical standpoint, the higher is the value of the main effect index, the more influential the parameter is on the model response, thus having more chances to be estimated with high precision. However, main effect indexes do not consider the impact on the response variables of the interaction between the j-th parameter and the others. Thus, total effect indices are useful since they also provide information on the interaction between parameters. For the j-th parameter, a considerable difference exists between S_j and S_{Tj}, is a signal of an important interaction with other parameters.

To analyse the practical identifiability of the mathematical model developed in Chapter 4, a global sensitivity analysis was performed on the parameters K_{cx}, a, b, c, w_{10} employing the Matlab toolbox developed in Pianosi et al. (2015). The analysis was based on the simulation scenario of Figure 4.9 due to the large range of experimental conditions analysed, and the response variable y_i has been computed as the sum of squares of the model prediction at each experimental condition. Box plots of the computed main and total effects, for each parameter are shown in Figure A.1.

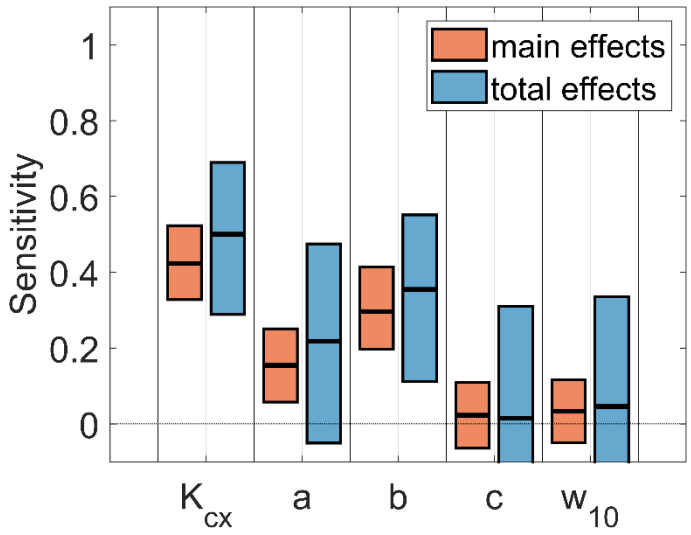

Figure A.1: *Global sensitivity indices (main and total effects) for K_{cx}, a, b, c, w_{10}.*

From the median of both main and total effects in Figure A.1, it is possible to conclude that parameters K_{cx}, b, a have the highest impact on the model prediction and, despite some interaction shown by a partial mismatch between main and total indices, are practically identifiable. On the other hand, both main and total effects of parameters c and w_{10} show that they only have a small impact on the model and thus, could have identifiability issues.

References

Aiba, S. (1982). Growth kinetics of photosynthetic microorganisms: in microbial reactions. *Adv. Biochem. Eng.*, *23*, 85–156.

Andrews, J. F. (1968). A mathematical model for the continuous culture of microorganisms utilizing inhibitory substrates. *Biotechnology and Bioengineering*, *10*(6), 707–723.

Asprey, S. P., & Naka, Y. (1999). Mathematical problems in fitting kinetic models—some new perspectives. *Journal of Chemical Engineering of Japan*, *32*(3), 328–337.

Bailey, J. E., & Ollis, D. F. (1976). Biochemical engineering fundamentals. In *Chem. Eng. Educ.*

Barbera, E., Sforza, E., Grandi, A., & Bertucco, A. (2020). Uncoupling solid and hydraulic retention time in photobioreactors for microalgae mass production: A model-based analysis. *Chemical Engineering Science*, *218*, 115578. https://doi.org/10.1016/j.ces.2020.115578

Barbera, E., Sforza, E., Guidobaldi, A., Di Carlo, A., & Bertucco, A. (2017). Integration of dye-sensitized solar cells (DSC) on photobioreactors for improved photoconversion efficiency in microalgal cultivation. *Renewable Energy*, *109*, 13–21. https://doi.org/10.1016/j.renene.2017.03.013

Barbera, E., Turetta, M., & Sforza, E. (2022). The effect of the internal nutrient quota accumulation on algal-based wastewater treatment: Decoupling HRT and SRT to improve the process. *Journal of Water Process Engineering*, *49*, 103112.

Barbosa, M. J., Janssen, M., Ham, N., Tramper, J., & Wijffels, R. H. (2003). Microalgae cultivation in air-lift reactors: Modeling biomass yield and growth rate as a function of mixing frequency. *Biotechnology and Bioengineering*, *82*(2), 170–179. https://doi.org/10.1002/bit.10563

Barbosa, M. J., Janssen, M., Südfeld, C., D'Adamo, S., & Wijffels, R. H. (2023). Hypes, hopes, and the way forward for microalgal biotechnology. *Trends in Biotechnology*, *41*(3), 452–471. https://doi.org/10.1016/j.tibtech.2022.12.017

Baroukh, C., Mairet, F., & Bernard, O. (2022). The paradoxes hidden behind the Droop model highlighted by a metabolic approach. *Frontiers in Plant Science*, *13*. https://doi.org/10.3389/fpls.2022.941230

Béchet, Q., Shilton, A., & Guieysse, B. (2013). Modeling the effects of light and temperature on algae growth: State of the art and critical assessment for productivity prediction during outdoor

cultivation. *Biotechnology Advances*, *31*(8), 1648–1663. https://doi.org/10.1016/j.biotechadv.2013.08.014

Bekirogullari, M., Figueroa-Torres, G. M., Pittman, J. K., & Theodoropoulos, C. (2020). Models of microalgal cultivation for added-value products - A review. *Biotechnology Advances*, *44*(August), 107609. https://doi.org/10.1016/j.biotechadv.2020.107609

Benavides, M., Telen, D., Lauwers, J., Logist, F., van Impe, J., & Wouwer, A. vande. (2015). Parameter Identification of the Droop Model using Optimal Experiment Design. *IFAC-PapersOnLine*, *48*(1), 586–591. https://doi.org/https://doi.org/10.1016/j.ifacol.2015.05.094

Bernard, O. (2011). Hurdles and challenges for modelling and control of microalgae for CO 2 mitigation and biofuel production. *Journal of Process Control*, *21*(10), 1378–1389. https://doi.org/10.1016/j.jprocont.2011.07.012

Bernard, O., & Lu, L. Di. (2022). Optimal optical conditions for Microalgal production in photobioreactors. *Journal of Process Control*, *112*, 69–77. https://doi.org/10.1016/j.jprocont.2022.03.001

Bernard, O., Mairet, F., & Chachuat, B. (2016). Modelling of Microalgae Culture Systems with Applications to Control and Optimization. *Adv. Biochem. Eng. Biotechnol.*, *153*, 59–87.

Bernard, O., & Rémond, B. (2012). Validation of a simple model accounting for light and temperature effect on microalgal growth. *Bioresource Technology*, *123*, 520–527. https://doi.org/10.1016/j.biortech.2012.07.022

Bernardi, A., Nikolaou, A., Meneghesso, A., Morosinotto, T., Chachuat, B., & Bezzo, F. (2016). High-fidelity modelling methodology of light-limited photosynthetic production in microalgae. *PLoS ONE*, *11*(4), 10–11. https://doi.org/10.1371/journal.pone.0156922

Bernardi, A., Nikolaou, A., Meneghesso, A., Morosinottoc, T., Chachuat, B., & Bezzo, F. (2015). Using fluorescence measurements to model key phenomena in microalgae photosynthetic mechanisms. *Chemical Engineering Transactions*, *43*, 217–222. https://doi.org/10.3303/CET1543037

Bernardi, A., Perin, G., Sforza, E., Galvanin, F., Morosinotto, T., & Bezzo, F. (2014). An identifiable state model to describe light intensity influence on microalgae growth. *Industrial and Engineering Chemistry Research*, *53*(16), 6738–6749. https://doi.org/10.1021/ie500523z

Blankenship, R. E., Tiede, D. M., Barber, J., Brudvig, G. W., Fleming, G., Ghirardi, M., Gunner, M. R., Junge, W., Kramer, D. M., Melis, A., Moore, T. A., Moser, C. C., Nocera, D. G., Nozik, A. J., Ort, D. R., Parson, W. W., Prince, R. C., & Sayre, R. T. (2011). Comparing photosynthetic

and photovoltaic efficiencies and recognizing the potential for improvement. In *Science* (Vol. 332, Issue 6031). https://doi.org/10.1126/science.1200165

Borella, L., Diotto, D., Barbera, E., Fiorimonte, D., Sforza, E., & Trivellin, N. (2022). Application of flashing blue-red LED to boost microalgae biomass productivity and energy efficiency in continuous photobioreactors. *Energy*, *259*(June), 125087. https://doi.org/10.1016/j.energy.2022.125087

Borella, L., Ortolan, D., Barbera, E., Trivellin, N., & Sforza, E. (2021). A multiwavelength model to improve microalgal productivity and energetic conversion in a red-blue light emitting diodes (LEDs) continuous photobioreactor. *Energy Conversion and Management*, *243*, 114330. https://doi.org/10.1016/j.enconman.2021.114330

Borella, L., Sforza, E., & Bertucco, A. (2021). Effect of residence time in continuous photobioreactor on mass and energy balance of microalgal protein production. *New Biotechnology*, *64*(May), 46–53. https://doi.org/10.1016/j.nbt.2021.05.006

Borovkov, A. B. A. B., Gudvilovich, I. N. I. N., Lelekov, A. S. A. S., & Avsiyan, A. L. A. L. (2023). Effect of specific irradiance on productivity and pigment and protein production of Porphyridium purpureum (Rhodophyta) semi-continuous culture. *Bioresource Technology*, *374*(January), 128771. https://doi.org/10.1016/j.biortech.2023.128771

Borowitzka, M. A. (1995). Microalgae as sources of pharmaceuticals and other biologically active compounds. *Journal of Applied Phycology*, *7*(1). https://doi.org/10.1007/BF00003544

Brindley, C., Acién Fernández, F. G., & Fernández-Sevilla, J. M. (2011). Analysis of light regime in continuous light distributions in photobioreactors. *Bioresource Technology*, *102*(3), 3138–3148. https://doi.org/10.1016/j.biortech.2010.10.088

Brindley, C., Jiménez-Ruíz, N., Acién, F. G., & Fernández-Sevilla, J. M. (2016). Light regime optimization in photobioreactors using a dynamic photosynthesis model. *Algal Research*, *16*, 399–408. https://doi.org/10.1016/j.algal.2016.03.033

Busnel, A., Samhat, K., Gérard, E., Kazbar, A., Marec, H., Dechandol, E., Le Gouic, B., Hauser, J.-L., & Pruvost, J. (2021). Development and validation of a screening system for characterizing and modeling biomass production from cyanobacteria and microalgae: Application to Arthrospira platensis and Haematococcus pluvialis. *Algal Research*, *58*(May), 102386. https://doi.org/10.1016/j.algal.2021.102386

Camacho, J., Picó, J., & Ferrer, A. (2008). Bilinear modelling of batch processes. Part I: Theoretical discussion. *Journal of Chemometrics*, *22*(5), 299–308. https://doi.org/10.1002/cem.1113

Camacho Rubio, F., García Camacho, F., Fernández Sevilla, J. M., Chisti, Y., & Molina Grima, E. (2003). A mechanistic model of photosynthesis in microalgae. *Biotechnology and Bioengineering*, *81*(4), 459–473. https://doi.org/10.1002/bit.10492

Caperon, J., & Meyer, J. (1972a). Nitrogen-limited growth of marine phytoplankton—I. Changes in population characteristics with steady-state growth rate. *Deep Sea Res. Oceanogr. Abstr.*, *19*, 601–618.

Caperon, J., & Meyer, J. (1972b). Nitrogen-limited growth of marine phytoplankton—II. Uptake kinetics and their role in nutrient limited growth of phytoplankton. *Deep Sea Res. Oceanogr. Abstr.*, *10*, 619–632.

Castaldello, C., Sforza, E., Cimetta, E., Morosinotto, T., & Bezzo, F. (2019). Microfluidic Platform for Microalgae Cultivation under Non-limiting CO2 Conditions. *Industrial and Engineering Chemistry Research*, *58*(39), 18036–18045. https://doi.org/10.1021/acs.iecr.9b02888

Chalker, B. E. (1980). Modeling light saturation curves for photosynthesis: An exponential function. *Journal of Theoretical Biology*, *84*(2). https://doi.org/10.1016/S0022-5193(80)80004-X

Chiang, L. H., Russell, E. L., & Braatz, R. D. (2001). *Fault Detection and Diagnosis in Industrial Systems* (1st ed.). Springer London.

Chioccioli, M., Hankamer, B., & Ross, I. L. (2014). Flow cytometry pulse width data enables rapid and sensitive estimation of biomass dry weight in the microalgae Chlamydomonas reinhardtii and Chlorella vulgaris. *PLoS ONE*, *9*(5), 1–12. https://doi.org/10.1371/journal.pone.0097269

Cirulis, J. T., Scott, J. A., & Ross, G. M. (2013). Management of oxidative stress by microalgae. *Canadian Journal of Physiology and Pharmacology*, *91*(1), 15–21.

Cogne, G., Gros, J. B., & Dussap, C. G. (2003). Identification of a Metabolic Network Structure Representative of Arthrospira (Spirulina) platensis Metabolism. *Biotechnology and Bioengineering*, *84*(6), 667–676. https://doi.org/10.1002/bit.10808

Cogne, G., Rügen, M., Bockmayr, A., Titica, M., Dussap, C. G., Cornet, J. F., & Legrand, J. (2011). A model-based method for investigating bioenergetic processes in autotrophically growing eukaryotic microalgae: Application to the green algae Chlamydomonas reinhardtii. *Biotechnology Progress*, *27*(3), 631–640. https://doi.org/10.1002/btpr.596

Combe, C., Hartmann, P., Rabouille, S., Talec, A., Bernard, O., & Sciandra, A. (2015). Long-term adaptive response to high-frequency light signals in the unicellular photosynthetic eukaryote Dunaliella salina. *Biotechnology and Bioengineering*, *112*(6), 1111–1121. https://doi.org/10.1002/bit.25526

Concas, A., Pisu, M., & Cao, G. (2016). A novel mathematical model to simulate the size-structured growth of microalgae strains dividing by multiple fission. *Chemical Engineering Journal*, *287*, 252–268. https://doi.org/10.1016/j.cej.2015.11.021

Cornet, J. F., & Dussap, C. G. (2009). A simple and reliable formula for assessment of maximum volumetric productivities in photobioreactors. *Biotechnology Progress*, *25*(2), 424–435. https://doi.org/10.1002/btpr.138

Cornet, J. F., Dussap, C. G., Cluzel, P., & Dubertret, G. (1992). A structured model for simulation of cultures of the cyanobacterium Spirulina platensis in photobioreactors: II. Identification of kinetic parameters under light and mineral limitations. *Biotechnology and Bioengineering*, *40*(7). https://doi.org/10.1002/bit.260400710

Cornet, J. F., Dussap, C. G., & Gros, J. B. (1994). Conversion of radiant light energy in photobioreactors. *AIChE Journal*, *40*(6). https://doi.org/10.1002/aic.690400616

Cornet, J. F., Dussap, C. G., & Gros, J. B. (1998). Kinetics and energetics of photosynthetic micro-organisms in photobioreactors. *Bioprocess and Algae Reactor Technology, Apoptosis*, *59*, 153–224. https://doi.org/10.1007/bfb0102299

Cornet, J. F., Favier, L., & Dussap, C. G. (2003). Modeling stability of photoheterotrophic continuous cultures in photobioreactors. *Biotechnology Progress*, *19*(4), 1216–1227. https://doi.org/10.1021/bp0340411

Costache, T. A., Gabriel Acien Fernandez, F., Morales, M. M., Fernández-Sevilla, J. M., Stamatin, I., & Molina, E. (2013). Comprehensive model of microalgae photosynthesis rate as a function of culture conditions in photobioreactors. *Applied Microbiology and Biotechnology*, *97*(17), 7627–7637. https://doi.org/10.1007/s00253-013-5035-2

Cullen, J. J. (1990). On models of growth and photosynthesis in phytoplankton. *Deep Sea Research Part A, Oceanographic Research Papers*, *37*(4). https://doi.org/10.1016/0198-0149(90)90097-F

Darvehei, P., Bahri, P. A., & Moheimani, N. R. (2018). Model development for the growth of microalgae: A review. *Renewable and Sustainable Energy Reviews*, *97*(July), 233–258. https://doi.org/10.1016/j.rser.2018.08.027

Dauchet, J., Cornet, J. F., Gros, F., Roudet, M., & Dussap, C. G. (2016). Photobioreactor Modeling and Radiative Transfer Analysis for Engineering Purposes. *Advances in Chemical Engineering*, *48*, 1–106. https://doi.org/10.1016/bs.ache.2015.11.003

De-Luca, R., Bano, G., Tomba, E., Bezzo, F., & Barolo, M. (2020). Accelerating the Development and Transfer of Freeze-Drying Operations for the Manufacturing of Biopharmaceuticals by

Model-Based Design of Experiments. *Industrial & Engineering Chemistry Research*, *59*(45), 20071–20085. https://doi.org/10.1021/acs.iecr.0c03115

Dermoun, D., Chaumont, D., Thebault, J.-M., & Dauta, A. (1992). Modelling of growth of Porphyridium cruentum in connection with two interdependent factors: Light and temperature. *Bioresource Technology*, *42*(2), 113–117.

Deschênes, J.-S., & Wouwer, A. vande. (2016). Parameter identification of a dynamic model of cultures of microalgae scenedesmus obliquus-an experimental study. *IFAC-PapersOnLine*, *49*(7), 1050–1055.

Diotto, D., Barbera, E., Borella, L., Trivellin, N., & Sforza, E. (2022). Modeling Approach to Capture the Effect of High Frequency Flashing Light in Steady-State Microalgae Cultures. *Industrial and Engineering Chemistry Research*, *61*(50), 18258–18269. https://doi.org/10.1021/acs.iecr.2c03258

Droop, M. R. (1968). Vitamin B12 and Marine Ecology. IV. The Kinetics of Uptake, Growth and Inhibition in Monochrysis Lutheri. *Journal of the Marine Biological Association of the United Kingdom*, *48*(3), 689–733.

Duffie, J. A., Beckman, W. A., & Blair, N. (2020). Solar engineering of thermal processes, photovoltaics and wind. In *American Journal of Physics* (Vol. 53, Issue 4). John Wiley & Sons, Inc.

Eilers, P. H. C., & Peeters, J. C. H. (1988). A model for the relationship between light intensity and the rate of photosynthesis in phytoplankton. *Ecological Modelling*, *42*(3–4), 199–215. https://doi.org/10.1016/0304-3800(88)90057-9

Enes, I., & Saraiva, P. (1996). Optimization of operating strategies in β-carotene microalgae bioreactors. *Computers and Chemical Engineering*, *20*(SUPPL.1). https://doi.org/10.1016/0098-1354(96)00094-4

Fachet, M., Flassig, R. J., Rihko-Struckmann, L. K., & Sundmacher, K. (2017). Carotenoid Production Process Using Green Microalgae of the Dunaliella Genus: Model-Based Analysis of Interspecies Variability. *Industrial and Engineering Chemistry Research*, *56*(45), 12888–12898. https://doi.org/10.1021/acs.iecr.7b01423

Fernández, I., Acién, F. G., Fernández, J. M., Guzmán, J. L., Magán, J. J., & Berenguel, M. (2012). Dynamic model of microalgal production in tubular photobioreactors. *Bioresource Technology*, *126*, 172–181. https://doi.org/10.1016/j.biortech.2012.08.087

Filali, R., Tebbani, S., Dumur, D., Isambert, A., Pareau, D., & Lopes, F. (2011). Growth modeling of the green microalga Chlorella vulgaris in an air-lift photobioreactor. *IFAC Proceedings Volumes (IFAC-PapersOnline)*, *44*(1 PART 1). https://doi.org/10.3182/20110828-6-IT-1002.01955

Fleck-Schneider, P., Lehr, F., & Posten, C. (2007). Modelling of growth and product formation of Porphyridium purpureum. *Journal of Biotechnology*, *132*(2), 134–141. https://doi.org/10.1016/j.jbiotec.2007.05.030

Fleitmann, L., Pyschik, J., Wolff, L., Schilling, J., & Bardow, A. (2022). Optimal experimental design of physical property measurements for optimal chemical process simulations. *Fluid Phase Equilibria*, *557*, 113420.

Flynn, K. J. (2002). How critical is the critical N:P ratio? *J. Phycol.*, *56*(2), 249–279.

Flynn, K. J. (2020). *Enhancing Microalgal Production*.

Flynn, K. J., Marshall, H., & Geider, R. J. (2001). A comparison of two N-irradiance interaction models of phytoplankton growth. *Limnology and Oceanography*, *46*(7), 1794–1802. https://doi.org/10.4319/lo.2001.46.7.1794

Franceschini, G., & Macchietto, S. (2008). Model-based design of experiments for parameter precision: State of the art. *Chemical Engineering Science*, *63*(19), 4846–4872. https://doi.org/10.1016/J.CES.2007.11.034

Fu, W., Guomundsson, Ó., Paglia, G., Herjólfsson, G., Andrésson, Ó. S., Palsson, B. O., & Brynjólfsson, S. (2013). Enhancement of carotenoid biosynthesis in the green microalga Dunaliella salina with light-emitting diodes and adaptive laboratory evolution. *Applied Microbiology and Biotechnology*, *97*(6), 2395–2403. https://doi.org/10.1007/s00253-012-4502-5

Fuente, D., Keller, J., Conejero, J. A., Rögner, M., Rexroth, S., & Urchueguía, J. F. (2017). Light distribution and spectral composition within cultures of micro-algae: Quantitative modelling of the light field in photobioreactors. *Algal Research*, *23*, 166–177. https://doi.org/10.1016/j.algal.2017.01.004

García, J. L., de Vicente, M., & Galán, B. (2017). Microalgae, old sustainable food and fashion nutraceuticals. In *Microbial Biotechnology* (Vol. 10, Issue 5). https://doi.org/10.1111/1751-7915.12800

García-Camacho, F., Sánchez-Mirón, A., Molina-Grima, E., Camacho-Rubio, F., & Merchuck, J. C. (2012). A mechanistic model of photosynthesis in microalgae including photoacclimation dynamics. *Journal of Theoretical Biology*, *304*, 1–15. https://doi.org/10.1016/j.jtbi.2012.03.021

García-Malea, M. C., Acién, F. G., Fernández, J. M., Cerón, M. C., & Molina, E. (2006). Continuous production of green cells of Haematococcus pluvialis: Modeling of the irradiance effect. *Enzyme and Microbial Technology*, *38*(7). https://doi.org/10.1016/j.enzmictec.2005.08.031

Geider, R. J., MacIntyre, H. L., & Kana, T. M. (1996). A dynamic model of photoadaptation in phytoplankton. *Limnology and Oceanography*, *41*(1), 1–15. https://doi.org/10.4319/lo.1996.41.1.0001

Geider, R. J., MacIntyre, H. L., & Kana, T. M. (1997). Dynamic model of phytoplankton growth and acclimation: Responses of the balanced growth rate and the chlorophyll a:carbon ratio to light, nutrient-limitation and temperature. *Marine Ecology Progress Series*, *148*(1–3), 187–200. https://doi.org/10.3354/meps148187

Geider, R. J., MacIntyre, H. L., & Kana, T. M. (1998). A dynamic regulatory model of phytoplanktonic acclimation to light, nutrients, and temperature. *Limnology and Oceanography*, *43*(4), 679–694. https://doi.org/10.4319/lo.1998.43.4.0679

Geladi, P., & Kowalski, B. R. (1986). Partial least-squares regression: a tutorial. *Anal. Chim. Acta*, *185*, 1–17.

Gojkovic, Z., Lu, Y., Ferro, L., Toffolo, A., & Funk, C. (2020). Modeling biomass production during progressive nitrogen starvation by North Swedish green microalgae. *Algal Research*, *47*, 101835.

Gonçalves, A. L., Pires, J. C. M., & Simões, M. (2017). A review on the use of microalgal consortia for wastewater treatment. In *Algal Research* (Vol. 24). https://doi.org/10.1016/j.algal.2016.11.008

Gorman, D. S., & Levine, R. P. (1965). Cytochrome f and plastocyanin: their sequence in the photosynthetic electron transport chain of Chlamydomonas reinhardi. *Proceedings of the National Academy of Sciences of the United States of America*, *54*(6), 1665–1669. https://doi.org/10.1073/pnas.54.6.1665

Graham, P. J., Riordon, J., & Sinton, D. (2015). Microalgae on display: a microfluidic pixel-based irradiance assay for photosynthetic growth. *Lab on a Chip*, *15*(15), 3116–3124. https://doi.org/10.1039/c5lc00527b

Grivalský, T., Ranglová, K., da Câmara Manoel, J. A., Lakatos, G. E., Lhotský, R., & Masojídek, J. (2019). Development of thin-layer cascades for microalgae cultivation: milestones (review). *Folia Microbiologica*, *64*(5), 603–614. https://doi.org/10.1007/s12223-019-00739-7

Hamed, I. (2016). The Evolution and Versatility of Microalgal Biotechnology: A Review. *Comprehensive Reviews in Food Science and Food Safety*, *15*(6). https://doi.org/10.1111/1541-4337.12227

Han, B. P. (2002). A mechanistic model of algal photoinhibition induced by photodamage to photosystem-II. *Journal of Theoretical Biology*, *214*(4), 519–527. https://doi.org/10.1006/jtbi.2001.2468

Hempel, F., Bozarth, A. S., Lindenkamp, N., Klingl, A., Zauner, S., Linne, U., Steinbüchel, A., & Maier, U. G. (2011). Microalgae as bioreactors for bioplastic production. *Microbial Cell Factories*, *10*. https://doi.org/10.1186/1475-2859-10-81

Houf, W. G., & Incropera, F. P. (1980). An assessment of techniques for predicting radiation transfer in aqueous media. *Journal of Quantitative Spectroscopy and Radiative Transfer*, *23*(1). https://doi.org/10.1016/S0022-4073(80)80009-4

Hu, J. Y., & Sato, T. (2017). A photobioreactor for microalgae cultivation with internal illumination considering flashing light effect and optimized light-source arrangement. *Energy Conversion and Management*, *133*, 558–565. https://doi.org/10.1016/j.enconman.2016.11.008

Jayaraman, S. K., & Rhinehart, R. R. (2015). Modeling and optimization of algae growth. *Industrial and Engineering Chemistry Research*, *54*(33). https://doi.org/10.1021/acs.iecr.5b01635

Karam, A. L., Lai, Y. C., de los Reyes, F. L., & Ducoste, J. J. (2021). Chlorophyll a and non-pigmented biomass are sufficient predictors for estimating light attenuation during cultivation of Dunaliella viridis. *Algal Research*, *55*(September 2020), 102283. https://doi.org/10.1016/j.algal.2021.102283

Khan, M. I., Shin, J. H., & Kim, J. D. (2018). The promising future of microalgae: Current status, challenges, and optimization of a sustainable and renewable industry for biofuels, feed, and other products. *Microbial Cell Factories*, *17*(1), 1–21. https://doi.org/10.1186/s12934-018-0879-x

Khichi, S. S., Rohith, S., Gehlot, K., Dutta, B. C., & Ghosh, S. (2019). Online estimation of biomass, lipid and nitrate dynamic profile using innovative light evolution kinetic model in flat panel airlift photobioreactor for Botryococcus braunii under varying light conditions. *Bioresource Technology Reports*, *6*(November 2018), 6–14. https://doi.org/10.1016/j.biteb.2019.01.023

Kim, H. S., Devarenne, T. P., & Han, A. (2018). Microfluidic systems for microalgal biotechnology: A review. *Algal Research*, *30*(November 2017), 149–161. https://doi.org/10.1016/j.algal.2017.11.020

Kroon, B. M. A., & Thoms, S. (2006). From electron to biomass: A mechanistic model to describe phytoplankton photosynthesis and steady-state growth rates. *Journal of Phycology*, *42*(3), 593–609. https://doi.org/10.1111/j.1529-8817.2006.00221.x

Kumar, M., Sun, Y., Rathour, R., Pandey, A., Thakur, I. S., & Tsang, D. C. W. (2020). Algae as potential feedstock for the production of biofuels and value-added products: Opportunities and challenges. In *Science of the Total Environment* (Vol. 716). Elsevier B.V. https://doi.org/10.1016/j.scitotenv.2020.137116

Kumar, V., Sharma, N., Jaiswal, K. K., Vlaskin, M. S., Nanda, M., Tripathi, M. K., & Kumar, S. (2021). Microalgae with a truncated light-harvesting antenna to maximize photosynthetic efficiency and biomass productivity: Recent advances and current challenges. *Process Biochemistry*, *104*(September 2020), 83–91. https://doi.org/10.1016/j.procbio.2021.03.006

Lee, E., Jalalizadeh, M., & Zhang, Q. (2015). Growth kinetic models for microalgae cultivation: A review. *Algal Research*, *12*, 497–512. https://doi.org/10.1016/j.algal.2015.10.004

Lee, H. Y., Erickson, L. E., & Yang, S. S. (1987). Kinetics and bioenergetics of light-limited photoautotrophic growth of Spirulina Platensis. *Biotechnology and Bioengineering*, *29*(7), 832–843.

Legrand, J., Artu, A., & Pruvost, J. (2021). A review on photobioreactor design and modelling for microalgae production. *Reaction Chemistry and Engineering*, *6*(7), 1134–1151. https://doi.org/10.1039/d0re00450b

Lehman, J. T., Botkin, D. B., & Likens, G. E. (1975). The assumptions and rationales of a computer model of phytoplankton population dynamics 1. *Limnology and Oceanography*, *20*(3), 343–364.

Lehmuskero, A., Skogen Chauton, M., & Boström, T. (2018). Light and photosynthetic microalgae: A review of cellular- and molecular-scale optical processes. *Progress in Oceanography*, *168*(August), 43–56. https://doi.org/10.1016/j.pocean.2018.09.002

Leong, W. H., Kiatkittipong, W., Lam, M. K., Khoo, K. S., Show, P. L., Mohamad, M., Chong, S., Abdurrahman, M., & Lim, J. W. (2022). Dual nutrient heterogeneity modes in a continuous flow photobioreactor for optimum nitrogen assimilation to produce microalgal biodiesel. *Renewable Energy*, *184*, 443–451. https://doi.org/https://doi.org/10.1016/j.renene.2021.11.117

Leong, W. H., Lim, J. W., Lam, M. K., Lam, S. M., Sin, J. C., & Samson, A. (2021). Novel sequential flow baffled microalgal-bacterial photobioreactor for enhancing nitrogen assimilation into microalgal biomass whilst bioremediating nutrient-rich wastewater simultaneously. *Journal of Hazardous Materials*, *409*, 124455. https://doi.org/https://doi.org/10.1016/j.jhazmat.2020.124455

Levasseur, W., Perré, P., & Pozzobon, V. (2020). A review of high value-added molecules production by microalgae in light of the classification. *Biotechnology Advances*, *41*(April), 107545. https://doi.org/10.1016/j.biotechadv.2020.107545

Luke, C. S., Selimkhanov, J., Baumgart, L., Cohen, S. E., Susan, S., Cookson, N. A., & Hasty, J. (2017). *dynamic environment*. *5*(1), 8–14. https://doi.org/10.1021/acssynbio.5b00094.A

Luzi, G., & McHardy, C. (2022). Modeling and Simulation of Photobioreactors with Computational Fluid Dynamics—A Comprehensive Review. *Energies*, *15*(11), 1–63. https://doi.org/10.3390/en15113966

Mairet, F., Bernard, O., Masci, P., Lacour, T., & Sciandra, A. (2011). Modelling neutral lipid production by the microalga Isochrysis aff. galbana under nitrogen limitation. *Bioresource Technology*, *102*(1), 142–149. https://doi.org/10.1016/j.biortech.2010.06.138

Markou, G., Vandamme, D., & Muylaert, K. (2014). Microalgal and cyanobacterial cultivation: The supply of nutrients. *Water Research*, *65*, 186–202.

Marshall, H. L., Geider, R. J., & Flynn, K. J. (2000). A mechanistic model of photoinhibition. *New Phytologist*, *145*(2), 347–359. https://doi.org/10.1046/j.1469-8137.2000.00575.x

Martínez, M. E., Camacho, F., Jimenez, J., & Espinola, J. (1997). Influence of light intensity on the kinetic and yield parameters of Chlorella pyrenoidosa mixotrophic growth. *Process Biochemistry*, *32*, 93–98.

Martínez Sancho, M., Jimenez Castillo, J., & El Yousfi, F. (1997). Influence of phosphorus concentration on the growth kinetics and stoichiometry of the microalga Scenedesmus obliquus. *Process Biochemistry*, *32*(8), 657–664.

Martín-Girela, I., Curt, M. D., & Fernández, J. (2017). Flashing light effects on CO2 absorption by microalgae grown on a biofilm photobioreactor. *Algal Research*, *25*(January), 421–430. https://doi.org/10.1016/j.algal.2017.06.008

Mata, T. M., Martins, A. A., & Caetano, N. S. (2010). Microalgae for biodiesel production and other applications: A review. *Renewable and Sustainable Energy Reviews*, *14*(1), 217–232. https://doi.org/10.1016/j.rser.2009.07.020

Mayers, J. J., Flynn, K. J., & Shields, R. J. (2014). Influence of the N: P supply ratio on biomass productivity and time-resolved changes in elemental and bulk biochemical composition of Nannochloropsis sp. *Bioresource Technology*, *169*, 588–595.

Milledge, J. J. (2011). Commercial application of microalgae other than as biofuels: A brief review. In *Reviews in Environmental Science and Biotechnology* (Vol. 10, Issue 1). https://doi.org/10.1007/s11157-010-9214-7

Miyachi, S., Izawa, S., & Tamiya, H. (1955). Effect of oxygen on the capacity of carbon dioxide-fixation by green algae. *Journal of Biochemistry*, *42*(3). https://doi.org/10.1093/oxfordjournals.jbchem.a126526

Molina Grima, E., Fernández Sevilla, J. M., Sánchez Pérez, J. A., & García Camacho, F. (1996). A study on simultaneous photolimitation and photoinhibition in dense microalgal cultures taking into account incident and averaged irradiances. *Journal of Biotechnology*, *45*(1), 59–69. https://doi.org/10.1016/0168-1656(95)00144-1

Monod, J. (1949). The growth of bacterial cultures. *Annu. Rev. Microbiol.*, *3*(1), 371–394.

Muller-Feuga, A. (1999). Growth as a function of rationing: A model applicable to fish and microalgae. *Journal of Experimental Marine Biology and Ecology*, *236*(1), 1–13. https://doi.org/10.1016/S0022-0981(98)00194-4

Muñoz-Tamayo, R., Martinon, P., Bougaran, G., Mairet, F., & Bernard, O. (2014). Getting the most out of it: Optimal experiments for parameter estimation of microalgae growth models. *Journal of Process Control*, *24*(6), 991–1001. https://doi.org/https://doi.org/10.1016/j.jprocont.2014.04.021

Nicholls, David. G., & Ferguson, Stuart. J. (1992). *Bioenergetics 2*. Academic Press.

Nikolaou, A., Bernardi, A., Meneghesso, A., Bezzo, F., Morosinotto, T., & Chachuat, B. (2015). A model of chlorophyll fluorescence in microalgae integrating photoproduction, photoinhibition and photoregulation. *Journal of Biotechnology*, *194*, 91–99. https://doi.org/10.1016/j.jbiotec.2014.12.001

Nikolaou, A., Hartmann, P., Sciandra, A., Chachuat, B., & Bernard, O. (2016). Dynamic coupling of photoacclimation and photoinhibition in a model of microalgae growth. *Journal of Theoretical Biology*, *390*, 61–72. https://doi.org/10.1016/j.jtbi.2015.11.004

Nomikos, P., & MacGregor, J. F. (1995). Multi-way partial least squares in monitoring batch processes. *Chemometrics and Intelligent Laboratory Systems*, *30*(1), 97–108. https://doi.org/10.1016/0169-7439(95)00043-7

Packer, A., Li, Y., Andersen, T., Hu, Q., Kuang, Y., & Sommerfeld, M. (2011). Growth and neutral lipid synthesis in green microalgae: A mathematical model. *Bioresource Technology*, *102*(1), 111–117. https://doi.org/10.1016/j.biortech.2010.06.029

Papadakis, I. A., Kotzabasis, K., & Lika, K. (2012). Modeling the dynamic modulation of light energy in photosynthetic algae. *Journal of Theoretical Biology*, *300*, 254–264. https://doi.org/10.1016/j.jtbi.2012.01.040

Park, K. H., & Lee, C. G. (2000). Optimization of algal photobioreactors using flashing lights. *Biotechnology and Bioprocess Engineering*, *5*(3), 186–190. https://doi.org/10.1007/BF02936592

Pastore, M., Barbera, E., Panichi, A., & Sforza, E. (2020). Application of photorespirometry to unravel algal kinetic parameters of nitrogen consumption in complex media. *Algal Research*, *47*(February), 101837. https://doi.org/10.1016/j.algal.2020.101837

Peng, L., Fu, D., Chu, H., Wang, Z., & Qi, H. (2020). Biofuel production from microalgae: a review. *Environmental Chemistry Letters*, *18*(2), 285–297. https://doi.org/10.1007/s10311-019-00939-0

Perin, G., Bernardi, A., Bellan, A., Bezzo, F., & Morosinotto, T. (2017). A mathematical model to guide genetic engineering of photosynthetic metabolism. *Metabolic Engineering*, *44*(October), 337–347. https://doi.org/10.1016/j.ymben.2017.11.002

Perin, G., Cimetta, E., Monetti, F., Morosinotto, T., & Bezzo, F. (2016). Novel micro-photobioreactor design and monitoring method for assessing microalgae response to light intensity. *Algal Research*, *19*, 69–76. https://doi.org/10.1016/j.algal.2016.07.015

Pfaffinger, C. E., Severin, T. S., Apel, A. C., Göbel, J., Sauter, J., & Weuster-Botz, D. (2019). Light-dependent growth kinetics enable scale-up of well-mixed phototrophic bioprocesses in different types of photobioreactors. *Journal of Biotechnology*, *297*(January), 41–48. https://doi.org/10.1016/j.jbiotec.2019.03.003

Pianosi, F., Sarrazin, F., and Wagener, T. (2015). A Matlab toolbox for Global Sensitivity Analysis. *Environ. Model. Softw.* 70, 80–85. doi: 10.1016/j.envsoft.2015.04.009.

Polimene, L., Brunet, C., Allen, J. I., Butenschön, M., White, D. A., & Llewellyn, C. A. (2012). Modelling xanthophyll photoprotective activity in phytoplankton. *Journal of Plankton Research*, *34*(3), 196–207. https://doi.org/10.1093/plankt/fbr102

Porcelli, A. (2023). *Effetto del tempo di buio e del cammino ottico sulla coltivazione in continuo di Arthrospira maxima in regime di luce pulsata*. University of Padova.

Pottier, L., Pruvost, J., Deremetz, J., Cornet, J. F., Legrand, J., & Dussap, C. G. (2005). A fully predictive model for one-dimensional light attenuation by Chlamydomonas reinhardtii in a torus photobioreactor. *Biotechnology and Bioengineering*, *91*(5), 569–582. https://doi.org/10.1002/bit.20475

Pruvost, J., & Cornet, J.-F. (2012). *Knowledge models for the engineering and optimization of photobioreactors* (C. Posten & C. Walter, Eds.). De Gruyter.

Qiang, H., Richmond, A., & Zarmi, Y. (1998). Combined effects of light intensity, light-path and culture density on output rate of spirulina platensis (cyanobacteria). *European Journal of Phycology*, *33*(2), 165–171. https://doi.org/10.1080/09670269810001736663

Quinn, J. C., & Davis, R. (2015). The potentials and challenges of algae based biofuels: A review of the techno-economic, life cycle, and resource assessment modeling. *Bioresource Technology*, *184*. https://doi.org/10.1016/j.biortech.2014.10.075

Rahman, K. M. (2020). Food and high value products from microalgae: Market opportunities and challenges. In *Microalgae Biotechnology for Food, Health and High Value Products*. https://doi.org/10.1007/978-981-15-0169-2_1

Ratkowsky, D. A., Lowry, R. K., McMeekin, T. A., Stokes, A. N., & Chandler, R. E. (1983). Model for bacterial culture growth rate throughout the entire biokinetic temperature range. *Journal of Bacteriology*, *154*(3). https://doi.org/10.1128/jb.154.3.1222-1226.1983

Ratkowsky, D. A., Olley, J., McMeekin, T. A., & Ball, A. (1982). Relationship between temperature and growth rate of bacterial cultures. *Journal of Bacteriology*, *149*(1). https://doi.org/10.1128/jb.149.1.1-5.1982

Razzak, S. A., Hossain, M. M., Lucky, R. A., Bassi, A. S., & De Lasa, H. (2013). Integrated CO2 capture, wastewater treatment and biofuel production by microalgae culturing - A review. In *Renewable and Sustainable Energy Reviews* (Vol. 27). https://doi.org/10.1016/j.rser.2013.05.063

Richmond, A. (1996). Efficient utilization of high irradiance for production of photoautotropic cell mass: A survey. *Journal of Applied Phycology*, *8*(4–5), 381–387. https://doi.org/10.1007/BF02178581

Richmond, A., Cheng-Wu, Z., & Zarmi, Y. (2003). Efficient use of strong light for high photosynthetic productivity: Interrelationships between the optical path, the optimal population density and cell-growth inhibition. *Biomolecular Engineering*, *20*(4–6), 229–236. https://doi.org/10.1016/S1389-0344(03)00060-1

Ringsmuth, A. K., Landsberg, M. J., & Hankamer, B. (2016). Can photosynthesis enable a global transition from fossil fuels to solar fuels, to mitigate climate change and fuel-supply limitations? *Renewable and Sustainable Energy Reviews*, *62*, 134–163. https://doi.org/10.1016/j.rser.2016.04.016

Rio-Chanona, E. A. del, Ahmed, N. rashid, Zhang, D., Lu, Y., & Jing, K. (2017). Kinetic Modeling and Process Analysis for Desmodesmus sp. Lutein Photo-Production. *AIChE Journal*, *63*(7), 2546–2554. https://doi.org/10.1002/aic

Rippka, R., Deruelles, J., Waterbury, J. B., Herdman, M., & Stanier, R. Y. (1979). Generic assignments, strain histories and properties of pure cultures of cyanobacteria. *Microbiology*, *111*(1), 1–61.

Rizwan, M., Mujtaba, G., Memon, S. A., Lee, K., & Rashid, N. (2018). Exploring the potential of microalgae for new biotechnology applications and beyond: A review. *Renewable and Sustainable Energy Reviews*, *92*(March 2017), 394–404. https://doi.org/10.1016/j.rser.2018.04.034

Ross, O. N., & Geider, R. J. (2009). New cell-based model of photosynthesis and photo-acclimation: accumulation and mobilisation of energy reserves in phytoplankton. *Marine Ecology Progress Series*, *383*, 53–71. https://doi.org/10.3354/meps07961

Rosso, L., Lobry, J., & Flandrois, J. (1991). A FORTRAN subroutine for the determination of parameter confidence limits in non-linear models. *Binary*, *3*(25), 86–93.

Rosso, L., Lobry, J. R., & Flandrois, J. P. (1993). An Unexpected Correlation between Cardinal Temperatures of Microbial Growth Highlighted by a New Model. *Journal of Theoretical Biology*, *162*(4). https://doi.org/10.1006/jtbi.1993.1099

Rudnicki, P., Gao, X., Kong, B., & Vigil, R. D. (2017). A comparative study of photosynthetic unit models for algal growth rate and fluorescence prediction under light/dark cycles. *Algal Research*, *24*(January), 227–236. https://doi.org/10.1016/j.algal.2017.03.028

Saad, M. G., Dosoky, N. S., Khan, M. S., Zoromba, M. S., Mekki, L., El-Bana, M., Nobles, D., & Shafik, H. M. (2019). High-throughput screening of Chlorella Vulgaris growth kinetics inside a droplet-based microfluidic device under irradiance and nitrate stress conditions. *Biomolecules*, *9*(7), 1–11. https://doi.org/10.3390/biom9070276

Saad, M. G., Selahi, A., Zoromba, M. S., Mekki, L., El-Bana, M., Dosoky, N. S., Nobles, D., & Shafik, H. M. (2019). A droplet-based gradient microfluidic to monitor and evaluate the growth of Chlorella vulgaris under different levels of nitrogen and temperatures. *Algal Research*, *44*(May). https://doi.org/10.1016/j.algal.2019.101657

Saltelli, A., Ratto, M., Andres, T., Campolongo, F., Cariboni, J., Gatelli, D., Saisana, M., Tarantola, S. (2008). *Global Sensitivity Analysis. The Primer*. John Wiley & Sons, Ltd

Schoolfield, R. M., Sharpe, P. J. H., & Magnuson, C. E. (1981). Non-linear regression of biological temperature-dependent rate models based on absolute reaction-rate theory. *Journal of Theoretical Biology*, *88*(4). https://doi.org/10.1016/0022-5193(81)90246-0

Schulze, P. S. C., Guerra, R., Pereira, H., Schüler, L. M., & Varela, J. C. S. (2017). Flashing LEDs for Microalgal Production. *Trends in Biotechnology*, *35*(11), 1088–1101. https://doi.org/10.1016/j.tibtech.2017.07.011

Sforza, E., Barbera, E., & Bertucco, A. (2015). Improving the photoconversion efficiency: An integrated photovoltaic-photobioreactor system for microalgal cultivation. *Algal Research*, *10*, 202–209. https://doi.org/10.1016/j.algal.2015.05.005

Sforza, E., Calvaruso, C., La Rocca, N., & Bertucco, A. (2018). Luxury uptake of phosphorus in Nannochloropsis salina: Effect of P concentration and light on P uptake in batch and continuous cultures. *Biochemical Engineering Journal*, *134*, 69–79. https://doi.org/10.1016/j.bej.2018.03.008

Sforza, E., Enzo, M., & Bertucco, A. (2014). Design of microalgal biomass production in a continuous photobioreactor: An integrated experimental and modeling approach. *Chemical Engineering Research and Design*, *92*(6), 1153–1162. https://doi.org/10.1016/j.cherd.2013.08.017

Sforza, E., Urbani, S., & Bertucco, A. (2015). Evaluation of maintenance energy requirements in the cultivation of Scenedesmus obliquus: effect of light intensity and regime. *Journal of Applied Phycology*, *27*(4), 1453–1462. https://doi.org/10.1007/s10811-014-0460-x

Sharma, N. K., & Rai, A. K. (2011). Biodiversity and biogeography of microalgae: Progress and pitfalls. *Environmental Reviews*, *19*(1). https://doi.org/10.1139/A10-020

Sharpe, P. J. H., Curry, G. L., DeMichele, D. W., & Cole, C. L. (1977). Distribution model of organism development times. *Journal of Theoretical Biology*, *66*(1). https://doi.org/10.1016/0022-5193(77)90309-5

Sharpe, P. J. H., & DeMichele, D. W. (1977). Reaction kinetics of poikilotherm development. *Journal of Theoretical Biology*, *64*(4). https://doi.org/10.1016/0022-5193(77)90265-X

Sierra, L. S., Dixon, C. K., & Wilken, L. R. (2017). Enzymatic cell disruption of the microalgae Chlamydomonas reinhardtii for lipid and protein extraction. *Algal Research*, *25*. https://doi.org/10.1016/j.algal.2017.04.004

Simionato, D., Block, M. A., la Rocca, N., Jouhet, J., Maréchal, E., Finazzi, G., & Morosinotto, T. (2013). The response of Nannochloropsis gaditana to nitrogen starvation includes de novo biosynthesis of triacylglycerols, a decrease of chloroplast galactolipids, and reorganization of the photosynthetic apparatus. *Eukaryotic Cell*, *12*(5), 665–676.

Sivakaminathan, S., Hankamer, B., Wolf, J., & Yarnold, J. (2018). High-throughput optimisation of light-driven microalgae biotechnologies. *Scientific Reports*, *8*(1), 1–13. https://doi.org/10.1038/s41598-018-29954-x

Slegers, P. M., Wijffels, R. H., Straten, G. Van, & Boxtel, A. J. B. Van. (2011). *Design scenarios for flat panel photobioreactors*. *88*, 3342–3353. https://doi.org/10.1016/j.apenergy.2010.12.037

Sommer, U. (1991). A comparison of the Droop and the Monod models of nutrient limited growth applied to natural populations of phytoplankton. *Functional Ecology*, 535–544.

Stanier, R. Y., Deruelles, J., Rippka, R., Herdman, M., & Waterbury, J. B. (1979). Generic Assignments, Strain Histories and Properties of Pure Cultures of Cyanobacteria. *Microbiology*, *111*(1), 1–61. https://doi.org/10.1099/00221287-111-1-1

Steele, J. H. (1962). ENVIRONMENTAL CONTROL OF PHOTOSYNTHESIS IN THE SEA. *Limnology and Oceanography*, *7*(2). https://doi.org/10.4319/lo.1962.7.2.0137

Sukenik, A., Falkowski, P. G., & Bennett, J. (1987). Potential enhancement of photosynthetic energy conversion in algal mass culture. *Biotechnology and Bioengineering*, *30*(8). https://doi.org/10.1002/bit.260300808

Takache, H., Christophe, G., Cornet, J. F., & Pruvost, J. (2010). Experimental and theoretical assessment of maximum productivities for the microalgae Chlamydomonas reinhardtii in two different geometries of photobioreactors. *Biotechnology Progress*, *26*(2), 431–440. https://doi.org/10.1002/btpr.356

Takache, H., Pruvost, J., & Cornet, J. F. (2012). Kinetic modeling of the photosynthetic growth of Chlamydomonas reinhardtii in a photobioreactor. *Biotechnology Progress*, *28*(3), 681–692. https://doi.org/10.1002/btpr.1545

Talbot, P., Tébault, J. M., Dauta, A., & De la Noüe, J. (1991). A comparative study and mathematicalmodeling of temperature, light and growth of three microalgae potentially useful for wastewater treatment. *Water Research*, *25*(4), 465–472.

Tamiya, H., Hase, E., Shibata, K., Mituya, A., Iwamura, T., Nihei, T., & Sasa, T. (1953). Kinetics of growth of Chlorella, with special reference to its dependence on quantity of available light and on temperature. *Algal Culture from Laboratory to Pilot Plant*, 204–232.

Tibocha-Bonilla, J. D., Zuñiga, C., Godoy-Silva, R. D., & Zengler, K. (2018). Advances in metabolic modeling of oleaginous microalgae Mike Himmel. *Biotechnology for Biofuels*, *11*(1), 1–15. https://doi.org/10.1186/s13068-018-1244-3

Trentin, G., Lucato, V., Sforza, E., & Bertucco, A. (2021). Stabilizing autotrophic cyanophycin production in continuous photobioreactors. *Algal Research*, *60*, 102518.

Turetta, M., Barbera, E., Trentin, G., Bertucco, A., & Sforza, E. (2022). Modeling the production of cyanophycin in Synechocystis sp. PCC 6803 cultivated in chemostat reactors. *Bioresource Technology Reports*, *19*(June), 101132. https://doi.org/10.1016/j.biteb.2022.101132

Vanthoor, B. H. E., Stanghellini, C., Van Henten, E. J., & De Visser, P. H. B. (2011). A methodology for model-based greenhouse design: Part 1, a greenhouse climate model for a broad range of designs and climates. *Biosystems Engineering*, *110*(4), 363–377. https://doi.org/10.1016/j.biosystemseng.2011.06.001

Wágner, D. S., Valverde-Perez, B., Sæbø, M., de la Sotilla, M. B., van Wagenen, J., Smets, B. F., & Plosz, B. G. (2016). Towards a consensus-based biokinetic model for green microalgae–The ASM-A. *Water Research*, *103*, 485–499.

Waldron, C., Pankajakshan, A., Quaglio, M., Cao, E., Galvanin, F., & Gavriilidis, A. (2020). Model-based design of transient flow experiments for the identification of kinetic parameters. *Reaction Chemistry & Engineering*, *5*(1), 112–123.

Walter, É., & Pronzato, L. (1990). Qualitative and quantitative experiment design for phenomenological models—a survey. *Automatica*, *26*(2), 195–213.

Ward, A. J., Lewis, D. M., & Green, F. B. (2014). Anaerobic digestion of algae biomass: A review. In *Algal Research* (Vol. 5, Issue 1). https://doi.org/10.1016/j.algal.2014.02.001

Weikai, Y., & Hunt, L. A. (1999). An equation for modelling the temperature response of plants using only the cardinal temperatures. *Annals of Botany*, *84*(5). https://doi.org/10.1006/anbo.1999.0955

Westerwalbesloh, C., Brehl, C., Weber, S., Probst, C., Widzgowski, J., Grünberger, A., Pfaff, C., Nedbal, L., & Kohlheyer, D. (2019). A microfluidic photobioreactor for simultaneous observation and cultivation of single microalgal cells or cell aggregates. *PLoS ONE*, *14*(4), 1–13. https://doi.org/10.1371/journal.pone.0216093

Wold, S., Esbensen, K., & Geladi, P. (1987). Principal components analysis. *Chemometr. Intell. Lab. Syst.*, *2*, 37–52. https://doi.org/10.1016/B978-0-12-824447-0.00012-1

Wold, S., Sjöström, M., & Eriksson, L. (2001). PLS-regression: A basic tool of chemometrics. *Chemometrics and Intelligent Laboratory Systems*, *58*(2), 109–130. https://doi.org/10.1016/S0169-7439(01)00155-1

Wolf, J., Ross, I. L., Radzun, K. A., Jakob, G., Stephens, E., & Hankamer, B. (2015). High-throughput screen for high performance microalgae strain selection and integrated media design. *Algal Research*, *11*, 313–325. https://doi.org/10.1016/j.algal.2015.07.005

Wolf, J., Stephens, E., Steinbusch, S., Yarnold, J., Ross, I. L., Steinweg, C., Doebbe, A., Krolovitsch, C., Müller, S., Jakob, G., Kruse, O., Posten, C., & Hankamer, B. (2016). Multifactorial comparison of photobioreactor geometries in parallel microalgae cultivations. *Algal Research*, *15*, 187–201. https://doi.org/10.1016/j.algal.2016.02.018

Wu, X., & Merchuk, J. C. (2001). A model integrating fluid dynamics in photosynthesis and photoinhibition processes. *Chemical Engineering Science*, *56*(11), 3527–3538. https://doi.org/10.1016/S0009-2509(01)00048-3

Zarmi, Y., Bel, G., & Aflalo, C. (2013). Theoretical Analysis of Culture Growth in Flat-Plate Bioreactors: The Essential Role of Timescales. *Handbook of Microalgal Culture: Applied Phycology and Biotechnology: Second Edition*, 205–224. https://doi.org/10.1002/9781118567166.ch12

Zarmi, Y., Gordon, J. M., Mahulkar, A., Khopkar, A. R., Patil, S. D., Banerjee, A., Reddy, B. G., Griffin, T. P., & Sapre, A. (2020). Enhanced Algal Photosynthetic Photon Efficiency by Pulsed Light. *IScience*, *23*(5), 101115. https://doi.org/10.1016/j.isci.2020.101115

Zeller, M. A., Hunt, R., Jones, A., & Sharma, S. (2013). Bioplastics and their thermoplastic blends from Spirulina and Chlorella microalgae. *Journal of Applied Polymer Science*, *130*(5). https://doi.org/10.1002/app.39559

Zhang, X., Zhao, J., Zhang, J., Su, S., Huang, L., & Ye, J. (2022). Kinetic modelling of microalgal growth and fucoxanthin synthesis in photobioreactor. *International Journal of Chemical Reactor Engineering*, *20*(7), 723–734. https://doi.org/10.1515/ijcre-2021-0169

Zhang, X.-W., Chen, F., & Johns, M. R. (1999). Kinetic models for heterotrophic growth of Chlamydomonas reinhardtii in batch and fed-batch cultures. *Process Biochemistry*, *35*, 385–389.

Zou, N., & Richmond, A. (2000). Light-path length and population density in photoacclimation of Nannochloropsis sp. (Eustigmatophyceae). *Journal of Applied Phycology*, *12*(3–5), 349–354. https://doi.org/10.1023/a:1008151004317

Zwietering, M. H., De Koos, J. T., Hasenack, B. E., De Wit, J. C., & Van 'T Riet, K. (1991). Modeling of bacterial growth as a function of temperature. *Applied and Environmental Microbiology*, *57*(4). https://doi.org/10.1128/aem.57.4.1094-1101.1991

Acknowledgements

No man is an island. Many people made my PhD an invaluable adventure and I feel so lucky to have lived it.

My profound gratitude goes to my supervisor, Prof. Fabrizio Bezzo, for all the shaping and refining work done on me during my first steps as a scientist, and for preparing me for what lies ahead. Thank you, Fabrizio, for guiding me in this journey, and for the amazing opportunities you gave me during this PhD. You showed me how to see things that I cannot see. Thanks to Prof. Eleonora Sforza, for sharing her deep experience on microalgae and for encouraging me through the challenges I encountered during my PhD. I owe you a lot. Thanks to Prof. Massimiliano Barolo and Prof. Pierantonio Facco, for their advice and for fostering an intellectually stimulating environment in the CAPE-Lab. Many thanks also to current and former members of CAPE-Lab: Daniel, Beatriz, Elia, Margherita, Francesca, Francesco, Gianmarco, Francesco D., Luca Z. and everyone else. You truly make academic life enjoyable and create an environment where research can flourish.

Sincere thanks to Prof. Ben Hankamer for mentoring me during my research period at The University of Queensland, and for inspiring me with his passion for research. Many thanks also to John and Juliane, for the support and for always been available for precious conversations. During my staying in Brisbane, I met many people that made my Down Under experience special. Many thanks especially to Elaine, and Ellen, Sabar, Eduardo and all the members of Prof. Hankamer's group. You made me feel at home even on the other side of the world.

Special thanks to my loyal mates Floris, Carlone, Niccolò, Ciccio, Elia and Guido. Years go by but, despite being far from each other, our bounds do not weaken.

Infine, grazie alla mia famiglia: Silvia, mamma e papà. Ho viaggiato lontano, conosciuto e visto molte cose, ma voi siete sempre quella più bella. Grazie mamma e papà per tutto il supporto che mi date. Non sarei qui senza di voi.